UNIVERSITY OF LEEDS

Time Dependent Multifluid Magnetohydrodynamic Models of C-type Shocks in Weakly ionized, Dusty Media

Ian Ashmore

September 2011

Submitted in accordance with the requirements for the degree of Doctor of Philosophy.

The University of Leeds

School of Physics & Astronomy

Papers Included in this Thesis

Work from the following papers has been included in this thesis:

1. "Time-dependent simulations of steady C-type shocks", van Loo, S., Ashmore, I., Caselli, P., Falle, S. A. E. G., & Hartquist, T. W. 2009, MNRAS, 395, 319.

2. "Transient evolution of C-type shocks in dusty regions of varying density", Ashmore, I., van Loo, S., Caselli, P., Falle, S. A. E. G., & Hartquist, T. W. 2010, A&A, 511, A41.

Paper 1 forms chapter 3. The source terms in the code remained as presented to the author at the beginning of the research project. The MHD model calculations were performed by Ian Ashmore, with the subsequent analysis being jointly performed by Sven Van Loo and Ian Ashmore. Sven Van Loo wrote the initial draft of the paper with contributions from Ian Ashmore. The other co-authors provided useful advice and discussions.

Paper 2 forms chapter 4. The modifications to the source terms and MHD model calculations and primary analysis were performed by Ian Ashmore. Sven Van Loo contributed invaluable assistance with re-drafting the document for publication and responding to the referees comments. The other co-authors contributed useful advice and discussions.

The work in chapter 5 is entirely by Ian Ashmore, including all modifications to the multi-fluid MHD scheme, testing of the new terms, the MHD model calculations and analysis. Paola Caselli provided useful discussions. It is the intention of the author to write this chapter up for publication in the period between submitting the thesis and being examined on it.

Abstract

During the star formation process, low mass protostars go through a period of mass loss which involves expelling as much as half of the material from the accretion disk along their polar axes. The ejected material affects the environment surrounding the protostar as it interacts with the quiescent material of the core. Some of the core material is entrained and accelerated above the local sound speed, ensuring that shocks are present at the interfaces with the undisturbed cloud.

Because of the high densities, appreciable magnetic field and low fractional ionization in such regions, ambipolar diffusion allows the ram pressure of the flow to be dissipated over an extended distance instead of one or two collisions. This precludes collisional ionization and reduces molecular dissociation in the shock front and therefore guarantees efficient cooling. The entrained cloud material is known as a molecular outflow and the extended associated shocks are denoted C-type. In addition, the conditions in the shocks produce streaming velocities between the charged and neutral species. This allows the dust grains present to become negatively charged and facilitates collisions and chemical reactions both in the gas phase and on grain surfaces.

Although previous work exists into the structure and processes in C-type shocks, computational limitations have restricted most studies to either shocks at steady state or ones which are perpendicular to the magnetic field. The conditions in molecular clouds make steady shocks unlikely and the outflows make an arbitrary angle with the magnetic field making it unlikely that an individual outflow is even nearly perpendicular to the upstream field. A new MHD scheme is available which allows numerical models the structures of non-steady oblique shocks to be made.

This thesis details multifluid MHD models of the C-type shocks in molecular outflows using this scheme. Steady perpendicular and oblique C-type shock structures are obtained for suitable molecular outflow conditions and compared to previous models to confirm the schemes accuracy. The first non-steady simulations are undertaken to investigate the interaction of steady,

oblique C-type shocks with perturbations in the upstream density which are chosen to simulate the clumpy nature of molecular cloud cores. Finally terms are developed to describe the systematic collisions between charged grains and neutrals which are thought to return icy mantle and refractory grain core material to the gas phase in a process known as sputtering. A region of parameter space suitable for the molecular outflows from low mass protostars is explored. The results are compared to previous observations and theoretical investigations.

Chemical segregations are noted along the outflow axis, most notably between HCO^+, which is common in the upstream region and the edge of the precursor and water and SiO, which become common in the shock and remain so in the downstream region. It is found that the formation and sputtering of water directly causes the HCO^+ abundance to fall. This finding is in harmony with recent observations.

Further investigation also reveals a that the material sputtered from the grains has a dependence on the angle between the shock normal and the upstream magnetic field. Such a dependence follows from the expressions employed for the sputtering rates, but has not been previously noted or quantified. It is found that the angular dependance is important over a wide region of the parameter space and the insights gained are likely to affect the interpretation of observations of the gas phase products of sputtering in the future.

Contents

List of Figures

List of Tables

List of Abbreviations

IR - infrared

SFR - star forming region

YSO - young stellar object

HST - Hubble Space Telescope

HH - Herbig-Haro (object)

UV - ultraviolet

MHD - magnetohydrodynamic

ISM - interstellar medium

FUV - far ultraviolet

AGB - asymptotic giant branch

LTE - local thermodynamic equilibrium

HI - neutral atomic hydrogen

HII - ionized atomic hydrogen

PDR - photodissociation region

CII - singly ionized carbon

GMC - giant molecular cloud

amu - atomic mass unit

Acknowledgements

Firstly I should like to thank Sven Van Loo. Both for setting the code up for this project in the first place and then helping me to understand it well enough to complete the work. Without his input this thesis would certainly not have been completed. I would also like to thank Sam Falle for developing the MHD code in the first place and also for making it available for this project. I thank Tom Hartquist for allowing me to become a graduate student and both Tom and Paola Caselli for being my supervisors.

I thank my dad: Bruce for passing on his love of science and my mum: Susan for bringing me up and making it her duty to have me educated to the level which made tackling a PhD possible. I thank all of my friends: from Leeds, from snowboarding and skateboarding and from elsewhere for providing an often much needed, but temporary, escape.

Finally, I would like to thank my wonderful lady: Yawen Ho. Her general love and tireless patience allowed me to undertake this work and was especially valuable in the writing up period. If there was one other person who was made to suffer in order for the thesis to be completed, it was her, and I am eternally indebted to her for that.

I would like to dedicate this work to my late grandfather: Morris Ashmore. Although not a man of science himself, he was the best grandad a boy could hope for and the funds he bequeathed to me gave me the breathing space that i desperately needed in order to finish this thesis. He is missed, but lives on in my memories of him.

Chapter 1

Introduction

Since the advent of infrared (IR) astronomy in the 1970s, regions of both low and high mass star formation (SFRs) have been the subject of intensive observations, modeling and discussion. Stars form within dense cores of cold molecular gas, which may form part of larger, more tenuous molecular cloud complexes. These cores are largely opaque at optical wavelengths, which necessitates IR or radio observations. The material from which a star forms is mainly molecular, with a small fraction consisting of atomic or ionized components. Molecular clouds are usually threaded by magnetic fields and are observed to consist of complex and inhomogeneous structures on all scales of interest (see figure 1.1). A star represents an equilibrium between gravity, which causes compression and thermal, magnetic and radiation pressures as well as angular momentum, which all cause expansion. Once formed, low mass young stellar objects (YSOs) may interact with their surroundings by deflecting material from their equatorial accretion disks and collimating it into outflows along their polar axes. These outflows often propagate above the sound speeds in such regions, ensuring that shocks form. Shocked material can entrain and accelerate ambient cloud material and give rise to a secondary, low velocity molecular outflow. The secondary outflow may also have associated shocks where it impinges on the quiescent cloud. Shocks are therefore a ubiquitous feature of the star formation process.

Astrophysical shocks form whenever an energy source drives a flow of material through an ambient medium at supersonic velocities. Every such flow is thus bounded by shocks. Often a shock can be represented by a discontinuous transition in the state of a medium since the supersonic velocity of the flowing material ensures that no information about its approach can travel ahead. In this case, the ordered kinetic energy of the flow is converted into random thermal energy of individual particles over a few elastic collision mean free paths.

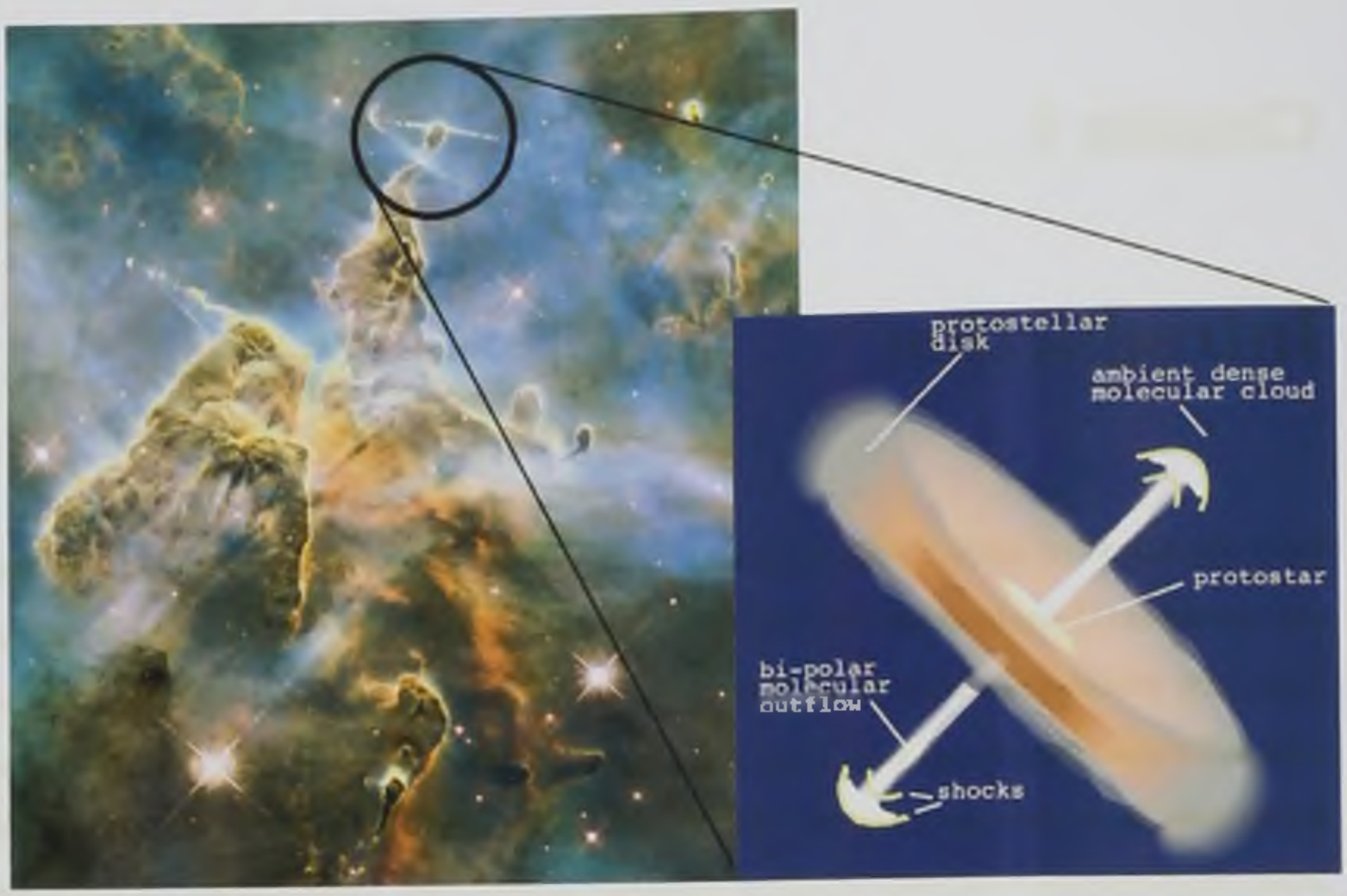

Figure 1.1: On the left is an HST composite image of Herbig Haro 901 and 902 in the Carina nebula, comprising of the visible and IR channels of the WFC3 camera (wide field camera). Reflection nebulae, dark clouds and Herbig Haro (HH) objects are clearly visible. The top object (inside the circle) consists of an obscured protostar and a bipolar outflow which terminates with oppositely oriented bow shocks. The right image is a schematic of this region including the protostar, accretion disk and a bipolar outflow bounded by shocks.

The thermal energy is then dissipated through inelastic collision processes and photon emission over a much wider post-shock relaxation zone. This is known as a J-type shock structure. In regions possessing high density, low ionization and appreciable magnetic fields, such as SFRs, higher signal speeds and ambipolar diffusion permit information to travel ahead of the shock, mediated by the charged particles. This can occur as long as ion-neutral collisions are rare enough for the fluids to decouple, allowing the ions to respond to the field by moving with one velocity whilst the neutrals move with the flow at a different velocity. A component of the magnetic field transverse to the flow direction must be present, otherwise the field plays no dynamic role. Combinations of density, field strength, field orientation and fractional ionization are thought to exist for which the discontinuous shock front is transformed into a much wider

continuous transition. This is achieved through the indirect action of the magnetic field on the neutrals. In such cases, efficient radiative line cooling keeps the post-shock temperatures low enough to suppress molecular dissociation and atomic ionization. The result is a vastly different (C-type) shock structure and emission spectra. The moderate increase in temperature and density found in a C-type shock together with the longer flow time through the shock structure allows endothermic chemical reactions to proceed. These alter the relative chemical abundances in the post-shock gas as well as enriching chemical diversity.

SFRs are also observed to contain dust. Dust grains are responsible for some of the extinction of ultraviolet (UV) photons in molecular clouds. This shields the inner regions, reducing the likelihood of molecular dissociation. Moreover, their surfaces can catalyse chemical reactions, most notably molecular hydrogen formation. Each grain exhibits an effective charge equal to the net sum of the electrons resident on its surface. Grains may therefore move with the charged particles (along the field lines), with the neutrals (along the flow) or between the two. The presence of charged dust may alter both the shock structure and the pre-shock magnetic field configuration. Collisions between charged dust grains and ions, atoms or molecules can result in the liberation of chemically bonded grain material in a process known as sputtering. In fact sputtering is required to explain the observed abundances of certain species (especially SiO) in the shocks associated with some SFRs.

This research represents the most accurate attempt to date of time dependent simulations of C-type shock waves in cold, dense, dusty, weakly ionized media. A numerical multifluid description is adopted, where each species (neutrals, ions, electrons and "N" grain species) is treated as a separate fluid which can move independently, but is coupled to the others through collisional interactions. The multifluid magnetohydrodynamic (MHD) scheme proposed by Falle (2003) is employed, with source terms to describe mass, momentum and energy transfer between the fluids as well as energy sources and sinks. Initially, the scheme is used to re-create earlier theoretical studies to confirm that it is robust and effective, but also to check for any differences which have arisen due to the new, more accurate treatment. From there, the project develops by considering situations not previously modeled due to computational or model limitations. These include the interaction of steady C-type shocks with density perturbations: representative of the inhomogeneous nature of molecular clouds, the inclusion of a more comprehensive chemical model to investigate the effect of chemistry on shock structure and an

evaluation of the effects of grain sputtering on the post-shock gas.

Section 1.1 begins with an overview of molecular clouds since they are the regions in which stars form and through which YSO outflows propagate. This description includes the important components and processes. Section 1.2 concerns the star formation process including the production of outflows which give rise to C-type shocks and the evolution of such outflows. Section 1.3 introduces the concept of an astrophysical shock in its two usual guises, with emphasis on C-type shocks. This includes a description of shock structures, their associated mathematics, as well as an outline of the important radiative and collisional processes within such shocks. Sections 2.1 - 2.3 summarise previous theoretical studies into the properties and behaviours of the various shock types associated with molecular outflows. Section 2.4 gives an introduction to the numerical scheme used throughout this report. It details the relevant equations, the approximations made and the numerical methods employed to obtain time dependent solutions. Section 2.5 describes the initial source terms which model the mass, momentum and energy coupling between various fluids due to collisions, ionizations, recombinations, and cooling emission. Whilst the progress of this project is largely marked by the inclusion of extra, or the modification of existing source terms, those described in Section 2.5 are exact for Chapter 3 and the modifications for later simulations are explained in each subsequent chapter. Section 2.6 presents a concise overview of the remaining chapters in this thesis.

1.1 The interstellar medium

The interstellar medium (ISM) includes any region of galactic space between stars. The ISM exhibits complex structures on all length scales and in all density regimes observed to date. This has become steadily apparent since the early part of the twentieth century, when it was first realised that the space between stars is not empty (e.g. Barnard 1927). In fact, the ISM consists of a tenuous mix of hydrogen and helium gas with trace amounts of heavier elements. These may be atomic, molecular, ionized (§1.1.1) or even in a solid state as dust (§1.1.2). ISM regions that are visible in optical observations include dark clouds, reflection nebulae and supernova remnants. The ISM is heated by the combined radiation fields of any nearby stars as well as shocks and cosmic rays (highly energetic particles). Bulk flows result in shock waves which deposit their energy in the ISM and are produced by supernovae, planetary nebulae and protostars.

Phase	Typical density (cm^{-3})	Temperature (K)	Estimated volume (%)
Hot intercloud	0.003	10^6	~ 50
Warm neutral	0.5	8000	30.0
Warm ionized	0.1	8000	25.0
Cold neutral	50	80	1.0
Molecular clouds	> 100	10	0.05
HII regions	$1 - 10^5$	10^4	-

Table 1.1: Phases of the ISM, showing estimates of the number density and temperatures in each region as well as a highly uncertain estimate of what percentage of the ISM volume each phase accounts for. HII stands for a region of ionized, atomic hydrogen. Adapted from Tielens (2005).

The ISM cools by emitting radiation, the detailed nature of which depends on local conditions. Components of the ISM may be in either cold ($T < 100$ K), warm ($T \sim 10^4$ K) or hot ($T \sim 10^6$ K) phases (Field et al. 1969; McKee & Ostriker 1977). Heating and cooling are discussed in §1.1.3.

The material constituting the ISM is enriched by the previous generation of stars which deposit heavy elements and dust grains towards the end of their lives. This material is incorporated into molecular clouds which themselves give rise to the subsequent stellar generation. The continual enrichment of the ISM in heavier elements produced by stellar nucleosynthesis results in a feedback which permits observers to distinguish discrete populations of stars by their metallicity. In this way the ISM plays a key role in the evolution of a galaxy by bridging the gap between stellar and galactic length scales. The ISM possesses kinetic energy which is supplied by stellar winds and outflows, supernovae explosions and collisions between clouds. These compress the gas of the ISM and set it into motion. The motion is unstable to both Rayleigh-Taylor and Kelvin-Helmholtz instabilities and tends to become turbulent (see e.g. Hueckstaedt et al. 2006). A basic calculation reveals that stars and their associated planetary systems fill a fraction of only $\sim 3 \times 10^{-10}$ of the available space in the Milky Way (Tielens 2005). In the remaining space, the gas of the ISM is organised into phases which are summarised in table 1.1.

The phases noted in table 1.1 are not neatly delineated and for each there will be a gradient

of conditions linking it to its neighbours.

1.1.1 Molecular, atomic and charged material

Molecular material forms the vast majority of the regions within molecular clouds which go on to form stars (§1.2). This is because stellar photons capable of dissociating molecules are rare, and dust is present. The dust surfaces catalyse molecular association reactions. In one model, atomic material collides with and sticks to a grain then migrates around the surface until it meets a reactant. After an association reaction, the products leave the grain surface, returning to the gas phase.

At low ($T \leq 100$ K) temperatures most H_2 is thought to form on grain surfaces (see e.g. Hollenbach & Salpeter 1971; Tielens 2005), since there is no known mechanism to form it via gas phase reactions in the abundances observed (Gould & Salpeter 1963). The high gas phase abundance of H in interstellar clouds, the presence of dust to mediate H_2 formation, the low temperatures and the shielding of dense regions from the surrounding FUV flux means that almost all atomic hydrogen should be molecular on a timescale which is shorter than both the cloud lifetime and the formation time for a protostar ($\sim 10^6$ years, see Lipshtat & Biham 2005). Cazaux & Tielens (2004) report surface H_2 recombination efficiencies approaching 1 for dust temperatures between 10 and 50 K independant of the composition of the grains. Because H_2 is destroyed by photodissociation, the outer layers of a cloud are able to shield the deeper regions very effectively. Beyond a critical column density H_2 is only destroyed via cosmic ray ionizations. The scarcity of cosmic rays therefore ensures that in the depths of the cloud nearly all hydrogen will be molecular.

In addition to H_2 there are other abundant gas phase molecules, most notably CO. In the case that a dense cloud core contains more oxygen than carbon, CO is thought to lock up almost all of the carbon (see §1.1.2). Prior to forming a dense core, the material existed in a more rarefied state. In diffuse clouds, most carbon is ionized since its ionization potential is less than 13.6 eV (the ionization potential of hydrogen) and there is little shielding from the surrounding stellar radiation field. Ion-molecule reactions with H_2 yield species such as CH_2^+ and CH_3^+. As the cloud becomes denser, reactions with atomic oxygen can proceed which produce CO (via a reaction with H_2). Because photoionization and photodissociation are negligible in dense cores, this molecule is stable.

Molecular cloud cores are often studied through millimetre and sub-mm emission from species such as CO, HCO^+ and NH_3. Observations of these species constrain the cloud temperature and density (e.g. Walmsley 1987 and see Figure 1.2 and §1.3.4). Figure 1.2 shows the temperature and density conditions required for various molecular rotational and vibrational states to become excited. If a line is observed, its presence necessarily implies that the emitting region possesses a temperature and density in the range indicated in figure 1.2. Dense cores are also probed via infrared absorption lines towards young stars embedded in them. Such spectra typically reveal solid state species (ices) such as H_2O, CO and CO_2, (Whittet 1993 and see Figure 1.3).

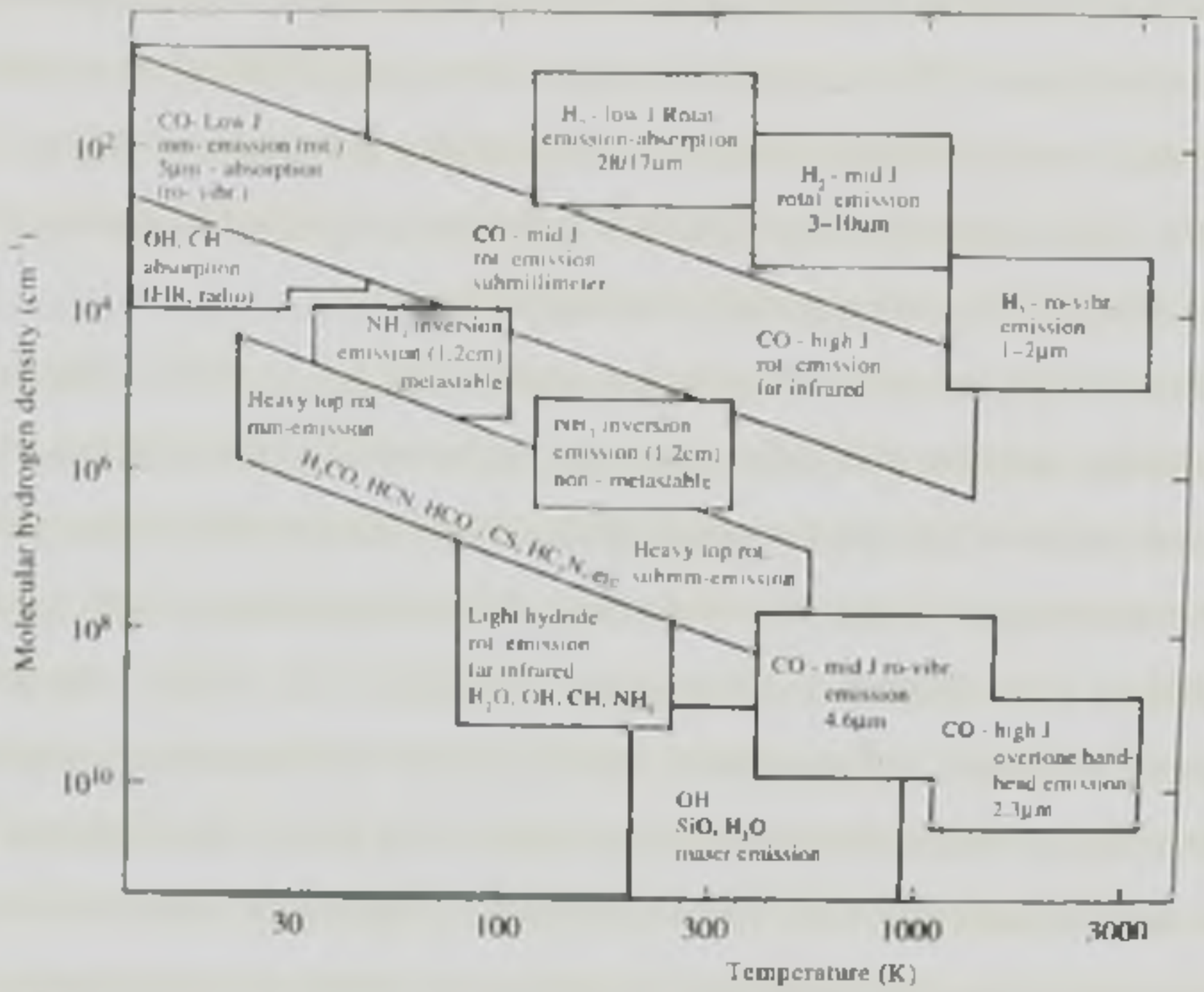

Figure 1.2: A diagram of the molecular emission from a dense cloud demonstrating under what temperature and density conditions each line is a useful probe. Taken from Genzel (1991).

Although atomic material is common in the more diffuse parts of molecular clouds where the far ultra violet (FUV) flux (photons which have a maximum energy of 13.6 eV) is fairly unattenuated, it is relatively rare in dense cores. The atomic material which remains present can provide an efficient line cooling mechanism. The most notable atomic species is oxygen, the third most common element in the galaxy (after hydrogen and helium). Observations suggest that almost none of the oxygen not in CO ($\sim 6\%$), silicate grain material ($\sim 20\%$) or water ice ($\sim 24\%$)

is molecular, (Draine et al. 1983; Combes & Wiklind 1995). This is because oxygen chemistry is started with a series of neutral-neutral reactions which are endothermic or require activation energies to proceed ($T > \sim 250$ K) and the FUV flux is still capable of photo-dissociating any oxygen bearing molecules. Oxygen has several fine structure levels that are close to its ground state caused by relativistic (spin) effects. Under the influence of an external magnetic field, the symmetry in electron states (energies) are broken and this splits a single state in a process known as degeneracy. Since different energies infer photons of different wavelengths the spectral line is also split. Fine structure lines are closely spaced and readily excited. Cooling occurs when they spontaneously de-excite and emit a photon which escapes the region (see §2.5.3). Observations of the neutral oxygen [OI] 63 μm fine structure line in absorption suggest that in molecular clouds over 40% of oxygen is in atomic form, (e.g. Poglitsch et al. 1996). It is also mainly neutral, even in diffuse clouds, since its ionization potential is 13.618 eV (Hollenbach et al. 2009). This is higher than that of atomic hydrogen, so outside HII regions oxygen is very effectively shielded from any potentially ionising radiation.

In diffuse clouds the fractional ionization can be high ($\chi_i \geq 10^{-4}$). This is because the FUV interstellar radiation field will ionise any species with a potential below 13.6 eV. C^+ is the dominant ion as it is the most common species below this threshold. Since photons capable of carbon ionization are largely absorbed near a clouds outer edges, at high column densities C^+ recombines with electrons to form neutral carbon (§1.1.3). Dense cores therefore have low fractional ionization. For more detail on the reactions which operate in various regions of molecular clouds as well as their products see figure 1.9 in §1.3.4. The fractional ionization in all but the densest molecular cloud regions are directly related to the visual extinction and hence the column density from the clouds edge. In dense cores (where no ionising radiation remains), the main source of ions and electrons are cosmic ray ionizations of H_2 (since hydrogen is by far the most abundant molecule). Since the magnetic field only acts directly on charged particles and its effect is mediated to the neutrals via collisions, in the case that ion-neutral collisions are rare the neutrals can "slip" through the field lines in a process known as ambipolar diffusion (Mestel & Spitzer 1956). The speed at which they slip is limited by their rate of collisions with the ions (see §1.3.3). In the densest regions of molecular clouds the fractional ionization deduced from model calculations are as low as $6 \times 10^{-9} < \chi_e < 5 \times 10^{-8}$ (Schilke et al. 1991), which is close to that inferred from observations (Caselli et al. 1998). In such cases, collision

rates are small and the speed of ambipolar diffusion can be high.

1.1.2 Dust grains

The presence of sub-micron scale solid particles in the ISM was first inferred by observations of the reddening of distant starlight (Trumpler 1930), although the extinction of starlight in some regions of the Milky Way had been noticed much earlier. Dust is an important component of the ISM since it locks up substantial fractions of many heavy elements, produces the dominant contribution to opacity for radiation longward of the Lyman limit and provides a surface onto which chemical species can accrete and react. Insterstellar dust grains form a significant fraction of the mass of interstellar clouds ($\sim$ 1%). This "canonical" value comes from constraints imposed by observable processes such as the extinction, scattering or polarisation of background starlight and IR dust emission. It is further constrained by the demand that dust grains do not consume any element in excess of its inferred cosmic value minus the observed gas phase abundance. Models for the dust population in the ISM must satisfy the following observational restrictions (Draine 2009): 1) Around two thirds of the dust mass exists in grains with radii larger than 5×10^{-6} cm. This is required to fit the observed extinction, polarisation and scattering of optical light. 2) Around one fifth of the dust mass is in very small grains, with radii less than 2.5 $\times 10^{-6}$ cm. This is required to explain the steep rise in UV extinction. Whilst these constraints are suitable for most of the ISM they may not be representative of dense cores. Interstellar dust grains are thought to follow the size distribution first proposed by Mathis et al. (1977) and later modified by Weingartner & Draine (2001). This is a power law distribution such that if r is the grain radius:

$$n(r) \propto r^{-3.5}. \tag{1.1}$$

For many years the notion that grains predominantly form in the cool regions (T $\sim$ 500 - 1500 K) of evolved stellar envelopes (giants and supergiants) and supernovae remnants was prevalent and favoured by astronomers. Dust of this type is known as stardust. Stardust forms through the coalescence of refractory atoms and molecules, which, by their chemical properties possess a tendency to coagulate (e.g. Rawlings 1998). All evolved low to medium mass stars on the Asymptotic Giant Branch (AGB) display very extended envelopes (up to 1000 times their

original radii of around one AU, Habing & Olofsson 2003) and high mass loss rates (10^{-8} - 10^{-4} $M_\odot$ yr^{-1} where $M_\odot$ is the mass of the Sun, e.g.Wood et al. 2007). Strong stellar winds are able to expel a large fraction ($\sim 40\%$) of the original mass, which is only weakly bound by the gravitational field at such large radii. AGB stars also display a strong excess in the IR. The excess has been ascribed to dust grains, which absorb stellar photons, and re-emit them as an IR continuum.

The composition of stardust depends on the details of the environment in which it forms, i.e. whether carbon or oxygen rich. If $C/O < 1$, the parent star is denoted M type. CO will lock up almost all of the carbon before dust can form and grains will be silicate based. If $C/O > 1$, the star is denoted C type and the grains will be carbonaceous (amorphous carbon or soot). Stardust forms from "seed" particles (atoms or molecules). The seeds have high bond energies, are stable at high temperatures and possess high sticking coefficients. Examples include Mg, Fe, TiO and AlO. M-type stars are observed to constitute the vast majority (~ 76 %) of main sequence stars (Ledrew 2001). From consideration of elemental abundances, most dust formed around M-stars is thought to be of a magnesium-iron-silicate nature, (see Gail & Sedlmayr 1998, and references therein). The seed molecules can then act as nucleation centres or stick together, forming amorphous clusters, and eventually dust grains (see e.g. Rawlings 1998). Once formed in the outer envelope of an evolved star, stellar winds transport a dust grain into the ISM where it will later form part of a molecular cloud. Detailed theories about the nucleation and growth of dust grains in the envelopes of evolved stars are reveiwed in Salpeter (1977). Over time, this process results in several species becoming heavily depleted from the gas phase as collisions incorporate them into dust grains ranging in size from large molecules (such as polycyclic aromatic hydrocarbons) up to amorphous solids on a micro meter scale (Draine 1995).

This simple scenario of dust formation is complicated somewhat when one compares the frequency of supernovae driven shocks to calculations of grain destruction rates in those shocks. Jointly, these lead to stardust lifetime estimates of ~ 3 - 5×10^8 years, (Draine & Salpeter 1979; Seab 1987). Renewal of the stardust occurs over a timescale of $\sim 2.5 \times 10^9$ years, (Jones & Tielens 1994). From this, one would expect only $\sim 10\%$ of refractory elements to be locked up in stardust. Since over 90% of some elements are observed to be missing from the gas, it seems that much of the solid material must have condensed in the ISM and is therefore not stardust

(e.g. Draine 1995; Draine 2009). One process by which this may happen is that rarer species with high condensation temperatures (e.g. Al_2O_3 or corundum) solidify first, assuming the role of seeds and thus determining the number density of the grains. As the temperature drops further, more abundant atoms such as Mg and Si are able to condense and they preferentially do so by accretion onto the pre-existing seeds. So, although the mass of the final grains is dominated by silicates, the seed is of another material (e.g. Salpeter 1977). Nearby supernovae will largely destroy the grains but the most refractory components may be bonded strongly enough to remain intact. These can later act again as the seeds for dust reformation in the cooling post-shock region. Draine (2009) presents model calculations for dust re-formation in the ISM and concludes that as long as seeds are present, depletion and grain growth can occur on timescales of $\sim 2 \times 10^5$ years, even in neutral atomic hydrogen clouds with $n_H \approx 30$ cm^{-3}.

When an atom or molecule collides with a grain, it may stick to the surface. The likelihood of it sticking is determined by a coefficient which depends on the impinging species and the temperature. Even in the diffuse ISM, efficient IR continuum emission ensures that grains with radii larger than $\sim 10^{-6}$ cm remain very cold ($T \leq 20$ K). At this temperature, almost any atom or ion incident on the grain surface is expected to stick to it. Such atoms are only physisorbed (i.e. attached via van der Waals forces), with binding energies (B) in the range $\sim 0.05 \leq B \leq \sim 0.5$ eV. Accreted species have thermal desorption probabilities determined by their binding energies, i.e. at T = 20 K, for a particle with a binding energy of 0.05 eV the thermal desorption timescale is 1 second, whereas with a binding energy of 0.1 eV it is 5×10^5 years. The binding energies to amorphous silicate surfaces are only poorly known, but the dependance of the thermal desorption timescale on the binding energy may explain why only some species (i.e. those with binding energies $\gtrsim 0.1$ eV) are depleted onto grains (Draine 2009).

There is another possible explanation of the selective elemental depletion onto grains: In the diffuse ISM grains are exposed to UV photons. These photons photo-excite any states with E < 13.6 eV in the atoms adsorbed on their surfaces. If the UV excitation rate is $\sim 10^{-10}$ s^{-1}, then an adsorbed atom experiences $\sim 10^4$ photo-excitations before a single layer of atoms larger than H is deposited on top of it. Because photo-excitation is so frequent, the only materials that can form via accretion in the diffuse ISM are those that are not desorped, destroyed or altered by interactions with UV radiation. This might account for the selection of silicate and carbonaceous materials. In fact, the presence of UV radiation could actually assist the formation of new layers

of amorphous silicate since photo-excitations allows for the re-arrangement of chemical bonds between the new O, Mg, Si and Fe atoms (which are added one at a time). Such rearrangements may result in refractory material bound with energies up to 50 times higher than physisorbed material. FUV processing may also retain a partition between amorphous silicate and carbon material, even in regions where both species are present. If a carbon atom is physisorbed onto an amorphous silicate surface and subsequently photo-excited to a state which is repelled by the surface, it will be ejected. A silicate surface is hence kept carbon free (Draine 2009).

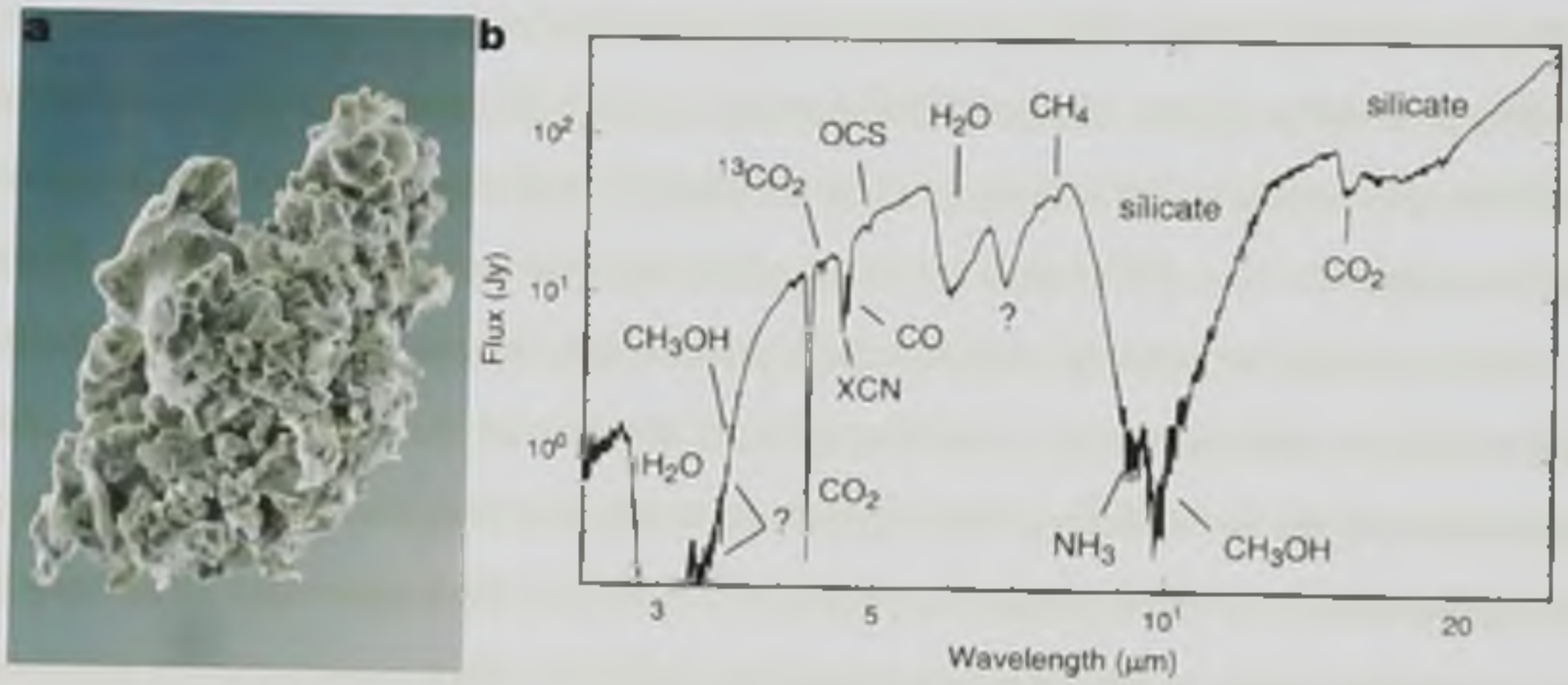

Figure 1.3: (a) Photograph of an interplanetary dust particle with a size of $\sim 10\mu$m. The granular nature where smaller sub units have coalesced into the final grain is clearly shown. Photograph from www.cosmotography.com (b) Mid IR spectra of the protostar W33A obtained from ISO showing solid features in absorption. Except for the 10 μm and 18 μm absorption bands, these features are due to simple solid state molecules in icy mantles. The species responsible for absorption are indicated if known (from Gibb et al. 2000)

In dense molecular clouds where there are few energetic photons, accretion occurs as gas phase molecules "freeze out" (adsorb onto the grain surface) during low temperature collisions. Adsorption refers to the process whereby particles are able to stick to a surface because the surface layer of previously adsorbed surface atoms are not completely surrounded and so have free bonds available. Bonds formed in this way may be either covalent, or due to intermolecular (van der Waals) forces. In the absence of processes to provide energy to eject accreted atoms or molecules the only possible removal mechanism is random thermal fluctuations. Occasionally these provide sufficient energy for a particle to evaporate from the surface. The timescale for

gas phase species to be depleted by freezing out is of the order of 10^5 years at densities of 10^4 cm^{-3}. This is shorter than both the evolution timescale for molecular clouds ($\sim 10^7$ years) and the free fall collapse time for a dense core ($\sim 10^6$ years). Accretion and subsequent grain surface reactions can form a volatile mantle of water ice mixed with CO, CO_2 and trace amounts of other molecules (e.g. OCS, SiO and methanol: see Tielens et al. 1994; Jiménez-Serra et al. 2008; Arce et al. 2008). The ice abundances inferred from absorption studies cannot be the sole result of water molecules being adsorbed directly onto grain surfaces and therefore include some which have formed in reactions on the grain surface (e.g. Ioppolo et al. 2009). The ice molecules are physisorbed to the surface under van der Waals (intermolecular) forces. As such, they are much more weakly bound than the refractory material of the grain core. Physisorbed particles are bound to the surface with typical energies less than 0.1 eV. Once there is more than a single layer of ice on a surface, the bonds are between hydrogen atoms in different water molecules. Because hydrogen atoms are involved, the van der Waals force increases and the binding energy rises to ~ 0.5 eV (e.g. Sandford & Allamandola 1988; Dartois 2006). IR spectra of objects in or behind molecular clouds reveal absorption features from molecules embedded in icy mantles. Figure 1.3 (b) shows such a spectra. If the mantle is subsequently exposed to FUV radiation the process may be reversed, but at the very least photolysis will result in the formation of an organic residue mantle (Tielens & Allamandola 1987).

Since electrons have much higher thermal speeds than ions, a neutral grain in a plasma with equal number densities of ions and electrons is much more likely to encounter an electron. Most grains are therefore negatively charged (Spitzer 1978). The magnitude of the charge depends on the grain size and the gas temperature. Model calculations reveal most grains to carry a single electron in quiescent dense core material (Flower et al. 2007). In sufficiently dense, shocked regions of molecular clouds dust grains can become highly negatively charged and play an important role in determining the fractional ionization and the width of the ambipolar diffusion region (e.g. Caselli et al. 1997). The grain charge and the grain-neutral collision rate jointly determine the degree to which the charged dust grains are coupled to the magnetic field and hence their contribution to friction with the neutrals (see §1.3.3).

In order to complete the description of the ISM, an explanation of how energy is partitioned between its constituents is required. This involves the transfer of energy, via heating and cooling and the equilibrium obtained.

1.1.3 Heating and cooling

1.1.3.1 Heating

Typically the ISM is far from local thermodynamic equilibrium (LTE). A system is said to be in LTE when thermal, mechanical, radiative and chemical equilibriums are simultaneously obtained. In such a system collisions in a gas are frequent enough to thermalise the velocities of the particles. The temperature is then the kinetic temperature. In most regions of the ISM the local stellar flux is too dilute and collisions are too rare for LTE to be obtained. This means that the atomic and molecular bound energy levels are rarely populated in the ratios one would expect from the Boltzmann equation (Spitzer 1978). In the absence of LTE, the balance between various heating and cooling mechanisms determines the temperature of the gas. The contribution of each mechanism depends on the local density, temperature and ionization state. Sometimes one must also consider processes occurring nearby, especially those producing high energy photons or resulting in bulk flows of material.

The most obvious gas heating mechanism is the absorption of photons from the interstellar radiation field. Three modes of excitation can result from photon absorption: 1) Electronic excitation of atoms, ions and molecules occurs when an orbiting electron jumps to a higher energy state. With sufficient energy the electron may escape (photoionization), carrying away kinetic energy and resulting in an excited electron and ion. The excess kinetic energy is quickly shared with other atoms and electrons through collisions, thus heating the gas. Electronic excitation of hydrogen requires a substantial fraction of the energy needed to ionise it so its electronic transitions result in photons in the optical through extreme UV region of the spectrum. Ions with unpaired electrons in low lying energy levels may have electronic transitions in the visible range. 2) Vibrational excitation of molecules. In this case the absorbed photon energy accentuates the bending and stretching of the bonds between the atoms within a molecule. Because such excitations involve the motions of heavier atoms as opposed to electrons, the associated transitions are shifted to the mid IR. 3) Rotational excitation of molecules. A molecule rotates with discrete energies and the absorbed photon energy may cause it to jump to a higher rotational level. Since the rotational energy of a molecule is proportional to the inverse of its reduced (or inertial) mass, molecular rotational levels are much more closely spaced than the electronic or vibrational energies. These transitions result in photons at sub-millimeter wavelengths ($0.1 \leq \lambda$

$\leq$ 1 mm).

A stellar radiation field typically includes FUV photons (E $>$ 10 eV). Their absorption results in the photoionization of gas phase atoms and molecules. All photons with E $\geq$ 13.6 eV are absorbed (mainly by hydrogen) in the region immediately surrounding the star, producing a bubble of ionized atomic hydrogen (HII region). Few photons above this energy remain outside such regions. Immediately surrounding a HII region, photons are still present which are capable of dissociating molecular hydrogen and ionising trace elements. These dissociations are self-shielding and result in a photodissociation region (PDR), mainly consisting of neutral atomic hydrogen and singly ionized carbon (HI/CII region). This results in three distinct regions: HII regions where very energetic photons are available, PDRs where trace elements with potentials below 13.6 eV are ionized and hydrogen is mainly atomic and molecular clouds, where molecules remain mostly un-dissociated and un-ionized. In HII regions H ionization dominates the heating of the gas. In PDRs photoionization of large molecules and small dust grains as well as photodissociation of molecular hydrogen takes over. In molecular regions, photodissociation of small molecules can play a similar role to photoionization, but this is only important in dense regions illuminated by a strong FUV flux. When this kind of flux is lacking, cosmic ray ionizations provide the dominant source of heating, (see below).

Dust grains also absorb photons. UV and optical starlight absorbed by dust will excite atoms within the grain. This may result in the emission of photoelectric electrons and the possible ejection of those electrons from the grain. If the photon energy is below the ionization potential of the atom which absorbs it then its energy converted into thermal energy of bound particles. Thus the dust grains are heated. They relax either through collisions with gas particles or by emitting IR continuum photons both of which couple dust grains to the rest of the gas. Dust grains maintained at temperatures above $\sim$ 10 K by the absorption of stellar photons, in regions where collisions do not dominate, will efficiently radiate in the sub-millimetre range. Observations in this region of the spectrum reveal structures in SFRs which are heavily obscured in the optical due to dust extinction and scattering. Hot dust in regions where the FUV flux is fairly unattenuated may also radiate in specific IR bands which are associated with the molecular bonds of the grain material.

The ISM is pervaded by x-rays and energetic particles. Absorption of x-rays and collisions with low energy cosmic rays (a few MeV) provide additional methods to heat the ISM. Both

transfer energy primarily through ionization. Cosmic ray heating is dominated by collisions between gas particles and low energy cosmic rays since these are believed to be much more numerous than high energy ones. Cosmic rays are able to penetrate the densest regions of the ISM and are therefore particularly important in molecular regions where the FUV flux is strongly attenuated. In the most shielded regions of molecular clouds where there are no ionising photons, cosmic rays provide the only source of ionization. Thus they determine the fractional ionization as well as providing thermal energy to the gas. X-rays are prevalent near bright sources of energetic photons such as supernovae remnants. When a cosmic ray particle or x-ray photon ionises a neutral particle, an ion (possibly excited) and an energetic electron are produced. Subsequent collisions then distribute this energy amongst other particles and may result in further molecular dissociations (e.g. Draine et al. 1983).

The passage of a strong shockwave from a nearby supernova heats gas and dust causing ionization, molecular dissociation and excitation (for further detail see §1.3.1) as well as grain destruction (see §1.3.5). The remnant of a supernova explosion consists of a compact object and a rapidly expanding shock wave where the ejecta (1 - 5 $M_{\odot}$) impinges on quiescent cloud material. The expanding ejecta (launched at $\sim 10^4$ km s^{-1}) sweeps up the surrounding ISM during a free expansion phase which lasts until the entrained cloud material contains roughly the same mass as the original ejecta. The remnant then undergoes a period of adiabatic expansion (no heat is gained or lost from the system) where it gradually decelerates (deceleration is proportional to $1/r^{3/2}$ where r is the radius of the remnant) and cools (ejecta temperature is proportional $1/r^3$) due to mixing with the entrained ISM. This occurs over a period of about 10^4 years. When the shell has cooled to $\sim 10^6$ K, the remnant enters the radiative phase. Electrons recombine with ions, which permits more efficient cooling. The enhancement in cooling results in thin, dense shells where the expansion velocity varies proportional to $1/r^3$. Eventually the expansion stops and the remnant is absorbed into the ISM. In addition to supernovae, shockwaves can also be produced by the outflows from young and evolved stars and cloud-cloud collisions. Any combination of low density, high fractional ionization, low magnetic field and high shock speed results in a narrow shock front. In this case, collisions in the front convert the ordered kinetic energy of the flow into thermal energy of individual particles in just one or two interactions. If sufficient, the increased thermal energy first causes ionization and molecular dissociation. High velocity ($v_s > 50$ km s^{-1}) shocks are required for this. Next to occur are electronic, vibrational and ro-

tational excitations due to both collisions and the absorption of photons. Having passed through the shock front, the gas cools in a relaxation layer through radiative de-excitation, electron recombination and molecule reformation. Recombination photons from the post-shock region can travel upstream exciting and ionising gas ahead of the shock front, forming a radiative precursor, (see §1.3.1). The inelastic processes occur over a much longer timescale than the elastic conversion of kinetic energy to heat. Any radiation escaping the shock region without re-absorption contributes to the post-shock cooling of the gas.

Shockwaves passing through cool dense regions with appreciable magnetic fields may operate a different dissipation mechanism. This converts the ram pressure of the flow into thermal energy over a much wider region. When such dissipation occurs, different shock structures are obtained and different heating and cooling mechanisms dominate. These shocks and dissipation mechanisms form the basis of §1.3.2 and §1.3.4 as well as subsequent chapters.

1.1.3.2 Cooling

When a gas particle has been heated by any of the mechanisms above, its occupies an excited state. It may then dissipate the extra energy by exciting other particles in inelastic collisions or else by emitting photons. Any excited gas particle will eventually de-excite on a timescale determined by either the density for collisional de-excitation, or a spontaneous de-excitation rate coefficient for radiative relaxation. The cooling of gas in the ISM can be a complex problem since both collisions and radiative transfer must be considered. With sufficient density, collisions always dominate but at lower densities radiative de-excitations take over. This can be elucidated by considering a two level system (levels denoted u for upper and l for lower). Collisions have coefficients γ_{ul} for de-exciation and γ_{lu} for excitation. Radiative de-excitations have Einstein coefficients A_{ul}. So in statistical equilibrium the two levels are connected by the expression:

$$n_l n \gamma_{lu} = n_u n \gamma_{ul} + n_u A_{ul}, \tag{1.2}$$

where n denotes a number density. This allows for the definition of a critical density, above which collisions dominate and below which radiative de-excitation dominate the de-excitation process. For any upper level:

$$n_{cr} = \frac{\sum_{l<u} A_{ul}}{\sum_{l \neq u} \gamma_{ul}}. \tag{1.3}$$

Above the critical density, LTE is obtained and the level populations are given by the Boltzmann expression solved at the kinetic gas temperature. The collisional de-excitation rate coefficients depend on whether neutral-neutral, electron-neutral or ion-electron collisions are under consideration since each involves different forces. The critical densities for allowed electronic transitions are very high, so in the ISM these levels will not usually be in LTE. Because they possess low collisional excitation rate coefficients, the vibrational transitions of molecules also have high critical densities. Optical forbidden transitions in the ISM usually occur on far shorter timescales than those implied by their collisional de-excitation rate coefficients even in hot ($\sim 10^4$ K) HII regions, in which case, collisions are not important. However, far-IR atomic fine structure lines may have critical densities in the regions of interest. Likewise, low lying molecular rotational levels have critical densities which span the range encountered in molecular clouds.

The absorption of radiation must also be taken into account when calculating the level populations. If the mean radiation field (abundance) of photons with energies corresponding to the transition between u and l is given by J_{ul}, equation (1.2) becomes:

$$n_l n \gamma_{lu} + n_l B_{lu} J_{ul} = n_u n \gamma_{ul} + n_u A_{ul} + n_u B_{ul} J_{ul}, \tag{1.4}$$

the B terms are Einstein coefficients for absorption and stimulated emission. Stimulated emission refers to the process where an excited atomic or molecular electron interacts with an electromagnetic wave of a given frequency and drops to a lower energy level. The energy is transferred to the field by the emission of a photon with the same phase, frequency, polarisation and direction of travel as the photons of the incident field. By considering the escape probability of a photon in terms of the optical depth of the region, the problem can be simplified. In this approximation, the net absorptions (corrected for stimulated emission) equals the number of photons which do not escape. If $\beta(\tau)$ is the probability that a photon formed at optical depth τ escapes, equation (1.3) becomes:

$$n_{cr} = \frac{\beta(\tau_{ul}) A_{ul}}{\gamma_{ul}}, \tag{1.5}$$

Thus photon trapping lowers the density at which LTE is approached. This is to be expected since an emitted photon which is quickly re-absorbed has the same effect on the absorbing particle as a collision with another particle. Whether collisional or radiative de-excitation dominates therefore depends on the detailed conditions in the gas. Excitation by inelastic collisions behind any type of shock is dependent on the composition of the gas, and its temperature and density.

When a medium is largely ionized, collisional excitation is always dominated by electrons due to their high kinetic speeds. Quiescent ionized hydrogen gas has a temperature of $\sim 10^4$ K and may cool through electron recombination and free-free transitions (where an electron is decelerated in the electric field of a proton). Free-free transitions only become important when $T \geq \sim 10^7$ K. Both electron recombination and free-free transitions are unimportant when other species are present even in trace amounts since such species possess lower lying electronic states. However, above 10^5 K most species (except Fe) retain few bound electrons so such cooling is suppressed. Above around 10^4 K cooling is mainly due to collisional excitation of H but a sharp increase in collisional ionization also results in more efficient excitation by electrons (see above). For temperatures well below this, electronic excitation rates of H will be very small. Typical densities in ionized regions of the ISM are far below the critical densities for collisional electronic de-excitation so spontaneous de-excitations are usually more important, even for forbidden transitions.

In neutral atomic gas, collisions with hydrogen dominate inelastic excitation due to its high abundance. Cooling is dominated by the de-excitation of low lying electronic states. The lowest electronic level of atomic hydrogen is 10.5 eV ($\sim 1.2 \times 10^5$ K) above the ground state. Such temperatures are only obtained near hot stars and in very strong shockwaves. Even when most hydrogen is atomic and neutral, some electrons may still be present from the ionization of trace elements with potentials below 13.6 eV, (e.g. C, S, Si). Cosmic rays also maintain a small amount of ionized hydrogen and helium even in the absence of capable photons. If the total fractional ionization is moderate (i.e. the density is low), excitations of trace elements by these electrons can be very important because of their lower lying energy levels. At higher densities, collisional excitation of trace elements by atomic or molecular hydrogen becomes dominant, i.e. for $10^4 < T < 5 \times 10^5$ K, excitation of the permitted lines of H and various ionization stages of He, C, N and O are common whenever the density permits.

At temperatures above around 5000 K molecular dissociation is prevalent but low lying

electronic states of atomic trace species become excited. Metastable states (such as [OI] λ 6300 $\AA$) of these species can also be excited. In all but the most rarefied vacuums, excited metastable states persist long enough to be collisionally de-excited (milliseconds to seconds compared to microseconds for permitted states). In the ISM however, collisions are often rare enough for metastable states to spontaneously de-excite, resulting in "forbidden" emission. Such transitions are denoted using square brackets. Excitation is dominated by the most abundant species until it becomes fully ionized.

At low temperatures ($T < 5000$ K), the gas remains mostly molecular. This allows molecules, ions and atoms to be all involved in cooling, which is consequently very efficient. The fine structure levels of ions and neutral atoms are readily excited. As the name implies, these levels are closely spaced. At low densities ($n < 10^4$ cm^{-3}), excitation of the singly ionized carbon line [CII] at 158 μm dominates, whilst at higher densities, neutral atomic oxygen [OI] at 63 μm takes over. This is discussed in more detail in §1.3.4. In addition to fine structure levels, many excited molecular vibrational and rotational levels can become populated, (see figure 1.2). Rotational levels are also very numerous and closely spaced, so the existence of molecules permits highly effective post-shock cooling. The close spacing of the molecular rotational levels and the ease with which they are excited is also the reason that molecular clouds are cold. The molecular cooling rates depend on the ratio of the level populations of interest to the local velocity gradient (which sets the optical depth of a transition). At low densities CO dominates the cooling due to its high abundance. Because the low level transitions of CO have low critical densities, CO cooling diminishes at high densities. Other molecules (most notably atomic oxygen and water) start to contribute and may even surpass CO (see figure 1.10). Water also becomes progressively more important at higher temperatures, since it is efficiently formed from atomic oxygen (see §1.3.4) and solid state water is returned from grain surfaces to the gas phase (see §1.3.5).

1.2 Star formation

1.2.1 Molecular clouds: stellar nurseries

Although the ISM may exist in different phases (see §1.1), new stars only form in its coldest, densest regions. These are the dense cores embedded within clumps, which are themselves contained in giant molecular clouds, (GMCs). Some phases of the ISM such as diffuse molecular

Cloud Region	Density (cm^{-3})	Size (pc)	Temperature (K)	Mass ($M_\odot$)
Giant Molecular Cloud	100	50	15	10^5
Dark Cloud Complex	500	10	10	10^4
Clump within a GMC	~ 500	~ 2	10	~ 250
Dark Cloud (Individual)	1000	2	10	30
Dense Core / Bok Globule	10^4	0.1	10	10

Table 1.2: Physical properties of molecular clouds, showing estimates of the average number density, size, temperature and mass within each region. The values for clumps within a GMC are the typical values for a clump in the Rosette Molecular Cloud (see below). Adapted from Stahler & Palla (2005).

and atomic (HI) clouds are contained by the pressure of a surrounding, more rarefied and warmer medium. In GMCs however, the main cohesive force is the clouds own gravity even though it is only the denser clumps and cores which are gravitationally bound. Their low temperatures ensure that thermal pressure plays only a minor role in the balance of forces, which is why such environments are favourable to star formation (e.g. Stahler & Palla 2005). Like the ISM in general, molecular clouds consist of gas and dust in various configurations, i.e. the line denoted molecular clouds in table 1.1 contains further substructure. These phases are detailed in table 1.2.1, which shows them all to have low temperatures, but widely ranging densities, masses and sizes. Each phase is again connected to its neighbours via transition layers with intermediate properties.

GMC complexes are clustered along the spiral arms in both the Milky Way and other spiral galaxies. As atomic material flows into the potential well of an arm, molecular pockets form within it because the higher densities result in efficient H_2 formation on dust grains. High column densities ensure effective H_2 self shielding so the inner molecular regions are not exposed to FUV photons, (see §1.1.1). The absence of GMCs outside the spiral arms suggests that they do not survive as long as the time taken to traverse between two adjacent arms ($\sim 10^8$ years at the galacto-centric radius of the Sun). A typical GMC complex survives for around 3×10^7 years, or a few percent of the galactic rotation period at the solar galactic radius. After that period around three percent of its mass has been converted into stars. GMC complexes are nor-

mally destroyed by the intense winds emanating from embedded O and B type stars. In fact, every galactic OB association observed to date is closely associated with a GMC (see Stahler & Palla 2005 and references therein).

GMCs may be contained by gravity but they persist for longer than their free fall times ($\sim 10^6$ years). This implies that they must be supported in some way. If a cloud is in virial equilibrium then the sum of the bulk kinetic energy (K), the energy in random thermal motion (P) and the magnetic energy (B) must equal the gravitational potential energy (Ω) within it: K + P + B - Ω = 0. A simple analysis indicates that thermal energy is incapable of supporting the cloud since the temperatures are so low (e.g. Lizano 1989). This is supported by the observation of broad non-thermal lines. Support must therefore come from a combination of magnetic pressure and the kinetic energy of bulk motions within the cloud (see Tielens 2005).

The galactic disk is permeated by a large scale magnetic field. The local direction of this field can be inferred via polarisation observations of emission either passing through or originating within the region (e.g. Hildebrand 1988). If this were the only field component present, ambipolar diffusion would cause a self gravitating cloud to settle into a planar configuration with its long axis perpendicular to the field lines (see §1.2). Observations of the polarisation of starlight by grains however reveals the field on small scales to display significant scatter. This is consistent with a random magnetic field component on top of a smooth background. The random component is at least partly due to the propagation of MHD waves (§1.3.2). These waves may retard the flattening of the cloud and assist the formation of inhomogeneities throughout it. The remaining support is provided by bulk kinetic energy within the cloud due to clump motions and turbulence. This kinetic energy matches the total energy in the magnetic field (background plus a significant random component). Each mechanism contributes roughly half of the support due to an equipartition of energy mediated via MHD waves (see §2.2 and Stahler & Palla 2005): If there is much more energy in the field, this directly affects the charged particles, which dissipate the extra energy to the neutral molecules through collisions, increasing their kinetic energy. If there is more energy in the bulk motions, then some of this is passed to the charged particles through collisions and thus alters the field configuration (e.g. Myers & Goodman 1988).

The type of chemistry which occurs in molecular clouds is determined by the interplay of various phenomena. These include the winds and radiation fields of any nearby stars, the gas temperature, the presence and abundance of dust grains (to mediate grain surface reactions)

and the relative abundances of atomic and molecular species in the material from which the cloud formed. Modern networks developed to describe the chemistry in diffuse and dark clouds contain up to 4000 different reactions between several hundred species, (see e.g. Millar et al. 1997) However there are only a few different types of reaction and these can be categorised as bond-formation, bond-destruction or bond rearrangement reactions. In molecular clouds, a few simple rules determine the chemistry:

For atomic ions (X^+), reactions with H_2 which yield molecular ions (XH^+) of the type:

$$X^+ + H_2 \rightarrow XH^+ + H, \tag{1.6}$$

are most important due to the prevalence of H_2 unless they are limited by an activation barrier. If they are, molecular dissociative recombinations of the type:

$$XY^+ + e^- \rightarrow X + Y, \tag{1.7}$$

take precedence since they occur efficiently at low temperatures. Atomic ions may also be involved in charge transfer reactions:

$$X^+ + Y \rightarrow X + Y^+, \tag{1.8}$$

which have coefficients that are often independent of temperature, in which case, the reaction rates depend only on the abundances of the reactants and a constant cross section. For neutral molecules, proton transfer with ionic species:

$$X^+ + YH \rightarrow XH^+ + Y, \tag{1.9}$$

are important at all temperatures. If such transfer is inhibited by low abundances, then neutral-neutral reactions of the type:

$$X + YZ \rightarrow XY + Z, \tag{1.10}$$

may be considered. By a process of elimination, any species exhibiting an abundance which cannot be reproduced by reactions of the above types is assumed to have been augmented by grain surface reactions. Such reactions involve the same radiative (atomic ions) or dissociative (molecular ions) recombinations with electrons as happen in the gas phase, but including the grain as a third body. The reaction products are then immediately returned to the gas phase (see §1.1.3).

GMCs are far too cold to radiate at visible wavelengths. Except for regions where there is enough dust to produce significant extinction of background starlight, their presence can only be detected through radio emission from trace molecules such as CO. The true extent of such complexes was first discovered in the 1970s through CO studies of the sky near HII regions, IR sources and regions of high visual extinction. Collisional excitation of different molecular transitions become important at various ambient densities, e.g. collisional excitation of the 2.6 mm transition of CO($J = 1 \rightarrow 0$) becomes important at number densities of around 10^3 cm^{-3} whereas collisional excitation of the 3.1 mm line of CS requires abundances closer to 10^4 cm^{-3}. This allows specific density regimes in the emitting gas to be targeted for observation (see figure 1.2). Surveys of the Milky Way in the CO($J = 1 \rightarrow 0$) line reveal much of the molecular gas (over 80 %) to exist in discrete clouds at radii between 6 and 10 kpc from the galactic centre, mostly confined to the galactic plane and within the spiral arms. The CO($J = 1 \rightarrow 0$) is usually optically thick in giant molecular clouds meaning that the detectable emission comes from the surface layers. This makes it useful for mapping the galactic distribution of molecular gas but corresponding lines from rarer isotopes such as ^{13}CO must be used to probe the internal structures of individual clouds. Isotope emission lines are excited at the same ambient densities, but lower fractional abundances ensure that the medium is optically thin to their photons to much higher column densities (see §1.3.4).

Combinations of observations from species whose transitions are excited at various densities (e.g. CO, CS, NH_3) with data from various isotopes (e.g. $^{12}C^{16}O$, $^{13}C^{16}O$, $^{12}C^{18}O$), have revealed complex structures throughout GMCs; from diffuse regions down to the densest cores. Such observations have demonstrated not only that stars form in the densest regions of GMCs, but also that they do so predominantly as clusters rather than in isolation. The ubiquitous inhomogeneity in GMCs is often manifested as denser clumps and filaments within an atomic envelope. Inside such clumps, densities are often sufficiently high for most background starlight

to be absorbed or scattered by gas phase atoms and molecules or be absorbed by interstellar dust grains and re-radiated as an IR continuum. These processes make clumps largely opaque to visible light (see §1.1.2). Outside of GMCs there exist regions with similar conditions to clumps. These are known as dark clouds since they were originally discovered in optical images as dark patches on the sky silhouetted against background stars or nebulae (e.g. Barnard 1927). Such observations were among the first indications of matter in the ISM. Dark clouds are found in complexes such as the Taurus Molecular Cloud ($M \sim 10^4$ $M_\odot$) and as isolated entities. The peak of the observed molecular emission is often spatially co-incident with the darkest areas in optical images, reinforcing the association of molecular gas and interstellar dust grains.

A survey in $^{12}CO(J = 1 \rightarrow 0)$ and $^{13}CO(J = 1 \rightarrow 0)$ was conducted on the Rosette molecular cloud by Williams et al. (1995). The cloud mass was found to be $1 - 2 \times 10^5$ $M_\odot$, with a mean H_2 number density of around 30 cm^{-3} and a column density of 4×10^{21} cm^{-3}. Most of the molecular material however exists in around 70 clumps which fill only about 8% of the cloud volume but have masses between 30 $M_\odot$ and 2500 $M_\odot$ and H_2 number densities of at least 200 cm^{-3}. Around half of them are gravitationally bound with the rest contained by the pressure of the surrounding medium. The clumps have random velocities dispersed around some mean value (the bulk velocity of the cloud as a whole).

On still smaller scales than clumps are the dense cores. These are the sites of individual star formation. An observed empirical relation known as Larson's Law (Larson 1981) states that the non-thermal velocity dispersion (inferred from the measurement of non-thermal line widths) within a cloud region varies systematically with the size of that region. This is because the bulk kinetic energy is responsible for the non-thermal velocity dispersion and is coupled to the magnetic field energy. A smaller cloud possesses a lower magnetic energy density and hence displays a lower velocity dispersion. This allows for the definition of a cloud size, where the non-thermal velocity dispersion equals to the ambient thermal speed (< 1 pc at 10 K). Such regions are more quiescent than the clumps as magnetic and bulk kinetic energy are no longer the dominant terms in the virial equation. Instead, thermal pressure provides the support needed for the core to maintain hydrostatic equilibrium (see §1.2.2). Cores on the scale of ~ 0.1 pc are observed in GMCs and dark clouds across the galaxy. Cores are also observed in isolation (often inside HII regions) where they are known as Bok Globules (Bok & Reilly 1947). With densities in excess of 10^4 cm^{-3}, even $^{13}C^{16}O$ emission is optically thick, so species such as NH_3, $C^{18}O$

and CS must be employed to probe their structures instead. A typical core is found to consist of several solar masses at a temperature of around 10 K. Hydrostatic cores are the immediate precursors to star formation (see §1.2.2), but not all cores go on to produce stars (e.g. Lee & Myers 1999).

1.2.2 Young stellar objects

In standard low mass star formation theory, any part of a molecular cloud can become unstable to gravitational collapse if it lacks the gaseous pressure to balance the force of gravity. In practice this means that once a critical mass (the Jeans mass; M_J) is exceeded in a region with a given number density (n in units of m^{-3}), mass density (ρ in units of kg m^{-3}) and temperature (T in units of K), that region will contract until some other force impedes the collapse. The Jeans mass is given by:

$$M_J = \frac{10^5 T^{\frac{3}{2}} m_H n^{\frac{1}{2}}}{\rho} M_\odot, \tag{1.11}$$

in units of solar masses, where m_H is the mass of a hydrogen atom (kg). For typical dense molecular core values (T = 10 K, n = 10^{11} m^{-3}), $M_J \sim 8$ $M_\odot$. This is similar to the mass of a dense core or Bok Globule (table 1.2.1). The initial core collapse is isothermal since the cooling time (thermal energy divided by the rate of thermal energy loss) is significantly less than the free fall time. Because the Jeans mass decreases as density increases, during an isothermal contraction smaller sub units will become unstable to collapse in a process known as fragmentation. This process allows a single dense core to produce more than one star. During collapse, a fragments density increases. At some point the density becomes sufficient that its own cooling photons are unable to escape so the fragment becomes optically thick and is no longer able to cool effectively. Once cooling is suppressed, the Jeans mass increases with temperature and fragmentation halts.

An opaque fragment will radiate almost as a blackbody. By equating the rate at which it radiates to the rate at which it gains gravitational energy the mass of the smallest fragment can be calculated. It is found to be around 0.003 $M_\odot$. This process can therefore explain the lowest stellar masses. Once fragmentation has ceased, the temperature and pressure increase, halting free fall collapse and leading to the formation of a hydrostatic dense core. An accretion shock

occurs where material continues to fall onto the core and is decelerated and compressed. The molecular gas is thus steadily heated. When the temperature is high enough to dissociate H_2, ($T \sim 2000$ K) the γ value (ratio of specific heats) of the gas increases (from 7/5 for molecular material to 5/3 for atomic material). Since:

$$T^{\frac{3}{2}} \propto \left(\rho^{\gamma-1}\right)^{\frac{3}{2}}, \tag{1.12}$$

$$\gamma = \frac{5}{3} \rightarrow T^{\frac{3}{2}} \propto \left(\rho^{\frac{2}{3}}\right)^{\frac{3}{2}} \propto \rho, \tag{1.13}$$

$$\gamma = \frac{7}{5} \rightarrow T^{\frac{7}{2}} \propto \left(\rho^{\frac{2}{5}}\right)^{\frac{3}{2}} \propto \rho^{\frac{3}{5}}, \tag{1.14}$$

once the gas is atomic, equation 1.11 becomes $M_J \propto n^{\frac{1}{2}}$ and so rises with density. Eventually accreted material allows the mass of the protostar to exceed the Jeans Mass. This initiates a further collapse and a second, deeper accretion shock. The centre of the protostellar object now becomes dense and hot enough to start burning hydrogen. This process explains why only clumps observed to be above a certain column density ($N(H_2) > 10^{16}$ cm^{-2}) appear to contain embedded protostars, (e.g. Hartquist et al. 1998; Krumholz & McKee 2008).

If the collapsing cloud region was initially rotating or was permeated by a magnetic field, then the subsequent evolution of the system will be affected. In the case of rotation, assuming that the cloud rotates with a constant angular speed, the centrifugal force is proportional to r, whereas the gravitational force is proportional to $1/r^2$. At large radii the centrifugal force is larger than gravity, but a radius exists where the two forces are balanced. This halts the collapse perpendicular to the rotation axis for all of the cloud outside of this radius. Collapse can still continue parallel to the axis, resulting in a flattened disk structure. Calculations reveal that if angular momentum were conserved, the final star would rotate at a sizeable fraction of the speed of light and break up. The favoured method of removing angular momentum is shear viscosity in the disk, which can simultaneously transfer mass inwards and angular momentum outwards.

If an initially spherical cloud were threaded by a magnetic field and the flux was frozen into the cloud material, then although the magnetic force cannot overcome gravity once collapse had started (since $F_M \propto F_G \propto 1/r^2$), all the field lines in the original cloud would end up in the final star. This would yield field strengths much above those observed. Ambipolar diffusion (see §1.1.1) provides the solution by allowing the neutrals to drift relative to the magnetic field opposed only by rare ion-neutral collisions (as long as χ_i is small). Therefore the field is only

frozen into the ion and electron fluids, not the neutrals. As neutrals slip through the field lines, they end up in the star but the lines themselves do not. Ambipolar diffusion therefore amplifies the formation of an accretion disk which is threaded by open magnetic field lines from the ISM (i.e. lines which extend to infinity).

At the onset of hydrogen burning, a protostar is still embedded in the larger cloud of dust and gas from which it formed. This means that any radiation (optical or UV) from nuclear reactions or accretion shocks is absorbed and re-emitted in the IR. Initially the envelope is very optically thick. As radiation pressure, outflows and stellar winds begin to clear the envelope, the observable emission moves to shorter wavelengths until the star and accretion disk are revealed. Any bipolar jets, molecular outflows and associated shocks also become visible as the envelope is dissipated (see §1.2.3). Eventually these processes will clear the infalling envelope and the parts of the accretion disk which have not fragmented and coalesced to form proto-planetary objects. A new star is finally left in splendid isolation (see Figure 1.6 in §1.2.3).

The star forming process involves bulk flows of gas and dust both onto and away from the protostar, often at high velocities. This implies that shocks will be a ubiquitous feature of star formation.

1.2.3 YSO jets and outflows

The study of mass loss from YSOs began with the discovery of a class of optical line emission nebulae by Herbig (1951) and Haro (1952). Although originally assumed to be regions of star formation, it was later noted that the spectra of Herbig-Haro (HH) objects bear a striking similarity to those of supernova remnants. This lead to the suggestion that HH objects form in the interactions of supersonic stellar winds with surrounding, ambient media, (e.g. Schwartz 1975). Kwan & Scoville (1975) and Zuckerman et al. (1976) discovered broad (> 75 km s^{-1}) CO line emission at millimetre wavelengths from gas shocked and accelerated by the outflow from a YSO in the Orion A Molecular Cloud. The first surveys revealed these outflows to be extremely common around young stars, (Bally & Lada 1983; Edwards & Snell 1982, 1983, 1984), and the structures of such outflows are usually bipolar, (Snell et al. 1980; Rodriguez et al. 1980).

Outflows from YSOs can be observed over a wide range of the electromagnetic spectrum, from the UV (e.g. recombination of H^+ and He^+), through optical (e.g. optical transitions of shocked, ionized gas e.g. H_α and [SII]), to the radio. Observations of ionized material at the base

of the jet reveal free-free continuum emission which is usually very well aligned with the outflow axis. Together with the interferometric observation that jet velocities are typically close to the local escape velocity, the radio results imply that jets originate very close (< 10 AU) to their associated protostar (Shang et al. 2004 and references therein). The primary outflow is thought to consist of deflected material from the accretion disk which has been collimated and accelerated along the polar axis. It subsequently impinges on the surrounding dense cloud material, sweeping up the quiescent material in its path and carving out two oppositely oriented cavities if it is bipolar (see Snell et al. 1980). CO($J = 2 \rightarrow 1$) and ($J = 1 \rightarrow 0$) observations of HH211 reveal a high velocity (~ 80 km s^{-1}) component which traces a dense ($> 10^3$ cm^{-3}), highly collimated (length/width > 10) molecular jet emanating from the region of the central protostar. This jet terminates at the position of a strong H_2 bowshock approximately 400 AU from the protostar. The fractional ionization in the jet is around 10% (see Gueth & Guilloteau 1999 and references therein). Further observations suggest that outflows are often inhomogeneous with knotty structures visible along the length of the jet (e.g. Falle & Raga 1993). Herbig-Haro objects are nebulous optical patches located at the ends of the jets and are associated with bow shocks.

Since rotating magnetic fields can accelerate gas, magnetic stresses in the circumstellar accretion disk are thought to launch the jet (Snell et al. 1980; Meyers-Rice & Lada 1991). Uncertainty remains as to whether the launch occurs from the surface of the rotating disk, along open magnetic field lines from the ISM (the disk wind model) or from the interface between the disk and the YSOs magnetosphere, along broken stellar field lines (the X-wind model).

The X-wind model was developed in a series of papers beginning with Shu et al. (1994). In their model, the X-point (R_x) is defined as the radius where the Keplerian orbital frequency of the disk material is the same as the stellar rotation frequency. At this point the stellar magnetosphere co-rotates with the disk and the centrifugal and gravitational forces exactly balance. The accretion process involves disk material spiraling inwards until it reaches the magnetosphere where it meets closed stellar field lines. This truncates the disk at R_t. Viscous coupling in the disk transports angular momentum outwards, allowing gravity to move disk material closer to the star than R_t. The disk material can then be loaded onto the closed field lines and falls onto the surface at close to the free fall speed (through the region denoted funnel flow in figure 1.4(b)). As long as the truncation radius is larger than the stellar radius, closed stellar field lines

originating near the equator are not affected and retain the standard dipole configuration (resulting in a dead zone through which accreted material does not travel). This is not so for lines originating near the poles. If the disk has non-zero conductivity, then the diamagnetic properties of its plasma envelope produce shielding currents which prevent the vertical threading of stellar field lines through the disk at all radii larger than R_t. Instead, stellar field lines originating near either pole must turn (at very large radii, where the field strength is weak) so that they skim the surface of the disk and then make another sharp turn (kink), finally meeting near the disk edge (R_t). This results in stellar field lines which would otherwise intersect the disk being bowed inwards so they intersect the midplane inside the truncation radius. At $R = R_t$ disk material must co-rotate with the star in order for the outermost (still closed but highly bowed and kinked) field line not to become stretched and warped as the star rotates. This mean that the X-point must occur close to the truncation radius; $R_t \approx R_x$. The disk also possesses a non-zero but finite magnetic diffusivity meaning that its material has a slight tendency to allow the diffusion of the kinked magnetic field lines through it (due to resistivity and ambipolar diffusion). Magnetic diffusivity ensures that some disk material up to and slightly beyond R_x will become threaded with closed stellar field lines. All closed field lines and any material loaded onto them must rotate at the stellar rotation frequency. At any $R > R_x$ this frequency is larger than the local Keplerian orbital frequency so any such loaded material rotates with enough energy to overcome gravity and can be driven into an outflow. The Alfvén speed is defined in equation (1.17) as $v_A \propto B/\rho^{1/2}$. Moving outwards from the X-point, B and ρ both diminish with B falling more than $/\rho^{1/2}$, causing the Alfvén speed to also fall. There exists a surface (dotted line in figure 1.4(b)) where the outflow speed equals the local Alfvén speed. Inside this surface the flow is sub-Alfvénic and outside it is super-Alfvénic. If the ram pressure of the outflow is sufficient, material reaches the point where the field lines turn back to the stellar pole with sufficient kinetic energy to have become super-Alfvénic and it thus tears those lines open. The newly open field lines are still anchored in the equatorial plane by the combined effect of the inward press of the accretion flow and the outward press of closed stellar field lines. Therefore in the case when the the stellar magnetic field is strong enough to truncate the accretion disk (at the magnetosphere), it can also accelerate a magneto-centrifugally driven wind. These winds can produce mass loss rates which are comparable to the accretion rate, by loading disk material onto newly open stellar field lines. The outflowing material also carries away angular momentum not removed by viscous torques.

Since the newly open field lines still rotate close to the stellar rotation frequency, the generated configuration of their lines becomes toroidal. In this case the magnetic force is directed radially inwards allowing the outflow to be collimated into a jet as it leaves the system (Shu et al. 1995).

The disk wind model was proposed by Pelletier & Pudritz (1992) and later refined by Ouyed & Pudritz (1997). It states that the jet originates as a centrifugally driven hydromagnetic wind emanating from the surface of the accretion disk. Since a Keplerian disk always locally rotates at close to its breakup velocity, large centrifugal forces exist along much of its surface (which extends from the stellar magnetosphere to around 1000 times that radius). This can provide an effective centrifuge and hence produce an outflow. Such outflows can efficiently extract and carry off angular momentum from the disk, limiting that which reaches the central object. In addition, as accreted material approaches the protostar it moves deeper into the gravitational potential well and gains energy. It was traditionally supposed that viscous stress converted this energy into heat, but having field lines that thread the disk means that the gravitational energy can be converted into the mechanical energy of the wind. Cloud collapse together with ambipolar diffusion results in an hour glass field configuration with open field lines from the ISM anchored in the disk. Rotating field lines enforce a co-rotation of the material in the atmosphere of the disk. Such rotation is above the local Keplerian orbital speed, which is itself close to the breakup speed. This allows centrifugal acceleration to overcome gravity and form a wind, which is effectively a rotating, magnetised outflow that expels matter along open field lines. The wind will expand most rapidly in the direction of lowest density so it tends to form a bipolar outflow. The field lines return to being aligned to the rotation axis at large distances from the disk, giving the field an hour glass configuration. This provides the initial collimation of the jet (see §1.2.2). The jet may later become self collimating since its rotation again generates a predominantly toroidal magnetic field, directing the magnetic force radially inwards.

However the jet is launched, it is likely to be driven magentocentrifugally, with the outflow occurring along open field lines anchored on or near the circumstellar accretion disk. Either mechanism helps limit accretion by clearing molecular cloud material in the vicinity of the protostar (see figures 1.4 and 1.6). The main difference between the two models is the location where the outflow field lines are anchored in the disk: near the radius where the stellar magnetosphere meets the disk (R_x) for X-winds (figure 1.4b), or over a wider range of disk radii for disk winds (figure 1.4a). Either model assists in the removal of magnetic field lines and angular

momentum which would otherwise reach the protostar.

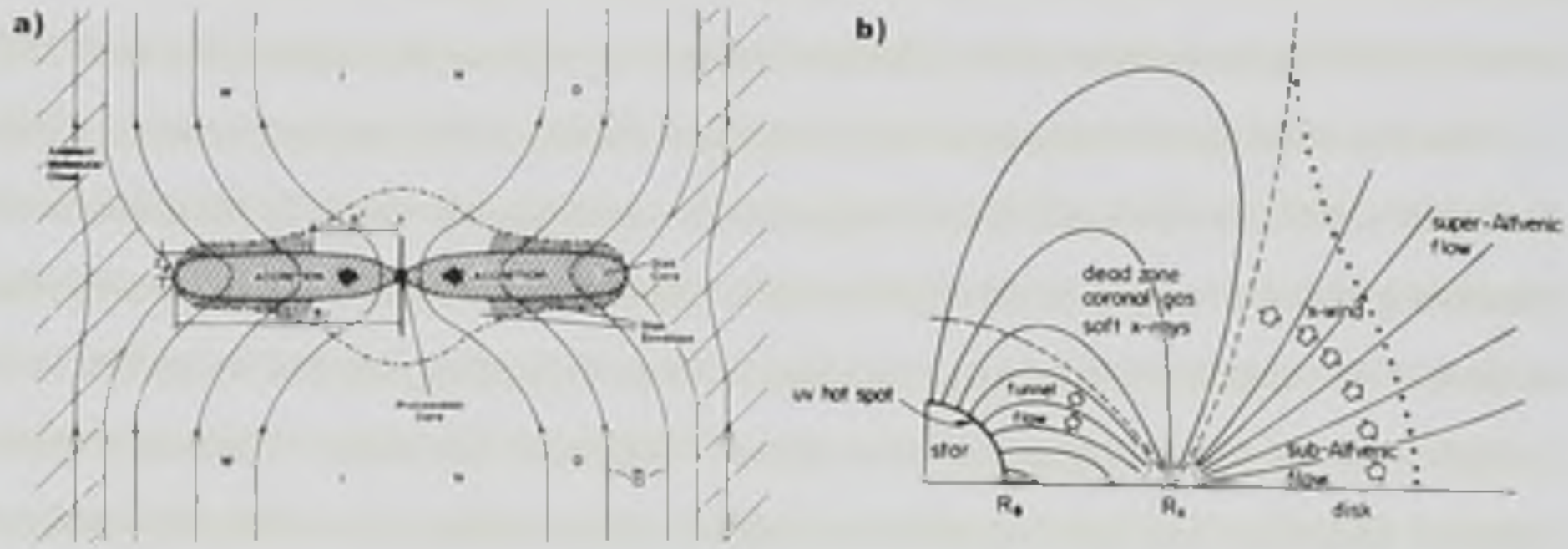

Figure 1.4: A schematic of the outflow launching mechanisms. Diagram (a) shows a disk wind where the surface material of the disk is magnetocentrifugally accelerated and subsequently collimated by the open field lines which thread the disk. R_I is the radius to which envelope material is ionized by photons from the accretion shock. The neutral envelope extends to R_d (dotted region) and is heated by a longer wavelength FUV flux. Adapted from Pudritz (1985). Diagram (b) shows an X-wind where the disk material is accelerated from the X-point (R_x). Roughly equal amounts of disk material are loaded onto either the closed stellar field lines (which results in accretion) and the newly opened field lines from the stellar magnetosphere (which results in the outflow). The dotted line depicts the Alfvén surface (see text). Adapted from Shu et al. (1994). The reader is referred to that paper for a more detailed diagram and explanation.

Selecting between these models will require high resolution techniques able to resolve the inner few AU of protostellar and accretion disk systems. In this project however, the primary jet is not modeled either during its launch or at later times, so it is sufficient to note that there is strong evidence for a physical link between accretion (infall) and the launched jet (outflow) and that magnetic stresses in the system initially launch the outflowing material.

The primary outflow from a protostar injects energy and momentum into the surrounding cloud at distances from a few AU up to tens of parsecs. It can contribute significantly to mass loss from the dense envelope immediately surrounding the YSO (within 0.3 - 0.5 pc), as well as introducing turbulence into the wider core which may assist its dispersion (e.g. Myers et al. 1988). Mass loss rates of 10^{-8} - 10^{-4} $M_\odot$ yr^{-1} have been inferred (e.g. Shang et al. 2004; Lee

et al. 2007), which seem to be dependent on the age of the system (see below). Jets and outflows are therefore able to modify the kinematics and distribution of the dense gas surrounding the protostar, for example by elongating density structures and producing velocity gradients along the outflow axis (e.g. Gueth et al. 1997). In some cases (e.g. L1448-mm) the terminal velocity of the jet component is observed to decrease with distance from the central source, whereas the terminal velocity of the molecular component is observed to increase. This result demonstrates decisively that the jet is injecting momentum into the ambient gas (e.g. Arce et al. 2007).

Primary outflows entrain dense gas from the surrounding envelope and thus produce secondary molecular outflows. There are a number of models by which the ambient cloud material can be entrained and accelerated. These can be put into distinct classes including; (1) jet driven turbulence, i.e. Kelvin-Helmholtz instabilities along the boundary between the jet and the cloud produce a turbulent layer where jet and cloud materials mix. This can be viscous enough to entrain cloud material; (2) jet driven bow shocks, i.e. bow shocks associated with the interface between the primary outflow and quiescent cloud sweep up and entrain ambient molecular cloud material; (3) wide angle wind driven shells, i.e. a wide angle wind emanating from the surface of the accretion disk and protostar sweeps up the surrounding core/cloud material into thin shells (see Figure 1.5 for schematics of each mechanism and Arce et al. 2007 for further detail). The most promising of these are (2) and (3) and a combination of the two may provide the most satisfactory match to the available CO data. In this case, there is a two component stellar wind, comprising of a slow disk wind and (for example) an X-wind jet. The disk wind could then help to collimate the X-wind into the jet component. When the jet impacts ambient material, a pair of shocks form (one where ambient material is accelerated and one where jet material is decelerated). Gas between the shocks is at high pressure and can be ejected perpendicular to the jet where it interacts with the ambient cloud via a broader bow shock to produce an outflow shell around the jet. The wind from the disk can also provide a slow, wide angle component which contributes to the driving of the secondary outflow.

As mentioned above, HH211 has been observed in two CO transitions. These observations reveal low velocity (< 10 km s^{-1}) CO at the boundaries of the cavities which are surrounded by the terminal bow shock at the end of the jet. Emission from this CO strongly supports the view that ambient cloud material is entrained by shocks in the jet, creating a secondary, low velocity molecular outflow component (Raga & Cabrit 1993; Masson & Chernin 1993; Chernin

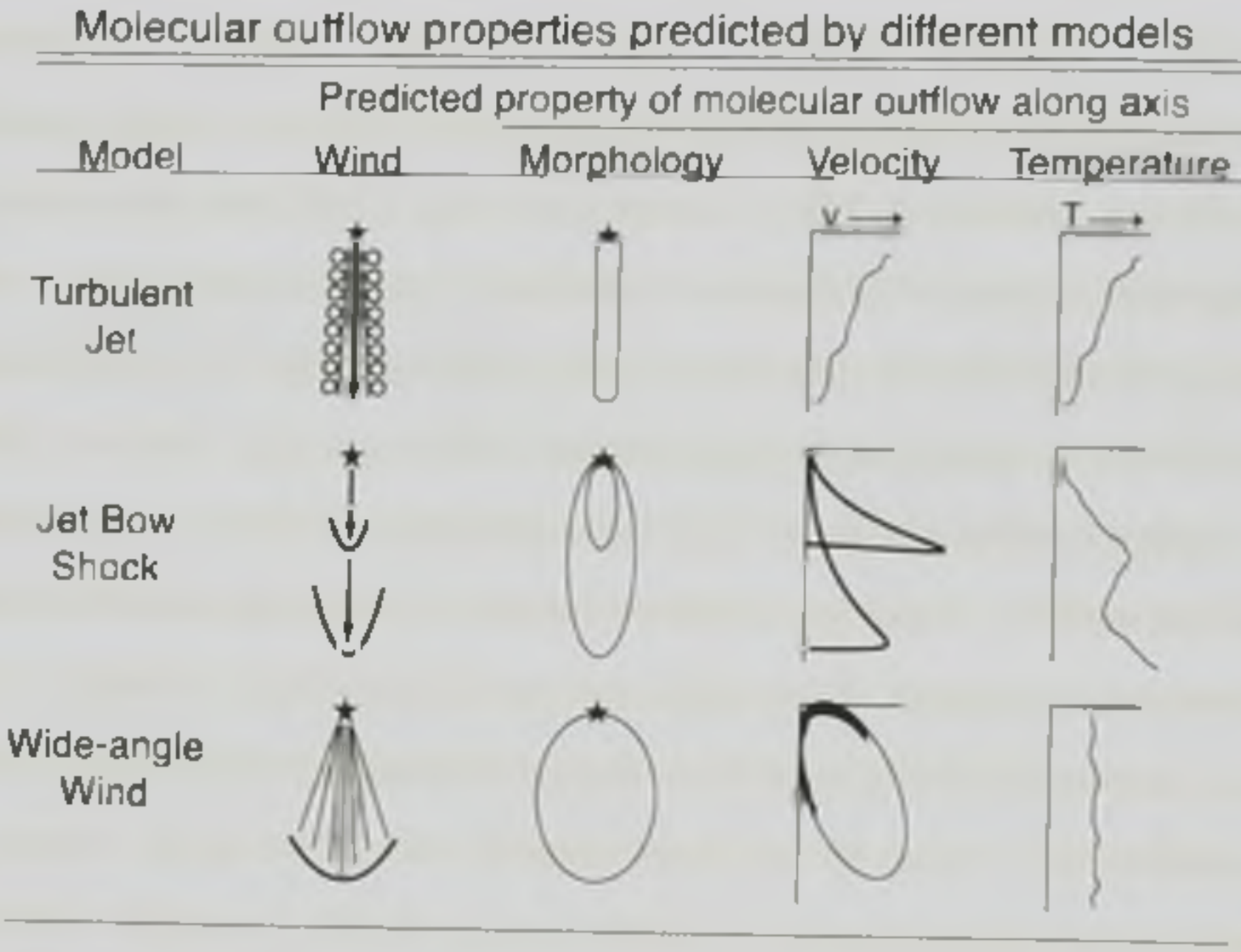

Figure 1.5: Three models of how a primary jet entrains cloud material into a secondary molecular outflow. Displays a schematic of each mechanism, the expected observable morphology as well as velocity and temperature profiles along the outflow axis. Note that the jet bow shock diagram and morphology already assumes episodic ejection events (see text). Jet bow shocks and wide angle winds are the most promising models (see text). Adapted from Arce et al. (2007).

et al. 1994). Observations of SiO (Martin-Pintado et al. 1992; Schilke et al. 1997; Gibb et al. 2004), further support this claim (see §1.3.5). The outflowing and entrained material includes all components of molecular clouds; neutral molecules, atoms, ions and electrons (see §1.1.1), all of which can exist in a wide range of excitation states. The material also contains dust grains with a variety of sizes, compositions and charges (§1.1.2). Even the entrained material can be accelerated to speeds beyond the adiabatic sound speed, so shocks are likely to exist in the molecular outflow. Whether these shocks are J-type or C-type will depend on (for example) the upstream density, the strength and orientation of the magnetic field and the presence and abundance of charged grains, (see §1.3.3). However, infrared observations of line of H_2, CO, H_2O and some atomic lines have made it possible to estimate the temperature and physical conditions in a large sample of outflows, (see §1.3.4 and e.g. Johnstone et al. 2010; Lefloch et al. 2011). Interpretation of these studies suggest that often a combination of both J- and C-type

shocks is required to account for the observations, (see e.g. review by van Dishoeck 2004). This could happen in the case of the overlap of multiple outflow episodes due to non-steady accretion from the disk (e.g. Santiago-García et al. 2009), an initially J-type shock slowly evolving into a C-type shock ($\sim 10^5$ years) over the lifetime of the outflow (e.g. Flower et al. 2003), or bow shock geometry where the shock may be J-type at its apex, but C-type along its flanks where the ram pressure is lower (e.g. Smith et al. 1991).

The accretion driven outflow process in low mass YSOs persists for around 10^6 years. Over that time the rate of infalling and outflowing material changes as do the properties of the cloud through which the outflows travel. Different observable properties have been interpreted as being representative of different stages in that process.

Observations of the outflows from a large sample of low mass YSOs have lead to to the classification of four types of object based on evolutionary progress (Andre & Montmerle 1994). Class 0 objects have strong sub-mm continuum emission (top row in figure 1.6) which is indicative of a dusty circumstellar envelope with more mass than the hydrostatic core. These objects have the fastest and most collimated jets (Bachiller et al. 1990), presumably related to large accretion rates and the high density of the envelope. Class I objects (second row) display strong NIR emission (~ 2 μm) with only moderate sub-mm continuum emission. They are perceived as a protostar with an accretion disk and a residual circumstellar envelope now with less mass than the protostar (which is approaching its final mass). Hence their accretion and outflow rates are lower than Class 0 objects. Class II and Class III objects are T-Tauri stars (bottom two rows) with either optically thick (Class II) or thin (Class III) disks and no detectable envelopes. These two classes mark the end of the outflow phase and by Class III, the star has joined the main sequence.

Bontemps et al. (1996) conducted a CO survey of 45 Class 0 and Class I objects, comparing the CO momentum flux in the outflow to the mass accretion rate. They found the two quantities to be tightly correlated, and (together with the mass of the envelope) to decrease simultaneously and self consistently. Furthermore, they fitted their observations with a model where the envelope is dissipated by accretion and eroded by a wind with a progressively wider opening angle. The widening wind can be understood in terms of the dissipation of the envelope: As the remaining envelope becomes increasingly limited to the equatorial plane (the accretion disk), there is a successively more solid angle through which the stellar wind can pass without significant

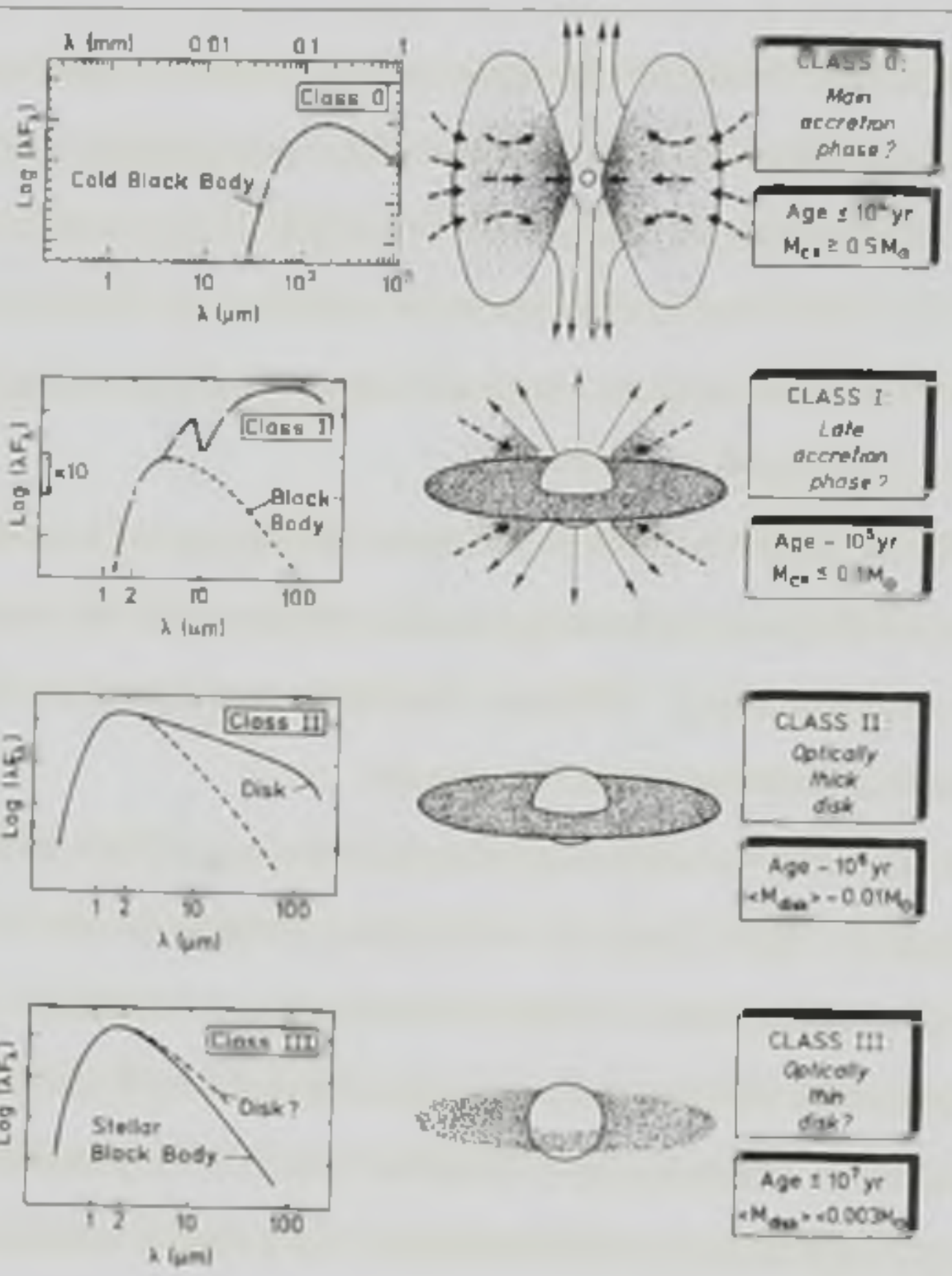

Figure 1.6: An overview of the evolution of a low mass YSO. The left plots show the observed spectra, the middle column is a schematic of the system, and the right column details processes, timescales and other relevant data. Note that in moving from Class 0 to Class I, the protostar gains most of its final mass at the same time as clearing much of the non-equatorial material. The outflow phase is finished in less than 10^6 years, so the driving source lasts only ~ 10 times longer than the time required for a C-type shock to reach steady state, (see §2). Therefore time dependent simulations are highly desirable to model the outflows from YSOs. Diagram from Bachiller (1996).

attenuation. Assuming that the inflow and outflow mechanisms are linked, and that the outflowing material entrains surrounding cloud material resulting in the molecular outflow, the outflow must come to an end when accretion ceases. i.e. A combination of successful accretion onto the star together with the outflowing material having left the stars gravitational influence whilst transferring momentum to the surrounding cloud eventually clears the remaining envelope. A main sequence star is left, possessing a normal stellar wind. Observations of some outflows

indicate episodic ejection events (e.g. Bachiller et al. 1990) and/or precession of the jet axis (e.g. Tafalla & Bachiller 1995). These processes may accelerate the clearing of the surrounding envelope but are unlikely to affect the accretion disk, which is confined to the equatorial plane.

Conditions in the secondary molecular outflow suggest that C-type shocks will be prevalent (see §1.3.2). In such shocks, different species of particles possess different velocities and temperatures over an extended region. Different velocities facilitate collisions between species. In addition to permitting chemical reactions which are endothermic or possess activation barriers, collisions involving charged dust grains instigate other processes which can affect the composition of the post-shock flow in important ways and lead to observable consequences. These processes are explored in §1.3.4 and §1.3.5.

1.3 Shock structure

1.3.1 J-type shock structure

A shock is defined as a wave across which the energy of the medium is irreversibly re-distributed. Shocks may propagate through all phases of matter; solids, liquids, gases and plasmas. They are often characterised by an abrupt change in the properties of the medium. Across a shock front there is a rapid rise in temperature, pressure and density. Behind the front, the pressure of the shocked medium drops over a much wider region known as the expansion fan or relaxation layer. This is primarily achieved through dissipation followed by cooling. Shock waves are common in the ISM, occurring whenever a perturbation travels faster than information about its approach can propagate ahead. They may move if driven by a steady energy source (e.g. YSOs, Active Galactic Nuclei, planetary nebulae) or a blast wave (e.g. supernovae). Shocks may also appear to be stationary when a supersonic flow is incident on a static obstacle (e.g. the steady accretion shock near the surface of a hydrostatic core). In either case, upstream material is unable to respond to the perturbation until it arrives, at which point it is swiftly compressed, heated and accelerated through the sonic point. Shocks are supersonic with respect to material upstream, but subsonic with respect to material downstream. Upstream refers to undisturbed material ahead of the perturbation and downstream refers to disturbed material which the perturbation has already passed.

When the gas is dense enough for particle collisions to be common but is neutral or only

weakly ionized, the shock front consists of a thin viscous layer where the motion of the pre-shock and post-shock gas is thermalised. Consider the frame co-moving with the shock (shock frame). From this frame, the shock is stationary and upstream material moves towards it supersonically at the shock speed. Downstream material flows away at a lower, sub-sonic speed. As upstream material enters the shock it collides elastically with shocked gas and is decelerated on the order of one elastic collision mean free path. Elastic collisions therefore convert the ordered kinetic energy of the flow into random thermal energy held by individual particles. This energy conversion ensures that the action of any shock increases entropy and is therefore irreversible. The thermal energy is then dissipated through inelastic collision processes (e.g. ionization, collisional excitation and molecule dissociation) and emitted as radiation over the relaxation layer. Because the inelastic collision and cooling region is much wider than the viscous layer, a shock front is often represented as a discontinuity across which the properties of the medium abruptly change. Such shocks are termed J-type. In this case the hydrodynamic conservation equations assume the form of the Rankine-Hugoniot jump conditions, named after the authors who first derived them towards the end of the nineteenth century (see §3.3.1). These conditions state that the mass, momentum and energy inflow rate per unit area to the shock must equal the outflow rate per unit area. This is the simplest model of an interstellar shock wave and is applicable when either the flow is neutral or there is little or no magnetic field. Radiation from the relaxation layer is able to propagate upstream. If sufficiently intense, the optical and UV components of such radiation will dissociate and ionise gas upstream of the shock front increasing its temperature and pressure. This creates what is known as a radiative precursor which broadens the shock structure.

The shocks associated with SFRs often do not fall into this category since the molecular cloud cores through which they propagate are dense, dusty and magnetised but only weakly ionized. In this regime, the physical conditions result in an entirely different type of shock structure. Such shocks will be under consideration for the remainder of this project.

1.3.2 C-type shock structure

The low velocity shocks associated with molecular outflows from YSOs (see §1.2.3) propagate through cold, dense regions with appreciable magnetic fields (5 - 30 μG; Myers 1991; Crutcher et al. 2010), but very low fractional ionization. Estimates of the magnetic field strength come

from OH and HI Zeeman measurements (e.g. Heiles 1976; Crutcher et al. 2003). i.e. The magnetic field splits a single excited electronic state into a number determined by its spin (S) and angular momentum (L) quantum numbers (J = L + S). This happens because in the absence of a field different combinations of these quantum numbers have the same energy, but by applying the field, these energies become distinct. The difference between the previously equal energies is determined by the magnetic field strength and the values of L and S. Mullan (1971) demonstrated that the assumption of the field being "frozen in" to the gas is only valid if the ions and electrons are sufficiently well coupled to the neutrals by collisions for all three to have the same bulk velocity. The low fractional ionization in molecular clouds means that this assumption is usually not fulfilled. When this is the case, the frozen field approximation must be replaced by a multifluid hydrodynamic description where the ions/electrons and the neutrals can possess different flow velocities and temperatures. The fluids also possess different signal speeds. Compressive disturbances in the neutral fluid propagate at the sound speed, but compressive disturbances in the ion/electron fluid can propagate perpendicular to the magnetic field at the ion magnetosonic speed. Magnetosonic waves are longitudinal (compressive) waves of ions and electrons in a magnetised plasma. When such waves travel parallel to the magnetic field, the ion and electron oscillations are transverse to the field lines and they are known as Alfvén waves. Waves may also exist at oblique incidence to the field in which case they possess longitudinal and compressive components and smoothly change into magnetosonic waves as the wave travels perpendicular to the field.

In a fully ionized fluid with no dust, information can be transported upstream, perpendicular to the magnetic field at the fast-mode magnetosonic speed:

$$c_f = (v_A^2 + c_a^2)^{\frac{1}{2}}. \tag{1.15}$$

Fast-mode refers to one of the characteristic roots (i.e. a propagation velocity) of the dispersion relation for such waves. If a wave travels obliquely or perpendicular to the background field, then its phase velocity is larger than the Alfvén speed (equation 1.17) and such waves are denoted fast-mode (see e.g. Kivelson & Russell 1995). Since magnetosonic waves are compressive, they are traveling perturbations in both the magnetic and plasma pressure. In a slow-mode wave these pressure perturbations are out of phase, whereas in a fast-mode wave they are in

phase. In equation (1.15), c_a is the adiabatic acoustic sound speed:

$$c_a = (\gamma P/\rho)^{\frac{1}{2}}, \tag{1.16}$$

where γ is the ratio of specific heats and P is the pressure. v_A is the Alfven speed:

$$v_A = \frac{B}{(4\pi\rho)^{\frac{1}{2}}}, \tag{1.17}$$

where B is the magnetic field strength. The Alfvénic Mach number M_A is defined as:

$$M_A = \frac{v_s}{v_A}, \tag{1.18}$$

where v_s is the shock speed. Ions and electrons respond directly to electric and magnetic forces by moving in a direction determined by their charge and at a speed determined by their mass. Neutral particles respond only indirectly through frictional coupling to the charged particles. This allows two Alfvén speeds to be defined:

$$v_{AC} = \frac{B}{[4\pi(\rho_i + \rho_e + \rho_n)]^{\frac{1}{2}}}, \tag{1.19}$$

$$v_{AU} = \frac{B}{[4\pi(\rho_i + \rho_e)]^{\frac{1}{2}}}, \tag{1.20}$$

where subscripts i, e and n denote ions, electrons and neutrals respectively. v_{AC} is the propagation speed of Alfvén waves with frequencies that are small compared to ν_{ni}, the inverse of the timescale for the neutrals to become coupled to the ions through collisions. v_{AC} is known as the Alfvén speed of coupled waves, i.e. waves which are coupled to, and hence affect, the neutrals. v_{AU} is the propagation speed of Alfvén waves with frequencies that are large compared to ν_{in}, the inverse of the timescale for the ions to become coupled to the neutrals through collisions. v_{AU} is known as the Alfvén speed of uncoupled waves, i.e. waves which are uncoupled from, and hence do not affect, the neutrals. Of course, there are now two Alfvénic Mach numbers:

$$M_{AC} = \frac{v_s}{v_{AC}}, \tag{1.21}$$

$$M_{AU} = \frac{v_s}{v_{AU}}. \tag{1.22}$$

If $M_{AU} > 1$, no information can propagate ahead of the disturbance and a thin, discontinuous J-type shock results. If $M_{AU} < 1$ then information can be carried upstream by charged species responding to the compression of the field. The information transfer is mediated by uncoupled waves moving ahead of the shock causing the charged fluids to be compressed and accelerated before the passage of the shock. The distance over which the ion and electron fluids have a different velocity to the neutrals can be very much longer than the mean free path for ion-neutral collisions. In this case ambipolar diffusion occurs as the charged particles stream through the neutrals. The collisional coupling between the ions and neutrals, together with the fact that $M_{AC} > 1$ (otherwise there would be no shock) limits the upstream response to a distance Δ. By balancing ion-neutral friction to the gradient of the magnetic pressure, Draine (1980) found:

$$\Delta = \frac{v_s}{2\nu_{ni} M_{AC}^2}. \tag{1.23}$$

When the charged species move relative to the neutrals ahead of the shock front ion-neutral friction generates heat in this region and creates a magnetic precursor (Mullan 1971). As the transverse component (perpendicular to the shock normal) of the pre-shock magnetic field gets larger, the ion-neutral slip region becomes wider. Infrequent ion-neutral collisions begin to accelerate the neutrals ahead of the J-type discontinuity, which now compresses the neutrals less. Above a critical pre-shock field strength, the ion-neutral slip region becomes so wide that enough momentum and energy is transferred to the neutrals in the magnetic precursor for the discontinuity to cease to exist. Such shocks are said to be continuous and denoted C-type (see Figure 1.7).

The inclusion of another fluid representing charged dust grains can, once again, drastically alter the shock structure. If they account for a significant portion of the interstellar mass ($\sim$1%) and are extremely well coupled to the magnetic field (i.e. are highly charged), then their mass density substantially lowers the Alfvén speed of uncoupled waves. This increases the uncoupled Alfvénic Mach number, thus lowering the maximum shock speed for which a magnetic precursor can exist. Grain-neutral friction may become comparable to, or even exceed the ion-neutral friction, so that in the precursor the grains impart more energy and momentum to the neutrals than the ions do. Considering only grains that are larger than 0.1μm, (Savage & Mathis 1979), and assuming that they move with the ions, by using the relationship between ν_{ni} and ν_{in}:

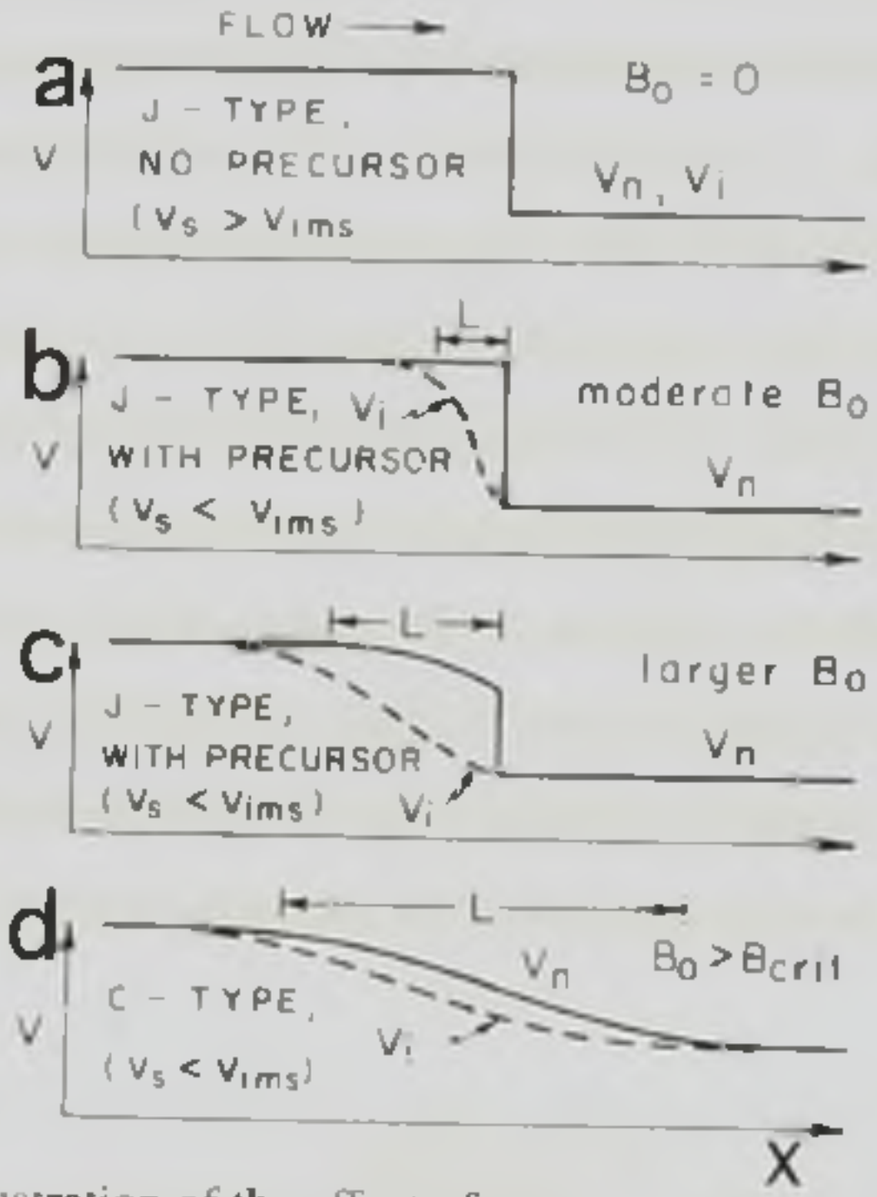

Figure 1.7: Schematic illustration of the effect of a transverse magnetic field (B_0) on the structure of a shock wave in a weakly ionized gas (in all diagrams the gas flows from left to right). Neutral (v_n) and ion (v_i) velocities are depicted from the frame co-moving with the shock, (see figure 1.8). (a) With $B_0 = 0$ the shock wave is of the familiar J-type; i.e. both fluids undergo a discontinuous jump, there is no magnetic precursor and v_i exactly follows v_n (b). If B_0 is now large enough for the ion magnetosonic speed (v_{ims}) to exceed the shock speed (v_s), the shock acquires a magnetic precursor. Magnetic field compression begins ahead of the discontinuity and v_i becomes a continuous function of position, being sub-magnetosonic everywhere. (c) As B_0 is further increased, the extent of the magnetic precursor (L) increases so that energy and momentum is transferred to the neutrals ahead of the J-front. Consequently, the neutral gas compression across the J-front decreases. (d) Finally, if B_0 exceeds some critical value (B_{crit}), the J-front ceases to exist and the shock becomes C-type: v_i and v_n are both continuous, the ion fluid is sub-magetosonic everywhere and the neutral fluid is supersonic everywhere. Adapted from Draine (1980).

$$\frac{\rho_i}{\rho_n}\nu_{in} = \nu_{ni} \approx 2 \times 10^{-9} n_i, \tag{1.24}$$

together with the relation:

$$\frac{< n_g \sigma_g >}{n_H} \approx 5 \times 10^{-22} cm^2, \tag{1.25}$$

where n_g is the number density of grains and σ_g is the cross section of dust grains (the triangle brackets denote a suitable averaging over an MRN size distribution), it can be shown that grain-neutral friction is of comparable importance to ion-neutral friction for accelerating the neutrals when:

$$\chi_i = 10^{-8} \left(\frac{v_s}{kms^{-1}} \right). \tag{1.26}$$

This is satisfied for some high density shocks of interest (e.g. Hartquist et al. 1998, chapter 8). In dense, shocked regions, the electron temperature can reach several thousand degrees Kelvin. The grains can then carry sufficient negative charge to be well tied to the magnetic field. In this case, ion recombination on their surfaces may proceed rapidly enough for dust to play an important role in establishing the fractional ionization in the shock front and hence Δ (e.g. Pilipp et al. 1990). The extent to which grains are coupled to the magnetic field is indicated by their Hall parameter (β_g):

$$\beta_g = \frac{|\Omega_g|}{\nu_{gn}}, \tag{1.27}$$

where Ω_g is the grain gyrofrequency and ν_{gn} is the inverse of the timescale for a grain to become coupled to the neutrals through collisions. If $\beta_g >> 1$ the grains spiral around the magnetic field lines much more often than they collide with the neutrals and are tied to the field. If $\beta_g << 1$ the grains collide with the neutrals much more often than they spiral around the field lines and therefore move with the neutrals. If $\beta_g \sim 1$ then the gryro- and collision frequencies are approximately equal and the grains move between the neutral and charged fluids. With this information it is possible to write down the fluid and field equations governing a multifluid MHD shock wave.

1.3.3 Mathematical description of multifluid shocks

The situation described in §1.3.2 is applicable across a wide range of conditions typically found in SFRs. This section describes the equations required for the MHD modeling of C-type shocks.

When a shock consists of several interpenetrating fluids coupled by collisions which are not common enough to result in a single bulk flow, it is termed multifluid. Suppose that the shock travels in the x-direction and that the magnetic field lies in the x-y plane (along the y-axis for perpendicular shocks). The z-direction is then perpendicular to the shock (x-y) plane (see figure 1.8).

Consider the plane parallel fluid equations for a set of N fluids (a = 1...N, b = 1...N and $a \neq b$). In the shock frame these are:

$$\frac{\partial \rho_a}{\partial t} + \frac{\partial}{\partial x}(\rho_a u_a) = \sum_{a \neq b} s_{ab}, \tag{1.28}$$

$$\frac{\partial}{\partial t}(\rho_a \mathbf{q}_a) + \frac{\partial}{\partial x}(\rho_a u_a \mathbf{q}_a + p_a) = \alpha_a \rho_a (\mathbf{E} + \mathbf{q}_a \wedge \mathbf{B}) + \sum_{a \neq b} f_{ab}. \tag{1.29}$$

$$\frac{\partial e_a}{\partial t} + \frac{\partial}{\partial x}[u_a(e_a + p_a + \frac{1}{2}\rho_a u_a^2)] = H_a + \sum_{a \neq b} G_{ab} + \alpha_a \rho_a \mathbf{q}_a (\mathbf{E} + \mathbf{q}_a \wedge \mathbf{B}). \tag{1.30}$$

These are the mass, momentum and energy equations respectively. The units for $\mathbf{E}$, $\mathbf{B}$ and $\mathbf{J}$ are in the natural Heaviside-Lorentz c.g.s. system such that the speed of light (c) and factors involving 4π do not appear. ρ_a is the mass density of fluid a, $\mathbf{q}_a = (\mathrm{u}_a, \mathrm{v}_a, \mathrm{w}_a)$ is the velocity of fluid a, where u_a, v_a and w_a denote its x, y and z components. p_a is the gas pressure of fluid a, e_a is the energy density of fluid a, α_a is the charge to mass ratio of fluid a, s_{ab} is the mass transfer rate per unit volume from fluid b to fluid a, f_{ab} is the momentum transfer rate per unit volume from fluid b to fluid a, G_{ab} is the energy transfer rate per unit volume from fluid b to fluid a and H_a are the external energy sources and sinks per unit time per unit volume for fluid a. Since mass, momentum and energy are conserved, $s_{ab} = -s_{ba}$, $f_{ab} = -f_{ba}$ and $G_{ab} = -G_{ba}$, i.e. the mass, momentum or energy change in fluid a due to collisions with b is exactly equal and opposite to the change in fluid b. The source terms (s, f, G and H) represent the coupling between the fluids due to collisions. They depend on the physical situation to be modeled and are discussed at length in §2.5 as well as in each subsequent chapter.

The fields are determined from Maxwells equations, which (in the units mentioned above) are:

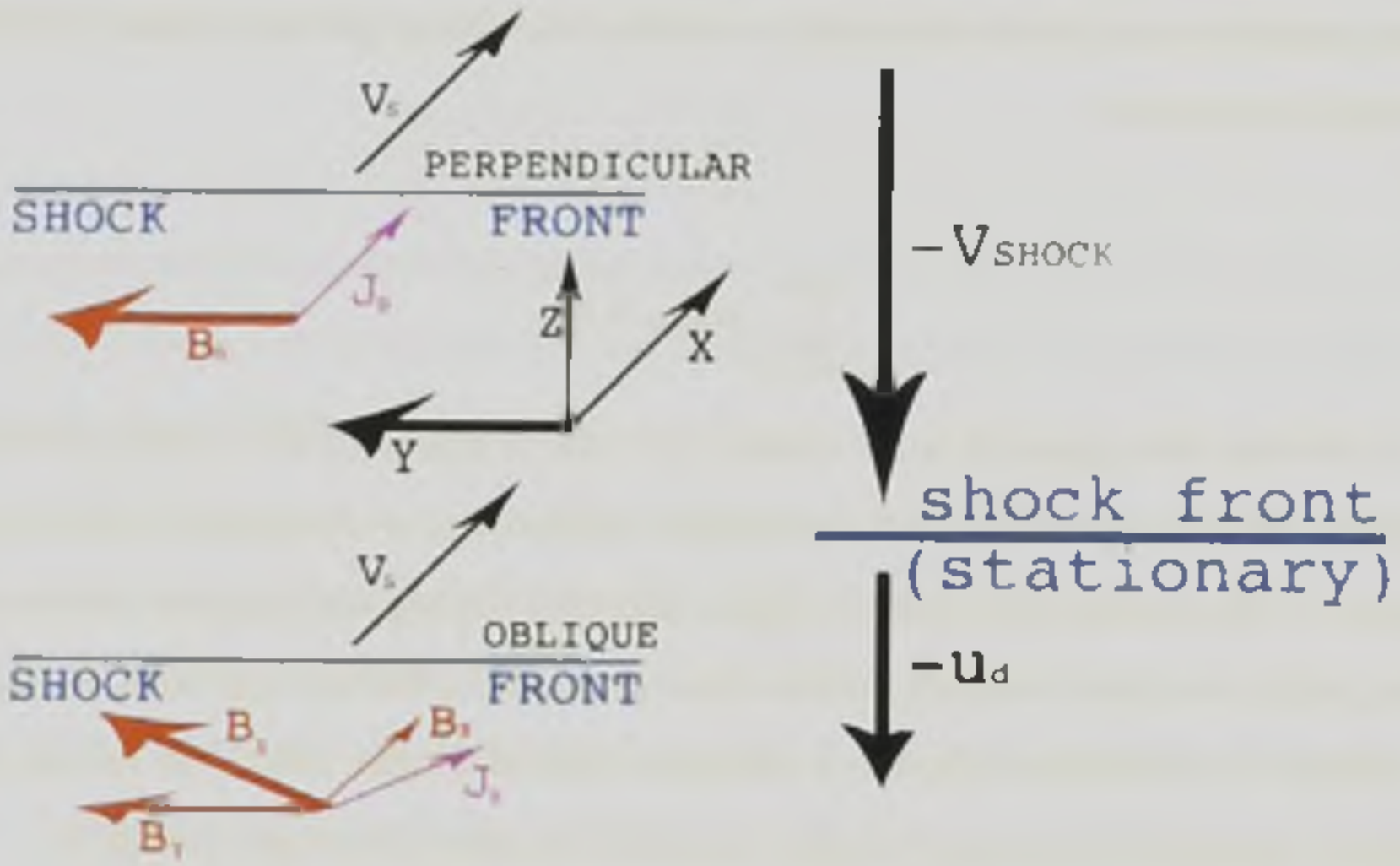

Figure 1.8: The left diagram shows the axes convention used throughout this thesis: the shock moves in the positive x-direction. The magnetic field is in the x-y plane (along the y-axis for perpendicular shocks as in the top left image) and the z-axis is perpendicular to the shock plane. The right diagram shows the flow from the shock frame (in which the shock is stationary). The upstream gas moves towards the shock at -v_{shock} and the downstream gas moves away from the shock front more slowly at -u_d.

$$\frac{\partial B_x}{\partial t} = 0, \tag{1.31}$$

$$\frac{\partial B_y}{\partial t} = \frac{\partial E_z}{\partial x}, \tag{1.32}$$

$$\frac{\partial B_z}{\partial t} = -\frac{\partial E_y}{\partial x}, \tag{1.33}$$

$$\frac{\partial B_x}{\partial x} = J_x, \tag{1.34}$$

$$\frac{\partial B_z}{\partial x} = -J_y. \tag{1.35}$$

Because all the fluid velocities are very much smaller than the speed of light ($\mathbf{q}_a << c$), the current J is given by:

$$\mathbf{J} = \sum_{a=1...N} \alpha_a \rho_a \mathbf{q}_a. \tag{1.36}$$

Charge neutrality must also be demanded so that the total charge per unit volume (summed over all fluids) equals zero:

$$\sum_{a=1...N} \alpha_a \rho_a = 0. \tag{1.37}$$

An obvious first approach to the solution of a set of equations for a steady flow involves the specification of upstream boundary conditions followed by an integration in the downstream direction. In the general (non-steady) oblique case with cooling and chemistry however, one is dealing with a two point boundary problem that can require a different approach. In some cases, the solution can be obtained through a relaxation method (Draine 1980), but the use of a time dependent approach is necessary in many cases and has other advantages (see §2.4).

The equations presented in this section are extremely general, but they already assume that each fluid can be treated with the hydrodynamic approximation (i.e. the evolution of the system can be described in terms of the macroscopic equations of hydrodynamics). This assumption is only valid if interactions between particles of different fluids are much weaker than those between particles of the same fluid. Draine (1986) showed that this approximation is valid for the neutrals and the electrons, which consequently both have Maxwellian distributions, but the same may not be true for the ions.

Let τ_{flow} be the time-scale for the fluid to flow a characteristic distance (L) over which the physical conditions change appreciably ($\tau_{flow} = L/v_s$). If τ_{ij} is the mean time between collisions involving particles of fluids i and j then τ_{ii} is the relaxation time for fluid i; $\tau_{ii} = (\Sigma_{j \neq i}\, \tau_{ij}^{-1})^{-1}$. $\tau_{ii}/\tau_{flow} << 1$ must be satisfied for a fluid to have a near Maxwellian distribution, i.e. collisions bring about equilibrium in the flow much faster than advection changes its properties. In simple terms this constraint demands that any time increments in the equations be larger than the time for relaxation to LTE, so equilibrium is always reached. If the ion fluid (i) streams through the neutral fluid (n) with a velocity ($\mathbf{v_i}$ - $\mathbf{v_n}$) which is at least comparable to the velocity dispersion of the neutrals, then a second condition for the ions to have a near Maxwellian distribution is that the heating rate per unit volume must be small compared to the thermal energy density divided by the relaxation time. This can be written as:

$$\frac{m_i m_n^2 |\mathbf{v}_i - \mathbf{v}_n|^2}{(m_i + m_n)^2 k_b T_i} \frac{\tau_{ii}}{\tau_{in}} << 1, \tag{1.38}$$

where k_b is Boltzmann's constant. By taking values suitable for a C-type shock, Draine (1986) noted that in order to assess whether the ion fluid has a Maxwellian distribution, inequality (1.38) may be more conveniently written as:

$$6 \times 10^{-4} \frac{n_n}{n_i} \left(\frac{|\mathbf{v}_i - \mathbf{v}_n|}{5 kms^{-1}} \right)^2 \left(\frac{T_i}{10^4 K} \right)^{\frac{1}{2}} << 1. \tag{1.39}$$

High ion temperatures (see §2.5.3) and large ion-neutral streaming velocities ensure that this inequality is not satisfied in many shocks of interest. In this case the magnetic field will enforce a Maxwellian distribution along the direction of the field lines, but the velocity distribution in the two directions perpendicular to the field may be strongly non-Maxwellian. This can have important implications for endothermic ion-neutral chemical reactions.

The equations presented in this section allow predictions to be made of the density and temperature profiles for each fluid through the shock structure. The parameters selected for the upstream gas and the chemical processes modeled will affect the molecular abundances and temperatures in the post-shock region. Conditions in the shocked region determine the emission and hence what is observable. Observations of molecular emission from SFRs can therefore provide information about the detailed state of the gas in the shock.

1.3.4 Shock chemistry and observational diagnostics

Section 1.1.3 described the general heating and cooling processes that operate in the ISM and the passage of a shock wave was noted as one method by which the ISM can be heated. As demonstrated in §1.3.1 and §1.3.2, passing through a shock increases the density, temperature and collision rates in any gas. Molecular excitation occurs through inelastic collisions, which dissipates the flow energy. Any radiation from subsequent spontaneous de-excitations which escapes the shock region contributes to the cooling of the gas. Such radiation is (in principle) observable from the Earth. Therefore detailed spectroscopy of the emission from shocked regions provides information about the physical conditions in the emitting gas. As well as confirming the presence of a shock wave as opposed to (for example) a HII (photoionization) or

PDR (photodissociation) region, such observations make it possible to distinguish the type and strength of the shock present.

The equations described in §1.3.3 can be solved using the following assumptions: steady state has been obtained and there is an upstream magnetic field which is perpendicular to the shock normal and scales as B (μG) $\sim$ (n_H/cm^{-3})$^{1/2}$ (see Troland & Heiles 1986). By using parameters suitable for the clumps within GMCs (see table 1.2.1), the solutions obtained strongly imply that the secondary shocks associated with molecular outflows in dense cloud will usually be of C-type (see §1.2.3 and §1.3.2). This is because the shock speeds are low and the medium is dense but only weakly ionized, (see §2). As opposed to J-type shocks, C-type shocks are often non-dissociating and non-ionising because the extended region over which ambipolar diffusion occurs allows the ram pressure of the flow to be converted to random thermal energy of the molecules over many collisions instead of just one or two. The molecules have time between collisions to radiate away much of this thermal energy, substantially lowering the peak temperatures obtained in the shock front.

Figure 1.9 (b) and §1.2.1 indicate that in quiescent, low temperature ($T \leq 10^2$ K) astrophysical media devoid of molecular oxygen and FUV photons, carbon chemistry is initiated by by ion-neutral reactions (of the type denoted by reaction 1.6) involving C^+. This is even valid in denser regions where most carbon is neutral because neutral-neutral reactions (of the type indicated by reaction 1.10) such as:

$$C + H_2 \rightarrow CH + H, \tag{1.40}$$

are very slow at low temperatures. Atomic oxygen cannot be ionized by stellar photons with wavelengths longward of the Lyman limit (i.e. those which remain outside HII regions). Instead, its chemistry must be initiated by neutral-neutral reactions (the vertical line from O in figure 1.9 (b) and see e.g. Sternberg & Dalgarno 1995) such as:

$$O + H_2 \rightarrow OH + H, \tag{1.41}$$

$$OH + H_2 \rightarrow H_2O + H. \tag{1.42}$$

Once the gas temperature has climbed to around 10^3 K, reactions (1.40) - (1.42) have ceased

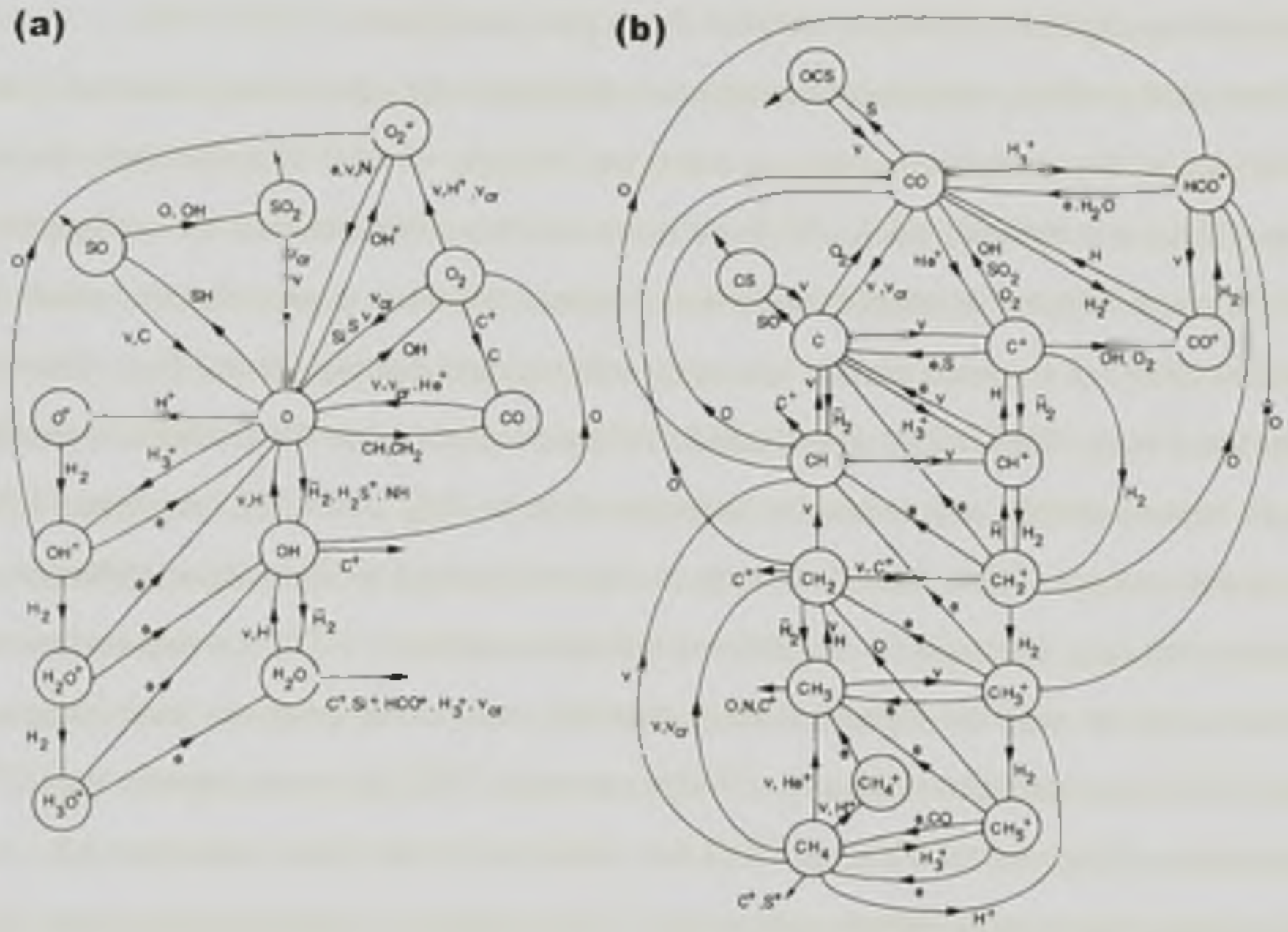

Figure 1.9: Schematic of (a) oxygen and (b) carbon chemistries in dense (10^6 cm^{-3}) molecular clouds exposed to FUV photons (a PDR). In this way, the networks encompass all reactions whether they occur in dense shielded regions or diffuse regions which are exposed to the surrounding stellar radiation field. In each network ν along the arrow indicates that the reaction is with a photon (unimportant in clumps and cores), ν_{cr} denotes a cosmic ray and e an electron as the reaction partner. All other reactions have the partners chemical symbol given explicitly. $\bar{\mathrm{H}}$ and $\bar{\mathrm{H}}_2$ are used to designate endothermic reactions involving atomic and molecular hydrogen. Adapted from Sternberg & Dalgarno (1995)

to be slow. The passage of a shock can heat gas well beyond this threshold. So long as the increase in temperature is not sufficiently large to ionise or dissociate molecules, collisions simply excite them and endow them with higher kinetic speeds. The moderately higher temperatures and densities to be found in C-type shocks permit chemical reactions (especially those involving molecular hydrogen) which are slow in quiescent clouds to proceed with ease. These reactions create molecules not present in the quiescent pre-shock gas which can often cool efficiently through rotational and vibrational transitions. The most effective coolant formed in this way 3is water, which possesses many closely spaced rotational levels. Multiline observations of the shock region can therefore be used together with shock models to infer details about the shock

speed and the properties of the pre- and post-shock gas, (see Figures 1.2 and 1.10).

Observations of rarer molecular isotopes can distinguish the region being observed, permit an inference of flow parameters (such as mass) and indicate whether emission from the most common isotope is optically thick. CO is the most common molecule used for such purposes. This is because it forms in intermediate density regions (between giant molecular clouds and clumps in table 1.2.1), when carbon ions react with oxygen bearing species (e.g. Flower & Pineau-Des-Forets 1990). CO is also formed in diffuse regions when the products of reactions between ionized carbon and molecular hydrogen such as CH_2^+ and CH_3^+ (see figure 1.9(b)) meet atomic oxygen. Once formed, so long as it is not exposed to dissociating radiation, CO is largely inert (e.g. Hartquist et al. 1998 and references therein). $C^{18}O$ is a rare isotope used to observe regions with the highest column densities, such as the protostar itself (where the normal ^{12}CO lines would be saturated). ^{13}CO is rarer than ^{12}CO but more common than $C^{18}O$. Observations of the ratio of ^{13}CO to ^{12}CO line emission (for the same transition, e.g. J = 1 $\rightarrow$ 0) indicate that in most outflow sources the ^{12}CO emission is optically thick (some of the emission from ^{12}CO is not detected due to absorption or scattering in the emission region). The only other possible cause for this would be that the ratio n(^{13}CO)/n(^{12}CO) is higher in the solar system than elsewhere in the Milky Way (a conjecture for which there is no evidence). ^{13}CO observations are therefore used to probe the structure of the outflow where ^{18}CO would be too rare to detect and ^{12}CO is saturated. Because it is sufficiently abundant to be detected but not so abundant that its emission is optically thick, ^{13}CO is the best probe of CO column density in YSO outflows (Lada 1985). Being the most common isotope, ^{12}CO is used to investigate structure in the more rarefied parts of such regions (where conditions are tenuous enough for its transitions to be unsaturated), or to obtain an overview of the morphology of the system. Comparison of interferometric maps in various isotopes of CO can also constrain the velocity distribution in the outflow.

Certain lines from some species (e.g. H_2O and SiO) are only observed in warm post-shock gas. Detection of such molecular emission can demonstrate spatial chemical differences (stratification) along the same outflow (e.g. Bachiller et al. 2001) for example due to shock processing of dust grains (e.g. SiO) or chemistry which has not had time to reach steady state (e.g. OH). Multiline observations of ammonia (NH_3) are a common method to infer the kinetic temperatures in shocked regions (e.g. Tafalla & Bachiller 1995). Some molecules and isotopes can only

be observed in the cold gas condensations around the core (e.g. C_3H_2, DCO^+ and others) and as such are used to study the infalling condensation as well as distinguish such regions from outflows (see below).

Copious collisional ionization only occurs in J-type shocks, where the flow kinetic energy is converted to thermal energy over a very narrow region. This results in high energy collisions and correspondingly high temperatures. Observations of ionized species can therefore be used to distinguish between J- and C-type shocks. Relevant lines to diagnose J-type shocks include [OII], [OIII], [SII] and others, but not [CII] or [FeII] since ionized carbon and iron are found in the more diffuse, un-shocked regions of GMCs (see 1.1.3) and it can also be excited in C-type shocks (Draine & McKee 1993). Since HII regions produce different line strength ratios from shocked regions, e.g. for [OI]$\lambda\lambda$6300,6364/H_α (caused by different pre-shock ionization states of oxygen), it is possible to distinguish between them and shocks. Once an observed region has been confidently associated with a shock, one of the best indicators of a J-type shock is copious far IR emission form ions. Similarly, optical metastable forbidden lines (such as [OI]λ6300) and hydrogen recombination emission are only produced in hot gas, so their detection would also imply a J-type shock (Hollenbach & McKee 1989).

In C-type shocks, the survival of molecules ensures efficient neutral cooling and this guarantees much lower peak temperatures ($T_n < 10^4$ K) than would be obtained in a J-type shock moving at the same speed. When coupled with low fractional ionization, this suggests that the peak flux in radiation from a C-type shock will be in the IR, from neutral molecular species.

For a C-type shock moving above 20 km s^{-1} through an upstream density below around 10^6 cm^{-3}, most cooling occurs through H_2 as its vibrational and rotational lines become excited. If the post-shock gas temperature in a dense region exceeds a few thousand Kelvin then the low lying vibrational states of H_2 become collisionally excited. Shocks with speeds from around 10 km s^{-1} up to the dissociation threshold for molecular hydrogen excite the $\nu = 1 \rightarrow 0$ and $\nu = 2 \rightarrow 1$ H_2 lines (at 2.122 and 2.247 μm). Such lines can be observed in young, optically invisible objects such as deeply embedded (Class 0) sources, e.g. L1448-mm (Bachiller 1996). However H_2 vibrational emission only dominates the radiative losses when $v_s \geq 20$ km s^{-1}.

Below 20 km s^{-1}, atomic fine structure lines (mainly [OI] 63μm) and CO line emission are more effective than vibrational H_2 regardless of the pre-shock density. Such emission can be used to probe neutral gas below about 500 K. Above this temperature atomic oxygen is

efficiently converted into water by reactions (1.41) and (1.42). Water itself makes an efficient coolant due to many closely spaced rotational lines and once formed it is fairly stable. This makes it a more effective coolant than atomic oxygen or CO. Water is a very efficient coolant over the range ~ 500 K $< T < \sim 2000$ K, above which it is dissociated and overtaken by H_2 vibrational excitation (see chapter 8 of Hartquist et al. 1998 and figure 1.10(c)). H_2O lines are difficult to detect on Earth due to atmospheric absorption. Plots (a) and (b) in figure 1.10 demonstrate water replacing atomic oxygen as the principal coolant when higher shock speeds increase the post-shock temperature and result in more oxygen being converted. Figure 1.10 (a) also shows that as the shock speed increases past ~ 20 km s^{-1}, H_2 cooling surpasses even water, resulting in stronger fluxes at shorter wavelengths (see also figure 1.10(c)).

No species or lines are unique to shocked regions in general or C-type shocks in particular. However, the detection of SiO emission would strongly suggest the passage of a shock since no other process is known to liberate silicon from the grains in dense molecular clouds (see §1.3.5). Therefore, a lack of detection of the ionic and recombination lines which are specific to J-type shocks, together with detections of both SiO and other molecular rotational lines is the strongest indication available both that a shock is present and that it is of C-type. Care must be given however since the lack of detection of a line could be caused by absorption or scattering of its radiation in either the Earths atmosphere or the emission region. An overview of molecular line emission over a range of shocks speeds for density and temperature conditions of interest is included as figure 1.10. By inspecting these plots and figure 1.2, it is clear to see how the presence and relative strength of various atomic and molecular lines permits a diagnosis of the densities, temperatures and velocities obtained in C-type shocks.

1.3.5 Sputtering and grain-grain collisions

As mentioned in the closing paragraph of §1.2.3, any relative velocity between the charged and neutral particles in a C-type shock wave results in collisions between the species. Since grains represent vast conglomerations of molecules as opposed to single particles, collisions involving dust grains may do more than simply transferring energy and momentum and exciting internal states.

Near the outflows associated with some protostars, silicon bearing species are observed to be prevalent. In quiescent dark clouds only upper limits on the SiO abundance can be ascertained

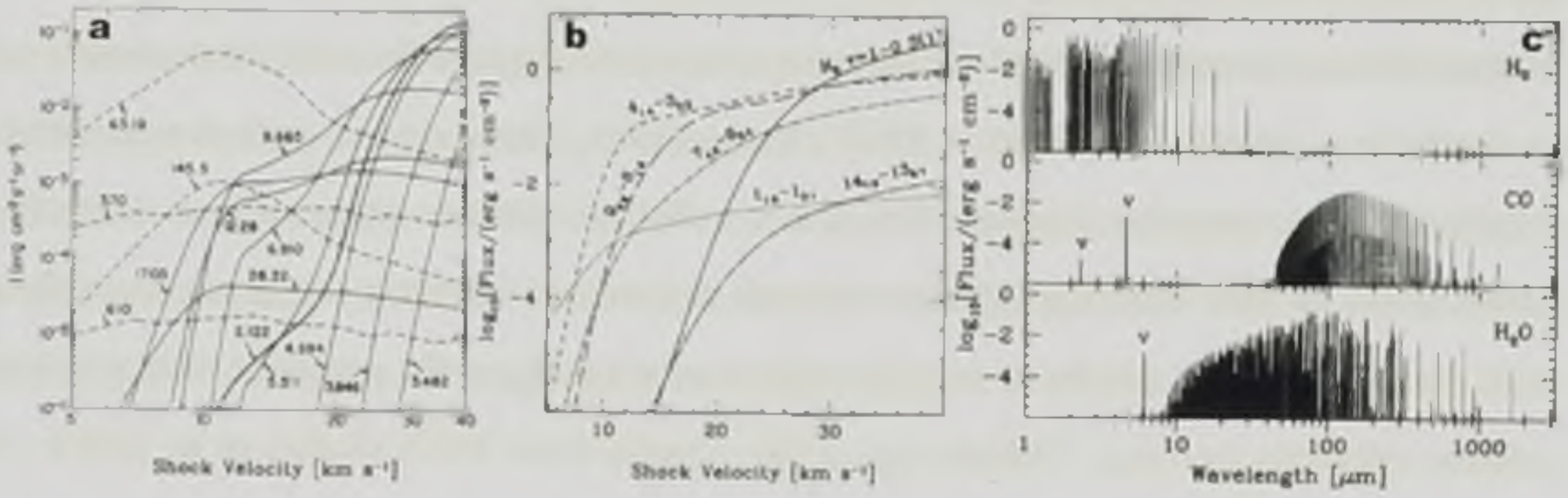

Figure 1.10: Calculated line intensities and spectra for C-type shocks. (a) presents calculated line intensities for C-type shocks of varying speeds propagating into a cloud of density 10^6 cm^{-3}, with a pre-shock perpendicular magnetic field of 10^{-3} G and a fractional ionization of 10^{-8}. The atomic fine structure line ([OI] 63 μm) is the top left dashed line, with the other dashed lines referring to atomic fine structure lines of [OI] and [CI]. The solid curves are rotational and rotational-vibrational transitions of H_2 (numbers denote wavelengths in μm). Taken from Draine et al. (1983). (b) displays calculated water line intensities for C-type shocks of varying speeds into a cloud with the same parameters as (a). For comparison, the rotational-vibrational transition of $H_2(\nu = 1 \rightarrow 0)$ at 2.12 μm is included which is equivalent to the bold curve marked 2.122 in (a). Taken from Kaufman & Neufeld (1996). (c) is a calculated molecular spectra for a 40 km s^{-1} C-type shock propagating into a cloud of density 10^5 cm^{-3} with a pre-shock perpendicular magnetic field of 4.47×10^{-3} G and a fractional ionization of 3×10^{-8}. Shows the expected flux as a function of wavelength as well as the wavelength of the peak emission for each species. Taken from Kaufman & Neufeld (1996).

($\chi_{SiO} < 3 \times 10^{-12}$ e.g. see Ziurys et al. 1989; Jiménez-Serra et al. 2010). Conversely, SiO is easily observable at the heads and along the axes of some molecular outflows from YSOs, implying that its abundance has been enhanced by several orders of magnitude, (factors of up to 10^6; e.g. Martin-Pintado et al. 1992; Bachiller 1996; Jørgensen et al. 2004). The first SiO lines detected in YSO outflows were broad ($\sim$ 50 km s^{-1}) and centred on different velocities ($30 < (v_{SiO} - v_{ambient}) < 50$ km s^{-1}) than the ambient cloud (e.g. Martin-Pintado et al. 1992). Measurements taken towards the outflows from high mass SFRs also demonstrate an association of SiO with shocked regions (e.g. Downes et al. 1982; Wright et al. 1983; Acord et al. 1997; Beuther et al. 2004). Its high condensation temperature and refractory nature ensures that gas

phase silicon is heavily depleted in the quiescent regions of dense molecular clouds, (see §1.1.2). If observed near a protostar, gas phase silicon species are likely to be the result of dust processing in shocks (e.g. Martin-Pintado et al. 1992; Draine 1995). There are two main mechanisms by which this processing can happen. The first is collisions between grain species which (by a combination of their differing effective charges and neutral collision rates) possess different Hall parameters. This results in varying degrees of coupling to the magnetic field and hence relative velocities (see e.g. Tielens et al. 1994; Caselli et al. 1997; Guillet et al. 2009). The second is charged grains drifting with respect to the neutrals and being impacted by them (see e.g. Draine et al. 1983; Flower & Pineau des Forets 1995; Caselli et al. 1997; Schilke et al. 1997; May et al. 2000), in a process known as sputtering. As long as the incident (projectile) atom or molecule has sufficient kinetic energy to overcome the binding energy of the target atom, the target can be released into the gas phase. Different bonding mechanisms result in different binding energies for the core (silicate) and mantle (mainly water ice with traces of organic compounds, see §1.1.2). Either process can only occur when relative velocities exist between the species in question to permit systematic collisions.

Since grains are much more massive than atoms or molecules they carry far more momentum at a given drift speed. This means that a single grain-grain collision can be highly disruptive. When a large, solid projectile strikes a target of comparable size, shock waves propagate into both. The shocked grain material is heated and compressed to very high pressures. Whichever grain is crossed first by the shock is denoted the projectile. When the shock reaches the edge of either grain, rarefaction waves are reflected back into the shocked regions, relieving the high pressures. Upon release of the pressure, so long as the solid has not attained a stable high pressure solid state (e.g. diamondization of graphite), the volume of the shocked material increases and it may pass from being solid into a liquid or a vapour phase. The shocked material may also shatter, producing a backsplash of ejected material and excavating a crater. Numerical and experimental studies have yielded a simple relationship between the mass and velocity of the impactor and the target mass shocked to a given pressure: $E \sim PV$. In other words, the energy (E) per unit volume (V) of the shocked material approximately equals the pressure (P). The damage inflicted upon the target can be measured in terms of the fraction of its volume shocked beyond some critical pressure.

In the case of vaporization, grain material is shocked to sufficient pressure for it to be re-

duced to its component atoms or molecules and returned to the gas phase. For the entire target to be vaporized, the internal energy (energy per unit mass of the shocked matter) must be about five times the binding energy of the grain material (Ahrens & O'Keefe 1972). Experiments on macroscopic samples however suggest that partial vaporization commences when the internal energy approximately equals the binding energy whereas appreciable ($\sim$ 25 %) vaporization requires twice the binding energy (see Tielens et al. 1994 and references therein).

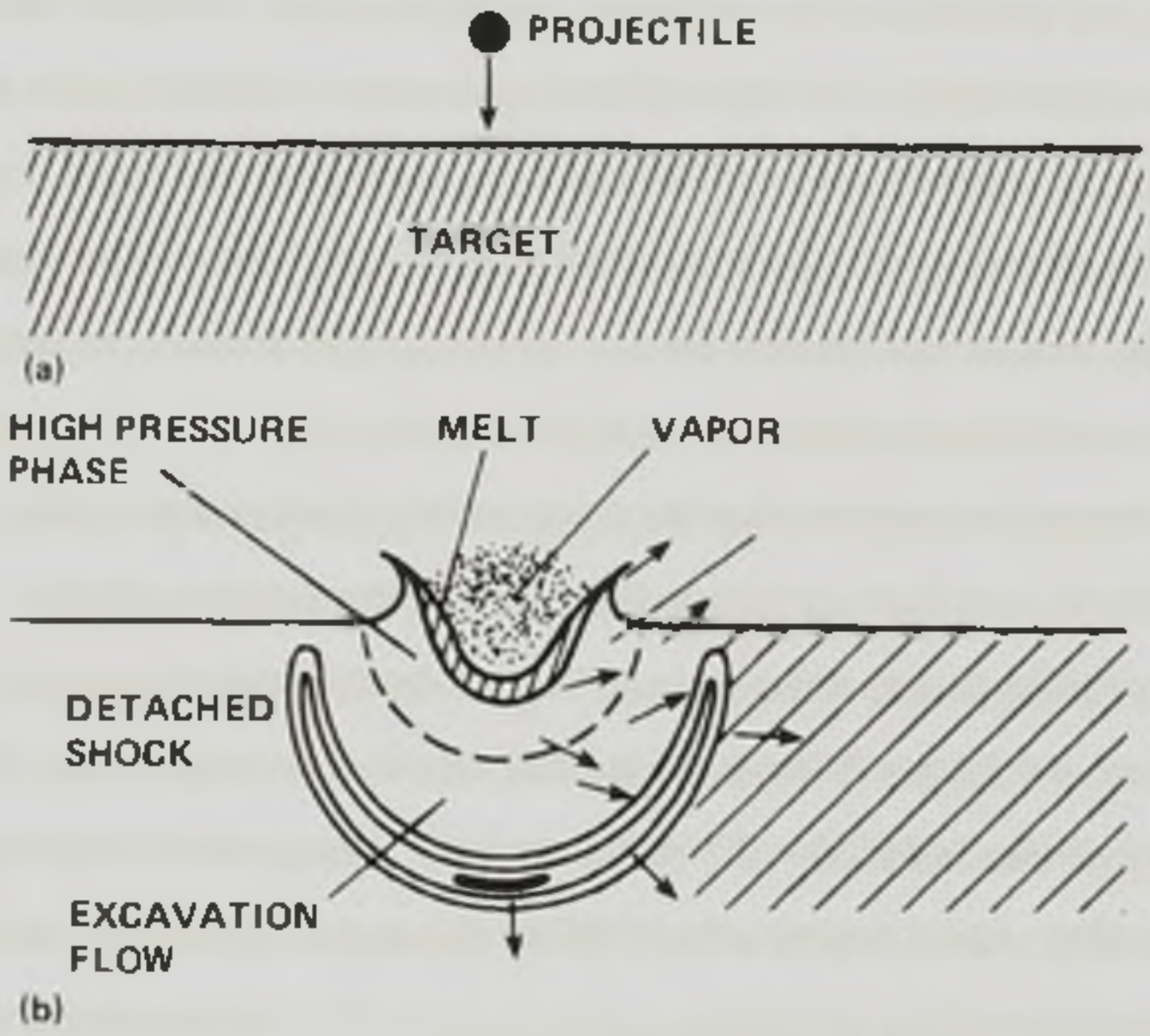

Figure 1.11: Schematic of the collision of a projectile with a planar target relevant for the collision of two dust grains of differing sizes. The fate of the shocked material will depend on the peak pressure attained in the shock. The peak pressure drops as the shock moves into the target and the impact energy is dissipated. Moving inwards from the impact point, one encounters successive zones where the target material has been vaporized, melted, or converted into a stable high pressure phase (see text). The arrows represent the velocity vectors in the excavation flow. It is these velocities that result in shattering and determine the size of the final crater. Taken from Tielens et al. (1994).

Shattering occurs when target material is broken into smaller pieces and ejected from the grain. The ratio of the target material disrupted to projectile mass scales as (Tielens 2005):

$$\frac{m_{crater}}{m_p} \propto \left(\frac{v_{impact}}{v_{cr}}\right)^{\frac{16}{9}}, \tag{1.43}$$

m_{crater} is the processed target mass, m_p is the projectile mass, v_{impact} is the relative speed between the two grains and v_{cr} is the critical velocity for shattering (if $v_{impact} = v_{cr}$ then the crater mass is directly proportional to the projectile mass). Below critical velocity, the crater mass is less than the projectile mass and drops rapidly towards zero with decreasing impact speed. Above critical velocity, the ratio of the crater mass to the projectile mass is greater than one and given by expression (1.43). When $m_{crater} = m_{grain}$, the target is destroyed. The critical pressure for shattering is much lower than that for vaporization. The size distribution of the fragments produced by this process are not experimentally known, but theoretical models suggest that they should have a power law size distribution; $dn(r)/dr \propto r^{-\alpha}$, with α around 3.5 (Tielens 2005). Theory also implies that the fragment size produced at a given depth depends on the pressure there, which drops almost linearly with the volume affected. The threshold relative velocities for producing fragments and vapour depends on the target material. For ice these are $\sim$ 1.8 and $\sim$ 6.5 km s^{-1} for shattering and vaporization respectively. For silicates the same models suggest thresholds of $\sim$ 2.7 and $\sim$ 19 km s^{-1} respectively (Tielens 2005). Thus, for shocks in the ISM, partial vaporization is likely dominated by the high velocity impact of medium sized grains onto large grains ($r_{target}/r_{projectile} \sim 3$). The percentage of silicate mass vaporized in such collisions is calculated to be only around 2.3% of the total disrupted mass so shattering is more important. This is especially true for large grains (Jones et al. 1994). At high enough impact velocities, the target is catastrophically destroyed. If a small grain with radius 10^{-6} cm was to impact a large grain of radius 10^{-5} cm, the critical relative velocity for total disruption of the silicate core of the large grain is approximately 55 km s^{-1}, (Tielens 2005).

Sputtering refers to the process where an energetic particle (the projectile) collides with a solid material (the target) and leads to the ejection of atoms or molecules from the target into the gas phase. The sputtering yield is defined as the average number of target atoms ejected per projectile impact. This parameter depends on the ratio of the energy deposited near the surface to the binding energy of the target material (i.e. whether refractory core or ice mantle). The projectile energy can be dissipated through inelastic nuclear interactions or via electronic excitation of target atoms. The projectile may be deflected or even back scattered. At high

enough energies, recoiling collision partners are able to create a cascade which ejects surface atoms. At low energies, the energy deposited depends on the projectile mass since heavier projectiles possess more momentum and kinetic energy at a given streaming velocity (Field et al. 1997). The deposited energy also depends on the mass ratio of the projectile to target atom, since higher values for this parameter increase the importance of back scattering near the surface. Near to the threshold, sputtering is dominated by back scattered projectile atoms which can transfer sufficient energy to target atoms on their way out of the surface to induce erosion (Tielens et al. 1994). The impact energy is determined by the relative velocity between the projectile and target. The case relevant for astrophysics is when the projectile mass is low and the impact energy is near the sputtering threshold. This allows heavier species to dominate the sputtering process despite their low abundances because their impact energies are higher at a given drift speed and their larger cross sections mean that they are more likely to be back scattered. The grain-neutral relative velocity may come about due to systematic grain-neutral streaming as in C-type shocks, known as inertial sputtering. It may also be due to the higher thermal speeds of gas particles in the post-shock region and is then denoted thermal sputtering. The latter is only important in hot gas ($T > 10^5$ K). In C-type shocks, efficient cooling ensures low post-shock neutral temperatures. When coupled with a grain-neutral relative velocity which is maintained over a wide region (e.g. Draine 1980), this implies that only inertial sputtering is relevant in such shocks.

The release of silicon bearing species from grain cores by sputtering has been previously considered by Draine (1995), Flower & Pineau des Forets (1995), Schilke et al. (1996) and May et al. (2000) as well as others. Draine et al. (1983) were amongst the first to undertake similar calculations for water ice being sputtered from grain mantles. Caselli et al. (1997) perform steady calculations for oblique multifluid shocks. Their work is analogous to the time dependent models presented in this report. They consider both sputtering and collisions between grains of different sizes to investigate the return of mantle and core material for a number of density regimes and shock speeds. They report that grain-grain collisions dominate the return silicon to the gas phase (i.e. through vaporization) for shock speeds between 25 and 35 km s^{-1} and only when the upstream hydrogen number density is above 5×10^5 cm^{-3}. That high densities are required for grain-grain collisions to be effective is to be expected since it is only in such regions that grain-neutral collisions occur often enough to partially decouple large ($r > 10^{-5}$ cm) grains

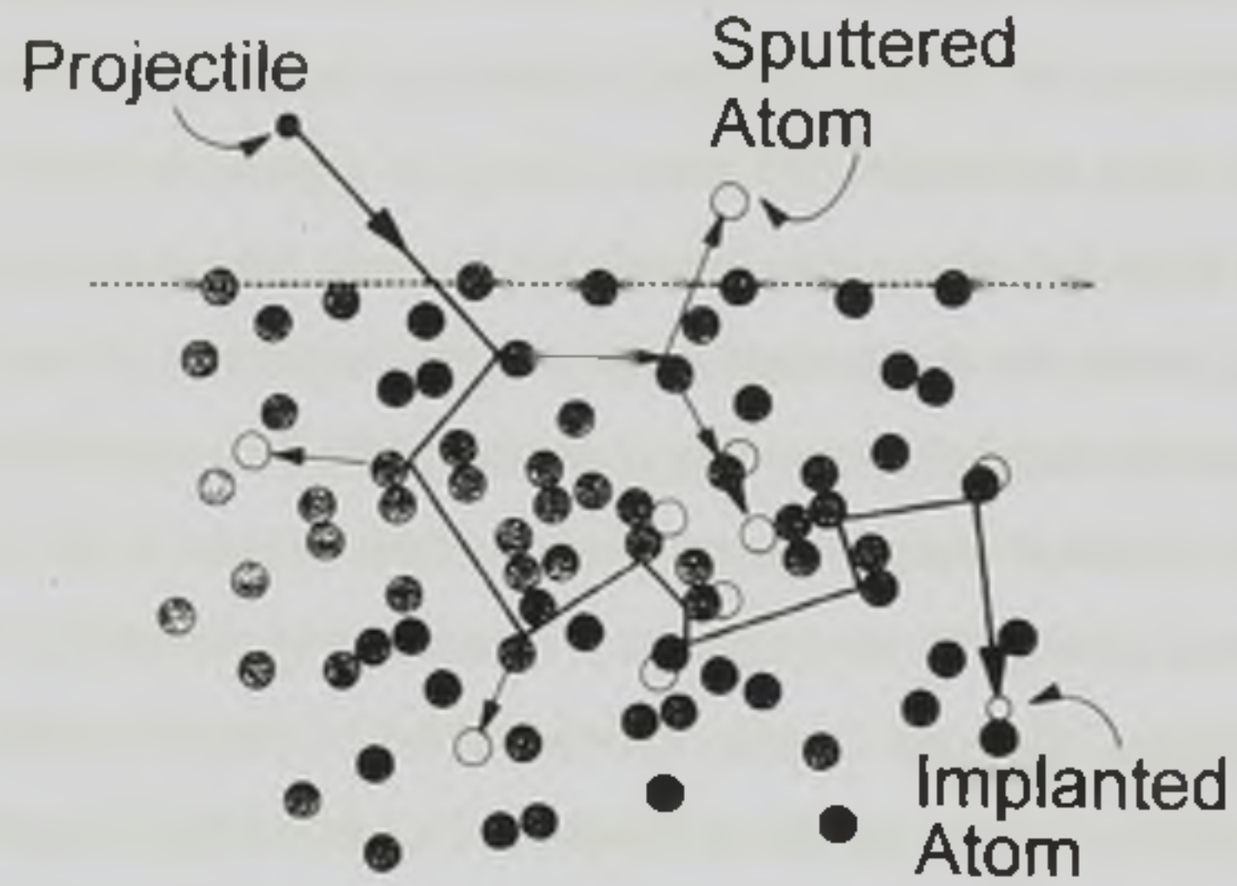

Figure 1.12: Schematic of the sputtering process. The projectile enters the grain surface and dissipates its impact energy in a series of binary collisions until insufficient energy is left to displace further target atoms and the projectile becomes implanted in the target. In this diagram, the first collision partner undergoes a subsequent collision with another target atom and is back scattered with enough energy to escape the grain surface as a sputtered atom (see text). Taken from Field et al. (1997).

from the field, resulting in a relative velocity between them and smaller grains (which have smaller collision cross sections). In the case of the mantles, grain-grain collisions dominate the return of water to the gas phase only for a very narrow range of pre-shock parameters ($v_s \leq \sim$ 15 km s^{-1}). In addition, their models find that sputtering alone is sufficient to completely erode the ice mantles for all densities considered when $v_s \geq 15$ km s^{-1}. They conclude that grain-grain collisions in an ambient gas through which an outflow is driving a shock can reproduce the (lower) SiO abundances observed in regions of high mass star formation ($\chi_{SiO} \sim 10^{-8}$ - 10^{-9}), but that the sputtering process is needed to explain the higher gas phase silicon abundances around low mass YSOs ($\chi_{SiO} \sim 10^{-6}$, see e.g. Martin-Pintado et al. 1992). Other authors, including Jones et al. (1994), concur that sputtering must be the dominant mechanism in the outflows from low mass YSOs. Hence, prominent SiO emission from low mass SFRs usually indicates that a shock has induced sputtering of the grains (e.g. Ziurys et al. 1989; Martin-Pintado et al. 1992) and released silicon bearing species to the gas phase.

Modeling such molecular emission from low mass YSOs demands a time dependent scheme

capable of simulating non-steady shocks in cold, dense, dusty, weakly ionized media, including source terms to describe chemistry and grain sputtering. Since the 1970s considerable effort has been expended in observing SFRs. Observational constraints on the physical conditions in the outflow have provided parameters with which to model such regions. From 1980 onwards there have been several theoretical studies concerned with the modeling of C-type shock waves in molecular clouds to investigate their structures and effects on quiescent cloud material.

Chapter 2

Modeling C-type shocks

2.1 Perpendicular multifluid shock models

During early theoretical investigations into C-type shock structure, computational and model limitations restricted studies to steady shocks, i.e. those which are not evolving with time. Assuming steady state allows the time derivative terms in equations (1.28) - (1.30) to be neglected. Initial studies considered only transverse magnetic fields, i.e. the field is exactly perpendicular to the shock normal. Draine (1980) and Draine et al. (1983) present two fluid treatments of steady perpendicular C-type shocks in molecular clouds. Draine et al. (1983) assume that the ions and electrons can be treated as a single fluid and give an approximate treatment of grain dynamics. After considering various density and shock velocity regimes, they deduce that in many cases the shocks propagating through molecular clouds will be C-type. Energy dissipation in their models occurs primarily through ion-neutral friction. They give detailed descriptions of momentum and energy transfer and heating and cooling processes, including relevant cross sections and rate coefficients. They also model the dissociation of molecular hydrogen, simple oxygen chemistry and grain mantle erosion via sputtering. Their approximate treatment of the grains is suitable for a broad region of parameter space, but its validity breaks down for upstream neutral number densities above $\sim 10^6$ cm^{-3} when combined with their assumptions about the nature of the grains. This is because such a scheme is unsuitable when grains become the dominant source of friction with the neutrals. Draine et al. (1983) find that in molecular clouds, for upstream densities in the range $10^2 < n_H\ (\mathrm{cm}^{-3}) < 10^6$, with an upstream magnetic field which scales as $B(\mu G) \sim (n_H/\mathrm{cm}^{-3})^{1/2}$ and for shock speeds below around 50 km s^{-1} one would expect the steady structure to be C-type. This speed is higher than earlier estimates because they also find the minimum speed for H_2 dissociation in the shock to be higher ($v_{dis} > 40$ km s^{-1}

for $n_H = 10^6$ cm^{-3}) than previously thought. The lack of dissociation allows efficient molecular line cooling to persist in faster shocks (see §1.1.3). In addition, their chemical model suggests that at high ($> 10^4$ cm^{-3}) densities, the formation of new species such as water can be important to the thermal structure of the shock (by providing closely spaced rotational energy levels and hence an efficient cooling mechanism; see §1.3.4 and §2.5.3). Therefore a fuller treatment of the grain dynamics is required to model dense cloud regions where grains have become the dominant source of friction on the neutrals.

Pilipp et al. (1990) construct steady perpendicular shock models for four fluids. If the shock propagates along the x-axis and the magnetic field lies along the y-axis, the shock plane is then the y-z plane. Ions and electrons are modeled as different fluids. They include grains explicitly, also as a separate fluid, assuming them to be spherical and of a uniform size (radii of either 1 or 4×10^{-5} cm). Charged particles moving through a magnetic field experience a force perpendicular to the field. The magnetic force on a charged particle is related to the field strength and the component of its velocity perpendicular to the field lines. It is given by $\mathbf{F} = q\mathbf{v} \wedge \mathbf{B}$. Since $\mathbf{F}$ is given by a cross product, the magnitude of $v_\perp$ stays the same but its direction changes. Hence the particle moves in a curve. The sense of the curve (whether clockwise or anti-clockwise about the field lines) depends on the charge sign of the particle. The resulting motion is indicated in figure 2.1a. If the charged particle were initially moving perpendicular to the field lines then a circular orbit would result, with a frequency that depends on the field strength and the particles charge to mass ratio ($\omega_c = qB/m$) and a radius given by $r_c = mv_\perp/qB$. This force only affects the charged particles. The adoption of the shock frame allows the charged particles to be advected with the flow (along v in figure 2.1a) but now they will also possess extra (orbital) velocity components in the x-z plane. This means that there is now a relative velocity between them and the neutrals.

The addition of an electric field $\mathbf{E}$ which is perpendicular to the magnetic field $\mathbf{B}$ changes the force experienced by a charged particle to:

$$\mathbf{F} = q(\mathbf{E} + \mathbf{v} \wedge \mathbf{B}). \tag{2.1}$$

This is known as the Lorentz force. There is no force on any charged particle along the magnetic field lines since the electric field cannot produce a force perpendicular to itself and the magnetic

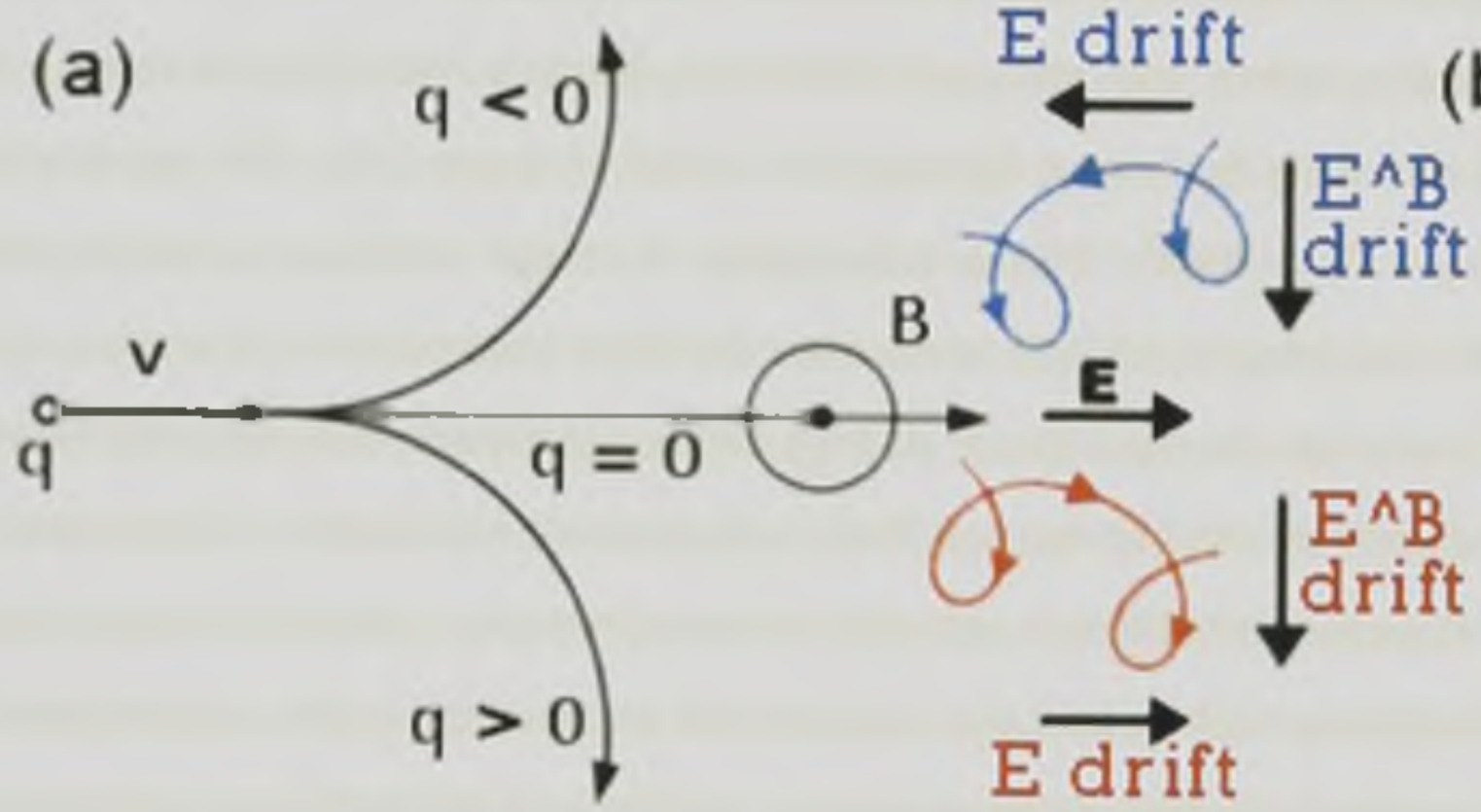

Figure 2.1: (a) Magnetic force on positive (lower curve) and negative (upper curve) charged particles initially moving left to right with a velocity v (x-direction) which is perpendicular to the magnetic field (directed perpendicular to the sheet, towards the reader, in the y-direction). The motion is a circular orbit, in the x-z plane, at frequency ω_c = qB/m. (b) The Lorentz force on a charged particle which is initially at rest in an electromagnetic field. The addition of an electric field denoted **E** produces a net force along **E** in the sense determined by the charge sign of the particle; along the arrows denoted **E** drift. It changes the circular orbits from (a) into cycloids. These paths are indicated for positive (red) and negative (blue) particles. Perpendicular magnetic and electric fields also result in a systematic drift velocity along the arrows denoted **E** $\wedge$ **B** drift. In the absence collisions the speed and direction of this drift is independent of the particles charge and mass. Diagram adapted from Wikimedia commons; http://en.wikipedia.org/wiki/File:Charged-particle-drifts.svg.

field cannot produce a force parallel to itself. As before, the component of the initial velocity parallel to the magnetic field remains unchanged. This force is therefore along **E**, in the sense determined by the charge (along the arrows denoted **E** drift in figure 2.1b). Regardless of the charge sign of the particle, for half of the orbit it moves along the electric field lines and is accelerated whereas for the other half it moves against the electric field lines and is decelerated. The circular orbit thus becomes a cycloid with opposite net motions for positive and negative charges. In a system initially at rest ambipolar diffusion would occur as the charged particles drift through the neutrals. These motions are parallel to the electric field lines and any associated

conductivities, resistivities and currents are denoted as Pedersen.

Over several gyrations, any orbit also drifts perpendicular to both **E** and **B**: in the z-direction in figure 1.8 and along the arrows denoted $\mathbf{E} \wedge \mathbf{B}$ drift in figure 2.1b. The speed of this drift is given by $v_d = (\mathbf{E} \wedge \mathbf{B})/\mathbf{B}^2$. This is independent of charge and mass so (in the absence of collisions) all charged particles drift in the same direction (determined by the signs of the field components) and with the same speed. At high densities however, collisions with neutrals will periodically decelerate charged species. Their subsequent re-acceleration is dependent on mass and charge. Together with different collision cross-sections (e.g. grains have much larger cross sections for collisions with neutral than ions do) this can lead to various charged species moving in different directions with different speeds. Such unmatched motions of charge constitute currents and lead to a separation of charges and an asymmetric charge density. The separation of charge establishes an electric field to oppose the migration of further charge, building up a steady electric potential, which is due entirely to the differing drift speeds of the various fluids. The motion is perpendicular to both the electric and magnetic fields and this process is known as the Hall effect. There are accompanying conductivities, resistivities and currents which are also denoted Hall.

Pilipp et al. (1990) note that for sufficiently high density regions of parameter space, (e.g. $v_s = 15$ km s^{-1}, $B_0 = 4.7 \times 10^{-3}$ G, $n_n = 10^7$ cm^{-3}), the fractional ionization in the precursor region can drop by two orders of magnitude from its upstream value, instigated by recombinations and the charging of the grains. The dust grains then become important carriers of negative charge. As the ratio of gas phase electrons to ions becomes lower, even with their lower kinetic speeds, the ions encounter grains more often than the (depleted) electrons do. Ions recombine with electrons on the grain surfaces. This leads to the grains becoming less negatively charged and being less influenced by the magnetic field. The grain Hall parameter can drop to unity or less. Each charged fluid (a) has its own Hall parameter denoted β_a. A small grain Hall parameter and a large ion Hall parameter results in a charge separation electric field component in the x-direction (along the shock normal). At the upstream edge of the shock, frequent collisions with neutrals ensure that the negative grains are accelerated later than the other charged fluids but still earlier than the neutrals. The ions move in the helical orbits described above whereas the trajectories of the grains are curved much less. There is also an $\mathbf{E} \wedge \mathbf{B}$ drift in the z-direction, but frequent grain-neutral collisions (which are a result of large grain sizes) ensure

that the negative grains drift at much lower speeds and in the opposite sense to the positive ions. In fact, the ion-neutral drift speed in the z-direction becomes comparable to the shock speed for the parameters above. A faster ion-neutral drift speed increases the ion-neutral collision rate and this heats the ions. Faster, hotter ions collide with and recombine on grain surfaces more often, reducing the grain charge and the fractional ionization. The x-component of the electric field is inversely proportional to the magnitude of the grain charge so it increases, accelerating the ions in the x-direction (along $\mathbf{E}$) and in the z-direction (along $\mathbf{E} \wedge \mathbf{B}$). The ion grain-grain collision rate again increases, further heating the ions and increasing the recombination rates. This can result in a runaway effect, which has serious consequences for the ionization structure and heating of the gas. Pilipp et al. (1990) note that the runaway effect is caused by the shock being exactly perpendicular. This is a contrivance unlikely to be physically realised. Therefore they suggest that models of oblique shocks are desirable. They also point out that the inclusion of a second (smaller) grain fluid, which carries much of the negative charge, but remains better coupled to the magnetic field tends to supress the runaway.

2.2 Oblique multifluid shock models

The existence of a component of the magnetic field along the shock propagation direction has important consequences, even in a single fluid treatment. It allows for the existence of three types of MHD waves which are able to propagate along the shock normal (introduced in §1.3.2). The three relevant speeds are the slow- (c_s), intermediate- (c_i) and fast-mode (c_f) wave speeds. The relationship between the upstream or downstream flow speeds (u_u and u_d respectively), as measured in the shock frame and the three MHD wave speeds determines the type of shock obtained. If the upstream flow is above the slow-mode wave speed and the downstream flow is below it ($u_u > c_s$ and $u_d < c_s$), then a slow-mode shock is present. Across a slow-mode shock the plasma pressure increases, the magnetic field strength decreases and the magnetic field lines bend towards the shock propagation direction. When the upstream flow is above the fast-mode wave speed and the downstream flow is below the fast-mode wave speed, but above the intermediate-mode wave speed ($u_u > c_f$ and $c_i < u_d < c_f$) then a fast-mode shock is present. Across a fast-mode shock both the plasma pressure and the magnetic field increase and the magnetic field lines bend away from the shock propagation direction. For both slow-

and fast-mode shocks the distant up and down stream magnetic fields lie in the same plane and their dot product is positive (see figure 2.2). If the fluid velocity ahead of the shock is above the intermediate-mode wave speed and behind the shock it is below it ($u_u > c_i$ and $u_d < c_i$), then an intermediate-mode shock exists. Intermediate-mode shocks do not compress the fluids, but rather induce a rotation of the magnetic field such that the distant up and down stream magnetic fields lie in the same plane but their dot product is negative (see below). Steady solutions do exist for intermediate-mode shocks but such shocks always evolve into a non intermediate-mode shock and a rotational discontinuity when time dependence is allowed (e.g. Falle & Komissarov 2001).

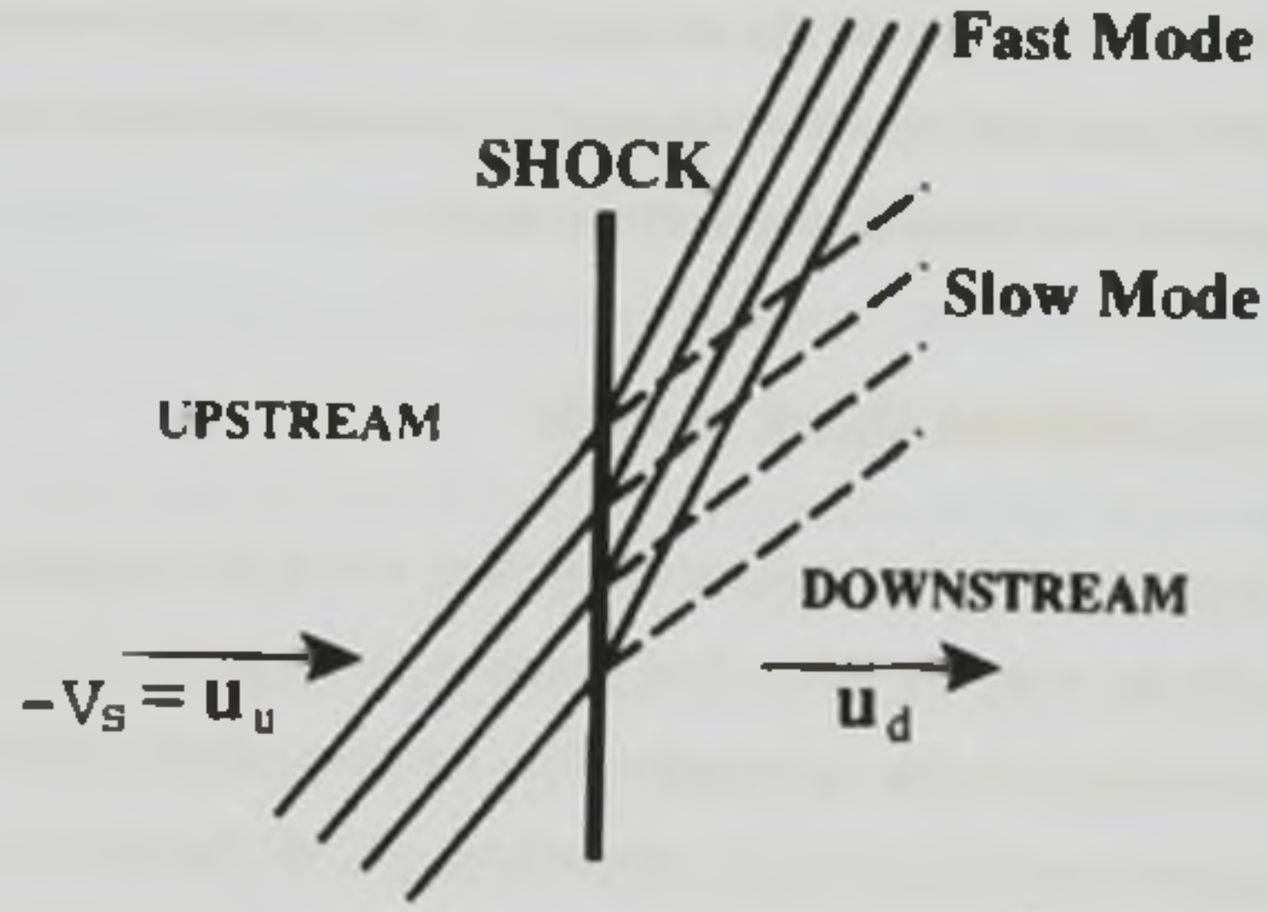

Figure 2.2: A schematic for the post-shock field configurations in a slow- and fast-mode shock. The pre-shock magnetic field is oblique to the shock normal, and the frame is chosen such that the shock is stationary. Taken from Kivelson & Russell (1995)

Pilipp & Hartquist (1994) give the first four fluid treatment (neutrals, ions, electrons and grains) of steady oblique C-type shocks in molecular clouds. They treat the grains explicitly as a separate fluid, assuming them to be spherical with radii of 4×10^{-5} cm. They draw on the findings of Pilipp et al. (1990) for the ionization balance and Havnes et al. (1987) to evaluate the currents of charged particles onto grains (see §2.5.4). In their models, the shock propagates along the x-axis and the upstream magnetic field takes the form $\mathbf{B} = B_{0x}\hat{x} + B_{0y}\hat{y}$. The current

due to the magnetic field therefore lies in the x-y plane and for this magnetic field configuration, the upstream electric field is in the z-direction; $\mathbf{E} = \mathrm{E}_{z0}\hat{z} = -(\mathrm{v}_s \mathrm{B}_{y0}/\mathrm{c})\hat{z}$.

In the discussion of perpendicular shocks, it was noted that the charged fluid velocity will have only components in two out of three directions (x and z) because a magnetic field cannot produce a force parallel to itself and an electric field cannot produce a force perpendicular to itself. Now that the upstream magnetic field exists in both the x- and y-directions, the charged fluid velocity has components in all three directions. It can be split into components which are parallel ($\mathrm{u}_{a//}$) and perpendicular ($\mathrm{u}_{a\perp}$) to the net magnetic field (a = i, e, g). The fact that the sense of the Lorentz force (equation 2.1) depends on the charge sign ensures that ambipolar diffusion occurs. The oblique field configuration allows the associated Pedersen current to be also decomposed into components parallel and perpendicular to the net magnetic field. The component parallel to **B** has non-zero projections onto the x- and y-axes and the component perpendicular to **B** has a non-zero projection onto the z-axis. Grain-neutral drag stops the grain fluid from conducting perfectly, causing it to move separately from the other charged fluids in both the **E** and $\mathbf{E} \wedge \mathbf{B}$ directions. For a perfectly conducting fluid where the particles have large Hall parameters and are well tied to the field lines (fluid a), $\mathbf{E} \wedge \mathbf{B}$ has an x-component, which is proportional to the component of the charged fluid velocity perpendicular to **B**. projected onto the x-axis ($u_{a\perp x}$):

$$(\mathbf{E} \wedge \mathbf{B})_x \propto u_{a\perp x} \propto E_y B_z. \tag{2.2}$$

The grain Hall parameter however may be close to unity. This implies that $u_{g\perp x} \neq u_{i\perp x}$, $u_{e\perp x}$, i.e. frequent grain-neutral collisions partially decouple the negatively charged grains from the field lines resulting in unmatched flows of charged particles along the shock normal. This charge separation results in a Hall current in the x-direction, however charge conservation demands that J_x be zero in a steady flow. In the models of Pilipp et al. (1990) the electric field produced by this charge separation initiated the $\mathbf{E} \wedge \mathbf{B}$ driven runaway. The oblique field configuration offers a solution: In addition to the Hall current perpendicular to **B** having an x-component, the Pedersen current now has a component of current parallel to **B** also with an x-component (proportional to $\mathrm{u}_{a//x}$) arising from ambipolar diffusion (see above). The Pedersen current also has a component (parallel to **B**) with a non-zero projection onto the y-axis and a

component (perpendicular to **B**) with a non-zero projection onto the z-axis such that $J_z \neq 0$. Ampere's law yields $dB_z/dx = -4\pi J_z/c$. The Pedersen current counteracts the x-component of the Hall current by inducing the transverse component of the magnetic field (B_y) to rotate about the shock propagation direction. This mobilizes enough charges along the x-axis to balance the Hall current in that direction. The amount of rotation depends on the degree of charge separation (and hence the Hall conductivity), since it is this which determines the current which must be balanced. The amount of rotation therefore depends on the ratio of the Hall to Pedersen conductivities.

The steady, oblique treatment of Pilipp & Hartquist (1994) yields only intermediate-mode shock solutions. They present these for shock speeds up to 2.3 km s^{-1} which is roughly the Alfvén speed in a medium with a hydrogen number density and an upstream ambient field strength (at 45° to the shock normal) of either 10^3 cm^{-3} and 50 μG or 10^7 cm^{-3} and 5 mG. They find that a wide range of perturbations in the upstream magnetic field give rise to a 180° field rotation, about the shock normal (B_z becomes non-zero in the rotation region). They suggest that their inability to find fast-mode solutions with field rotation demonstrates either a requirement for time dependent simulations, or that grain-neutral drag establishes a low speed limit for the existence of stable, steady C-type shocks.

Wardle (1998) also employs a four fluid treatment (again neutrals, ions, electrons and grains) of steady, oblique C-type shocks in molecular clouds. He demonstrates that Pilipp & Hartquist (1994) were only able to find shock solutions for a limited velocity range because of the nature of the permitted stationary points. By neglecting gas pressure, ionization balance and chemistry, he is able to express all the physical quantities in the shock in terms of the components (B_y and B_z) of $\mathbf{B}_0$ (the initial upstream magnetic field). This allows the shock solutions to be represented by curves in the phase space of $B_y(x)$ and $B_z(x)$, i.e. the perpendicular and rotational magnetic field components as functions of the distance through the shock structure (along x). In this phase space, the upstream and downstream boundary states (for any shock solution) correspond to stationary points where $\frac{d}{dx}(B_y(x)) = \frac{d}{dx}(B_z(x)) = 0$. Wardle shows that when parameters for which an upstream stationary point and a corresponding downstream fast-mode stationary point exist, then the downstream stationary point is a saddle point. He does this by linearising the equations for the shock structure about each stationary point, introducing a perturbation and then analysing the subsequent evolution by solving for the roots of the dispersion relation

(which in this case are real and of opposite sign). This analysis demonstrates the upstream stationary point to be a source (real parts of the roots of the dispersion relation are all positive). Furthermore, by applying the dispersion relation to the downstream stationary point, he finds that in the case of an intermediate shock, the roots have a negative real part, meaning that the stationary point is a sink.

His analysis therefore explains why Pilipp & Hartquist (1994) are unable to find fast-mode solutions. There is only one trajectory through the phase space which starts at the upstream state and finishes at the downstream fast-mode state. All the neighbouring trajectories peel off the fast-mode solution and head towards the downstream intermediate-mode stationary point, eventually becoming unphysical if the shock speed is too high for intermediate-mode solutions to exist (i.e. $v_s/v_A > \sqrt{2}\cos\theta$, where θ is the angle between the pre-shock magnetic field and the shock normal). So, unless the fast shock trajectory runs along the B_z axis (i.e. all charged fluids are tied to the field lines), an integration for the fast-mode solution will start off at the upstream state, but stumble onto one of the unphysical trajectories heading towards the downstream intermediate-mode stationary point. This happens because the inclusion of a grain fluid which is partially decoupled from the magnetic field and preferentially carries a negative charge destroys the symmetry of the phase space. The grains stop the fast-mode solution for $B_z(x)$ from running along the x-axis and allows it to numerically mix with neighbouring divergent trajectories during integration. The net asymmetry in the phase space imposes a "handedness" on the shock structure, producing significant z-components in the field and charged fluid velocities within the shock front. Therefore, when the downstream fast-mode boundary is a saddle point, one cannot integrate from the upstream stationary point and attain it.

Wardle solves that problem by starting at the downstream stationary point and performing the integration in the upstream direction. This corresponds to an integration backwards in time. In this way he is able to find a solution for each fast-mode shock. Such an integration requires exact thermal, ionization and chemical equilibrium. Any deviation from equilibrium demands that the integration to be performed forwards in time (from upstream to downstream) to avoid violating the principles of thermodynamics. A more pressing problem however is that an irreversible process occurs in the shock, so the direction of time cannot be reversed. This mans that his fast-mode solutions are always unphysical, a finding which supports the assertion of Pilipp & Hartquist (1994) that a time dependent scheme is required to investigate the behaviour of

non-steady, fast-mode shocks in dense molecular clouds.

In addition to the above, Wardle (1998) also notes that for some regions of parameter space, the grains become the dominant charge carriers and hence dominate the current within the shock front. In this case, most of the energy is dissipated via grain-neutral collisions over a very narrow region. As well as inducing substantial field rotation in the shock front, these conditions can modify the propagation of MHD wave modes in the upstream medium by changing the upstream stationary point from a normal source to a spiral node. A spiral node occurs because the roots of the dispersion relation become complex. The shock solution spirals outwards since the real part is positive. The change in the nature of the stationary point results in strongly oscillatory behaviour of the charged fluids in the magnetic precursor since the precursor begins immediately downstream from this point. This provides a simple diagnostic as to when the grains have become the dominant source of friction with the neutrals.

The unphysical mathematical constraints which are required to obtain steady fast-mode MHD shock solutions however makes further enquiry into chemistry using this method impossible. Other equilibrium requirements impose further restrictions. When coupled with the fact that steady simulations are necessarily limited to studying shocks in homogeneous media and such models explore states that nature is unlikely to have had time to attain, the prospect of a time dependent scheme seems highly attractive.

2.3 Time dependent multifluid shock models

Ciolek & Roberge (2002) make the first attempt to develop a time dependent numerical code to model C-type shocks in dusty, weakly ionized media. However, their scheme is only suitable for modeling perpendicular shocks. They assume that fluid motions along the magnetic field lines are uncoupled from those in the other two directions and can be ignored. Whilst this is indeed the case for perpendicular shocks (where those velocities are zero in a one dimensional treatment), in oblique shocks, the charged fluid motions (currents) in this direction are required to calculate the conductivities and resistivities along the field lines (see §2.2). These in turn are used to calculate the electric field and hence the evolution of the magnetic field (see §2.4). Their scheme is therefore restricted to perpendicular shocks. In addition, each dust grain in their model can either be uncharged or else they carry a single positive or negative charge. The fact

that the large grains cannot carry the substantial negative charge that they are thought to do in C-type shocks means that they cannot move between the neutrals and the charged (non-grain) fluids. This also guarantees that the shock structures obtained when grains become the dominant source of friction with the neutrals are outside the scope of their scheme.

Whilst other attempts at time dependent numerical schemes for multifluid MHD have been undertaken (e.g. Mac Low et al. 1995; Smith & Mac Low 1997; Chieze et al. 1998; Lesaffre et al. 2004a; Lesaffre et al. 2004b; Gusdorf et al. 2008), these all lack at least one aspect present in the current research. Mac Low et al. (1995) are interested in modeling ambipolar diffusion in accretion disks and so neglect grain dynamics and assume that the ions and neutrals have the same, constant temperature. They also assume the magnetic field to be perpendicular to the shock normal, and that the grains have a large Hall parameter and so remain tied to the field lines. Smith & Mac Low (1997) use the same assumptions as Mac Low et al. (1995) but allow the magnetic field to be oblique in some simulations. Chieze et al. (1998) treat the fluid temperatures more accurately, but they too neglect grain dynamics, assume a perpendicular magnetic field, and assume that the grains have a large Hall parameter. Lesaffre et al. (2004)a and Lesaffre et al. (2004)b also neglect the grains and their prescription relies on the assumption that for suitably late times, the evolution of a shock from J-type to C-type can be modeled as a sequence of truncated steady C-type shocks with a J-type neutral sub-shock inserted at the point where the ion flow time corresponds to the age of the shock. This means that their method is only quasi time dependent, and situations where such models break down can be envisaged (see Ashmore et al. 2010 and see Chapter 4 for profiles and analysis). Gusdorf et al. (2008) use the same prescription as Lesaffre et al. (2004)a & b but include dust grains, so although their system is viable to study of the evolution of a J-type to a C-type shock, it can do so only under the assumption that the flow will continue in a steady fashion until steady state is obtained. This is unlikely to be achieved by nature (see §1.2.3). Because of the inability of the scheme used by Lesaffre et al. (2004)a & b and Gusdorf et al. (2008) to accurately model the interaction of (for example) a C-type shock with a density perturbation, theirs is not truly time dependent. Section 2.4 describes the first scheme capable of simulating oblique C-type shocks in dense, dusty molecular clouds without assumptions about the flow at later times.

2.4 The time dependent multifluid MHD code

As noted in §1.3.2, the low fractional ionization in molecular clouds means that the plasma is best treated using a multifluid description of neutrals, ions, electrons, and N dust grain species. The scheme proposed by Falle (2003) solves approximations to the fluid and field equations (1.28 - 1.37). The resulting description is appropriate when the following assumptions are valid;

- The mass of the flow is dominated by the neutrals. This means that only collisions involving the neutral fluid are important for momentum and energy transfer. This assumption is valid since dense cores are mostly molecular and and have very low fractional ionization. Although collisions do occur between ions and electrons and these are modeled to ensure that the determination of the fractional ionization is accurate, those collisions are unimportant for the transfer of momentum and energy to the neutral fluid.

- The inertia and pressure terms in the momentum (1.29) and energy (1.30) equations of all fluids except the neutrals can be ignored. This is valid because these species are rare i.e. the fractional ionization and grain mass densities are low. Whilst the grain inertia cannot be neglected in J-type shocks, their inertial phase is short compared to the time to approach a steady C-type shock (e.g. Roberge & Ciolek 2007). Although the inertial phase of the grains does not affect the final steady shock structures in this report, this effect should not be ignored for some other time-dependent models.

- The velocity dispersion (and hence pressure and temperature) of the grains is zero. This is valid as the grains have a much larger mass than any of the other species, so they all move at exactly the same velocity.

The equations for the neutral fluid are simply equations (1.28) - (1.30), with $a = n$ and b representing any of the charged species. The first two assumptions above mean that as well as neglecting charged fluid inertia, collisions between charged species are rare, so only collisions involving neutrals are important for momentum and energy transfer (the collision partner with charged species b is always n; $a = n$). This allows equations (1.28) - (1.30) for each charged fluid (b) to be written as:

$$\frac{\partial \rho_b}{\partial t} + \frac{\partial}{\partial x}(\rho_b v_b) = -s_{bn}, \tag{2.3}$$

$$\alpha_b \rho_b \left(\mathbf{E} + \frac{\mathbf{q}_b \wedge \mathbf{B}}{c} \right) + \rho_b \rho_n K_{bn} (\mathbf{v}_n - \mathbf{v}_b) = 0, \tag{2.4}$$

$$H_b + G_{bn} = 0. \tag{2.5}$$

All terms retain their meanings from §1.3.3 and K_{bn} is the collision rate coefficient of fluid b with the neutrals. The expressions for K_{bn} and G_{bn} are given in Draine (1986). The grains are treated using a hydrodynamic approximation with zero pressure since the thermal velocity dispersions of the grains are small compared to the drift speed with the neutrals. This means that they are also assumed to have a temperature of zero (Falle 2003; van Loo et al. 2009).

The neutral fluid charge-to-mass ratio is zero ($\alpha_n = 0$). Using the reduced momentum equations for the charged fluids (2.4), the remaining term on the right hand side of equation (1.29) can be written as;

$$\sum_{b=2}^{N} \mathbf{f}_{nb} = -\sum_{b=2}^{N} \mathbf{f}_{bn} = \sum_{b=2}^{N} \alpha_b \rho_b \left(\mathbf{E} + \frac{\mathbf{q}_b \wedge \mathbf{B}}{c} \right) = \frac{\mathbf{J} \wedge \mathbf{B}}{c}. \tag{2.6}$$

Similarly, the neutral charge to mass ratio being zero means that the last term on the right hand side of equation (1.30) is zero. The conserved energy transfer term can be written as:

$$\sum_{b=2}^{N} G_{nb} = -\sum_{b=2}^{N} G_{bn} = \sum_{b=2}^{N} [H_b + \alpha_b \rho_b \mathbf{q}_b . (\mathbf{E} + \mathbf{q}_b \wedge \mathbf{B})] = \mathbf{J}.\mathbf{E} + \sum_{b=2}^{N} [H_b + \alpha_b \rho_b \mathbf{q}_b . (\mathbf{q}_b \wedge \mathbf{B})]. \tag{2.7}$$

Charge neutrality demands that the sum of the Lorentz force over all the fluids be zero. This implies that $\sum_{b=2}^{N} [\alpha_b \rho_b \mathbf{q}_b . (\mathbf{q}_b \wedge \mathbf{B})] = 0$. Equation (1.30) also includes the terms H_a and $\alpha_a \rho_a \mathbf{q}_a . (\mathbf{q}_a \wedge \mathbf{B})]$. If a = n = 1, then $H_a + \sum_{b=2}^{N} H_b = \sum_{b=1}^{N} H_b$ and $\alpha_a \rho_a \mathbf{q}_a . (\mathbf{q}_a \wedge \mathbf{B})] = 0$ since $\alpha_a = 0$. So, the equations for the neutrals (1.28 - 1.30, with a = n) have been simplified and their final forms are:

$$\frac{\partial \rho_n}{\partial t} + \frac{\partial}{\partial x} (\rho_n u_n) = \sum_{k \neq n} s_{bn}, \tag{2.8}$$

$$\frac{\partial}{\partial t} (\rho_n \mathbf{q}_n) + \frac{\partial}{\partial x} (\rho_n u_n \mathbf{q}_n + p_{n,x}) = \frac{\mathbf{J} \wedge \mathbf{B}}{c}, \tag{2.9}$$

$$\frac{\partial e_n}{\partial t} + \frac{\partial}{\partial x}[u_n(e_n + p_n + \frac{1}{2}\rho_n u_n^2)] = \mathbf{J}.\mathbf{E} + \sum_{b=1}^{N} H_b. \tag{2.10}$$

Equations (2.8) - (2.10) are the gas dynamic equations for the neutral fluid. They include source terms to describe their coupling (via mass, momentum and energy transfer) to the charged fluids. These equations have the general form:

$$\frac{\partial \mathbf{Q}}{\partial t} + \frac{\partial \mathbf{F}}{\partial x} = \mathbf{S}. \tag{2.11}$$

$\mathbf{Q}$ is a vector of conserved quantities, $\mathbf{F}$ is a vector of fluxes, i.e. the rate at which conserved variables cross a unit surface and $\mathbf{S}$ is a vector of source terms. The mathematics describing the flow therefore consists of the set of partial differential equations (PDEs), together with the equations for the field (1.31 - 1.35), the expression for the current (equation 1.36) and the charge neutrality condition (equation 1.37). These are continuous equations which are defined at every point in space. Any numerical scheme to describe PDEs requires the continuous nature of the equations to be expressed in a discrete form. Discretization is a process whereby the computational domain is subdivided into a grid of cells with the equations being expressed at points across the grid. This allows one to present and evaluate PDEs in the form of algebraic equations. In this case a Gudonov scheme is employed (see Falle 1991). The scheme looks at how the values of conserved quantities vary with time across a grid of cells by integrating equation (2.11) over each (jth) cell from time t_n to t_{n+1}. The neutral equations are solved using a second order Gudonov solver (Falle 1991) which proceeds by assuming that the conserved variable solution can be treated by a piecewise constant approximation over the grid cells. This approximation is defined as the average of the solution (at time t_n) over the cell of size Δx and is obtained using the finite volume method: If $\mathbf{Q}_j^{t_n}$ represents the average values of the conserved variables over the cell centred at j (adjacent cells are j-1 and j+1), at time t_n then the the numerical solution placed at the position j at time $t_n$is simply the cells volume average of the solution obtained after the previous time-step:

$$\mathbf{Q}_j^{t_n} = \frac{1}{\Delta x}\int_{(j-\frac{1}{2})\Delta x}^{(j+\frac{1}{2})\Delta x} \mathbf{Q}(t_n, x)dx. \tag{2.12}$$

Volume integrals in a PDE which contain a divergence term are converted to surface integrals (using divergence theorem) to be evaluated as fluxes at the surface of each finite volume. This

makes it possible to derive a discrete numerical scheme with cell centres indexed as j and cell boundaries indexed as $j \pm \frac{1}{2}$. In such a scheme, only the conserved variables have time derivatives, so the jth cell values for $\mathbf{Q}$ are integrated with respect to time over the time-step (from t_n to t_{n+1}; as per equation 2.13). Because $\mathbf{F}$ is the vector of fluxes, the time averages over the time-step of the $\mathbf{F}$ terms are estimated at the cell edges. In the first order approximation this estimate is obtained by assuming that the solution is uniform within each cell and constant over the time-step. The fluxes are then evaluated between two adjacent cells at time t_n and set equal to their values at the half time-step ($t_{n+\frac{1}{2}} = t_n + \Delta t/2$), at the cell boundary. The same reasoning allows the source terms to be estimated for a cell and set equal to the first order, half time-step values. This leads to the following discretised versions of equation (2.11):

$$\int_{t_n}^{t_{n+1}} \left(\frac{\partial \mathbf{Q}}{\partial t}\right) dt + \int_{(j-\frac{1}{2})\Delta x}^{(j+\frac{1}{2})\Delta x} \left(\frac{\partial \mathbf{F}}{\partial x}\right) dx = \int_{(j-\frac{1}{2})\Delta x}^{(j+\frac{1}{2})\Delta x} (\mathbf{S}) dx, \tag{2.13}$$

$$\rightarrow \frac{1}{\Delta t_n}(\mathbf{Q}_j^{t_{n+1}} - \mathbf{Q}_j^{t_n}) + \frac{1}{\Delta x}\left(\mathbf{F}_{j+\frac{1}{2}}^{t_{n+\frac{1}{2}}} - \mathbf{F}_{j-\frac{1}{2}}^{t_{n+\frac{1}{2}}}\right) = \mathbf{S}_j^{t_{n+\frac{1}{2}}}. \tag{2.14}$$

Equation (2.14) is then used to calculate a first order approximation to the solution for the conserved variables at half the time-step ($\mathbf{Q}_j^{t_{n+1/2}}$). The equation for the conserved variables at the half time-step is of the form;

$$\mathbf{Q}^{t_{n+\frac{1}{2}}} = \mathbf{Q}^{t_n} + \mathbf{F}^{t_n}\frac{\Delta t}{2}, \tag{2.15}$$

To estimate the first order fluxes, one ignores the source terms and solves a one dimensional Reimann problem at the cell interfaces (see e.g. Falle 1991; Laney 1998). The first order, half time-step fluxes are therefore approximated by the resolved state between two cells (j and j+1) at time t_n:

$$\mathbf{F}_{j+\frac{1}{2}}^{t_{n+\frac{1}{2}}} = \mathbf{F}_*(\mathbf{Q}_j^{t_n}, \mathbf{Q}_{j+1}^{t_n}). \tag{2.16}$$

The term on the right hand side of equation (2.16) is the flux in a resolved state for the gas dynamic Riemann problem for which the left and right states are $\mathbf{Q}_j^{t_n}$ and $\mathbf{Q}_{j+1}^{t_n}$ respectively. The solution to the Reimann problem involves a superposition of waves. The fastest of these

waves decides the stable time-step. The time-step is chosen so that the fastest wave does not have time to reach adjacent cell boundaries. This is known as the Courant condition.

The first order approximation of the source terms at the half time-step are simply their values at the end of the previous time-step:

$$\mathbf{S}_j^{n+\frac{1}{2}} = \mathbf{S}(\mathbf{Q}_j^{t_n}, \mathbf{V}_j^{t_n}). \tag{2.17}$$

Since the source terms describe the coupling between the neutrals and charged fluids, there is a dependence on the vector $\mathbf{V}$ which is a function of the field and the state of the charged fluids. The source terms depend on this vector and the vector of the conserved variables ($\mathbf{Q}$), however, the first order approximation of $\mathbf{S}$ only depends on the values of $\mathbf{V}$ at time t_n (the end of the last time-step). The first order half time-step solution for the neutrals can now be calculated using equation (2.15).

To make the scheme second order in both time and space, the first order, half time-step conserved solution for the neutrals ($\mathbf{Q}_j^{t_{n+1/2}}$) is used to construct an average spatial gradient of the primitive variables (primitive variables are measurable quantities: $\mathbf{P} = \mathbf{P}(\rho_n, \mathbf{q}_n, p_n)$) over the jth cell. The second order half time-step fluxes are then calculated from the half time-step values of the primitive variables and their spatial gradients. A suitable "switch" is included to retain a first order approximation in regions where the second derivatives are large, e.g. discontinuities.

The second order source terms in cell j at the half time-step are given by:

$$\mathbf{S}_j^{t_{n+\frac{1}{2}}} = \mathbf{S}\left(\mathbf{Q}_j^{t_{n+\frac{1}{2}}}, \mathbf{V}_j^{t_{n+\frac{1}{2}}}\right). \tag{2.18}$$

It is clear from equation (2.18) that although a solution for $\mathbf{Q}_j^{t_{n+1/2}}$ has been obtained, a method of advancing the vector ($\mathbf{V}$) of the variables describing the field and the charged fluids is required before the second order full time-step solution can be obtained. The state (charged fluid and field) variables obtained after the previous step (at time t_n) are averaged over each cell, defining a new piecewise constant approximation to the solution resulting from the wave propagation during the time interval Δt, i.e. equation (2.12) with $\mathbf{V}$ replacing $\mathbf{Q}$. To be consistent, the

time interval is again limited so that the fastest waves emanating from a boundary do not have sufficient time to reach adjacent interfaces.

Collisions between charged and neutral particles affect the evolution of the field. The reduced charged fluid momentum equation (2.4) is used together with the expression for the current (1.36) to express the electric field as:

$$\mathbf{E} = -\mathbf{q}_n \wedge \mathbf{B} + r_{//}\left(\frac{(\mathbf{J}.\mathbf{B})\mathbf{B}}{B^2}\right) + r_H\left(\frac{\mathbf{J}\wedge\mathbf{B}}{B}\right) - r_{AD}\left(\frac{(\mathbf{J}\wedge\mathbf{B})\wedge\mathbf{B}}{B^2}\right). \quad (2.19)$$

A resistivity and conductivity is defined in three separate directions: along the magnetic field lines (parallel, subscript //), along the direction in which the charged fluids stream through the neutrals due to ambipolar diffusion (Pedersen or ambipolar, subscript AD), and along the direction of unmatched flows of charged particles which result in Hall currents (Hall, subscript H). In the $\mathbf{E}\wedge\mathbf{B}$ direction, the trajectories of charged particles are curved by the Lorentz force (see §2.1). Nevertheless when the Hall parameter is low, their motion between two encounters with neutral particles is almost linear. If the Hall parameter is high however, the charged particle motions are highly curved. The Hall parameter was defined in equation (1.27), but can now be written for any charged fluid (b) as $\beta_b = \alpha_b|\mathbf{B}|/\mathrm{K}_{bn}\rho_n$. This is still the ratio of the gyro-frequency to the collision rate with the neutrals. This makes it clear that when positive and negative charge carriers experience different neutral collision rates they will move separately, resulting in unmatched flows of charge and (Hall) currents. The resistivities (r) and conductivities (σ) are strongly dependent on the Hall parameters and are defined as follows:

$$r_{//} = \frac{1}{\sigma_{//}} \rightarrow \sigma_{//} = \frac{1}{B}\sum_{b=2}^{N}\alpha_b\rho_b\beta_b, \quad (2.20)$$

$$r_H = \frac{\sigma_H}{\sigma_H^2+\sigma_{AD}^2} \rightarrow \sigma_H = \frac{1}{B}\sum_{b=2}^{N}\frac{\alpha_b\rho_b}{(1+\beta_b^2)}, \quad (2.21)$$

$$r_{AD} = \frac{\sigma_{AD}}{\sigma_H^2+\sigma_{AD}^2} \rightarrow \sigma_{AD} = \frac{1}{B}\sum_{b=2}^{N}\frac{\alpha_b\rho_b\beta_b}{(1+\beta_b^2)}. \quad (2.22)$$

Equation (2.19) is then substituted into Farday's equation:

$$\frac{\partial\mathbf{B}}{\partial t} = \nabla\wedge\mathbf{E} = \nabla\wedge\left[-\mathbf{q}_n\wedge\mathbf{B} + r_0\left(\frac{(\mathbf{J}.\mathbf{B})\mathbf{B}}{B^2}\right) + r_1\left(\frac{\mathbf{J}\wedge\mathbf{B}}{B}\right) - r_2\left(\frac{(\mathbf{J}\wedge\mathbf{B})\wedge\mathbf{B}}{B^2}\right)\right]. \quad (2.23)$$

A lot of mathematical analysis, using the fact that $\frac{\partial B_y}{\partial x} = J_z$ and $\frac{\partial B_x}{\partial x} = -J_y$ to eliminate $\mathbf{J}$. yields the induction equation:

$$\frac{\partial \mathbf{B}}{\partial t} + \frac{\partial \mathbf{M}}{\partial x} = \frac{\partial}{\partial x}\mathbf{R}\frac{\partial \mathbf{B}}{\partial x}. \tag{2.24}$$

$\mathbf{M}$ is the hyperbolic magnetic flux: $\mathbf{M} = \mathbf{M}(0,\ uB_y - vB_x,\ uB_z - wB_x) = \mathbf{q}_n \wedge \mathbf{B}$. which is perpendicular to both the flow and the magnetic field. $\mathbf{R}$ is the resistance matrix: $\mathbf{R} = r_0\mathbf{R}_0 + r_1\mathbf{R}_1 + r_2\mathbf{R}_2$. where:

$$\mathbf{R}_0 = \begin{pmatrix} \frac{B_y^2}{B^2} & \frac{-B_y B_z}{B^2} \\ \frac{-B_y B_z}{B^2} & \frac{B_y^2}{B^2} \end{pmatrix}, \tag{2.25}$$

$$\mathbf{R}_1 = \begin{pmatrix} 0 & \frac{B_x}{B} \\ \frac{-B_x}{B} & 0 \end{pmatrix}. \tag{2.26}$$

$$\mathbf{R}_2 = \begin{pmatrix} 1-\frac{B_x^2}{B^2} & \frac{B_y B_z}{B^2} \\ \frac{B_y B_z}{B^2} & 1-\frac{B_y^2}{B^2} \end{pmatrix}. \tag{2.27}$$

The induction equation contains terms which can vary the solution rapidly with time. making it stiff. Numerical methods to solve it explicitly are unstable unless the time-step is very small (If $Y(t)$ is the current state of variable Y and one wishes to find the state of Y at some later time: $Y(t+\Delta t)$, then $Y(t+\Delta t) = F[Y(t)]$ is explicit). The term on the right hand side of the induction equation includes diffusive terms and their presence forces the stable time-step to tend towards zero when the Hall term becomes large compared with ambipolar diffusion i.e. the diffusive flux becomes much larger than the hyperbolic flux. The only way to avoid this limitation would be to use an implicit scheme (i.e. one where $G[Y(t), Y(t+\Delta t)] = 0$), but this would be computationally expensive.

In order to obtain the state of the charged fluids at the half time-step ($\mathbf{V}_j^{t_{n+1/2}}$), the magnetic field is first advanced to the the half time-step ($\mathbf{B}_j^{t_{n+1/2}}$) using the first order explicit scheme:

$$\frac{1}{\Delta t}\left(\mathbf{B}_j^{t_{n+\frac{1}{2}}} - \mathbf{B}_j^{t_n}\right) + \frac{1}{\Delta x}\left(\mathbf{M}_{j+\frac{1}{2}}^{t_n} - \mathbf{M}_{j-\frac{1}{2}}^{t_n}\right) = \frac{1}{\Delta x^2}\mathbf{R}_j^{t_n}\left(\mathbf{B}_{j+1}^{t_n} - 2\mathbf{B}_j^{t_n} + \mathbf{B}_{j-1}^{t_n}\right), \tag{2.28}$$

where $\mathbf{R}_j^{t_n} = \mathbf{R}(\mathbf{V}_j^{t_n})$ is the cell volume average value of $\mathbf{R}$ at the start of the time-step. Both the term on the right hand side and the hyperbolic term are calculated explicitly. A Reimann problem cannot be used to obtain the hyperbolic flux since it would be a problem where the magnetic field does not exert a force on the gas. This implies that its solution will often include discontinuities in the tangential velocities which are incompatible with equation (2.24). Instead, a centred approximation (i.e. the solution at a cell interface is the average of the solutions in the centres of the two cells on either side of the interface) must be used. The hyperbolic fluxes are then given by:

$$\mathbf{M}_{j+\frac{1}{2}}^{t_n} = \frac{1}{2}(\mathbf{M}_{j+1}^{t_n} + \mathbf{M}_j^{t_n}). \tag{2.29}$$

This method is satisfactory so long as the grid resolution is high enough for $\mathbf{B}$ to appear continuous. The charged fluid densities at the half time-step are next calculated using their mass conservation equations (2.8) and the current from a centred approximation to Ampere's Law (equations 1.34 and 1.35), obtained using the field at the half time-step. The charged fluid velocities and temperatures (which, together with the charged fluid densities comprise $\mathbf{V}_j^{t_{n+1/2}}$) are then calculated using $\mathbf{B}$ at the half time-step, the neutral solution at the half time-step, the reduced momentum and energy equations (2.4 and 2.5) and the expression for the current (1.36). If the factor K_{in} depends on velocities, then the equations must be solved iteratively using the K_{in} value at t_n as an initial guess.

$\mathbf{V}_j^{t_{n+1/2}}$ is then used to calculate the second order source terms at the half time-step ($\mathbf{S}_j^{t_{n+1/2}}$; equation 2.18). Since $\mathbf{S}_j^{t_{n+1/2}}$ is now evaluated at second order accuracy, it is possible to advance the neutral solution to the full time-step by using equation (2.14) with the second order fluxes and source terms. The densities of the charged fluids can also be moved on using $\mathbf{V}_j^{t_{n+1/2}}$ in a second order approximation to their continuity equations (2.3 - 2.5). The magnetic field is next advanced explicitly to the full time-step using:

$$\frac{1}{\Delta t}\left(\mathbf{B}_j^{t_{n+1}} - \mathbf{B}_j^{t_n}\right) + \frac{1}{\Delta x}\left(\mathbf{M}_{j+\frac{1}{2}}^{t_{n+\frac{1}{2}}} - \mathbf{M}_{j-\frac{1}{2}}^{t_{n+\frac{1}{2}}}\right) = \frac{1}{\Delta x^2}\mathbf{R}_j^{t_{n+\frac{1}{2}}}\left(\mathbf{B}_{j+1}^{t_{n+\frac{1}{2}}} - 2\mathbf{B}_j^{t_{n+\frac{1}{2}}} + \mathbf{B}_{j-1}^{t_{n+\frac{1}{2}}}\right). \tag{2.30}$$

The neutral solution, the charged fluid densities and the magnetic field are used to calculate the charged fluid velocities and temperatures at the full time-step in the same way as $\mathbf{V}_j^{t_{n+1/2}}$ was

calculated. The solutions for all of the fluids at the end of the time-step have now been obtained, with all the vectors having been advanced over Δt.

This procedure results in a scheme which is both effective and robust. It is capable of modeling the conditions in the outflows from low mass YSOs even when the resolution is high or the Hall effect is large, albeit with small time-steps. Although this scheme is the first self consistent, fully time dependent, multifluid MHD treatment suitable for oblique shocks, it is very general. In order to investigate the effects of grains in fast-mode shocks the specification of source terms is necessary (**S** in equation 2.11) to describe the relevant physics. The source terms describe either mass, momentum or energy transfer between the different fluids as well as sources and sinks of energy. Since mass and momentum are conserved, their source terms are conservative, i.e. they describe transfer between the charged fluids and the neutrals, and one fluids loss is anothers gain. Energy may also be transferred between the fluids and in this sense it is also conserved, but energy can be absorbed from outside of the system (e.g. cosmic ray ionizations) or emitted and leave the system (e.g. cooling emission). The energy sources and sinks are accounted for by the H terms in equations (2.5) and (2.10).

In general, modeling different aspects of the outflows from YSOs involves the inclusion of new source terms and the modification of existing ones. Section 2.5 describes the source terms included at the beginning of the project. The modifications undertaken for subsequent chapters are explained in those chapters, but the terms as described in §2.5 are exact for chapter 3.

2.5 Source terms

As noted in §1.3.3, the s_{ab}, f_{ab}, G_{ab} and H_a terms in equations (1.28) - (1.30) represent mass, momentum and energy transfer due to collisions between charged species and neutrals as well as energy sources and sinks. The following sections will specify and justify the expressions for the source terms. Note that it is assumed throughout that all of the neutrals are H_2, i.e. $n_n = n_{H_2} = 2n_H$.

2.5.1 Mass transfer

Mass is transferred between the ion, electron and neutral fluids as particles are converted between neutral and ionized states and collide with dust grains. The mass transfer source terms

are conservative since mass is not added to or removed from the system. Any process adding mass to a fluid must remove the equivalent mass from other fluids. Mass is removed from the ion and electron fluids when those particles recombine in the gas phase or stick to dust grains. In the case of grain attachment, the grains are much more massive than either ions or electrons, so their mass is assumed to remain constant. The ions and electrons collide with the grains at a rate per unit volume of Γ_{ba} where subscript ba denotes the current of charged species b onto grain species a, (see §2.5.4).

When a neutral particle is ionized, mass is added to the ion and electron fluids and removed from the neutral fluid. The only ionizations in the model are cosmic rays ionizing H_2. This occurs at a rate per unit volume of ζn_n, where $\zeta = 10^{-17}$ s^{-1} is the cosmic ray ionization rate suitable for dark cloud regions (see Williams et al. 1998 for a justification of this value). When two charged particles recombine, mass is removed from the ion and electron fluids and added to the neutral fluid. Initially, the source terms do not include a comprehensive chemical network. Instead, the ion abundance (calculated at each time-step) is assumed to consist equally of two species; Mg^+ which is representative of metallic ions and HCO^+ which is representative of molecular ions.

This simplified model was utilised since in such a scenario electrons are produced directly from cosmic ray ionizations of H_2. They are removed via dissociative recombinations with molecular ions and radiative recombinations with metallic ions, both in the gas phase and on grain surfaces. The rate coefficient for the radiative recombination in this model is inversely proportional to the electron temperature and is much lower than those for dissociative recombinations. The total recombination rate per unit volume determines the overall ion abundance. Therefore the inclusion of at least one metallic and one molecular ion species significantly improves the accuracy of the fractional ionization calculation. HCO^+ forms directly from the products of cosmic ray ionizations of H_2 and in quiescent cores HCO^+ is primarily destroyed in dissociative recombinations with gas phase electrons. These electrons are the other product of cosmic ray ionization. This means that a higher ionization rate affects the formation and destruction of HCO^+ and its abundance tends to be rather insensitive to changes in the physical parameters (Williams 2007). HCO^+ is therefore chosen to be initially representative of molecular ions. Metallic ions form via ion-neutral reactions with molecular ions (e.g. Oppenheimer & Dalgarno 1974) so Mg^+ is selected for being the atomic ion with intermediate mass (roughly

half way between lithium and iron).

By using the rate coefficients for radiative recombinations of Mg^+ ($< \sigma v >_{Mg^+e^-}$) and dissociative recombinations of HCO^+ ($< \sigma v >_{HCO^+e^-}$) as given by Pilipp et al. (1990), the contributions from these processes may be combined into a total mass transfer terms for each the ion (s_{in}) and electron (s_{en}) fluids. These terms are analogous to the s_{ab} terms in equation (1.28). They are:

$$s_{in} = [\zeta n_n - \Gamma_{ig} n_g - \Gamma_{is} n_s - \frac{1}{2}(n_i n_e < \sigma v >_{Mg^+e^-} + n_i n_e < \sigma v >_{HCO^+e^-})]m_i, \quad (2.31)$$

$$s_{en} = [\zeta n_n - \Gamma_{eg} n_g - \Gamma_{es} n_s - \frac{1}{2}(n_i n_e < \sigma v >_{Mg^+e^-} + n_i n_e < \sigma v >_{HCO^+e^-})]m_e. \quad (2.32)$$

The factor of one half in front of the recombination terms is because at each time-step the calculated ion abundance is split equally between the species so only half of the ions can be involved in radiative recombinations (Mg^+) with the other half being available for dissociative recombinations (HCO^+).

2.5.2 Momentum transfer

Collisions transfer momentum between the fluids. Like mass transfer, momentum transfer is conservative. In the case of the neutral fluid, the total momentum transfer term from collisions with all of the other fluids is given by the right hand side of equation (2.6). This accounts for the fact that collisions between charged and neutral particles indirectly couples the neutrals to the magnetic field. The momentum transfer rates are also required to calculate the resistivities and the velocities of the charged fluids. Since only collisions with the neutrals are assumed to be important in momentum transfer for the charged fluids (see §2.4), the momentum transfer term for collisions with neutrals appears in the momentum equation of each charged fluid (equation 2.4). If K_{bn} is the momentum transfer term between charged species b and the neutrals (equation 2.4), $< \sigma v >_{bn}$ is the momentum transfer rate coefficient and m_b and m_n are the particle masses, then the momentum transfer collision terms are (Falle 2003):

$$\mathbf{f}_{bn} = \rho_b \rho_n K_{bn}(\mathbf{q}_n - \mathbf{q}_b) = \rho_b \rho_n \left(\frac{< \sigma v >_{bn}}{m_b + m_n} \right) (\mathbf{q}_n - \mathbf{q}_b). \quad (2.33)$$

The momentum transfer rate coefficients for ion-neutral and electron-neutral collisions are taken from Draine et al. (1983). In the case of grain-neutral collisions, the cross section is velocity independent and the corresponding expressions for the rate cofficients are somewhat more complicated. The prescription from Draine (1986) is adopted and the grain-neutral momentum transfer rates have the form:

$$\mathbf{f}_{gn} = \left(\frac{\rho_n \rho_g \pi r_g^2}{m_n + m_g}\right)\left(\frac{2k_b T_n}{\pi m_n}\right)^{\frac{1}{2}}\left[\frac{8}{3}\left(1 + \left(\frac{9\pi|\mathbf{q}_n - \mathbf{q}_g|^2}{128 k_b T_n}\right)^{\frac{1}{2}}\right)\right](\mathbf{q}_n - \mathbf{q}_g). \qquad (2.34)$$

2.5.3 Energy transfer - heating and cooling

Unlike mass and momentum transfer, energy transfer is not conservative since energy may enter or leave the system via heating and cooling mechanisms. It may also be transferred from one fluid to another in a conservative fashion. The energy transfer source term for the neutrals has already been described by the right hand side of equation (2.10). It describes the coupling of the neutrals to the magnetic field through collisions with charged particles plus any energy sources or sinks. Again, only collisions with the neutrals are of interest for energy transfer to the charged fluids. Consider initially the conserved energy transfer accompanying a momentum transferring collision between charged species (b) and the neutrals (n). With the general term from Falle (2003) and the detailed terms from Draine (1986), the energy transfer collision term is:

$$G_{bn} = \left(\frac{m_b m_n}{(m_b + m_n)^2}\right) n_b n_n < \sigma v >_{bn} (m_b|\mathbf{q}_b - \mathbf{q}_n|^2 + w k_b (T_n - T_b)), \qquad (2.35)$$

where w is an integer depending on whether an electron ($w = 4$) or ion ($w = 3$) is colliding with a neutral (see §IV of Draine et al. 1983). Individually these constitute the G terms in equation (2.5) and once summed over all charged fluids (b), this accounts for the G term in equation (2.10). The sources and sinks of energy represented by the H terms in equation (2.5) and (2.10) must still be specified.

The only source of energy (heating) aside from shock dissipation comes from cosmic ray ionizations of H_2. The primary electrons from these ionizations dissipate their energy to the neutral fluid. Each primary ionization is associated with (on average) 2.78 dissociations of H_2, which provides 4.8 eV of kinetic energy to the neutral dissociation products and 2.4 eV of kinetic

energy to the electron gas, (Draine et al. 1983). Therefore the energy deposited in the electron fluid; $(H_e)_{cr}$ and neutral fluid; $(H_n)_{cr}$ per ionization event is:

$$(H_n)_{cr} = 1.69 \times 10^{-11} \zeta n_n, \tag{2.36}$$

$$(H_e)_{cr} = 8.46 \times 10^{-12} \zeta n_n. \tag{2.37}$$

Energy is lost from the system through cooling mechanisms (radiative emission which escapes the region). The model assumes that there are no radiative losses from the ion fluid. For metallic ions, temperatures in the shock are never sufficiently high to excite them. In the case of molecular ions, temperatures are high enough to excite their states, but when the ions stream relative to the neutrals or there is a temperature difference between the two fluids that is an appreciable fraction of the ion temperature (as is the case throughout a C-type shock), then elastic collision processes dominate the energy transfer. Elastic collisions do not excite states within the ions since kinetic energy is conserved during the collision. Instead, elastic collisions simply change and re-direct the kinetic speeds of the collision partners. The lack of excitation precludes cooling emission and ensures that the extra energy can only be re-distributed through collisions. The neutrals and electrons may be excited in such collisions since their low masses guarantee an inelastic component to each interaction. Radiative losses therefore only occur in the electron and neutral fluids.

The electrons lose energy by exciting the neutrals during inelastic collisions. An electron collides with a hydrogen molecule and loses some of its kinetic energy by exciting a vibrational level. The H_2 subsequently spontaneously de-excites resulting in the emission of a photon; $e^- + H_2(\nu = 0) \rightarrow e^- + H_2(\nu = 1) \rightarrow e^- + H_2(\nu = 0) + \gamma_{(\nu=1\rightarrow 0)}$. The cross section for this reaction was derived by Draine et al. (1983) using the principle of detailed balance. Assuming a two level energy system for the electrons (excited or not), in a region that is sufficiently dense for collisions to dominate over spontaneous emission, it is possible to derive the rate of energy loss per unit volume per unit time:

$$(H_e)_{H_2} = n_e n_n 3.7 \times 10^{-11} \left(\frac{T_e^{\frac{1}{2}}}{1 + [\theta/(2k_b T_e)]} \right) k_b \theta T_e \tag{2.38}$$

where θ is the threshold temperature for the reaction to proceed ($\theta = 5987$ K).

The neutrals can cool through the line emission of various molecules (H_2, CO, O and H_2O). As mentioned in §1.3.4, the H_2 molecule has no dipole moment. Consequently, collisional de-excitation of its vibrational states are important for densities above 10^6 cm^{-3}. Its energy levels are widely spaced, so for neutral temperatures below 4000 K, vibrational cooling can be accurately modeled using only the $\nu = 0$, 1, and 2 vibrational levels. Table 1 of Hartquist et al. (1980) details the cooling rates of molecular hydrogen due to rotational and vibrational transitions at various temperatures. Although it represents a gross over-simplification of the cooling process, a best fit to the cooling rate yields:

$$(H_n)_{H_2} = -7.94 \times 10^{-34} n_n T_n^{4.1} \tag{2.39}$$

[OI] at 63 μm is the only fine structure line assumed to provide significant cooling to the shock and hence influence the shock structure (see §1.1.3.2 and §1.3.4). Oxygen fine structure cooling proceeds as follows. The neutral fluid is cooled when hydrogen excites oxygen into a meta stable state. The oxygen can then either spontaneously de-excite by emitting a photon or be collisionally de-excited. A three level system is assumed (subscript 0, 1 and 2). The partition function is calculated to determine the fractional populations (denoted P) of the energy levels, such that the fraction in state j is given by:

$$P_j = \left(\frac{g_j}{Z}\right) e^{\left(\frac{E_j}{k_b T}\right)}, \tag{2.40}$$

$$Z = \sum_j g_j e^{\left(\frac{E_j}{k_b T}\right)}, \tag{2.41}$$

where g_j is the degeneracy of the jth state, E_j is the energy of the jth state and T is the neutral temperature.

A critical density (n_{cr}) is defined, above which collisional de-excitation dominates and below which spontaneous de-excitation dominates (with Einstein coefficients A_{ab}, to define the probability per unit time of a spontaneous transition from b to a). E_{ab} is the energy difference between level a and b. Below the critical density, a photons escape probability must be taken into account. Hollenbach & McKee (1979) derive the cooling rates for the two regimes, which are:

$$n > n_{cr} \rightarrow (H_n)_{OI} = n_{OI} k_b (P_0 A_{01}(E_{02} - E_{12}) + P_1 A_{12} E_{12}), \quad (2.42)$$

$$n < n_{cr} \rightarrow (H_n)_{OI} = n_{OI} k_b (P_0 A_{01}(E_{02} - E_{12}) + P_1 A_{12} E_{12})(n_n / n_{cr}). \quad (2.43)$$

Hollenbach & McKee (1989) find the [OI] 63μm line to be the dominant atomic coolant for all shock velocities (30 < v_s < 150 km s^{-1}), when post-shock neutral temperatures are between 100K and 5000K, over the full density range they investigate (10^3 - 10^6 cm^{-3}). However their work is concerned with J-type shocks. In C-type shocks, where H_2 is not dissociated, [OI] cooling becomes less important as oxygen is converted to water in the shock and post-shock regions.

The neutral fluid can also cool through the rotational and vibrational transitions of CO molecules. Because CO is abundant but thought to be almost inert in dark molecular cloud regions, in this model it is assumed to have a fixed fraction of the neutral (H_2) abundance. The CO molecule has a dipole moment. A prescription of the rotational and vibrational cooling of molecules with dipole moments was given by Hollenbach & McKee (1979). These authors were the first to treat CO cooling as a multi level cooling problem (where subscript J denotes a level). In evaluating the line cooling due to rotational and vibrational transitions one must decide whether the medium is optically thin or thick. If it is thin, all the radiation escapes and the solution is trivial. If the medium is thick however, the line cooling coefficient must take into account the photons escape probability. When the optical depth of the line (τ_{ul}) is not negligible, the photons escape probability must be taken into account. This reduces the cooling rate. This factor becomes exact in the limit that the final escape is allowed by a large velocity gradient (Draine et al. 1983) as opposed to redistribution in frequency as per Hollenbach & McKee (1979) (i.e. Doppler broadening at large τ_{ul}). In other words, it is the systematic motion of the flow not the thermal motions of individual particles that provides the velocity required to Doppler shift the emitted photons to a frequency where they are no longer absorbed by particles outside of the flow. A line cooling coefficient (L(ul; n, τ_{ul})) is defined such that $nn(a)$L(ul; n, τ_{ul}) is the cooling rate per unit volume due to the transition $u \rightarrow l$ in a molecule of species a at an optical depth τ_{ul} from the shock front:

$$nn(a)L(ul; n, \tau_{ul}) = n_u A_{ul} \epsilon_{ul} (E_u - E_l), \quad (2.44)$$

where $(E_u - E_l)$ is the energy of the radiated photon, n_u the population in state u, A_{ul} the spontaneous transition rate from u to l, and ϵ_{ul} the photons escape probability. The evaluation of line cooling coefficient depends on the level populations. At steady state:

$$n_u \sum_l (A_{ul}\epsilon_{ul} + n_{ul}\gamma_{ul}) = \sum_l n_l (A_{lu}\epsilon_{lu} + n_{lu}\gamma_{lu}), \tag{2.45}$$

where $n_{ul}\gamma_{ul}$ is the collisional de-excitation rate for $u > l$. From this a critical density can be defined for each level (n_{cr}), below which collisional de-excitation is unimportant and the optically thin prescription is valid. In this case, the net radiative de-excitation rate from level u is larger than the collisional de-excitation rate. In order to ignore collisions $n << [n_{cr}(u) < \epsilon (u)>]$ must be satisfied for all u, where:

$$n_{cr}(u) = \frac{\sum_{l<u} A_{ul}}{\sum_i \gamma_{ul}}, \tag{2.46}$$

$$< \epsilon(u) >= \frac{\sum_{l<u} A_{ul}\epsilon_{ul}}{\sum_{l<u} A_{ul}}. \tag{2.47}$$

For a complete description of the line cooling coefficients, the line centred optical depths (τ_{ul}) are also required for each transition. In addition to the opacity due to hydrogen, there is opacity due to dust. Even though the ratio of dust opacity to line opacity is generally small for the lines of interest, the scattering events associated with the line opacity will increase the photons trajectory through the region. This makes dust absorption more probable. Hollenbach & McKee (1979) derived the result that the effects of dust should be included when $\lambda_{ul} \leq \sim 300(N/10^{23}$ $cm^{-2})$. All the photons in the current model are above this wavelength so dust opacity can be safely ignored for this project. Those authors also generalised the above results for a multilevel problem in molecules possessing a dipole moment, (now the energy levels denoted as either u of l become J and the solution is summed over J). In the absence of dust opacity they found that cooling is proportional to the inverse of the optical depth, so cooling is suppressed when n $< n_{cr}$, but if $n > n_{cr}$, then the cooling rate per unit volume is:

$$(H_n)_{CO} = n_{CO}\left(\frac{(k_bT)^2 A_0}{E_0}\right)\left(\frac{2 + y_m + 0.6y_m^2}{1 + c_\tau + (n_{cr}/n) + 1.5(n_{cr}/n)^{\frac{1}{2}}}\right), \tag{2.48}$$

$$y_m = ln\left(1 + \frac{-c_\tau}{1 + 10(n_{cr}/n)}\right), \tag{2.49}$$

$$c_\tau = \tau_T\left(2\pi ln\left(2.13 + \left(\frac{\tau_T}{e}\right)^2\right)\right). \tag{2.50}$$

In the equations above y_m defines the maximum value of E_J/k_bT for which optical depth effects are important and c_τ is a length scale which tends to zero as the escape probability tends to one and has the correct asymptotic behaviour for large values of τ_T. It ensures $0 < \epsilon_J < 1$. τ_T is the effective optical depth to the shock front and is inversely proportional to the local velocity gradient. This allows for the fact that photons emitted by fast moving gas are Doppler shifted. $A_0 = A_J/J^3$ and $E_0 = E_J/J^2$, with $J = 1$.

The final neutral cooling mechanism is the emission associated with rotational transitions of water molecules.Initially there is no gas phase water, since observations suggest that in molecular clouds most water is in the solid state (e.g. Caselli et al. 2010 and see §1.1.2). Water is produced through reactions between oxygen and molecular hydrogen once the temperature exceed ~ 500 K. One of the reactions in the chain is highly exothermic, so its reverse is negligably slow. This means that once formed, water is fairly stable and can act as the principle coolant of shocked gas over a wide range of shock velocities and densities. Because water is also a molecule with a dipole moment, a similar treatment to that for CO (Hollenbach & McKee 1979) is employed by Neufeld & Melnick (1987). Since water is a more complex molecule than CO, an application of exactly the same procedure as used for CO would seriously underestimate the cooling rate at large optical depth. To allow for the polyatomic nature of a water molecule, an approximate value for E_0 is chosen and η separate lines are included for the $J \rightarrow J$ -1 transition. The critical density for water cooling is 10^{10} cm^{-3}. As long as the density is far below this, the cooling of water is a function of temperature and η, defined by Neufeld & Melnick (1987) as:

$$\eta = n_{(o-H_2O)}\frac{n_n}{10^7 cm^{-3}}\frac{10^5 kms^{-1}pc^{-1}}{v_{grad}}, \tag{2.51}$$

where $n_{(o-H_2O)}$ is the number density of ortho-water, $v_{grad} = dv/dx$ is the local velocity gradient. In the case of a large velocity gradient, the cooling rate per unit volume is then:

$$(H_n)_{H_2O} = \frac{n_{(o-H_2O)} n_n 2.6 \times 10^{-23} (\frac{T}{1000K})^{1.95}}{1 + (\eta/(9 \times 10^4 (\frac{T}{1000K})^{2.4}))^{\frac{1}{2}}}. \quad (2.52)$$

2.5.4 Grain charging

In §2.5.1, it was stated that the charged fluids lose mass via their currents onto dust grains. These currents depend on the product of the charge of the impacting particle to the charge already on the grain (i.e. whether or not the impacting particle must overcome an electrostatic repulsion) and the ion-grain or electron-grain relative velocity. With reference to the current project, there are four regimes, defined by Havnes et al. (1987) using the result of Spitzer (1978). These are:

- (a) Grain and charged particle have the same charge sign (electrostatic repulsion). (b) Velocity distribution of the charged species is not velocity shifted in the frame of the grains (low streaming velocity).
- (a) Grain and charged particle have the same charge sign (electrostatic repulsion). (b) Velocity distribution of the charged species is velocity shifted in the frame of the grains (high streaming velocity).
- (a) Grain and charged particle have the opposite charge sign (electrostatic attraction). (b) Velocity distribution of the charged species is not velocity shifted in the frame of the grains (low streaming velocity).
- (a) Grain and charged particle have the opposite charge sign (electrostatic attraction). (b) Velocity distribution of the charged species is velocity shifted in the frame of the grains (high streaming velocity).

The main difference being that in the low streaming velocity cases (first and third), the charged fluid velocity has a normal Maxwellian distribution, but in the case of a high streaming velocity (second and fourth), a velocity shifted Maxwellian distribution is used, which yields a more complicated expression. Spitzer (1978) gives the general expression for the currents of charged particles onto grains:

$$\Gamma_b = 2\pi Z_b e S_b \int \int \sigma_b f_{pb}(\omega, \varphi) \omega^3 sin\varphi d\omega d\varphi, \quad (2.53)$$

where b represents either the ion or electron fluid, $Z_b e$ is the charge on a single particle in fluid b, ω is the particle speed, φ is the angle that the impacting particle trajectory makes with the grain surface and σ_b is the cross section for collision with a dust grain of radius r_g and charge $Z_g e$. Draine & Sutin (1987) note that charged particles polarize the grains. The polarization potential increases the cross section relative to its geometric value. The cross section is given by:

$$\sigma_b(\omega) = \pi r_g^2 \left(1 - \frac{2 Z_b Z_g e^2}{m_b \omega^2 r_g}\right), \tag{2.54}$$

where m_b is the mass of a particle in fluid b. In equation (2.53), the term $f_{pb}(\omega, \varphi)$ is the particle velocity distribution function. In the case that the grains drift relative to the charged species (with a drift velocity $\mathbf{q}_{bg}$) one must use a velocity shifted Maxwellian distribution for the charged species. Assuming that the velocity dispersion of the grains is zero, the particle velocity distribution function for species b is;

$$f_{pb}(\omega, \varphi, \mathbf{q}_{bg}) = n_b \left(\frac{m_b}{2\pi k_b T_b}\right)^{\frac{3}{2}} e^{-\frac{m_b}{2k_b T_b}(\mathbf{q}_{bg}^2 + \omega^2 - 2\mathbf{q}_{bg}\omega\cos\varphi)}. \tag{2.55}$$

This leads to the four regimes above: Whether the projectile must overcome an electrostatic potential or not and whether or not $\mathbf{q}_{bg}$ is close to zero. From this, Havnes et al. (1987) were able to derive expressions for the grain currents in each of the four regimes, which have been adopted here.

2.6 Overview of subsequent chapters

The purpose of this research is to investigate the shock structures of multifluid MHD shocks in dense, weakly ionized, dusty media. Since §2.4 describes the first completely self consistent, time dependent MHD scheme, chapter 3 describes simulations undertaken to reproduce the earlier work of Draine et al. (1983) and others. As well as investigating the shock structures obtained for similar initial conditions as used by those authors, their remit is expanded by considering various oblique shocks. Chapter 3 investigates the steady structures of fast-mode (v_s = 25 km s^{-1}) shocks moving through two different upstream densities ($n_H = 10^4$ or 10^6 cm^{-3}) with suitably scaled magnetic field strengths ($B_0 = n_H^{-1/2}$) that make an angle to the shock normal of $B_\theta = 30°$, 45°, 60° or 90°. Simulations were undertaken for both a single grain species

($r_g = 4 \times 10^{-5}$ cm) and for two grain species ($r_g = 4 \times 10^{-5}$ cm, $r_s = 4 \times 10^{-6}$ cm). The simulations are complete once steady state is obtained. One dimensional plots of temperatures, velocities, densities, grain charges and magnetic fields are compared to the findings of Draine et al. (1983).

There has been much discussion in the literature about the applicability of steady shock models, since the timescale to reach steady state is of the same order as the lifetime of the outflows driving source. All steady models are also forced to assume that the medium through which the shock propagates is homogenous. Observations of SFRs reveal that homogeneity is not the normal case, but to date no simulations of C-type shocks interacting with perturbations in the background medium have been possible. Chapter 4 presents the results of the first simulations of steady C-type shock waves (obtained as the final profiles in chapter 3) interacting with density perturbations in the upstream medium. The perturbations take three forms. Firstly a "step up" , where the shock moves up a density gradient from a semi-finite region of low density to a semi finite region of high density. Secondly a "step down" , where the shock moves down a density gradient from a semi-finite region of high density to a semi finite region of low density. Finally, a "clump" , where the steady shock encounters a density perturbation which rises and then falls back to the original value. In all cases the perturbation causes a drastic change in the shock structure which then relaxes to a new C-type shock structure. The temporal evolution of the changes are described. The main results are summarised and their relevance to other attempts at the time dependent modeling of such regions is discussed.

As discussed in §1.3.4, the abundances of various chemical species can affect the post-shock cooling and the fractional ionization in the shock front and hence the shock structure. Chapter 5 develops a more comprehensive chemical network (adapted from Pilipp et al. 1990) and describes the simulations undertaken to reveal the shock profiles of the various chemical species. The choice of certain ionic and neutral species over others is first motivated, then the source terms are developed for each species. These describe the net formation or destruction rate for that species and are obtained by employing the relevant coefficients for each important reaction. The fact that the dust grains are a charged species which do not necessarily move with either the neutrals or the ions and electrons means that they can collide with both. In some regions of the parameter space which is explored, the grain-neutral relative velocity is high enough for collisions to liberate atoms of the grain material in a process known as sputtering (see

§1.3.5). In chapter 5 a system of equations is also developed to describe both the sputtering of the grains icy mantles and the material making up the silicate cores. These are then incorporated into the source terms. Since the return of SiO and water to the gas phase is of considerable interest, a series of simulations is run to discover how the upstream density, shock speed and angle between the magnetic field and the shock normal affects the fractional abundances of SiO and H_2O obtained in the post-shock region.

Chapter 6 consists of a brief summary and discussion of the main results from this project as well as possible directions for relevant future research.

Chapter 3

Steady state C-type shock structures

3.1 Summary

The results presented in this chapter were obtained by applying the time dependent multifluid MHD code developed by Falle (2003) (see §2.4) to calculate the steady structures of perpendicular and oblique C-type shocks in dense, weakly ionized plasmas. Dust grains were included, either assuming them to be of a uniform radius, or allowing two fluids of different sized grains. Source terms were also present (as per §2.5) to describe mass transfer between the fluids, the momentum and energy transfer accompanying collisions, energy losses due to radiative cooling and the currents of charged particles onto grains. These models concern perpendicular and oblique fast-mode shocks in molecular clouds and include the most rigorous treatment to date of the grain dynamics together with a self consistent calculation of the thermal and ionization structure, including the appropriate micro physics. At low densities, dust grains do not play a significant role in shock dynamics. At higher densities however the fractional ionization becomes sufficiently low for dust grains to be important carriers of charge and hence mediators of current. In some cases it is the grains that determine the shock structure and instigate a significant rotation of the magnetic field out of its upstream plane. This rotation is most pronounced for simulations which include a single species of large grains and when the upstream magnetic field makes a small angle with the shock normal. These models are able to reproduce previous studies of steady C-type shocks, confirming that Falle's scheme is efficient, rigorous and robust. Unlike the methods employed in other recent detailed treatments of dust in steady, oblique fast-mode shocks, this scheme allows for reliable calculations even when chemical or other conditions deviate from local thermodynamic equilibrium. It can therefore be used to model transient phenomena.

3.2 Introduction

As discussed in Chapter 1, the outflows associated with low mass YSOs drive shocks through the dense cores of molecular clouds where the fractional ionization is low ($\chi_i < 10^{-6}$; Caselli et al. 1998). Low fractional ionization allows the neutral gas and magnetic field to be only weakly coupled. Charged particles are then pushed through the neutrals upstream of the shock by Lorentz forces (themselves a result of the compression of the magnetic field), in a process known as ambipolar diffusion (Mestel & Spitzer 1956). Rare collisions between charged and neutral particles may begin to accelerate, compress and heat the neutral gas ahead of the passage of the shock. This forms a magnetic precursor (Draine 1980). If the shock speed is low enough for the gas to have time to cool effectively within the shock, or the magnetic field is strong enough to create a magnetic precursor of sufficient width, the flow becomes continuous in all fluids (Mullan 1971). Such shocks are denoted C-type (Draine 1980). Chapter 2 described the rich history of modeling C-type shocks, with special emphasis on the work which is directly relevant to the current project: Draine (1980), Draine et al. (1983), Pilipp et al. (1990), Pilipp & Hartquist (1994) and Wardle (1998).

This chapter probes the steady structures of fast-mode C-type shocks using time dependent, multifluid MHD simulations. In section 3.3 the numerical scheme, physical processes and computational considerations are discussed. The code is then applied to perpendicular and oblique shocks with parameters similar to those used by Draine et al. (1983) and others. The results and analysis for simulations including a single species of grains comprise section 3.4, whilst those involving multiple grain species form section 3.5. The conclusions are laid out in section 3.6.

3.3 The model

The numerical scheme is exactly as described in §2.4 and the source terms are exactly as per §2.5. As noted in §2.5.3, ions are accelerated by the magnetic field gradient ahead of the shock and stream through the neutrals. When there is an ion-neutral relative velocity, collisions between the species are predominantly elastic. Elastic collisions do not excite internal states in the ions, but rather change their kinetic speeds. The absence of excitation precludes cooling emission and the extra kinetic energy can only be re-distributed through collisions. The lack of radiative losses from the ion fluid and the fact that the ion temperature depends on the collisional

coupling between the ions and the neutrals allows T_i to be calculated from:

$$T_i = T_n + \frac{m_n}{3k_b}(\mathbf{q}_n - \mathbf{q}_i)^2. \tag{3.1}$$

3.3.1 Initial Conditions

The initial conditions employed in this chapter were adopted from Draine et al. (1983) and other similar studies (e.g. Wardle 1998). This allows a comparison of the present results with those studies. The neutral fluid has an upstream atomic hydrogen number density of either $n_H = 10^4$ cm^{-3} or $n_H = 10^6$ cm^{-3}. All hydrogen is assumed to be molecular so that $m_n = 2m_H$ and $n_n = 1/2(n_H)$. Small amounts of other neutral species are also present. The initial abundances of O, CO, and H_2O are taken as 4.25×10^{-4} n_H, 5×10^{-5} n_H and 0 respectively. Since the abundances of O and H_2O evolve substantially as the gas is heated (see §2.5), the abundances of these coolants are recalculated at every time-step. CO is assumed to be inert so its abundance remains a fixed fraction of H_2. The ions are Mg^+ and HCO^+, which each comprise half of the total ion abundance (calculated for each simulation as per §2.5.1). The ion mass is taken to be $m_i = 30m_H$ and all ions are assumed to be singly ionized, i.e. $n_i = n_e$.

In the ISM, the magnitude of the magnetic field scales roughly as $B \sim 1\mu G(n_H/\text{cm}^{-3})^{1/2}$, so that $B = 10^{-4}$ G for $n_H = 10^4$ cm^{-3} and 10^{-3} G for $n_H = 10^6$ cm^{-3}. The Alfvén speed of the gas (calculated as per equation 1.17) is then the same for both densities; $v_A = 2.2$ km s^{-1}. In the upstream region, the magnetic field lies in the x-y plane and makes an angle of 30°, 45°, 60° or 90° (perpendicular shock) with the shock normal. All shocks propagate in the positive x-direction with a speed of 25 km s^{-1} and are therefore strong fast-mode shocks with an Alfvénic Mach numbers of ~ 11.5 (see §1.3.2).

The initial upstream abundances of ions and electrons are calculated via ionization equilibrium. The ion mass transfer term (2.31) is set equal to zero and the equation for ion currents onto grains is solved assuming that there is no ion-grain relative velocity and that the grains are negatively charged (as is assumed to be the case outside of the shock and precursor, see equation 2.53 and §1.1.2). This value is substituted into equation (2.31) for Γ_{ig} (and Γ_{is} in the case of two grain fluids, see §3.5). The rate coefficients for radiative and dissociative recombinations given in Pilipp et al. (1990) are adopted. The resulting equation is a quadratic in terms of n_i

with a trivial solution.

The initial mass densities of the large (subscript g) and small (subscript s) dust grain fluids in the upstream region are calculated by assuming the grains to be spherical, with radii of $r_g = 0.4$ μm and $r_s = 0.04$ μm and masses of $m_g = 8.04 \times 10^{-13}$ g and $m_s = 8.04 \times 10^{-16}$ g respectively. The initial upstream grain charge is close to -1e as the discussion in §1.1.2 suggests for quiescent molecular regions. The initial charge per grain is calculated from:

$$Z_{g,s} = \left[-2.5 - 1.8 \log\left(\frac{m_i}{m_H}\right)^{\frac{1}{2}} \right] \left(\frac{r_{g,s} k_b T}{e^2}\right), \tag{3.2}$$

where m_i is the mass of an ion, m_H is the mass of a hydrogen atom, $r_{g,s}$ is the grain radius, k_b is Boltzmanns constant, T is the temperature and e is the elementary charge. Assuming that all ions have a mass of $30 m_H$, this expression yields initial large grain charges of 1.33e and small grain charges of around one tenth of this value.

The mass density of the silicate material making up the grains ($\rho_{silicate}$) is taken to be 3 g cm^{-3}. The grain to hydrogen mass ratio in the upstream gas assumes the canonical value of 0.01, so the grains constitute 1% of the total flow mass (e.g. Draine 2009). For simulations with a single grain population (§3.4), $\rho_g = 0.01 \rho_n$. For the simulation with two grain fluids (§3.5), the grains follow the MRN size distribution (equation 1.1). To simulate that distribution using two discrete populations of grains, their abundances must be partitioned such that:

$$\rho_g + \rho_s = 0.01 \rho_n, \tag{3.3}$$

$$n_s = 10^{2.5} n_g. \tag{3.4}$$

Using the fact that $n_s = \rho_s / m_s$ and $m_s = 4/3(\pi r_s^3)\rho_{silicate}$, it is possible to re-arrange for ρ_g in terms of the grain radii and the mass density of the neutrals. It is then simple to obtain the mass densities of both grain fluids. The initial temperatures are the same for all fluids except the grains. To facilitate comparison with the results of Draine et al. (1983) an initial upstream temperature; $T_u = 8.4$ K is adopted for $n_H = 10^4$ cm^{-3} and $T_u = 26.7$ K for $n_H = 10^6$ cm^{-3} (subscripts u and d refer to upstream and downstream). Since the grains are treated using a hydrodynamic approximation with zero pressure (see §2.4), they have temperatures of zero throughout the shock.

Having specified the properties of the upstream flow, the Rankine-Hugionot jump conditions for an isothermal, magnetised shock are employed in order to calculate the initial flow parameters for the downstream gas. The Rankine-Hugionot jump conditions refer to quantities (those within square brackets in equations 3.5 - 3.9) which are conserved across any type of shock. In c.g.s. units these are:

$$[\rho q_x] = 0 \rightarrow \rho_u q_{ux} = \rho_d q_{dx}, \tag{3.5}$$

$$\left[\rho q_x^2 + P + \frac{\mathbf{B}^2}{2}\right] = 0 \rightarrow \rho_u q_{ux}^2 + P_u + \frac{\mathbf{B}_u^2}{2} = \rho_d q_{dx}^2 + P_d + \frac{\mathbf{B}_d^2}{2}, \tag{3.6}$$

$$[B_x] = 0 \rightarrow B_{ux} = B_{dx} = B_x, \tag{3.7}$$

$$\left[\rho q_x q_y - B_x B_y\right] = 0 \rightarrow \rho_u q_{ux} q_{uy} - B_x B_{uy} = \rho_d q_{dx} q_{dy} - B_x B_{dy}, \tag{3.8}$$

$$[q_x B_y - q_y B_x] = 0 \rightarrow q_{ux} B_{uy} - q_{uy} B_x = q_{dx} B_{dy} - q_{dy} B_x, \tag{3.9}$$

subscript x refers to the direction of the flow (along the shock normal) and y refers to the direction perpendicular to the shock normal which contains the transverse component of the upstream magnetic field. The compression ratio (r) across the shock is defined as the ratio of the up and downstream densities:

$$r = \frac{\rho_d}{\rho_u}. \tag{3.10}$$

This result is then used with equation (3.5) to define the downstream x-velocity (post-shock flow speed):

$$q_{dx} = \frac{q_{ux}}{r}. \tag{3.11}$$

The equation $P = \rho a^2$ (where a is the sound speed) is substituted into (3.6) to remove the downstream pressure from the list of unknowns. The relation $\mathbf{B}^2 = \mathbf{B}_x^2 + \mathbf{B}_y^2$, where $[\mathbf{B}_x] = 0$ (the component of the magnetic field along the flow remains unchanged across a shock), together with equations (3.10) and (3.11) may then be substituted into equations (3.6) - (3.9). In perpendicular shocks, several of these parameters are zero and consequently the solutions are trivial. In oblique shocks, there are four remaining equations and four unknowns (ρ_d, q_{dx}, q_{dy}, B_{dy}).

Further substitutions and rearrangements allow the compression ratio to be expressed in terms of upstream flow parameters only. By noting the sonic Mach number; $\mathrm{M}_S = \mathrm{q}_{ux}/\mathrm{a}$ and the Alfvénic Mach number; $\mathrm{M}_A^2 = \rho_u \mathrm{q}_{ux}^2/\mathrm{B}_x^2$, the expression for the compression ratio becomes:

$$r^3\Big(\frac{-1}{M_A^4}\frac{1}{M_S^2}\Big) + r^2\Big[\frac{1}{M_A^4} - 2\Big(\frac{1}{M_A^2}\frac{1}{M_S^2}\Big) + \Big(\frac{B_{uy}^2}{\rho_u q_{ux}^2}\frac{1}{M_A^2}\Big) - \Big(\frac{B_{uy}^2}{2\rho_u q_{ux}^2}\Big)\Big] + r\Big[-2\Big(\frac{1}{M_A^2}\Big) - \Big(\frac{1}{M_S^2}\Big) + \Big(\frac{B_{uy}^2}{2\rho_u q_{ux}^2}\Big)\Big] + 1 = 0. \tag{3.12}$$

This is a cubic equation in r which can readily be solved to yield the compression ratio. Once obtained, r can be used to calculate ρ_d and q_{dx} via (3.10) and (3.11). The other two unknown quantities then follow from eqations (3.8) and (3.9). The initial condition is therefore a J-type discontinuity with $x = 0$ separating the upstream and downstream regions. The evolution from an initially unsteady J-type to a steady C-type shock is followed in the shock frame.

3.3.2 Computational Details

The size of the computational domain is assumed to be a few times the final shock width to ensure that the whole shock structure is on the grid, but the shock itself contains enough cells to be well resolved. By balancing the ion-neutral drag force with the Lorentz force, it is possible to estimate the final shock thickness (L_i, e.g. Draine & McKee 1993):

$$L_i = 7 \times 10^{15} \Big(\frac{v_A}{kms^{-1}}\Big)\Big(\frac{10^{-2}cm^{-3}}{n_i}\Big)\,\mathrm{cm}, \tag{3.13}$$

where v_A is the Alfvén speed and n_i is the ion number density. However, grain-neutral friction becomes comparable to ion-neutral friction when either of the following inequalties are satisfied:

$$\frac{\rho_i}{\rho_g} < \frac{K_{gn}}{K_{in}}, \tag{3.14}$$

$$\chi < 3 \times 10^{-9}\Big(\frac{v_s}{kms^{-1}}\Big), \tag{3.15}$$

where χ is the fractional ionization, v_s is the shock speed. K_{in} is the ion-neutral momentum transfer term, K_{gn} is the grain-neutral momentum transfer term (momentum transfer rate coefficients divided by the sum of the particle masses, see §2.5.2) and $\rho_{i,n}$ are the mass densities of the

ion and neutral fluids respectively. Relations (3.14) and (3.15) are derived from the expressions for the collision rates of grains with neutrals (Draine 1986), assuming the grain-neutral relative speed to be of the order of $v_s/2$. These constraints are satisfied in the magnetic precursor at both densities, so grain-neutral drag dominates the momentum transfer to the neutral fluid and determines the shock width. In this case, expression (3.13) becomes ;

$$L_g = 3 \times 10^8 \chi \left(\frac{v_s}{kms^{-1}} \right)^{-1} L_i, \tag{3.16}$$

where values of χ appropriate for the magnetic precursor must be used. Flower et al. (1985) first noted that chemistry can lead to a large drop in χ in the precursor in many shocks. This results in narrower shock widths than would otherwise be obtained. The numerical domain is chosen to be $-10L_g \leq x \leq 10L_g$ with a free flow boundary at the downstream edge and a fixed boundary at the upstream edge. This domain is split into 400 cells to ensure the shock region is well resolved.

Because the initial conditions are J-type discontinuities, the inertia of the charged fluids (especially the grains, but even the ions) cannot be neglected during the initial phase of evolution. However, the inertial phase of the charged fluids is short compared to the time for the shock to reach steady state (e.g. Roberge & Ciolek 2007).

3.4 Results: single grain species

3.4.1 Perpendicular shock models

Figure 3.1 shows the perpendicular shock structure in various variables for upstream hydrogen number densities of 10^4 and 10^6 cm^{-3}. It is obvious that both shocks are C-type. Since the current models are similar to Draine et al. (1983), the results presented here can be compared with figures 2 and 3 of their paper. The shapes of the shocks are qualitatively similar, but in the current models the widths are around four times larger despite the shock structure being determined by grain-neutral friction. This is because the fractional ionization in the current models is calculated as a consequence of the chemistry rather than by assuming a constant flux of ions as Draine et al. (1983) did. The lower fractional ionizations obtained via the more accurate treatment causes the total drag force on the neutrals to be lower. This drag is balanced

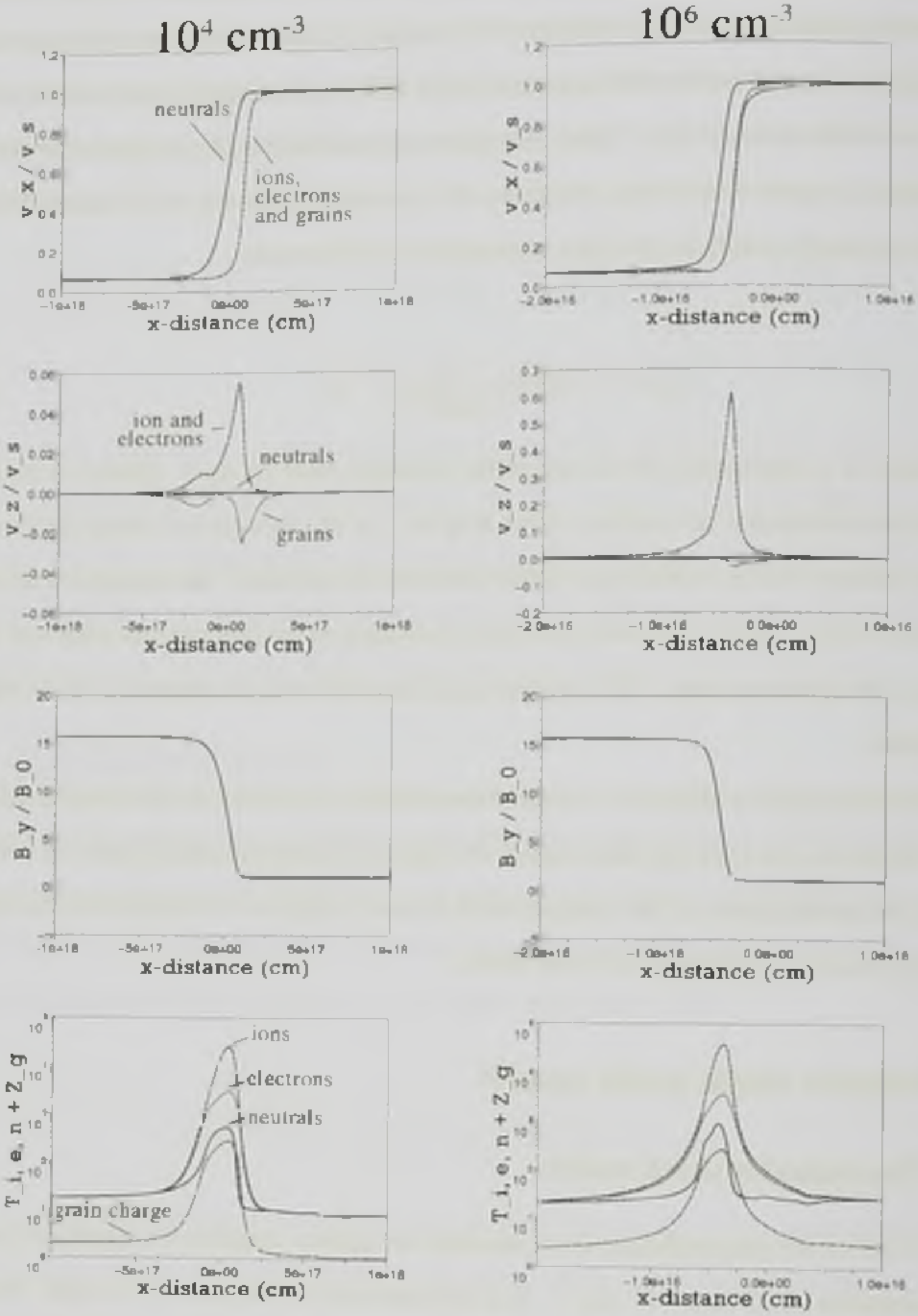

Figure 3.1: The shock structure for a perpendicular shock propagating through a quiescent region with $n_{\rm H} = 10^4 {\rm cm}^{-3}$ (left column) and $n_{\rm H} = 10^6 {\rm cm}^{-3}$ (right column). The top two rows are velocities in the x- and z-directions for the neutrals (solid), ions/electrons (dashed) and grains (dotted). The third row shows the tangential magnetic field and the bottom row displays the temperatures (in Kelvin) of the ions (dashed), electrons (dotted) and the neutrals (solid) as well as the absolute value of the grain charge (dash-dotted). The velocities are normalised with respect to the shock speed and the magnetic field with respect to the total upstream magnetic field.

by the magnetic pressure over a wider region. A wider shock has more time to radiate energy, so the maximum neutral temperatures reached in the shock front are only 530 K for $n_H = 10^4$ cm^{-3} and 905 K for $n_H = 10^6$ cm^{-3}, whereas Draine et al. (1983) obtained 1223 K and 1334 K respectively.

The velocity difference between the ions and electrons and the neutrals gives rise to collisional heating and allows the temperature of the ions to be determined by equation (3.1). The maximum ion-neutral streaming velocity in the current models is approximately the shock speed, which yields a maximum ion temperature of a few times 10^4 K. The total streaming velocity includes x- and z-components. In the x-direction the streaming velocity is roughly the same at both densities. In the z-direction however the ions and electrons stream through the neutrals at much greater velocities in the high density model due to stronger field components. Since the ions do not radiatively cool, they also achieve higher temperatures in the 10^6 cm^{-3} model ($\sim 4 \times 10^4$ K as opposed to $\sim 2.5 \times 10^4$ K). Electron cooling becomes important for temperatures above $\sim$ 1000 K (see §2.5.3). The peak electron temperature is therefore limited to $\sim 3 \times 10^3$ K in both density regimes (see bottom row of figure 3.1). The electron temperature in the shock front determines the grain charge and β_g (the Hall parameter, see §1.3.2). The electron temperature in turn dictates the grain charge:

$$Z_g e \sim -\frac{4k_b T_e r_g}{e}, \tag{3.17}$$

for $|Z_g| >> 1$ and $n_g |Z_g| << n_e$ (e.g. Draine 1980). The bottom row of figure 3.1 shows that the grain charge profile follows that of the electron temperature, as one would expect from (3.17). The grains reach a maximum charge of around -250 e in both models.

It was noted in §2.1 that the magnetic force on a charged particle depends on the magnetic field strength and the component of the particle velocity transverse to the field lines. The magnetic force is perpendicular to both the field lines and the transverse velocity. In the frame of the upstream gas, there is no net velocity or magnetic force in any direction. Individual charged particles follow either circular or spiral orbits about the field lines depending on whether or not they have a velocity component parallel to those lines. This is because the acceleration produced by the perpendicular velocity component is directed towards the field line whilst the parallel component remains unchanged. Upon entry to the precursor, compression of the mag-

netic field accelerates the charged fluids down its gradient (in the direction of the flow, ahead of the shock). Since $\mathbf{E} \propto \mathbf{q}_{i,e} \wedge \mathbf{B}$. with $\mathbf{q}_{i,e}$ being along the x-direction and $\mathbf{B}$ lying along the y-direction, this acceleration produces an electric field in the z-direction (E_z). Charged particles move along electric field lines so E_z accelerates them in the z-direction. This results in another electric field component, this time in the x-direction. When a charged particle moves through magnetic and electric fields, it experiences the Lorentz force, which is perpendicular to both. The motion induced by the Lorentz force is hence known as $\mathbf{E} \wedge \mathbf{B}$ drift (see figure 2.1). The drift speed is independent of a particles mass and charge so, in the absence of collisions, all charged particles drift in the same direction at the same speed. Like the electric field, $\mathbf{E} \wedge \mathbf{B}$ has x- and z-components within the shock, therefore both $\mathbf{E}$ and the $\mathbf{E} \wedge \mathbf{B}$ drift contribute to the streaming velocities of the charged particles. The z-velocities of the charged fluids may become a large fraction of the shock speed. The acceleration of charged species by electromagnetic forces results in systematic collisions with the neutrals. Such collisions tend to decelerate the charged species and can excite as well as accelerate the neutrals. After colliding with neutrals, charged particles are re-accelerated via the gradient in field strength and the induced $\mathbf{E} \wedge \mathbf{B}$ drift.

From the shock frame, upstream gas approaches the shock at $-\mathrm{v}_s$. This causes E_z to be non-zero in the upstream region (see top plot of figure 3.2). Figure 3.1 shows that even in the low density case (left column) when all the charged fluids move together along the flow direction (x), the z-component of the grain-neutral relative speed is less than that of the ion-neutral relative speed. This is due to the different response of the fluids to the Pedersen current along $\mathbf{E}^{'}$ ($\mathbf{E}^{'} = \mathbf{E} + \mathbf{q}_n \wedge \mathbf{B}$) and the Hall current along $\mathbf{E}^{'} \wedge \mathbf{B}$. Pedersen currents occur when charged particles stream through the neutrals due to the presence of a magnetic field (ambipolar diffusion). Hall currents occur when the same particles, moving under the influence of the magnetic field produce an electric field component and then drift perpendicular to both.

As noted in §2.1, there is no force along the magnetic field (in the y-direction) because a magnetic field cannot produce a force parallel to itself and an electric field cannot produce a force perpendicular to itself. This guarantees that there is then no systematic motion of any fluid in the y-direction in a perpendicular shock. Inside such a shock (where $\mathrm{B}_x = \mathrm{B}_z = 0$ and $\mathrm{q}_y = 0$), $\mathbf{E}^{'}$ and $\mathbf{E}^{'} \wedge \mathbf{B}$ have only x- and z-components. The relative contribution of $\mathbf{E}^{'}$ and $\mathbf{E}^{'} \wedge \mathbf{B}$ in either direction depends on the electric field strength and neutral velocity along, as well as the magnetic field strength perpendicular to, that direction. These jointly determine the charged

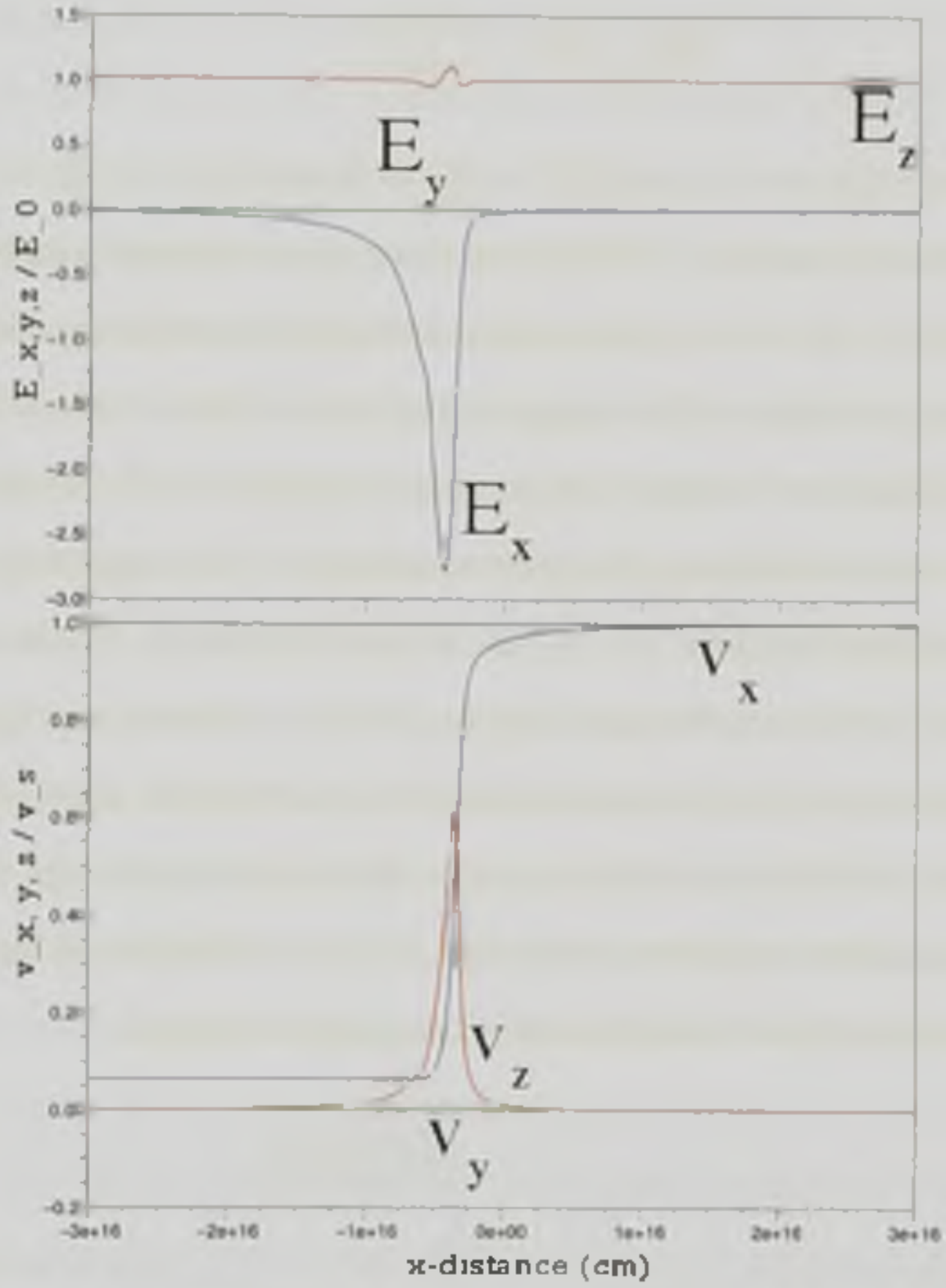

Figure 3.2: Plots of the electric field components with respect to the total upstream electric field (top) and ion/electron velocity components with respect to the shock speed (bottom). Both plots are for a 25 km s^{-1} perpendicular shock propagating through an upstream density of $n_H = 10^6$ cm^{-3}. Blue lines correspond to x-components, green lines to y-components and red lines to z-components.

fluid velocity. Subtracting the neutral velocity then gives the drift speed. Equation (2.9) may be rearranged to yield the streaming velocity between any charged fluid (b) and the neutrals (n):

$$\frac{\mathbf{q}_b - \mathbf{q}_n}{c} \sim \frac{\beta_b^2}{1+\beta_b^2}\left(\frac{\mathbf{E}' \wedge \mathbf{B}}{B^2}\right) + \frac{\beta_b}{1+\beta_b^2}\left(\frac{\mathbf{E}'}{B}\right). \tag{3.18}$$

For the electrons and ions $|\beta_{e,i}| >> 1$, so $\beta_b^2/(1+\beta_b^2) \approx 1$ and $\beta_b/(1+\beta_b^2) \approx 0$. The particles are therefore tied to the field lines and:

$$\frac{\mathbf{q}_{i,e} - \mathbf{q}_n}{c} \sim \frac{\mathbf{E}' \wedge \mathbf{B}}{B^2}. \tag{3.19}$$

In the other extreme, $|\beta_b| << 1$, so $\beta_b^2/(1 + \beta_b^2) \approx 0$ and $\beta_b/(1 + \beta_b^2) \approx 0$. The particles remain coupled to the neutral flow. Effectively then, the maximum possible contribution of each term in equation (3.18) to the grain-neutral drift speed is determined by the components of the neutral velocity and those of the magnetic and electric fields. However the weighting of each contribution depends on the grain Hall parameter (equation 1.27) which may result in the numerically smaller term dominating the grain-neutral drift. The weighting of each term as a function of β_b is included in figure 3.3. It can be seen that for $\beta_b > 0$ the terms outside the brackets in equation (3.18) carry the same sign but for $\beta_b < 0$ they carry opposite signs. That $\beta_b/(1 + \beta_b^2)$ changes sign with β_b takes account of the fact that the acceleration of a charged particle along electric field lines is in the direction determined by the sign of its charge. That $\beta_b^2/(1 + \beta_b^2)$ remains positive regardless of the sign of β_b is a reflection of the fact that the $\mathbf{E}' \wedge \mathbf{B}$ drift is in the same direction for both positive and negative charges.

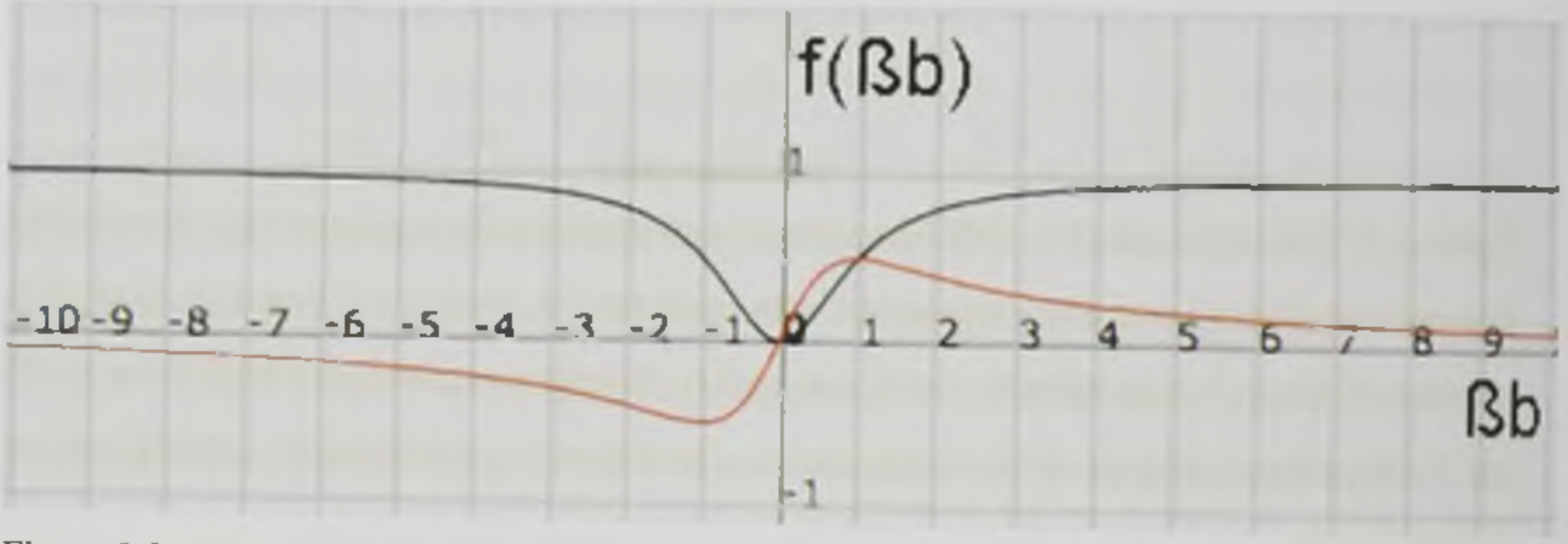

Figure 3.3: The values of $f(\beta_b) = \beta_b^2/(1 + \beta_b^2)$ (in black) and $f(\beta_b) = \beta_b/(1 + \beta_b^2)$ (in red), plotted for Hall parameters (β_b) between -10 and 10. Since the grains only carry net negative charges in these simulations, the sign of the $\mathbf{E}'$ term in equation (3.18) is always switched.

In the $n_H = 10^6$ cm^{-3} models, the grains have Hall parameters ranging from -0.1 far upstream to -1.5 inside the shock front. These values ensure that both terms in equation (3.18) remain important throughout the shock. In the upstream region, the grains carry a single negative charge so their Hall parameter is very small and negative. When $|\beta_g| < 1$, the contribution from the $\mathbf{E}'$ term carries a larger weighting, e.g. at β_g = -0.1 the contribution of E_x' is weighted

to be ten times that of $(\mathbf{E}' \wedge \mathbf{B})_x$. Between $-1 < \beta_g < -0.1$, the weighting of both terms grows, but the $\mathbf{E}' \wedge \mathbf{B}$ weighting grows faster, so although $\mathbf{E}'$ remains dominant, this dominance drops as β_g gets closer to -1. At $\beta_g = -1$ the contributions are weighted equally. For $-1.5 < \beta_g < -1$, the weighting of $\mathbf{E}'$ starts to move back from -0.5 towards zero and the weighting of $\mathbf{E}' \wedge \mathbf{B}$ continues to grow towards one. This means that the $\mathbf{E}' \wedge \mathbf{B}$ contribution to the drift becomes dominant but both terms remain significant.

In the x-direction, the deceleration of the ions and electrons commences as soon as $(\mathbf{E}' \wedge \mathbf{B})_x$ becomes non-zero. In this region the grains carry so few charges ($|Z_g| \leq 5$), that they do not respond to electromagnetic forces and move with the neutral flow. Because the grain Hall parameter is low at the upstream edge of the shock, the $\mathbf{E}'$ term induces their initial decoupling from the neutrals. The maximum weighting of the $\mathbf{E}'$ contribution (when $|\beta_g| < 0.5$) coincides with the region where E'_x becomes non zero. This occurs when the electric field acquires an x-component (E_x). In this region $\mathrm{E}'_x \approx \mathrm{E}_x$. E_x is a result of the ion and electron z-velocities, themselves produced by E_z. A non zero E'_x allows the grains to overcome collisions with the neutrals and switch from moving with them to the ions and electrons (see top right plot on Figure 3.1).

E'_x and $(\mathbf{E}' \wedge \mathbf{B})_x$ carry opposite signs but the Hall parameter weighting term in equation (3.18) switches the sign of E'_x, causing the grains to be decelerated like the other charged fluids. The grains catch up with the ions and electrons as β_g continues to fall below -1. The $(\mathbf{E}' \wedge \mathbf{B})_x$ term then makes the dominant contribution to the drift speed. Since $(\mathbf{E}' \wedge \mathbf{B})_x$ is the only term which is important for the ion and electron dynamics in the x-direction (equation 3.19), when this term dominates the dust motion, all the charged fluids tend to move in the same sense and with comparable speeds. Because both contributions work in the same sense along the x-direction, their contributions are added together. This results in grain-neutral drift speeds which are roughly the same as those of the other charged fluids. The grains then move with the ions and electrons until the downstream edge of the shock where they become de-charged and collisionally re-couple to the neutrals.

In the z-direction, $(\mathbf{E}' \wedge \mathbf{B})_z$ accelerates the ions and electrons in the positive sense to $\sim$ 60% of the shock speed (see right column, second row in figure 3.1). At the upstream edge of the shock where the grain charges are small, E'_z makes the dominant contribution to the grain-neutral drift speed because of the Hall parameter weighting in equation (3.18). The grains

de-couple from the neutrals in the x- and z-directions at the same point. Unlike the x-direction, $\mathrm{E}_z^{'}$ and $(\mathbf{E}^{'} \wedge \mathbf{B})_z$ work in opposite senses so the grains are initially accelerated in the negative sense along the z-direction to the ions and electrons. Upon entry to the shock, β_g drops below -1, the neutral x-velocity falls, the magnetic field strength and fluid mass densities rise and E_x appears. When $|\beta_g| > 1$, the $(\mathbf{E}^{'} \wedge \mathbf{B})$ term carries the larger weighting in equation (3.18) and so provides the dominant contribution to the grain-neutral drift speed. Because $\mathrm{E}_z^{'}$ and $(\mathbf{E}^{'} \wedge \mathbf{B})_z$ work in opposite senses along the z-direction, the effect of $(\mathbf{E}^{'} \wedge \mathbf{B})_z$ is to cancel that of $\mathrm{E}_z^{'}$ as far as possible. As the Hall parameter reaches its maximum value, the two contributions are comparable, causing the grains to move with the neutrals along the z-direction (second row in the right column of Figure 3.1). Because the grains are moving with the neutrals in the z-direction over the same region that they move with the ions and electrons in the x-direction, the lack of a z-component of the grain-neutral drift speed must be due to the balance of electromagnetic forces on the grains rather than collisions with neutrals.

The $\mathrm{n}_H = 10^4\ \mathrm{cm}^{-3}$ model displays similar effects but to a lesser extent. This is because the Hall parameter (β_g) now takes values between -1 (far upstream) and -20 (inside the shock front). The Hall parameters differ because in the low density model, the field strength is one tenth of its value and the neutral density is one hundredth of its value from the high density model. The low density Hall parameters are therefore around ten times larger. Inspection of figure 3.3 reveals that the $(\mathbf{E}^{'} \wedge \mathbf{B})$ term is favoured throughout the shock for these values, so the dynamics of the grains are closer to those of the other charged species. By the time $\beta_g = -10$, the $\mathbf{E}^{'}$ term is weighted to contribute only $\sim 1\%$ of the total. Past $\beta_g = -10$, the grain-neutral drift speed may effectively be treated in the same way as the ions and electrons, i.e. by using equation (3.19).

$(\mathbf{E}^{'} \wedge \mathbf{B})_x$ is both numerically larger than $\mathrm{E}_x^{'}$ and favored by the Hall parameter weighting terms. This ensures that the grains decouple from the neutrals at the same point as the other charged fluids and move with them along the x-direction through the entire shock structure. Likewise in the z-direction, the larger $|\beta_g|$ suppresses $\mathrm{E}_z^{'}$, which would otherwise provide a significant contribution to the drift speed. Without $\mathrm{E}_z^{'}$ to cancel $(\mathbf{E}^{'} \wedge \mathbf{B})_z$, the grain-neutral drift speed is non zero throughout the shock structure. The z-components of the ion and electron velocities are now around 10% of their values in the $10^6\ \mathrm{cm}^{-3}$ model ($\sim 6\%$ of the shock speed) because the field strength is also smaller by the same factor. The grains on the other hand retain $\sim 50\%$ of their maximum z-velocity from the high density regime ($\sim 2\%$ of the shock

speed). This is because they had not reached their maximum velocity in the 10^6 cm^{-3} model when $(\mathbf{E}' \wedge \mathbf{B})_z$ cancelled E'_z.

These simulations have shown that regardless of the upstream density, the $\mathbf{E}'$ term can either cause the grains to overcome collisions with neutrals to move with the ions and electrons or cancel the $\mathbf{E}' \wedge \mathbf{B}$ force, causing the grains to move with the neutrals. Which effect occurs depends on whether the terms in equation (3.18) have equal or opposite signs.

3.4.2 Oblique shock models

The existence of an upstream magnetic field component along the shock propagation direction (B_x), results in field and charged fluid velocity components in all three directions inside the shock. Like the perpendicular cases, differing Hall parameters permit these velocities to vary by species. The x-component of the magnetic field results in upstream orbital motions of the charged species about the field lines (induced by the magnetic force), with components in all three directions. As compression of the transverse part of the magnetic field begins in the precursor, the charged species are now also accelerated in the y-direction. They reach their maximum y-velocity at the point where grain-neutral collisions begin to accelerate the neutrals in the y-direction. Downstream of this point, the charged fluid y-velocities become smaller and the neutral y-velocity becomes larger until they converge at a downstream velocity determined by the value of B_x.

In the oblique models, the Hall current along $\mathbf{E}' \wedge \mathbf{B}$ has a component along the x-direction and the Pedersen current includes a component parallel to $\mathbf{E}'$ with a non-zero projection onto the x-axis. It was noted in §2.2 that the x-component of the Pedersen current causes the field to rotate in order to counteract the Hall current and thus maintain a total current of zero in the x-direction (as required by equation 1.37). Significant magnetic field rotation occurs when the Hall conductivity is larger than the Pedersen conductivity (Wardle 1998). Large Hall conductivities occur when the grains carry a substantial fraction of the negative charge and B_x is large. Since the total field strength only varies with the upstream neutral density, it is the same in each oblique model as it was for the relevant perpendicular case. The Hall parameters are therefore also the same. Inside the shock, B_x and E_y now exist so $\mathbf{E}'$ and $\mathbf{E}' \wedge \mathbf{B}$ have components in all three directions.

In the $n_H = 10^4$ cm^{-3} models, the grain Hall parameters still favour the $\mathbf{E}' \wedge \mathbf{B}$ contribution

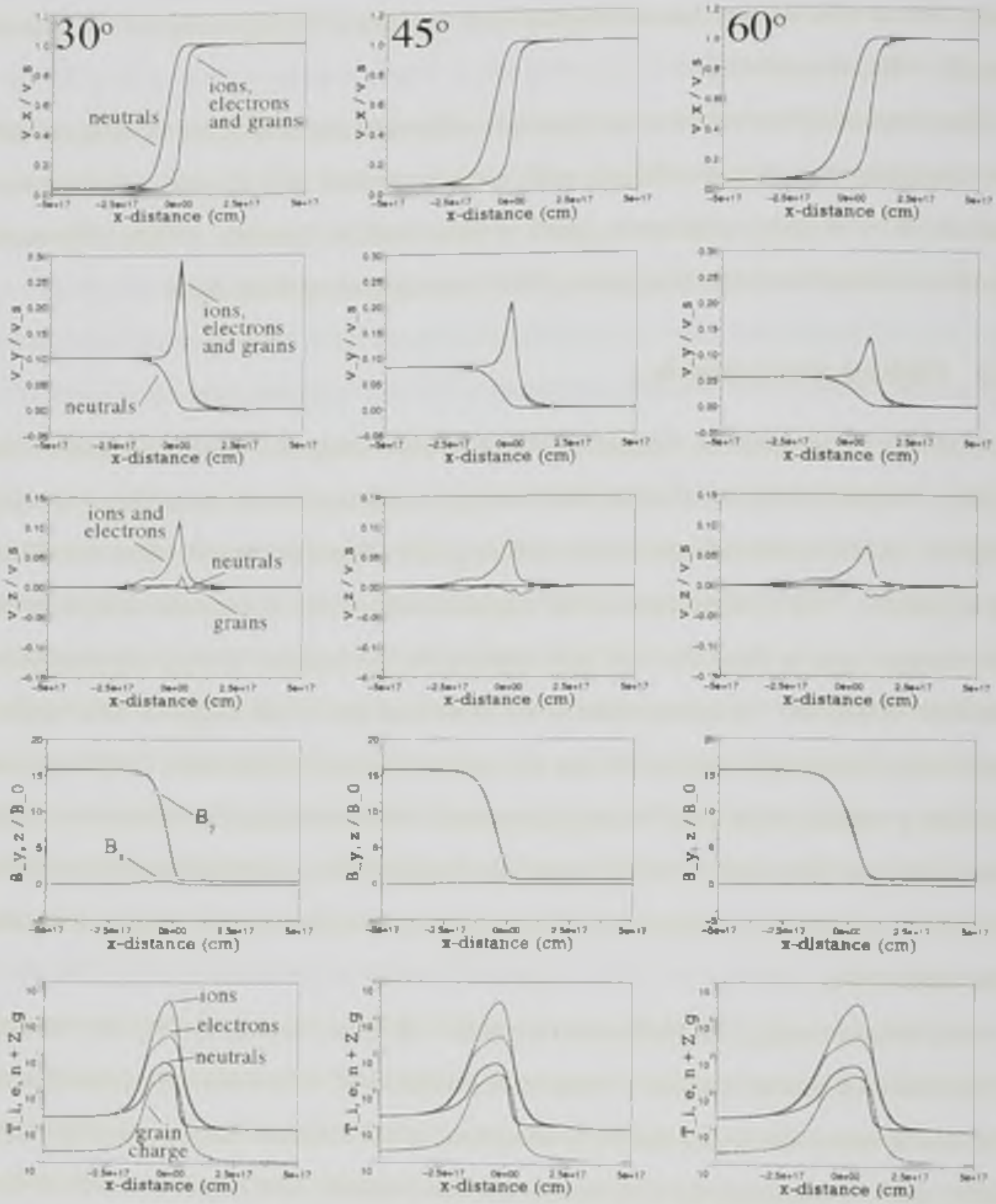

Figure 3.4: The shock structure for an oblique shock propagating at 25 kms^{-1} through a magnetic field of 10^{-4} G, which makes an angle of 30° (left), 45° (middle) and 60° (right) to the shock normal in a quiescent region with $n_{\mathrm{H}} = 10^{4}\mathrm{cm}^{-3}$. From top to bottom the plots are velocities in the x-, y- and z-directions, for the neutrals (solid), ions/electrons (dashed) and grains (dotted), the tangential magnetic field in the y-direction (solid) and z-direction (dashed), and the temperatures of the ions (dashed), electrons (dotted) and the neutrals (solid) as well as the absolute value of the grain charge (dash-dotted). The velocities are normalised with respect to the shock speed and the magnetic field to the total upstream magnetic field.

to the grain-neutral drift everywhere except the upstream and downstream edges of the shocks (where the contributions are equal). The Hall conductivity is always smaller than the Pedersen conductivity so there is no significant field rotation, (see the fourth row of plots in Figure 3.4). The small field rotation that is produced diminishes as θ increases because B_x becomes smaller. The other shock profiles do not change dramatically with the angle. Larger (nearer perpendicular) angles result in greater shock widths and smaller y-velocities. This is expected when more of the magnetic field lies perpendicular to the flow. Inspection of the second row in figure 3.4 demonstrates that all y-velocities tend to zero as the field configuration becomes perpendicular. The other profiles also converge on the perpendicular case as θ grows.

However, an obvious difference between the oblique and perpendicular simulations is the z-velocity of the grains. In the 30° case, the grains are still accelerated by $E_z^{'}$ in the opposite sense to the ions and electrons (negative electrons and grains move in opposite senses since the grains move due to $E_z^{'}$ whereas the electrons move due to $(\mathbf{E}^{'} \wedge \mathbf{B})_z$) at the upstream edge of the shock, but now to only half the speed they attained in the perpendicular model. Smaller values of θ result in a smaller $E_z^{'}$. This is because the extra term introduced to $E_z^{'}$ in oblique field configurations lowers its value by a factor of $q_{ny}B_x$, with both terms being largest at small angles. As $(\mathbf{E}^{'} \wedge \mathbf{B})_z$ becomes dominant, it again works in the opposite sense to $E_z^{'}$, but is now able to more than cancel that term, resulting in a net velocity in the same sense as the other charged fluids (q_{gz} changes sign). The grains keep moving in this sense until they approach the downstream edge of the shock where they lose charge and return to moving with the neutrals. As θ increases so does $E_z^{'}$, since B_x and q_{ny} drop and B_y rises. The z-velocities of the grains therefore converge on their perpendicular behaviour.

The fluid temperatures and grain charges are similar to the perpendicular case but the maximum ion temperature is slightly higher (by around 5000 K) in all the oblique cases than the perpendicular simulation. The increased ion temperature is a result of a non zero streaming velocity in the y-direction and is in harmony with the angular dependence reported by Chapman & Wardle (2006) for their steady, oblique shock models. The lack of an angular dependence in the $n_H = 10^4$ cm^{-3} models is because of the minor contribution of the grains to friction on the neutrals (inequality 3.15 is barely satisfied). Dust grains travel with the other charged species (as they did in the perpendicular 10^4 cm^{-3} simulation) and consequently do not alter the the shock structure (see the top row of Figure 3.4).

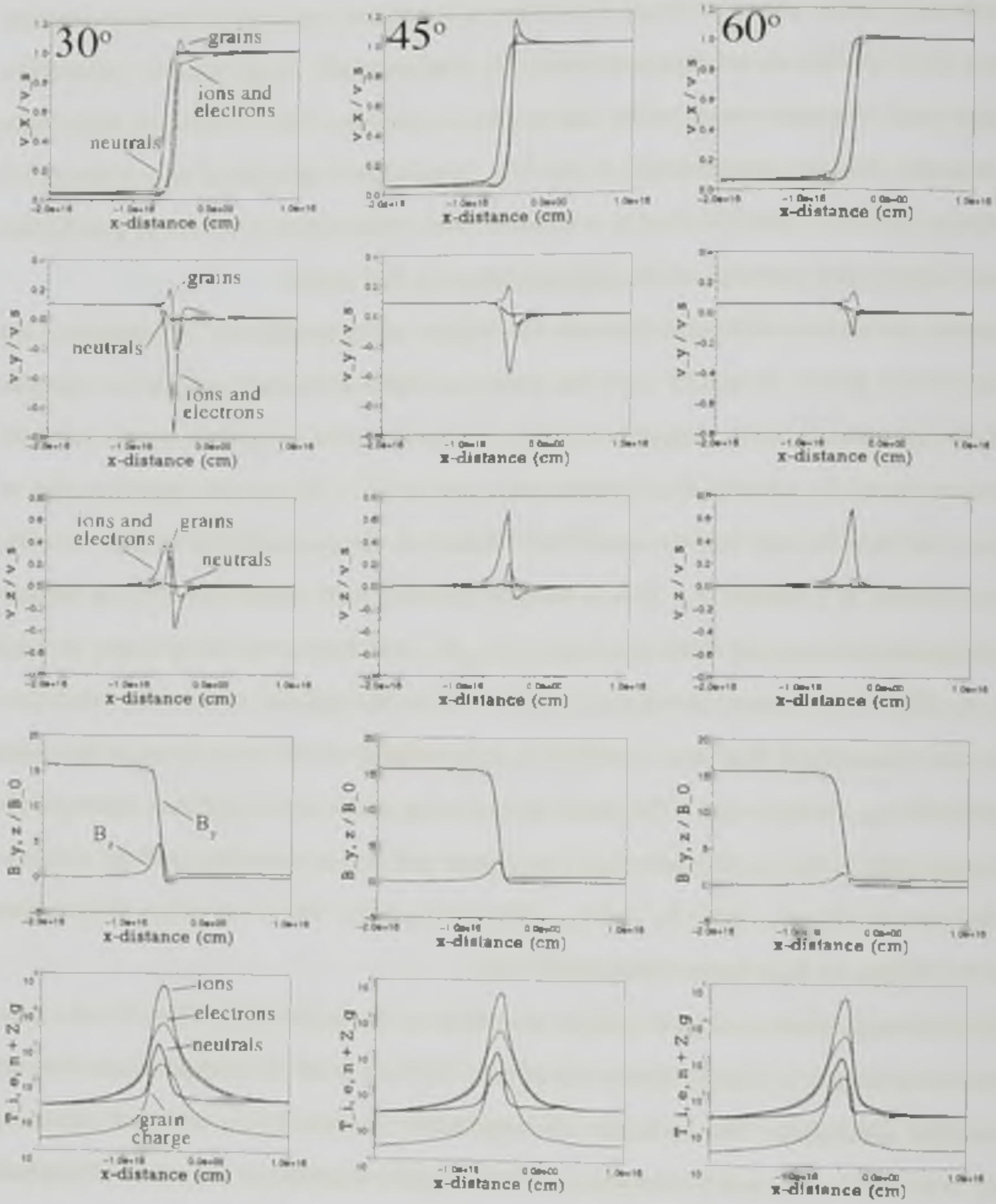

Figure 3.5: Same as in Fig. 3.4, but with an upstream density of $n_{\rm H} = 10^6 {\rm cm}^{-3}$.

The 10^6 cm^{-3} oblique models however are significantly different to the perpendicular case. The grains are now the dominant source of friction with the neutrals and carry a significant fraction of the negative charge. There is therefore a large charge separation, resulting in a high Hall conductivity. The magnetic field rotation is therefore more pronounced and B_z is larger. The upstream stationary point of the magnetic field (where $d/dx(B_y(x)) = d/dz(B_z(x)) = 0$) has switched to being a spiral node (for more information regarding magnetic field stationary points and spiral nodes see the section describing Wardle 1998 in §2.2) because the Hall conductivity alters the propagation of MHD waves upstream of the shock (Wardle 1998; Falle 2003). Like the low density models, the magnetic field rotation decreases and the shock width increases as θ_B grows. Larger field rotations have important consequences for the drift velocities of the charged particles, whose profiles now change drastically with θ_B. In contrast to the low density simulations, in the high density cases, the grain dynamics are different to those of the neutrals and other charged fluids in the x-, y- and z-directions instead of just the z-direction. This includes them moving in the opposite sense to the other charged species throughout parts of the shock at some angles (see figure 3.5). This can only occur when the grain motion is dominated by the $\mathbf{E}'$ term in equation (3.18) and $\mathbf{E}'$ carries the same sign as $\mathbf{E}' \wedge \mathbf{B}$ (see §3.4.1). Because the field rotation is largest and B_y is smallest, this effect is most noticeable in the 30° model.

The ion- and electron-neutral drift is determined by equation (3.19) with no dependence on the Hall parameter so their acceleration is directly related to $\mathbf{E}' \wedge \mathbf{B}$. When the ion and electron acceleration increases $\mathbf{E}' \wedge \mathbf{B}$ grows, when it decreases $\mathbf{E}' \wedge \mathbf{B}$ shrinks and when it switches sense $\mathbf{E}' \wedge \mathbf{B}$ changes sign. $\mathbf{E}' \wedge \mathbf{B}$ depends on the electric and magnetic field components and the neutral velocities. It is hence affected by the oscillations in the fields, themselves produced by the spiral node (see figure 3.6). At 30°, B_y becomes negative for a small region. In both the 30° and 45° models B_z first drops below zero before becoming positive and larger than B_y for a small region. These points correspond to changes in the velocities of the ions and electrons in all three directions. For example, in the 30° case, at the point where $|B_z|$ becomes larger than $|B_y|$, the ion and electron acceleration switches sense in the y-direction. When B_y reaches its minimum value, the ion and electron acceleration switches sense in the z-direction. In the 45° model, when $|B_z|$ becomes larger than $|B_y|$, the ion and electron acceleration switches sense in all three directions.

The charged particles are modeled to collide with the neutrals but not each other (see §2.4).

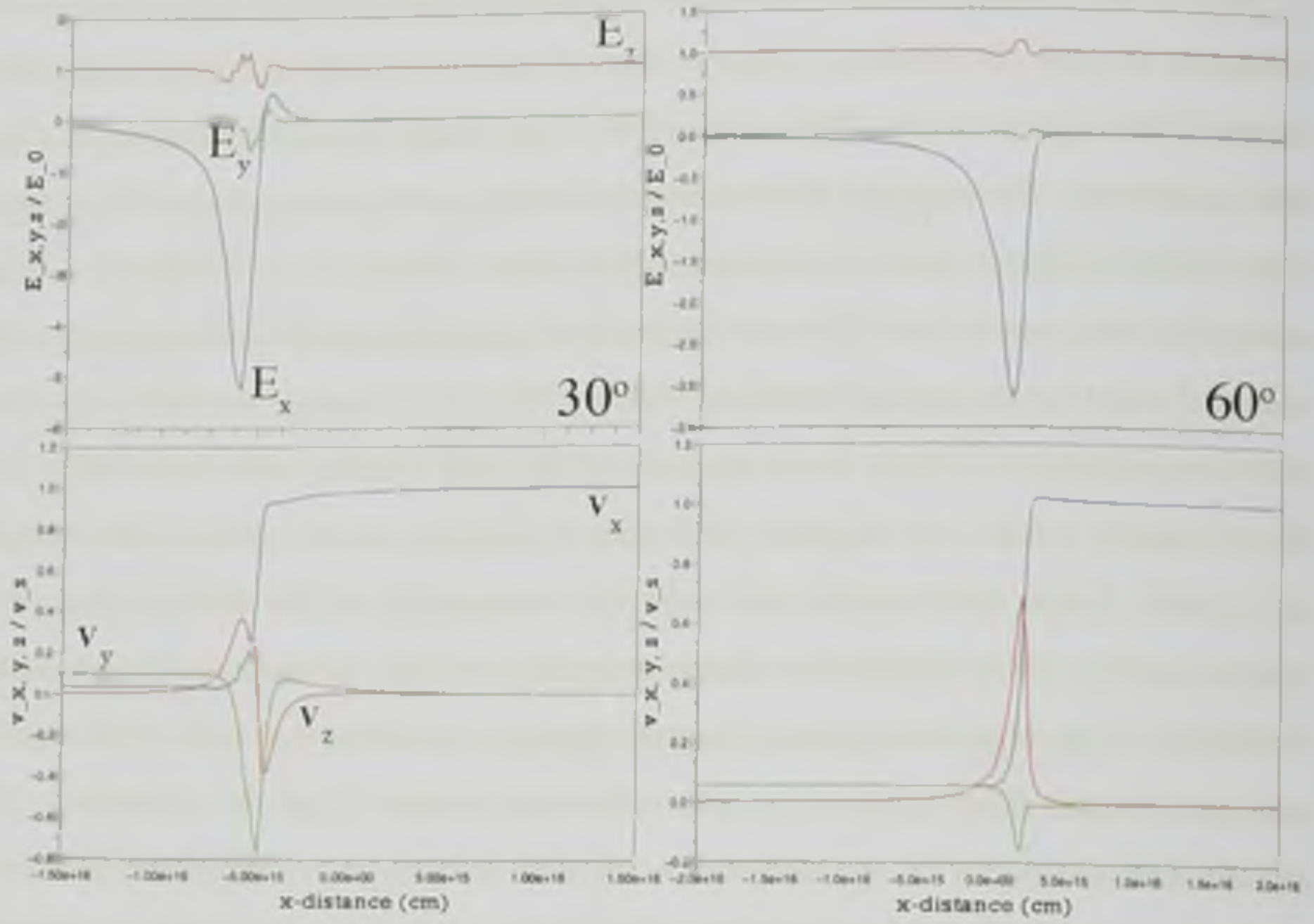

Figure 3.6: Plots of the electric field components with respect to the total upstream electric field (top row) and ion/electron velocity components with respect to the shock speed (bottom row). All plots are for a 25 km s^{-1} shock propagating through an upstream density of n_H = 10^6 cm^{-3}. Blue lines correspond to x-components, green lines to y-components and red lines to z-components. The left column is an oblique shock with the upstream magnetic field at 30° to the shock normal and the right column is an oblique shock with the upstream magnetic field at 60° to the shock normal (see §3.4.2).

This means that the only way that the grain dynamics can affect those of the ions and electrons is via the neutrals. Since the grains provide the dominant source of friction with the neutrals in the high density models, it is grain-neutral collisions which transfer most momentum to the neutrals. In addition to any oscillations in the field components, the sense and magnitude of the neutrals motion in all three directions contributes to $\mathbf{E}' \wedge \mathbf{B}$. This is clearly visible in the z-direction of the 45° model. The ions and electrons switch to being accelerated in the positive sense due to the field oscillations, but then become more strongly accelerated when the neutral z-velocity rises above zero. In the z-velocity profiles of the 30° model, the ion and electron

acceleration switches from being negative to positive in the region where the neutral z-velocity becomes larger than zero.

Near the upstream edge of the shocks, where the charged fluids first decouple from the neutrals, the grain dynamics are dominated by $\mathbf{E}'$. As noted in §3.4.1, this explains why the grains often remain at rest until further into the shock than the ions and electrons. When $|\mathbf{E}' \wedge \mathbf{B}|$ first rises above zero, the ions and electrons decouple from the neutrals but its effect on the grains is suppressed for as long as the grain charge remains small. As $\mathbf{E}'$ becomes non-zero, if it has the opposite sign to $\mathbf{E}' \wedge \mathbf{B}$, it causes the grains to initially move in the same sense as the other charged fluids. This occurs along the x-direction in the 45° model, along the y-direction in the 30° and 45° models and along the z-direction at 60°. If $\mathbf{E}'$ and $\mathbf{E}' \wedge \mathbf{B}$ carry the same sign, the initial grain motion is in the opposite sense to the other charged fluids. That is the case in the x-direction at 30° and 60°, in the y-direction at 60° and in the z-direction at 30° and 45°. This effect is most obviously manifested along the x-direction at 30°. The ions and electrons are decelerated immediately by $(\mathbf{E}' \wedge \mathbf{B})_x$, whereas the grains remain at rest until further into the shock and are initially accelerated by $\mathbf{E}'_x$. The velocity difference between the grains and the other charged fluids is already so large by the time that $\mathbf{E}'$ changes sign and the two contributions work in the same sense that the grains lag behind the ions and electrons throughout much of the shock. The signs of $\mathbf{E}'$ and $\mathbf{E}' \wedge \mathbf{B}$ depend on the signs of the field components, which oscillate strongly under the influence of the spiral node in the 30° and 45° cases, producing the complex velocity profiles in figure 3.5.

Further into the shock large electron currents allow the grains to become highly charged. This allows $\mathbf{E}' \wedge \mathbf{B}$ to contribute significantly to the grain-neutral drift. As was noted for the perpendicular models, when $\mathbf{E}'$ and $\mathbf{E}' \wedge \mathbf{B}$ provide similar contributions and carry the same sign the smaller contribution is cancelled so the grains move closer to the neutrals. This is most apparent in the z-direction at 60° because the ions and electrons move at a significant fraction of the shock speed but the grains do not, even though they carry many charges. When $\mathbf{E}'$ and $\mathbf{E}' \wedge \mathbf{B}$ carry opposite signs, their contributions work in the same sense and are summed. This can best be seen in the 60° model along the x-direction. The grains are gently decelerated by $\mathbf{E}'_x$ which carries the same sign as $(\mathbf{E}' \wedge \mathbf{B})_x$. $(\mathbf{E}' \wedge \mathbf{B})_x$ changes sign in the same region as the grains become highly charged. It then provides a considerable contribution to the drift and that contribution is in the same sense as $\mathbf{E}'_x$. The grains therefore become very strongly decelerated

and the ions and electrons switch from being accelerated to being decelerated.

3.5 Results: multiple grain species

Up to this point the grains have been considered to be uniformly spherical with the same radius. In molecular clouds however, the dust grain size distribution (Mathis et al. 1977) is thought to be represented by:

$$\frac{dn}{dr} \propto r^{-3.5}, \tag{3.20}$$

where dn is the number of grains with radii in the range r to $r + dr$. In order to model such a grain size distribution, a fluid of small grains with radius $r_s = 0.04$ μm ($r_s = 0.1 r_g$) and $m_s = 8.03 \times 10^{-16}$ g ($m_s = 0.001 m_g$) is included. The total mass density of both of the grain fluids remains at 1% that of the neutrals. The final model includes two grains species, so the total grain mass must be partitioned between them so as to maintain the relationship in equation (3.20). The partition described by equations (3.3) and (3.4) guarantees that most of the total grain mass density is in the large grain fluid, but the small grains are more numerous. This is expected from equations (3.4) and (3.20). The small grain fluid therefore dominates the grain-neutral friction and determine the shock dynamics since the grain-neutral collision coefficient is proportional to $r_{g,s}^2/m_{g,s}$ (Draine 1986). Inspection of Figure 3.7 reveals the shock width to be an order of magnitude smaller than it was in the equivalent single grain models. This is predicted by equation (3.16), given the change in the gas phase fractional abundance of electrons (χ_e).

The peak small grain charge is about an order of magnitude smaller than the large grain charge (equation 3.17). However, the lower masses of individual small grains ensures that their Hall parameter is larger than that of the large grains and means that they remain strongly tied to the magnetic field lines. Larger Hall parameters also mean that the $\mathbf{E}' \wedge \mathbf{B}$ term in equation (3.18) mainly determines the small grain-neutral drift speed. Even though each small grain carries only around 10% as many electron as each small grain, because they are far more numerous, more electrons are resident on small grains than large ones per unit volume. The additional small grains mean that free electrons become depleted from the gas phase (n_i becomes much larger than n_e).

Since the small grains move with the ions and carry much of the negative charge, charge separation, Hall conductivity and field rotation remain minimal. Also, the upstream magnetic field no longer becomes a spiral node.

Without the spiral node, the oscillations in the field components and charged fluid velocities near the upstream edge of the shock no longer occur. In the x-direction, the ions and electrons are no longer accelerated before being decelerated, but instead are smoothly decelerated through the shock. This is because $(\mathbf{E}' \wedge \mathbf{B})_x$ no longer becomes negative and $|\mathbf{B}_z|$ is always smaller than $|\mathbf{B}_y|$. The ions and electrons now move along the y-direction in the opposite (positive) sense than they did in the analogous single grain simulations. Their motions are equivalent to the single grain, 10^4 cm^{-3} model because $(\mathbf{E}' \wedge \mathbf{B})_y$ remains positive. In the z-direction, the ions and electrons move in the positive sense, but now reach only one third of the speed that they did in the equivalent single grain case because the lack of field rotation guarantees that $\mathbf{B}_z$ is now very much smaller (~ 10 %) and never becomes negative.

Inspection of the top three plots in figure 3.7 reveals that the small grains move in the same sense as the ions and electrons throughout the shock in all directions. This is a result of the strong coupling between them and the magnetic field.

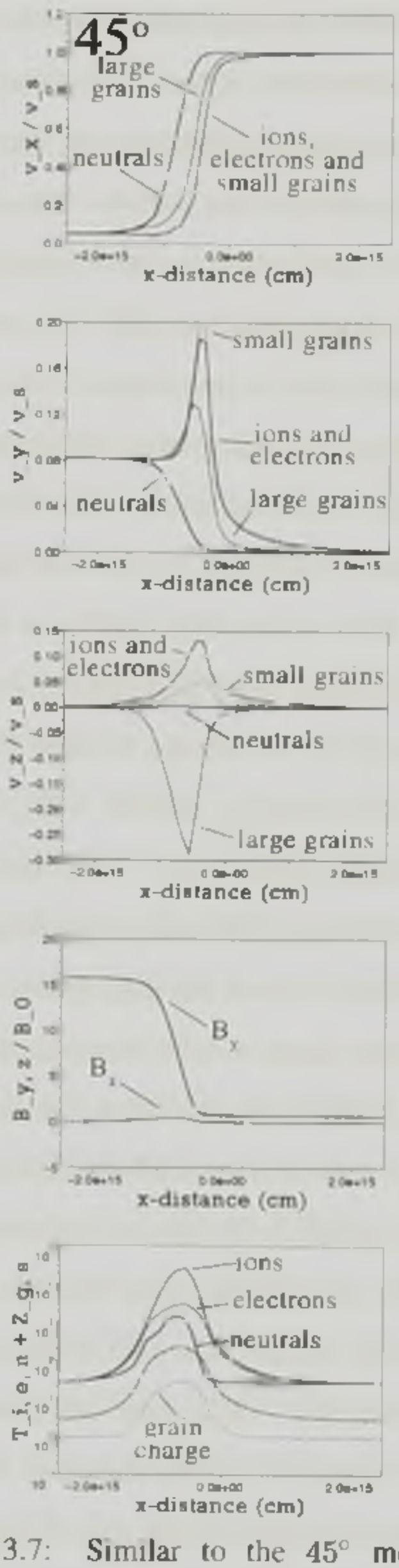

Figure 3.7: Similar to the 45° model of Fig. 3.5, but for two grain fluids. The small grains are indicated on the velocity components figures with a thin-dotted line, while their average charge is given by a thin dashed-dotted line.

Although their motion is dominated by $\mathbf{E}' \wedge \mathbf{B}$, the contribution of $\mathbf{E}'$ can be still seen in the x- and y-directions. In the y-direction, the small grains decouple from the neutrals at the same point as the ions and electrons and move exactly with them until E'_y allows the large grains to drift with respect to the neutrals. Since E'_y acts in the same sense as $(\mathbf{E}' \wedge \mathbf{B})_y$, its contribution allows the small grains to move incrementally faster and reach slightly higher peak velocities than the ions and electrons. $(\mathbf{E}' \wedge \mathbf{B})_z$ reaches only around half of $(\mathbf{E}' \wedge \mathbf{B})_y$ (from a comparison of the peak y and z components of the ion and electron velocities in figure 3.7), so even though the small grain Hall parameter still favours this term, E'_z is more significant. $(\mathbf{E}' \wedge \mathbf{B})_z$ and E'_z act in opposite senses and so cancel as far as possible. This partial canceling results in intermediate small grain z-velocities, i.e. between those of the ions and electrons and the neutrals.

The large grains have a different velocity than all of the other fluids throughout much of the shock, in all three directions. Even without the spiral node they lag behind the ions and electrons in the x-direction because E'_x remains zero until further into the shock than in the single grain model. E'_x and $(\mathbf{E}' \wedge \mathbf{B})_x$ still act in the same sense, so as the large grains become highly charged and the $(\mathbf{E}' \wedge \mathbf{B})_x$ becomes more significant, it acts in the same sense as E'_x. The deceleration of the large grains therefore follows the ions and electrons. Due to the fact that they are last to move, the large grains never quite catch them up and at any point in the shock they display larger x-velocities than the other charged fluids. In the y-direction, like the low density, single grain simulation, the large grains only move in the positive sense since there is no longer a spiral node. Like the high density, single grain simulation however, they move with different speeds to the ions and electrons throughout most of the shock. This is because E'_y and $(\mathbf{E}' \wedge \mathbf{B})_y$ are weighted such that they both remain significant throughout the shock, but E'_y is numerically smaller. The sum of the two weighted terms acting in the same sense is therefore less than the $(\mathbf{E}' \wedge \mathbf{B})_y$ term with a weighting factor of unity. Hence the large grains display lower y-velocities. In the z-direction, unlike any previous simulations, the large grains move in the opposite sense to all the other charged fluids and reach the highest peak velocity. The small grain Hall parameter ensured that E'_z could only partially cancel $(\mathbf{E}' \wedge \mathbf{B})_z$, but in the case of the large grains E'_z remains more significant. Because E'_z is numerically larger, $(\mathbf{E}' \wedge \mathbf{B})_z$ is more than cancelled, resulting in a net large grain velocity which is both larger than that of the ions and electrons and in the opposite sense.

The inclusion of the small grains therefore substantially alters the shock structure. Including

additional grain species (smaller than the large grains) would affect the structure still further by loading the magnetic field lines with more charged dust grains. This loading decreases the signal speed of ion-magnetosonic waves propagate (equation 1.20), narrowing the magnetic precursor. There is then the possibility that the resulting shock would be of J-type, in which case grain inertia cannot be neglected.

3.6 Conclusions

This chapter presents one dimensional, time dependent, multifluid MHD simulations of perpendicular and oblique C-type shocks in dusty plasmas. The simulations begin with a J-type shock which evolves in time to become a steady C-type shock. Relevant mass transfer and cooling processes are modeled. These include radiative electron recombinations with Mg^+, dissociative recombinations of electrons with HCO^+ and radiative cooling by O, CO, H_2 and H_2O. The currents of charged particles onto grains is also taken into account in order to calculate the average grain charge. These models are the first of oblique fast-mode shocks in dense molecular media in which a fluid treatment of grain dynamics has been combined with a self consistent calculation of the thermal and ionization balance. Simulations have been performed at different plasma densities for both one and two distinct dust grain species.

Dust does not affect the shock dynamics for $n_H = 10^4$ cm^{-3} and the structures of oblique and perpendicular shocks are qualitatively similar. On the other hand, in the $n_H = 10^6$ cm^{-3} models, grain-neutral friction dominates momentum transfer to the neutrals and determine the shock profiles. In oblique shocks, the magnetic field in the shock front is not confined to the shock plane and rotates about the shock normal. The amount of rotation depends on the ratio of the Hall to the Pedersen conductivities. For a single, large grain species the rotation is substantial and at its largest for small angles between the upstream field and the shock normal because the Hall and Pedersen conductivities are comparable in the shock. In some cases, the upstream field even spirals around the shock propagation direction. The addition of a smaller grain species which contains most of the grain mass and charge density largely suppresses this rotation since such grains remain coupled to the ions and electrons and carry most of the negative charge. Their presence consequently reduces the Hall conductivity.

These findings are in harmony with the main qualitative conclusions of previous studies

(Draine et al. 1983; Pilipp & Hartquist 1994; Wardle 1998; Chapman & Wardle 2006), which demonstrates that this numerical method is efficient, rigorous and robust. In addition, it is the first oblique shock code which is capable of producing reliable results for comparison with observations due to the rigorous treatment of grain dynamics and the thermal and ionization balances. However, the models presented here do have some limitations: The chemistry is far to simple for the results of these simulations to be compared to observations. Also, the drift velocities of the grains are determined by balancing grain-neutral friction with the Lorentz force, so grain inertia is neglected. This is a valid approximation for small grains, however the length scale over which the large grains are decelerated in collisions with the neutrals is appreciable. In some cases the drag length can be comparable to the length scale for magnetic field compression (Ciolek & Roberge 2002). In such cases, the inertia of the large grain inertia cannot be neglected. Also, the average charge on a small grain can be very close to the elementary charge. In real situations, there is always some fluctuation of charges around the average. This means that some small grains will carry zero, or even a single positive charge. Neutral grains decouple from the field, whilst positive grains can drift in different directions to the negative ones. Although this effect can alter the shock structure, the change is minimal (Guillet et al. 2007).

This time dependent method is able to find steady solutions for non-equilibrium conditions and model transient phenomena. In the vicinity of YSOs, the abundance of SiO is often significantly enhanced (e.g. Martin-Pintado et al. 1992; Jiménez-Serra et al. 2004). The SiO emission is thought to arise from the interaction of a protostellar jet with dense clumps in the surrounding molecular cloud (Lefloch et al. 1998). The sputtering of grains in C-type shocks releases SiO (which is incorporated into the grain material in quiescent regions) into the gas phase (Caselli et al. 1997; Schilke et al. 1997). Numerical models of grain sputtering in steady C-type shocks show good agreement with recent observations of SiO line intensities in the L1448 and L1157 molecular outflows (Gusdorf et al. 2008). Such observations are unlikely to be of steady shocks however, since the interaction of a shock with a clump will stop the shock from being steady for an extended period. Subsequent chapters explore the interaction of steady C-type shocks with perturbations in the upstream density and include terms to model grain sputtering in order to predict the return of SiO from grain cores, to the gas phase.

Chapter 4

Transient evolution of C-type shocks interacting with density perturbations

4.1 Summary

The outlows from low mass YSOs drive shocks through the densest regions of dusty molecular clouds. Since molecular clouds are observed to be inhomogeneous on all length scales, these shocks are likely to propagate through clumpy media and are therefore not steady. They are also unlikely to be perpendicular to the upstream magnetic field.

The results were obtained by applying the time dependent multifluid MHD scheme of Falle (2003), using oblique, steady C-type shocks (like those obtained in chapter 3) as initial conditions, to study the interaction of such shocks with perturbations in the upstream density. Any features which develop when the steady shocks encounter density inhomogeneities are identified in order to ascertain whether any part of the magnetic precursor region of a non steady multifluid shock ever behaves in a quasi-steady fashion. If it does, some time-dependent shocks in weakly ionized, dusty media may be modeled approximately without solving the time-dependent MHD equations.

Simulations were undertaken for initially steady C-type shocks encountering each of three types of density perturbation. When the shock encounters a semi-finite inhomogeneity of higher density, a transmitted shock evolves from being J- to C-type over a timescale comparable to the ion flow time through the new shock structure. Sufficiently upstream parts of the evolving J-type shocks precursor are found to be quasi-steady. As the precursor expands, progressively more of it becomes steady until it forms the new, stable C-type shock. The ion flow time is

also relevant for the evolution of a shock interacting with a perturbation of decreasing density. However, models for shocks interacting with clumps where the upstream density increases and then decreases again over a length scale representative of the clumps in molecular clouds cannot be entirely described by combining the results obtained for monotonically increasing and decreasing densities.

It is therefore noted that the transient evolution in structure when a steady C-type shock encounters an inhomogeneity always includes a transmitted J-type shock, and that the subsequent evolution back to being C-type cannot always be approximated by quasi-steady models.

The work comprising this chapter was described by Ashmore et al. (2010).

4.2 Introduction

Most previous studies of C-type shocks in dusty plasmas have focused on the shock structure at steady state (e.g. Draine et al. 1983; Pilipp et al. 1990; Pilipp & Hartquist 1994; Wardle 1998 and see §2.1). However, SiO observations suggest that proto-stellar jets and winds interact with clumpy structures along their propagation axes (Mikami et al. 1992; Lefloch et al. 1998; Jørgensen et al. 2004 and see §1.2.3). In this case, the steady state assumption must be relaxed. Ciolek & Roberge (2002) were the first to employ a time dependent multifluid MHD code, including dust grain dynamics, to study fast-mode C-type shocks (see §2.3). However their study was restricted (by model limitatons) to perpendicular shocks, even though the alignment of shocks with the background magnetic field in the ISM is likely to be arbitrary. The multifluid approach developed by Falle (2003) overcomes this limitation (see §2.4). Using that scheme, chapter 3 represents the first time dependent simulations of oblique, fast-mode C-type shocks that evolve to steady state and include a self consistent calculation of the thermal and ionization balances together with a fluid treatment of grain dynamics.

While being time dependent, the simulations in chapter 3 still concentrate on the steady state shock structures. In this chapter that work is extended to study the temporal evolution of fast-mode C-type shocks interacting with regions of inhomogeneous density. These perturbations are modeled to represent a shock either moving into a region of higher density (e.g. a shock from one YSO interacting with the dense envelope around another), moving into a region of lower density (e.g. a shock leaving the dense environment immediately surrounding its parent

YSO and moving into a more diffuse region) or interacting with a clump. Section 4.3 describes the numerical method and initial conditions adopted together with the relevant computational considerations. The code is than applied to oblique shocks propagating through regions of varying density in section 4.4. In section 4.5 the results and conclusions are discussed.

4.3 The model

4.3.1 Numerical code

The numerical scheme is exactly as detailed in §2.4. As in chapter 3, the scheme is advanced explicitly even though this implies a restriction on the time-step:

$$dt \leq \frac{r_{ad}}{(r_H^2 + r_{ad}^2)} \Delta x^2, \tag{4.1}$$

where r_{ad} is the ambipolar resistivity and r_H is the Hall resistivity (see §3.4.1). The time-step thus becomes small for high numerical resolution, or when the Hall resistivity becomes much larger than the ambipolar diffusion resistivity. In the simulations presented both in chapter 3 and here, the Hall resistivity only becomes comparable to the ambipolar resistivity and never much larger so the time-step is not severely restricted.

The source terms remain the same as they were for chapter 3, as described in §2.5. It is still assumed that every cosmic ray ionization (of H_2) leads immediately to the production of HCO^+. Ion-neutral reactions with magnesium (which is representative of all metals) create metallic ions. It is assumed that cosmic ray ionizations form ions of each type equally. Molecular and metallic ions may recombine with electrons both in the gas phase and on grain surfaces. Since gas phase dissociative recombinations of molecular ions have much larger cross sections than the radiative recombinations of metallic ions at a given electron temperature, at least one species of each type is required to accurately determine the fractional ionization. All reactions are assumed to occur with the rate coefficients given in Pilipp et al. (1990). Whilst grossly oversimplified, this chemical model is sufficient to provide a reliable calculation of the fractional ionization.

One neutral-neutral reaction is modeled, to simulate the conversion of atomic oxygen into water in the gas phase. The relevant reaction rates for this transfer increase by many orders of magnitude as the neutrals are heated from several hundred to a thousand degrees Kelvin. For

an upstream molecular hydrogen abundance of 10^5 cm^{-3}, the timescales for the removal of O in reactions with H_2 are 1.4×10^{12} s, 1.5×10^9 s and 6.7×10^7 s at 300 K, 600 K and 1000 K respectively. The corresponding timescales for OH removal with H_2 are 1.5×10^9 s, 3.2×10^7 s and 4.2×10^6 s. Instead of including explicit rate equations for this transfer, it is assumed that all of the oxygen not in CO is atomic until T_n = 500 K, at which point it is switched to being H_2O. Water is assumed to be stable. A more thorough treatment would have resulted in higher gas phase water abundances over the range $300 < T_n < 500$ K and lower gas phase water abundances over the range $500 < T_n < 700$ K. Because water is an important coolant (see §1.1.3.2, §1.3.4 and §2.5.3), this leads to an underestimate of the cooling rate and overestimate of the neutral temperature when $300 < T_n < 500$ K and an overestimate of the cooling rate and underestimate of the neutral temperature when $500 < T_n < 700$ K. Whilst the cooling rates do affect the shock profile, in this temperature regime the shock behaviour is much more strongly influenced by the ionization structure, which is determined primarily by the cosmic ray induced ionization rate, the recombination of ions and electrons on grains and the grain dynamics. The details of the neutral gas temperature profile are therefore not critical.

4.3.2 Initial conditions

Unlike the simulations presented in chapter 3, for which the initial conditions are J-type shocks, each of the simulations in this chapter begins with a steady C-type shock propagating through a medium with an upstream hydrogen abundance of either $n_H = 10^4$ cm^{-3} or $n_H = 10^5$ cm^{-3}. The shocks move along the x-axis with a velocity (v_s) of 25 km s^{-1} and represent the steady oblique (45°) shocks discussed in §3.4.2. Like there, a single fluids of grains with $r_g = 4 \times 10^{-5}$ cm is considered. This means that the initial upstream boundary conditions for the $n_H = 10^4$ cm^{-3} case are exactly as described in chapter 3. To obtain the initial conditions for the $n_H = 10^5$ cm^{-3} case, a J-type discontinuity (as per §3.3.1) was set up for that density and a simulation undertaken until a steady C-type shock was obtained. The upstream magnetic field and temperatures were kept the same as for the $n_H = 10^4$ cm^{-3} case (B = 10^{-4} G and $T_{n,0} = T_{i,0} = T_{e,0}$ = 8.4 K).

Since the aim of this chapter is to model the interaction of a C-type shock with an inhomogeneous medium, a density perturbation is introduced at the upstream boundary. The shape of the perturbation is chosen so that it reasonably reproduces all or part of the density profiles

observed in clumps or cores (e.g. Tafalla et al. 2004). Each perturbation can be described solely in terms of its width and the density contrast (i.e. the maximum multiple of the upstream density which it reaches). The inhomogeneities are assumed include no gradients in the temperatures, pressures or magnetic field.

4.3.3 Computational details

Some care must be given to the size of the computational grid for models where the upstream density varies. This is because a change in the upstream density alters the shock width (see equation 1.23). Like in chapter 3, the fractional ionization constraints (inequalities 3.14 and 3.15) are met, so the shock width is determined by grain-neutral drag via equation (3.16). When a shock interacts with a density perturbation, its width changes by the same factor as the density contrast. To ensure that the domain is wide enough to accommodate the widest shock whilst retaining sufficient cells for the narrowest shock to be well resolved, the grids are selected with consideration of the shock parameters at both densities. The shock width (L_g) is estimated in each regime using:

$$L_g = 2.1 \times 10^{24} \chi \left(\frac{v_s}{kms^{-1}} \right)^{-1} \left(\frac{v_A}{kms^{-1}} \right) \left(\frac{10^{-2} cm^{-3}}{n_i} \right) cm, \tag{4.2}$$

where v_A is the Alfvén speed, v_s the shock speed, χ is the fractional ionization and n_i is the ion number density. The numerical domain is then set to $-10L_g(\rho_{min}) < x < 10L_g(\rho_{min})$ with $L_g(\rho_{min})$ being the shock width at the lowest density. The shock width varies by an order of magnitude with a density contrast of ten, but any shock must contain at least ten cells to be resolved. Therefore a grid of twelve hundred cells is adopted for the domain to allow the broadest shock to be accommodated whilst ensuring that the narrowest shock includes more than ten cells. Like previously, there is a fixed inflow at the upstream boundary and a free-flow boundary condition at the downstream edge.

As well as altering the shock width, encountering a gradient in the upstream density also changes the propagation speed of the shock. Since the evolution is followed from the initial shock frame, the new shock structures (see §4.4) would eventually move off the grid. In order to keep the shocks within the computational domain, the velocity of the shock frame is manually

adjusted by employing a Lorentz transformation along the shock propagation direction (the x-axis).

Although the initial conditions are given by a C-type shock, an interaction with a density inhomogeneity always results in a J-type sub-shock in the neutral fluid (see §4.4). Within such sub-shocks, the assumption that charged fluid inertia is negligible (see §2.4) is no longer valid. Despite this, the J-type neutral sub-shock can be accurately modeled (see Falle 2003). Furthermore, the grain inertial phase is short compared to the other timescales of the shock-clump interaction and the subsequent return of the shock to steady state. It is to be expected that the evolution of the shock shortly after the interaction would be modified by the inclusion of charged fluid inertia, but that these changes would be modest (Roberge & Ciolek 2007).

4.4 Results

Several aspects of the interaction between the shock and density inhomogeneity are consistent across the simulations in this chapter. These will be discussed here before commenting on specific models in §4.4.1 - §4.4.3. In most models (except when the density falls) the initial shock width is comparable to or larger than that of the perturbation. The interaction then results in a pair of waves; one transmitted and one reflected. These are separated by a contact discontinuity (a transition point across which there is no particle transport). When the perturbation length scale is large compared to the shock width then there is no reflected wave and the relative strength of the transmitted and reflected waves is determined by the initial shock speed and the density contrast across the perturbation (see below).

The transmitted wave is always initially a J-type shock consisting of a precursor and sub-shock. The sub-shock develops because as the perturbation reaches the shock, the upstream conditions change faster than information can propagate across the shock front. After some time, collisions between the charged particles and neutrals generates a neutral precursor. The precursor then evolves into a new C-type shock. The transmitted C-type shock is narrower than the original if the upstream density increases and broader if it decreases.

While the transmitted wave is always a shock, the reflected wave which propagates into the post-shock flow can be either a rarefaction wave or a shock. Since the reflected wave connects the flow far downstream with that immediately downstream of the newly transmitted shock, it

is clear that a rarefaction wave forms when the post-shock density of the transmitted shock is smaller than that far downstream. A shock forms when the post-shock density of the transmitted shock is greater than that far downstream. Similarly to the transmitted shock, the reflected shock is initially J-type and evolves in time to become C-type.

This work only follows the long term evolution of the transmitted shocks and not the reflected waves. The reflected component thus eventually moves off the grid through the downstream boundary. However, numerical artifacts arise when shocks are reflected from free flow boundaries (e.g. Hedstrom 1979). Although non-reflecting boundary conditions can be used to overcome this problem, it is easier to simply remove reflected wave from the computational domain. This can be done because the transmitted shock and reflected wave are separated by a contact discontinuity. so are unable to physically affect each other.

4.4.1 Perturbation of increasing density

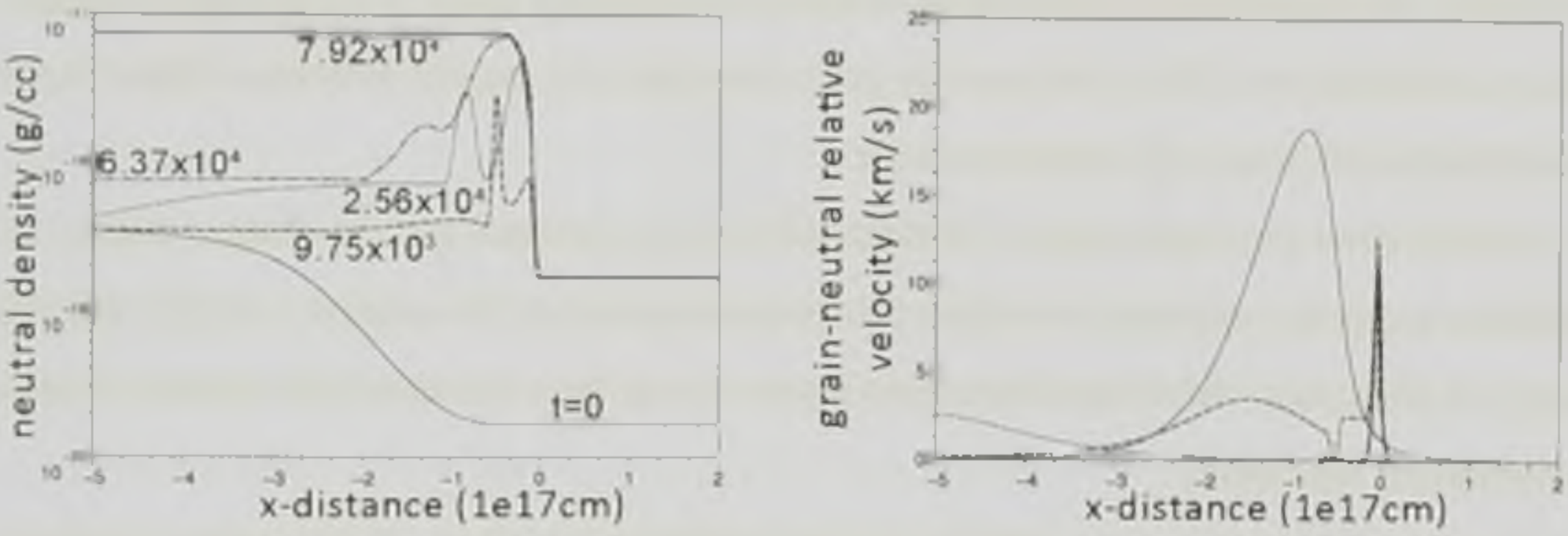

Figure 4.1: Evolution of the shock structure from the shock frame as a 25 km s^{-1} shock interacts with an semi finite perturbation in the upstream density from $n_H = 10^4$ cm^{-3} to $n_H = 10^5$ cm^{-3}. The left panel shows the neutral density and the right panel the grain-neutral relative speed. The profiles for the initial C-type shock are given by the thin solid lines, the dashed lines show the shock structure 9.75×10^3 years after the shock first interacts with the perturbation. The dotted and dash dotted lines are 2.56×10^4 and 6.37×10^4 years after the first intraction respectively. The thick solid lines show the final steady C-type shock structure obtained (after 7.92×10^4 years).

Figure 4.1 shows the density and grain-neutral drift speed profiles at different evolutionary stages of a C-type shock interacting with a semi-finite density perturbation, across which the

density increases by a factor of 10. It shows the initial and final structures as well as three intermediate stages.

This section follows the evolution of a C-type shock in the outflow from a proto-stellar object moving into a denser region. This may happen when the shock from one YSO interacts with a different dense core. The initial shock travels at 25 km s^{-1} through a region with n_H = 10^4 cm^{-3} and is therefore a strong fast-mode shock with an Alfvénic Mach number of $\sim$ 11.5. The initial shock meets a density perturbation in which the upstream density rises to $n_H = 10^5$ cm^{-3} (so the density contrast is 10). The density gradient follows a sinusoidal profile with a length scale of 10^{17} cm.

As expected from the discussion in §4.4, once the shock and perturbation have met, a reflected and transmitted J-type shock pair form. This occurs within 3×10^3 years. The neutral sub-shocks can be clearly seen in both the velocity and temperature profiles of figure 4.2, i.e. the discontinuous jump in the neutral velocity along the x-axis and the drastic cooling of all the fluids. The temperature plots also show that the transmitted shock is considerably stronger than the reflected one. This is because the peak temperature is roughly five times higher in the transmitted shock than in the reflected shock.

Initially there are large relative velocities between the neutrals and the charged fluids. As collisions accelerate and heat the neutrals (and form the precursor) the relative velocities fall and energy is dissipated. This causes the temperatures of both the transmitted and reflected shocks to decrease at later times.

Lower neutral temperatures and grain-neutral drift velocities imply that the higher upstream density regime will be less effective for grain sputtering. This agrees with the results of May et al. (2000) who report that for v_s = 25 km s^{-1}, the elemental fraction of silicon sputtered from olivine decreases with increasing upstream density. At higher shock speeds however they note that the elemental fraction of silicon sputtered becomes independent of the upstream density (see chapter 5).

In the early stages of evolution, it is already clear to see the effect of the higher density on the charged particles and magnetic field. Inside the perturbation where the density is higher, the Hall conductivity becomes larger than the Pedersen conductivity (see chapter 3). This changes the propagation of MHD waves in the upstream region and causes a spiral node to develop.

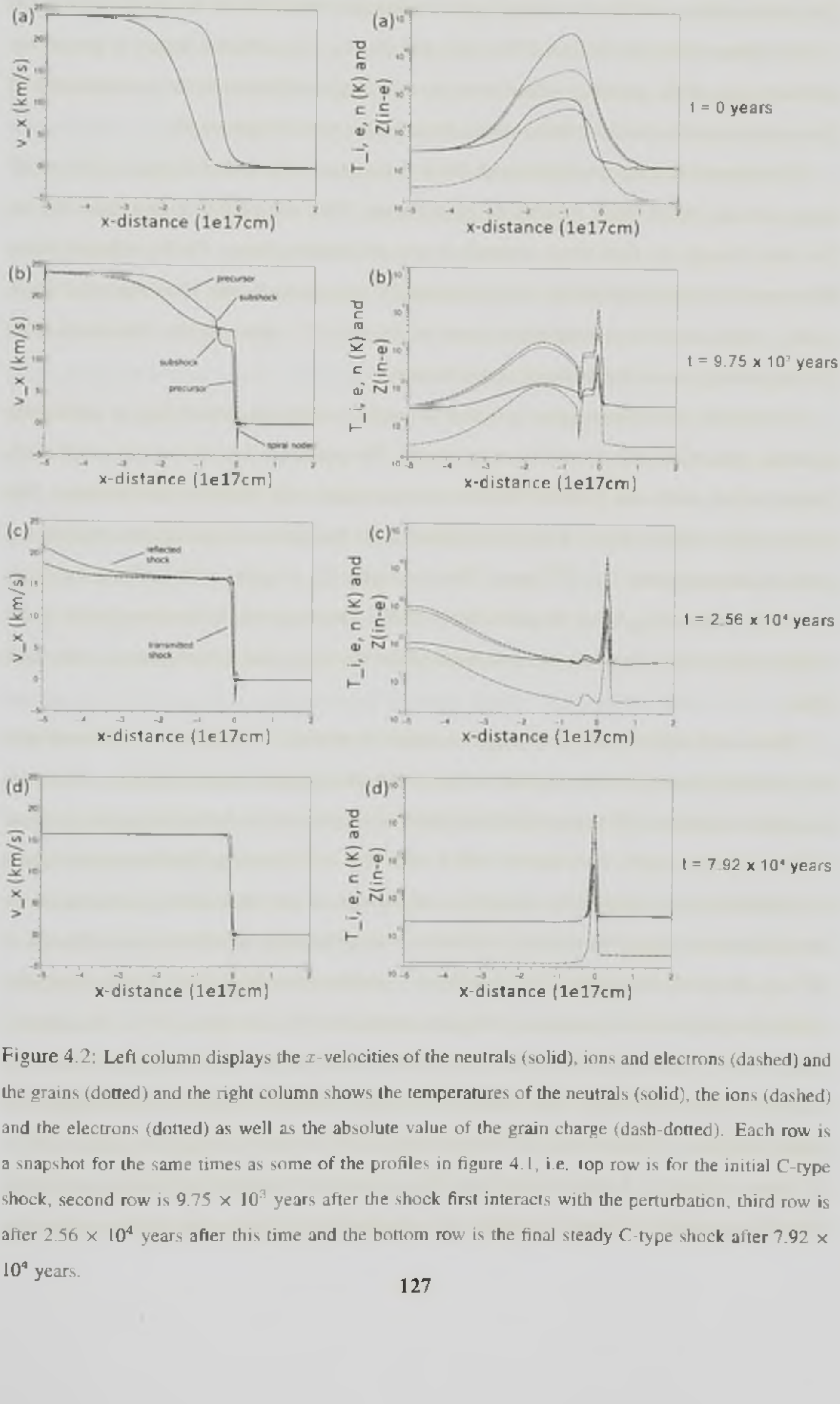

Figure 4.2: Left column displays the x-velocities of the neutrals (solid), ions and electrons (dashed) and the grains (dotted) and the right column shows the temperatures of the neutrals (solid), the ions (dashed) and the electrons (dotted) as well as the absolute value of the grain charge (dash-dotted). Each row is a snapshot for the same times as some of the profiles in figure 4.1, i.e. top row is for the initial C-type shock, second row is 9.75×10^3 years after the shock first interacts with the perturbation, third row is after 2.56×10^4 years after this time and the bottom row is the final steady C-type shock after 7.92×10^4 years.

The spiral node is a result of a change in the evolutionary trajectory of the shock in the $B_y(x)$ - $B_z(x)$ phase space (see Wardle 1998, §2.2 and §3.4.1). The affected region is around the upstream edge of the precursor where there are now large oscillations in the x-components of the ion and electron velocities (left column, bottom three rows in figure 4.2).

The timescale for the the transmitted shock to become stable and of C-type is 7.92×10^4 years from the initial shock meeting the perturbation. This corresponds to two times the ion flow time through the final shock structure or two ion crossing times. For the reflected shock this timescale is somewhat shorter. The transmitted C-type shock is only 1/8 of the initial shock width. It also has a lower propagation speed of 16.3 km s^{-1}, since shocks slow down when moving into regions of higher density and pressure.

The density and velocity plots in figures 4.1 and 4.2 show the neutral flow in sufficiently upstream parts of the precursor to be quasi-steady. The precursor does show some small oscillations in both width and gradient but these are associated with numerical uncertainties. The quasi-steady evolution does not start immediately after the shock and perturbation interact, but rather commences after 7×10^3 years. This is roughly $(L_s + L_p)/v_s$ with L_s being the original shock width and L_p being the perturbation width. This timescale is therefore known as the adaption phase and represents the time required for the shock and perturbation to cross each other.

Shocks with differing initial propagation speeds or moving into regions with different density contrasts have behaviours similar to that of the model shock described above. However, the relative strengths of the transmitted and reflected shocks vary as do the timescales for those shocks to become steady. For instance, with a lower (but still increasing) density contrast across the perturbation, the shock slows down less and the ratio of the transmitted to reflected shock strength becomes larger. For a density contrast of 3 which becomes manifested over a distance of 10^{17} cm, the shock slows from 25 to 21.25 km s^{-1} and the transmitted shock is only marginally weaker than the initial C-type shock, with peak temperatures of a few times 10^4 K. The adaption phase is lower because the transmitted shock travels faster so the shock and perturbation take less time to cross each other. This means that less time is needed to adjust to the change in upstream conditions. The timescale for the transmitted shock to become steady also falls to 6.02×10^4 years, or about 1.15 ion crossing times. This is because the transmitted shock moves faster than with a contrast of 10 and it broadens by a smaller factor ensuring that the time to become

steady falls. The post-shock density behind the transmitted shock is now closer to that behind the original C-type shock so the reflected shock is weaker. The peak temperature in the reflected shock is now only $\sim$ 300 K rather than a few times 10^3 K for a density contrast of 10. This temperature is below the threshold for electron cooling (see §2.5.3) so the ions and electrons have similar temperatures in the reflected shock. Furthermore, the grain-neutral relative speed scales with temperature and is too low in the reflected shock ($|\mathrm{v}_g\text{-}\mathrm{v}_n| < 2$ km s^{-1}) for even grain mantle sputtering to be important (see discussion in §4.5).

A simulation was also completed for a density contrast of 10 (also manifested over 10^{17} cm) and a shock speed of 6 km s^{-1}. The initial shock is therefore relatively weak ($\mathrm{M}_A \approx 3$). While strong fast-mode shocks considerably heat the incoming gas, weak fast-mode shocks do not. At this shock speed, the peak temperatures in the original shock are below 10^3 K and those in the transmitted and reflected shocks are even lower (400 and 80 K respectively). Though both are lower, this ratio of temperatures is similar to the 25 km s^{-1} case. Because of the low temperatures, the grains do not become highly charged and their Hall parameter is of the order of unity. They therefore move at different speeds to the other fluids throughout much of the shock. The grain-neutral drift speed remains small ($<<$ 1 km s^{-1}) so grain sputtering will not occur. Variations in the transmitted shock structure disappear after 9.20×10^4 years or about one ion shock crossing time and the shock becomes steady. The adaption phase is now longer than the 25 km s^{-1} case because the shock and perturbation cross each other more slowly. The time to become stable is also longer. This is because the ratio of the transmitted to original shock speeds is smaller than the ratio of new to original shock widths. This demands more time for the flow to become steady.

An interesting difference from the strong fast-mode case is that the transmitted shock width is not much smaller than the original C-type shock width. The ratio of the shock widths is 0.62. This is to be expected since the fractional ionization does not change much across the density perturbation, so from equation (1.23), the shocks should have similar widths. Another difference in the weak fast-mode case is that the shock trajectory through the $\mathrm{B}_y(\mathrm{x})$ - $\mathrm{B}_z(\mathrm{x})$ phase space no longer has a spiral node. At this shock speed the grains are not important charge carriers so the Hall conductivity remains well below the Pedersen conductivity. Field rotation is minimised and the propagation of MHD waves in the upstream region are no longer modified. Oscillations in the charged fluid velocities are now therefore absent at the upstream edge of the precursor.

4.4.2 Perturbation of decreasing density

In this model, a 25 km s^{-1} C-type shock propagates out of a dense region with $n_H = 10^5$ cm^{-3} into a more diffuse one with $n_H = 10^4$ cm^{-3}. This will occur whenever the molecular outflow associated with a YSO leaves the dense envelope immediately surrounding the protostar driving it and moves into a more diffuse molecular cloud region. The density contrast in this case is 0.1 but the length scale for the decrease is still 10^{17} cm. Note that the final shock structures in figure 4.1 are similar to the initial structures here (figure 4.3). Many features of the interaction between the shock and the inhomogeneity are reversed from §4.4.1. As a shock moves down the gradient into the lower density region, it speeds up. The final steady C-type shock in the lower density region is also broader (see figure 4.4). Furthermore, a spiral node is present in the original shock but disappears during the shock-clump interaction. Because the perturbation represents a reduction in the upstream density, a rarefaction wave is reflected into the post-shock gas to bridge the gap between the post-shock flow of the newly transmitted shock and that far downstream. This rarefaction wave is a slow-mode wave since the magnetic field decreases across the structure. Like for multifluid shocks, multifluid rarefaction waves also introduce ion-neutral drifts. However the relative speeds between the charged and neutral fluids in the rarefaction wave are negligible compared to those in the transmitted shock (see figure 4.4b).

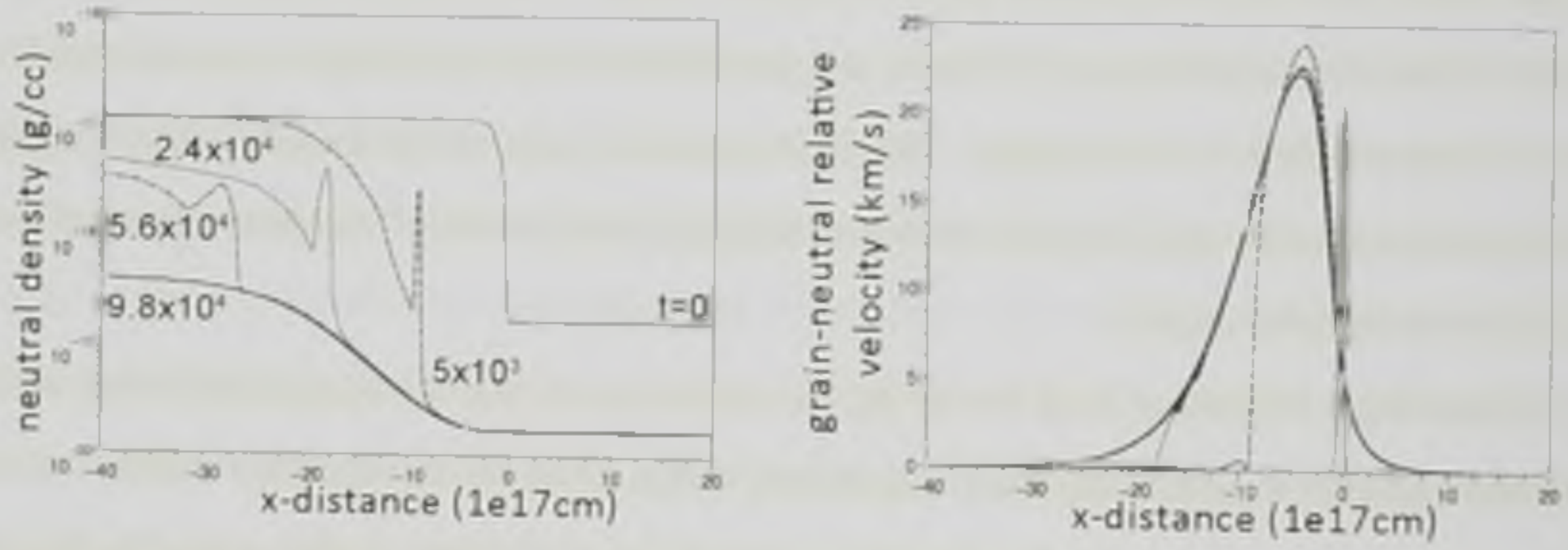

Figure 4.3: Similar to figure 4.1, but for a 25 km s^{-1} shock interacting with a semi finite density perturbation which falls from $n_{\rm H} = 10^5 {\rm cm}^{-3}$ to $n_{\rm H} = 10^4 {\rm cm}^{-3}$. The profiles for the initial C-type shock are given by the thin solid lines, the dashed lines show the shock structure 5×10^3 years after the shock first interacts with the perturbation. The dotted and dash dotted lines are 2.40×10^4 and 5.59×10^4 years after the first intraction respectively. The thick solid lines show the final steady C-type shock structure obtained (after 9.8×10^4 years).

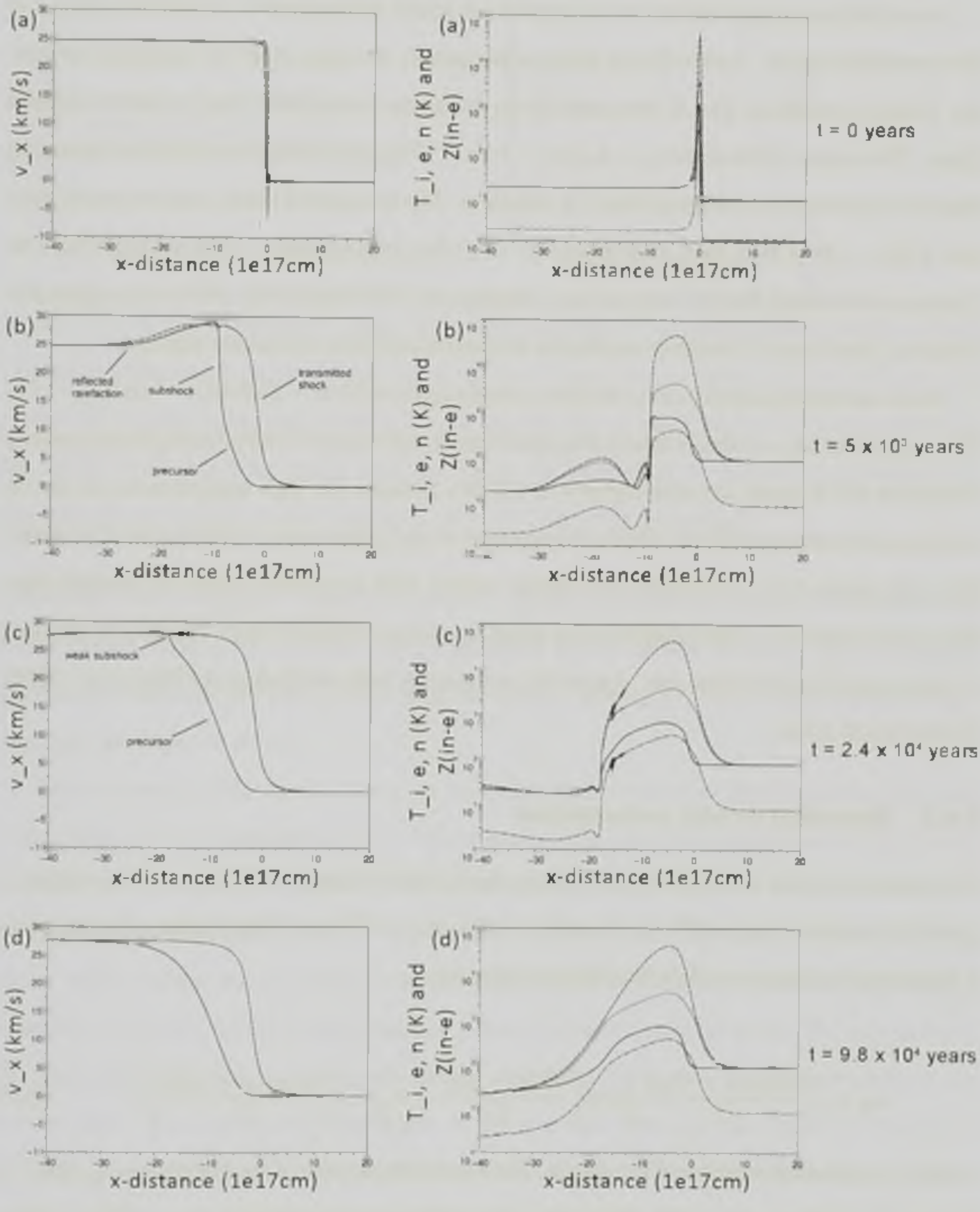

Figure 4.4: The columns are as per figure 4.2, but for the same shock as figure 4.3, i.e. the upstream density falls from $n_{\rm H} = 10^5 {\rm cm}^{-3}$ to $n_{\rm H} = 10^4 {\rm cm}^{-3}$. The top row shows the initial C-type shock, second row is 5×10^3 years after the shock first interacts with the perturbation, third row is after 2.4×10^4 years after this time and the bottom row is the final steady C-type shock after 9.8×10^4 years.

As in the increasing density case, a neutral sub-shock and precursor are initially present in the transmitted shock. A new C-type shock subsequently develops from the expanding precursor. Like the models in §4.4.1, the quasi-steady evolution commences after an initial adaption phase. This is now of the order $(L_s + L_p)/v_s = 1.70 \times 10^3$ years which is less than the increasing density case because the original shock is narrower. The transmitted shock reaches steady state after 9.80×10^4 years which corresponds to ~ 1.2 ion crossing times. This is longer than the analogous increasing density case because although the shock speeds up, the shock region also broadens. More time is therefore needed for the post-shock flow to become steady.

In the decreasing density case, the shock speeds up from 25 to ~ 28.6 km s^{-1} (or $M_A \sim 13$). The transmitted wave is thus a strong fast-mode shock and the gas is heated to high temperatures within the shock (peak ion temperatures of 10^5 K). Because the high temperatures are due to collisions between the different fluids, the ion-neutral and grain-neutral drift speeds also remain high (see figure 4.3). In addition, the spatial regions with large drift speeds are broader than the case in figure 4.1, which suggests that grain sputtering would be more effective in the final C-type shock than the initial one. Again this in harmony with the findings of May et al. (2000) for this shock speed.

4.4.3 Sinusoidal density perturbation

The final case is the interaction of a C-type shock with a clump. The shape of the clump is given by a cosine wave with a wavelength (λ) of 1.46×10^{17} cm. The hydrogen abundance as a function of x-distance within the clump is given by:

$$n_H = \left(\frac{n_{H,max} - n_{H,0}}{2}\right)\cos\left(\frac{2\pi(x - x_0)}{\lambda} - \pi\right) + \left(\frac{n_{H,max} + n_{H,0}}{2}\right), \qquad (4.3)$$

where x_0 is the start position of the clump. The maximum density of the clump ($n_{H,max}$) is 2×10^5 cm^{-3} which is twenty times higher than the original upstream density ($n_{H,0}$). These values are representative of the clump parameters measured by Tafalla et al. (2004).

Unfortunately the evolution of the shock structure cannot be described using a combination of the model results from §4.4.1 and §4.4.2. The initial behaviour of the shock as it moves up the density gradient is similar to the early evolution in figure 4.1.

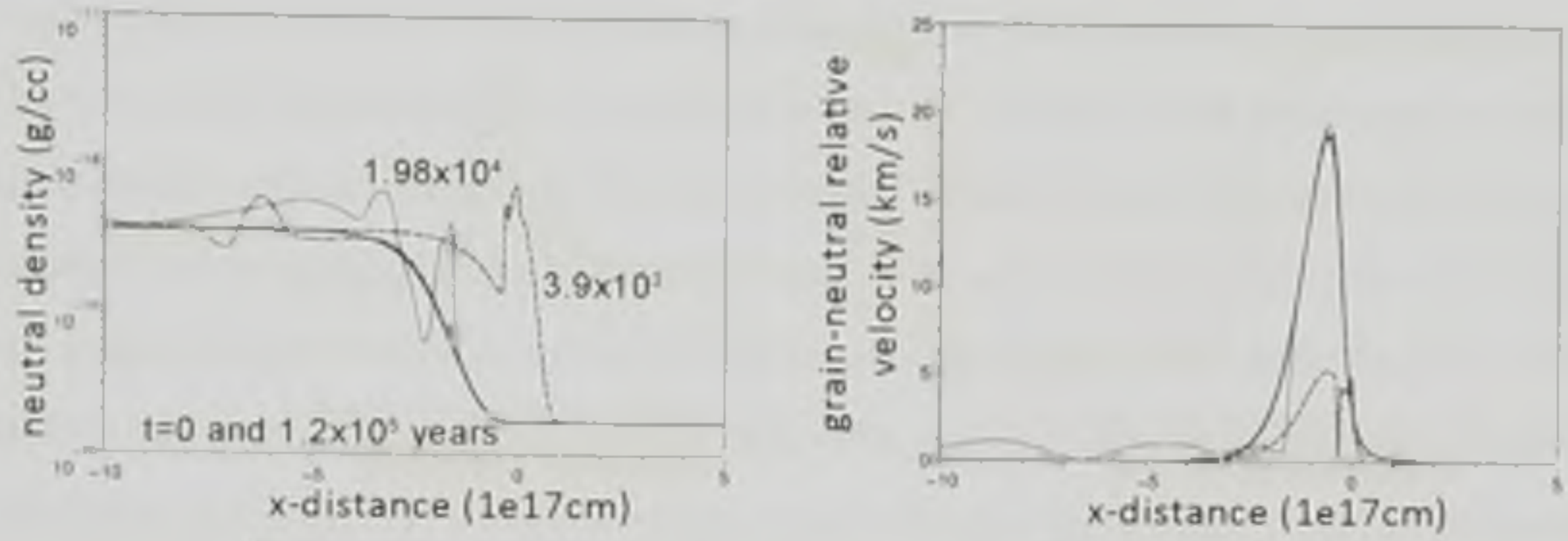

Figure 4.5: Similar to figures 4.1 and 4.3, but for a 25 km s^{-1} shock interacting with a clump which has a maximum density of $n_H = 2 \times 10^5$ cm^{-3} and a total width of 1.46×10^{17} cm. The profiles for the initial and final (after 1.2×10^5 years) C-type shock are given by the solid lines, the dashed lines shows the shock structure 3.9×10^3 years after the shock first interacts with the perturbation and the dotted lines are 1.98×10^4 after that interaction.

The dashed lines in figures 4.5 and the profiles in figure 4.6b show that reflected and transmitted J-type shocks form as the original shock propagates up the density gradient. The transmitted shock slows and narrows and a spiral node develops in the $B_y(x)$ - $B_z(x)$ phase space as happened in the model of §4.4.1.

The evolution of the shock during its transition back to the low density region does not resemble the model described in §4.4.2. This is because the shock transmitted during the density increase has had insufficient time to become steady and C-type before it meets the back side of the clump (the adaption phase to the density rise alone takes this long). Rather, a J-type shock with precursor moves down the density gradient. As this shock responds to the changing upstream conditions during its own adaption phase, it speeds up and broadens. The precursor of the J-type shock transmitted during the density rise develops another neutral sub-shock as the density falls. This sub-shock is analogous to the one that formed in the steady C-type shock in §4.4.2 (detailed in figure 4.3). Therefore the shock structure now simultaneously contains two neutral sub-shocks (see figure 4.6c). Interestingly, the velocities of the neutral and charged flows do not converge between the secondary and primary sub-shocks. This is to be expected since those relative velocities were non-zero in the precursor of the J-type shock transmitted by the interaction with the rising density portion of the clump.

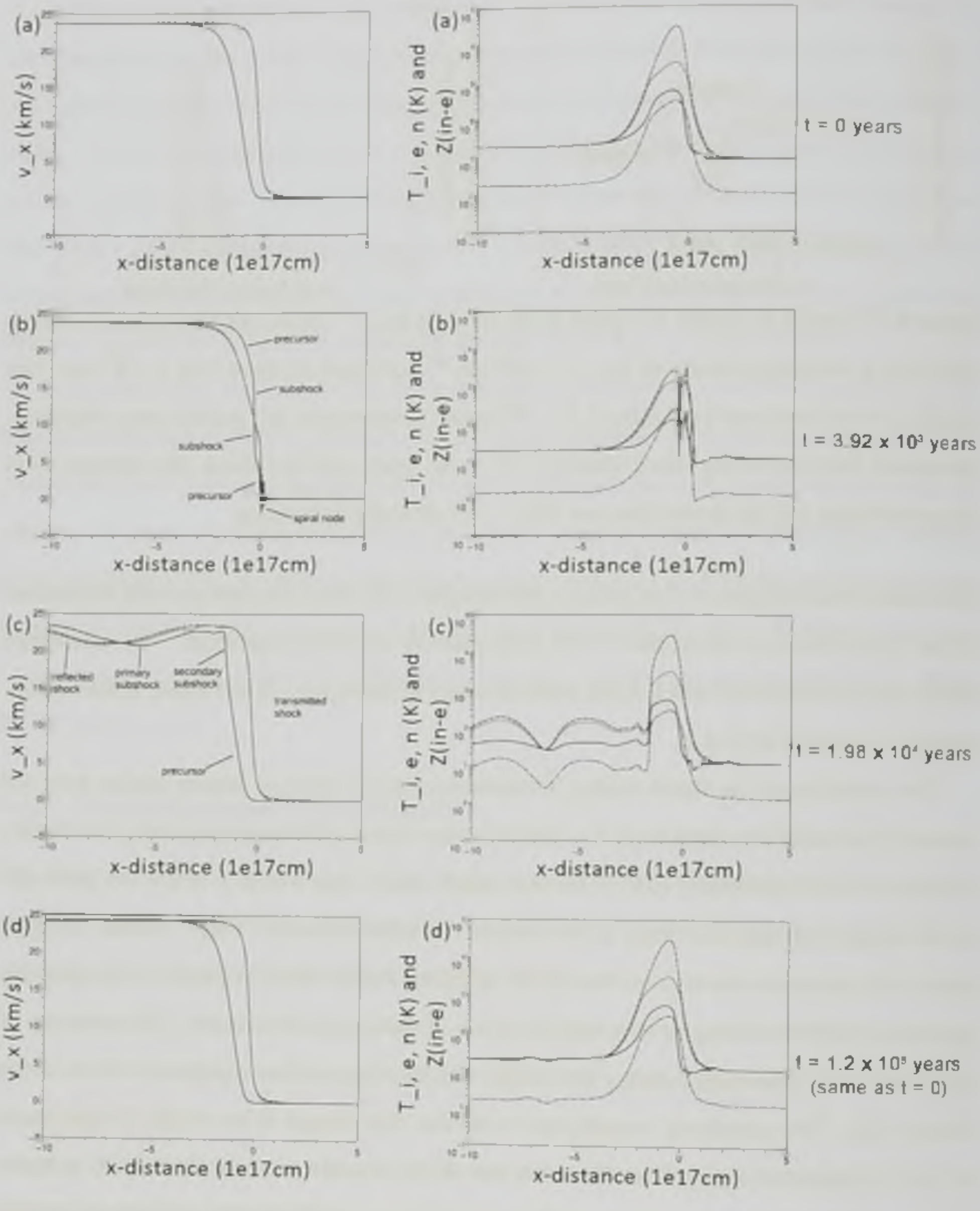

Figure 4.6: The columns are as per figures 4.2 and 4.4, but for the same shock as in figure 4.5, i.e. the upstream density follows a sinusoidal profile given by equation (4.3). The top row shows the initial C-type shock, second row is 3.9×10^3 years after the shock first interacts with the perturbation, third row is after 1.98×10^4 years after this time and the bottom row is the final steady C-type shock after 1.2×10^5 years.

Although the relative velocities between the primary and secondary sub-shocks are well below the sputtering thresholds derived by Caselli et al. (1997), other initial parameters (e.g. higher shock speeds or clumps of lower densities than the initial upstream region) may yield drift velocities that are sufficient to induce sputtering of the mantles. This sputtering would then occur over a spatial region which is larger than the initial shock width. The drift velocities steadily shrink as both sub-shocks subsequently weaken. The primary J-type sub-shock disappears after a few times 10^4 years and simultaneously, a steady C-type shock forms from the precursor of the secondary sub-shock (see figure 4.5). The timescale for the steady C-type shock to arise is 1.2×10^5 years or 1.2 ion crossing times. This time is longer than either the rising or falling density cases but is a little lower than the sum of those timescales. It is lower because the shock transmitted by the interaction with the density rise had already begun to evolve towards steady state by the time that it met the back side of the clump. Because the initial and final flow speed and upstream density are equal, the final C-type shock is identical to the initial condition.

4.5 Summary and discussion

This chapter has presented the first time dependent simulations of oblique C-type shocks in dusty plasmas interacting with density inhomogeneities. The transient evolution of the shock structure has been studied for three types of density perturbation, i.e. increasing, decreasing and clump-like. The dependance on shock speed and density contrast has been examined for each.

When a steady C-type shock encounters a region of inhomogeneous density, it reacts to the changing upstream conditions by breaking up into multiple waves. While a transmitted J-type shock moves into or out of the denser region, either a shock or rarefaction wave is reflected and propagates in the opposite direction to the original shock. A reflected component is necessary to connect the post-shock flow of the newly transmitted shock with that of the original C-type shock. The relative strength of the transmitted and reflected components is determined by the initial shock speed and the density contrast across the perturbation. For example, a lower density contrast results in a smaller difference between the transmitted post-shock flow and that far downstream. Hence a weaker reflected component is required to bridge this difference. For the interaction with a clump, where the density rises and then decreases again, the situation becomes more complicated since the transmitted J-type shock forms a second neutral sub-shock

in its precursor. It is thus important to realise that these results predict that a range of J- and C-type shocks as well as multifluid rarefaction waves will be associated with molecular outflows propagating through inhomogeneous molecular clouds.

These models have focused on the evolution of the transmitted shocks. Such shocks are always initially J-type, containing a sub-shock in the neutral flow. They evolve back to being steady C-type shocks but with different widths and velocities. The timescale to achieve steady state is of the same order as the ion flow time through the final shock structure, i.e. about 0.5 - 1.5×10^5 years. An important consequence of such timescales is that any shock encountering density inhomogeneities more often than this will not be steady and of C-type. In that case, the shocks are J-type although some will have weak sub-shocks and are hence only marginally distinguishable from C-type shocks.

These simulations show that the final, steady C-type shock develops from a J-type shock and precursor in which sufficiently upstream parts of the precursor are steady. Such an evolution was also noted for multifluid shocks in weakly ionized dust free gases (Flower & Pineau des Forêts 1999). Following the Flower & Pineau des Forêts (1999) results, Lesaffre et al. (2004) developed a quasi-steady method to follow the evolution of multifluid shocks in a semi time dependent fashion. Their method treats an evolving, non-stationary J-type shock as a sequence of truncated C-type shocks, each of which has a neutral sub-shock at the point where the ion flow time corresponds to the age of the shock. While this approach was only validated for dustless shocks, the results presented here justify the use of such methods to study the temporal evolution of dusty shocks as was done by Gusdorf et al. (2008). However the quasi-steady approach has some limitations when applied to the interaction between a shock and a density perturbation. Firstly, this method can only be used after an early adaption phase in which the shock adjusts to the changing upstream conditions. Secondly, this approach is only valid for a steady C-type shock interacting with a density perturbation. This is because when a J-type shock meets an inhomogeneity in the flow, a second neutral sub-shock forms in its precursor. Behind this secondary shock, the velocities of the neutral and charged fluids are not the same. Such a situation, which is likely to be prevalent in the shocks associated with molecular outflows from YSOs in clumpy molecular clouds, cannot be modeled with a quasi-steady approach.

In quiescent cold clouds, silicon is largely depleted from the gas phase, being stored in the refractory cores of dust grains (see §1.1.2). Observations of SiO emission near proto-stellar

objects reveal that some of this silicon has been returned to the gas phase. This is thought to occur due to sputtering of the grains and grain-grain collisions in C-type shocks (e.g. Martin-Pintado et al. 1992 and see §1.3.5). Although these processes are not included in the current code, the changes in the grain-neutral relative velocity serves as an indication of when and where sputtering may proceed. For example, Caselli et al. (1997) found grain-neutral relative speeds of $\sim$ 10 - 15 km s^{-1} are needed for sputtering to disrupt the mantles. Likewise, May et al. (2000) report that shock speeds of at least 25 km s^{-1} are required to even weakly sputter the grain cores. For the models presented in this chapter, the threshold for core sputtering is, at best, only weakly met. Therefore, not much SiO emission is to be expected, but grain mantle sputtering should be prevalent in all models. Jiménez-Serra et al. (2008) have suggested that if the grain mantles contained a small amount of silicon, sputtering by heavy molecules such as CO could erode the mantles even in low velocity shocks and account for narrow SiO line emission observed in some young outflows (e.g. L1448-mm; Jiménez-Serra et al. 2004). Silicon erosion from the mantles would become saturated for shock velocities between 10 and 20 km s^{-1}. This implies that the SiO enhancement from mantle erosion would be saturated in all the models presented here. Furthermore, a small contribution to grain mantle sputtering is to be expected from the reflected wave components.

The following chapter develops terms to accurately account for grain mantle and core sputtering. This allows the scheme describe the return of water and SiO from the grains to the gas phase due to systematic grain-neutral streaming. A more comprehensive chemical network will also be required in order to accurately calculate the abundances of the heavier molecules thought to dominate the sputtering process near threshold.

Chapter 5

Time dependent models of chemistry and sputtering in oblique C-type shocks

5.1 Summary

The gas phase abundances of silicon bearing species are observed to be enhanced by factors of up to 10^6 near the outflows associated with some low mass YSOs. The enhancement is thought to come about due the sputtering of the grains in high energy impacts with neutral atoms and molecules. Terms were added to the scheme of Falle (2003) to describe a more comprehensive chemical network and the sputtering of the icy mantles and refractory cores due to bombardment by neutrals. Simulations were then undertaken for initially J-type shocks which evolve into steady C-type shocks. The onset of important chemical reactions including the gas phase conversion of atomic oxygen into water was found to be retarded until higher shock speeds with lower upstream densities due to lower collision rates and temperatures. The same effect was noted for the formation of metallic molecular ion species. The threshold shock speeds for each material were noted as were any differences arising from differences in the upstream density. At each shock speed above threshold, the fraction of material ejected and the contribution to the sputtered species gas phase abundance were also noted. Given the differences between the models, these values broadly agreed with previous findings. They suggest that shocks propagating through the highest density regions of molecular clouds are unable to reproduce the enhancements of SiO observed in some outflows (e.g. L1448-mm). Lower upstream

densities are required to reproduce those findings. In addition, an important dependence of the gas phase enhancement due to sputtering on the alignment between the shock normal and upstream magnetic field is noted. This results in order of magnitude increases in the gas phase SiO abundance behind shocks whose speeds are close to the sputtering threshold, just by varying the angle between shock and upstream field by as little as 15°. This angular dependence of the sputtered SiO fraction is likely to be important in any bow shock and may result in distinct SiO components with different fractional abundances and velocities.

5.2 Introduction

Chapter 3 demonstrated how the presence of dust may significantly affect the structure of shock waves propagating through the densest regions of weakly ionized molecular cloud cores. Dust grains carry an effective charge which predominantly depends on the temperature and abundance of free electrons (Spitzer 1978; Havnes et al. 1987 and see equation 3.17 in §3.4.1). When sufficiently charged, the grains switch from being advected with the neutral flow to having their motions dominated by Lorentz forces and thus moving with the other charged species. Upon decoupling from the neutrals in dense enough regions, frequent grain-neutral collisions can result in dust velocities between those of the neutral components and the other charged fluids (Pilipp et al. 1990; Pilipp & Hartquist 1994; Wardle 1998). This only applies to large grains since small grains remain well coupled to the ions and electrons throughout all shocks of interest due to their larger Hall parameters (equation 1.27), themselves a result of smaller collision cross-sections (see §3.4). Dust grains carry an average negative charge even in quiescent regions due to the higher kinetic speeds of electrons (Flower et al. 2007 and see §1.1.2) but ions still occasionally collide with and stick to them. Such ions recombine with free electrons resident on the grains surface with the products being ejected back into the gas phase. Grain surface chemistry therefore plays in important role in determining the fractional ionization and chemical abundances in any gas where dust is present in significant concentrations (e.g. Pilipp et al. 1990; Caselli et al. 1997 and see §1.3.2).

Chapter 4 showed that when a shock propagates through an inhomogeneous upstream medium and interacts with clumps, it will break up into multiple transmitted and reflected wave components separated by contact discontinuities. The fact that GMCs contain substructure at all scales

makes it unlikely that any shocks propagating through them are steady (Mikami et al. 1992; Lefloch et al. 1998; Jørgensen et al. 2004 and see §1.2.3). It was shown that in some circumstances the break up of the shock may result in the grains and neutrals possessing different velocities over extended regions (see §4.4.3).

In addition to providing a surface to catalyse chemical reactions, dust grains themselves may be processed by the passage of a shock wave (e.g. Tielens et al. 1994; Draine 1995; Caselli et al. 1997 and see §1.3.5). For this to occur dust grains of different sizes and neutrals must possess relative velocities and thus stream through each other. Since the neutral component comprises the vast majority of a flows mass, whenever such streaming velocities exist grain-neutral collisions are common. If sufficiently energetic, these collisions will dislodge bonded grain material and return it to the gas phase in a process known as sputtering (e.g. Draine & Salpeter 1979; Field et al. 1997; May et al. 2000). Sputtering has been invoked to explain the observation of strongly refractory species such as SiO, Ca and Fe near some YSOs, with abundances enhanced by factors of over 10^6 (e.g. Martin-Pintado et al. 1992; Jiménez-Serra et al. 2004 and see §1.3.5). The return of solid state material to the gas phase alters the relative chemical abundances. Some of the species returned in this way (such as water) are important coolants so their presence affects the radiative cooling and neutral temperature profile. Sputtering may also change the abundance and nature of the grains themselves. This can have important consequences for shock dynamics, especially when dust provides the dominant source of friction on the neutral flow (see analysis in chapter 3).

Previous theoretical investigations into the dynamics of grains in C-type shocks associated with low mass YSO outflows have either concentrated on the steady state conditions (e.g. Flower & Pineau des Forets 1994; Caselli et al. 1997; May et al. 2000; Jiménez-Serra et al. 2008), introduced a pseudo time-dependence based on the assumption that the flow will remain steady until steady state is achieved (e.g. Gusdorf et al. 2008 and see §4.5) or have included time dependence but limited the study to perpendicular shocks (Ciolek & Roberge 2002). This chapter represents the first truly time dependent simulations of oblique C-type shocks in dusty media. It includes a rigorous treatment of grain dynamics to properly evaluate the grain-neutral drift speeds, a self consistent calculation of the chemical reactions occurring through the shock to properly evaluate the abundances of the sputtering projectiles as well as the thermal and ionization structures. Terms to describe the non-thermal sputtering process are also included.

Having developed an enhanced chemical network and terms to describe the sputtering of dust due to systematic grain-neutral streaming, time dependent MHD simulations are utilised to investigate how the relative chemical abundances due to gas phase reactions and grain surface recombinations as well as sputtering depend on the shock speed. The threshold shock speeds required for sputtering of the icy mantles and grain cores are also determined. The final (steady) C-type shock structures are used for this purpose. The results presented here can therefore be compared with previous studies; e.g. Flower & Pineau des Forets (1995); Caselli et al. (1997); May et al. (2000) and Jiménez-Serra et al. (2008).

Section 5.3 deals with the chemistry, including a discussion of the factors which motivate the inclusion of a more comprehensive chemical network, a description of that network, the form of the rate equations for each chemical species and how those rate equations are implemented into the existing code. Section 5.4 describes the sputtering process, including a mathematical treatment of the sputtering yields and rates both for ice mantles and silicate cores, together with the numerical tests undertaken to confirm that the sputtering treatment is reliable. Section 5.5 details the methods used to obtain the desired initial conditions and section 5.6 contains information about the parameter space explored by the simulations, as well as considerations relating to grid size and numerical resolution. The results of these simulations are given in section 5.7, where section 5.7.1 is devoted to chemistry and section 5.7.2 to sputtering. The results are discussed in section 5.7 and section 5.8 consists of a summary and conclusions.

5.3 Chemistry

The ISM consists of a dynamic and evolving system of gas and dust where old stars eject the heavy elements produced from fusion reactions during their later evolutionary stages together with dust grains and molecules formed in their cool outer atmospheres. Stellar winds, planetary nebulae and supernovae mediate this enrichment, the components of which are essential to create the GMCs that later form within the potential wells of galactic spiral arms. The physics and chemistry of quiescent molecular clouds was discussed in §1.1.1 - §1.2.1, the chemistry occuring in shocks formed §1.3.4 and the processing of cloud material in the outflows associated with low mass YSOs was briefly described in §1.2.3 and §1.3.5.

Since the detection of the first molecule in space early in the twentieth century (the methyli-

dyne radical CH; Swings & Rosenfeld 1937), more than 120 species have been observed. Complex reaction networks were devised to explain the relative abundances of various species as well as to predict new ones (Millar et al. 1997). Molecular observations can be as simple as the measurement of the strength of radiation from a single transition of one species, or may involve the comparison of several emission lines from a group of molecules. Both provide information about the physical conditions in the emission region (see figure 1.2 in §1.1.1).

In the preceding chapters, the source terms included a limited chemical network. The ion fluid was assumed to comprise equally of one metallic and one molecular ion species (Mg^+ and HCO^+ respectively) throughout the shock. At a given temperature, metallic ions radiatively recombine with electrons at lower rates than the dissociative recombination of molecular ions (see §2.5.1 and §4.3.1). The total recombination rate per unit volume determines the overall ion abundance so the inclusion of at least one metallic and one molecular ion species is necessary for a reliable calculation of the fractional ionization. Since the aim of this chapter is to model the sputtering of grains due to impacts by neutral atomic and molecular species, the initial step must be to include a more comprehensive chemical network. As well as providing a more accurate calculation of the fractional ionization and prevalence of coolants, such a network is also able to accurately predict the abundances of the chemical species which act as sputtering projectiles. These abundances are desirable since the efficiency of the sputtering process strongly depends on the mass of impacting particle (see §5.4). For consistency, the initial chemical abundances are kept the same as in previous chapters (see §5.5) but the inclusion of additional species permits chemistry to occur, even in the upstream region. The upstream chemical species are then further processed during their passage through the shock.

Like for the models described in previous chapters, Mg^+ and HCO^+ each account for half of the calculated initial ion abundance. Mg^+ remains the only metallic ion species in the model, but H_3^+, H_3O^+ (molecular ions) and MgH^+ (a metallic molecular ion) are now also included. All ions are assumed to be only singly ionized so they, together with electrons, respond to Lorentz forces in the shock by moving at the same bulk velocity, even though individual particles in the fluids possess different kinetic speeds. Since ionising photons are absorbed near the outer edge of a cloud, it is reasonable to assume that all ionizations in the interior are caused by cosmic rays. Furthermore, because molecular hydrogen is by far the most abundant species in such regions, it is also reasonable to assume that cosmic rays only collide with H_2 (e.g. Williams et

al. 1998 and see §1.1.3.1). These ionizations produce H_2^+ which very quickly reacts with H_2 to yield H_3^+. H_3^+ readily reacts with either oxygen or any water which is present, producing H_3O^+. H_3^+ is therefore included in the model to represent the intermediate step between a cosmic ray ionization of H_2 and the production of a molecular ion.

Mg^+ represents all metals. As well as being initially present, it may be formed in ion-neutral reactions between neutral magnesium and molecular ions and can be efficiently converted into MgH^+ in endothermic reactions. These reactions become prevalent in faster C-type shocks due to higher temperatures and non-zero ion-neutral streaming speeds. Metallic molecular ions recombine with electrons more efficiently than either metallic or molecular ions, both in the gas phase and on grain surfaces. This destruction commences as soon as the post-shock temperature begins to fall. The existence and abundance of MgH^+ would therefore infer the presence and strength of a C-type shock if it could be detected. Its formation also has important consequences for the fractional ionisaton (see §5.3.2 for further details).

5.3.1 Chemical Network

The new chemical network is detailed in table 5.1. It is adaptated from Pilipp et al. (1990) but adopts newer rate coefficients where available.

This chemical model assumes that every cosmic ray ionization leads to the production of a molecular ion. Molecular ions may be converted into metallic ions in ion-neutral reactions, with rates that only depend on to the abundances of the species involved and a constant (e.g. reaction 7). They may also be neutralised in dissociative and radiative recombinations, the rates of which depend on the abundances of both reactants and the inverse of the electron temperature (e.g. reaction 6). Metallic ions produce metallic molecular ions in association reactions (reaction 12) and are neutralised in radiative recombinations (reaction 10). All types of ions may be involved in recombinations on grain surfaces (e.g. reaction 14). These proceed at rates which depend on the ion-grain current and the abundances of the ion and grain species.

Molecular hydrogen, atomic oxygen, magnesium, carbon monoxide and water are the additional neutral species involved in the reactions in table 5.1. In addition, molecular hydrogen, atomic oxygen, carbon monoxide and water are all efficient coolants, so a better determination of their abundances improves the accuracy of the calculation of the shocks thermal structure.

Num.	Reaction	Rate Coefficient (k) ($cm^3\ s^{-1}$)	Ref.
1	$H_2 + CR \rightarrow H_3^+ + e + CR$	$3 \times 10^{-17}\ s^{-1}$ *$_1$	1
2	$H_3^+ + CO \rightarrow HCO^+ + H_2$	1.7×10^{-9}	1, 2, 3
3	$H_3^+ + H_2O \rightarrow H_3O^+ + H_2$	5.9×10^{-9}	2, 3
4	$H_3^+ + grain^- \rightarrow H_2 + H + grain$	$(\Gamma_{ig} + \Gamma_{is})(n(H_3^+)/n_i)$	4
5	$H_3^+ + O \rightarrow H_3O^+$	8.4×10^{-10}	2, 3
6	$HCO^+ + e \rightarrow H + CO$	$2.76 \times 10^{-7}(T_e/300)^{-0.64}$	3
7	$HCO^+ + Mg \rightarrow H + CO + Mg^+$	2.9×10^{-9}	2
8	$HCO^+ + H_2O \rightarrow H_3O^+ + CO$	2.5×10^{-9}	2, 3
9	$HCO^+ + grain^- \rightarrow H + CO + grain$	$(\Gamma_{ig} + \Gamma_{is})(n(HCO^+)/n_i)$	4
10	$Mg^+ + e \rightarrow Mg + h\nu$	$2.8 \times 10^{-12}(T_e/300)^{-0.86}$	1, 2
11	$Mg^+ + grain^- \rightarrow Mg + grain$	$(\Gamma_{ig} + \Gamma_{is})(n(Mg^+)/n_i)$	4
12	$Mg^+ + H_2 \rightarrow MgH^+ + H$	$3.0 \times 10^{-10}\exp(-27854/T_{eff})$ *$_2$	1
13	$MgH^+ + e \rightarrow Mg + H$	$1.1 \times 10^{-7}(T_e/300)^{-0.5}$	1
14	$MgH^+ + grain^- \rightarrow Mg + H + grain$	$(\Gamma_{ig} + \Gamma_{is})(n(MgH^+)/n_i)$	4
15	$H_3O^+ + e \rightarrow H_2O + H$	$3.29 \times 10^{-7}(T_e/300)^{-0.5}$ *$_3$	2, 3
16	$H_3O^+ + Mg \rightarrow H_2O + Mg^+ + H$	1.8×10^{-9}	1
17	$H_3O^+ + grain^- \rightarrow H_2O + H + grain$	$(\Gamma_{ig} + \Gamma_{is})(n(H_3O^+)/n_i)$	4
18	$O + H_2 \rightarrow H_2O$	$3.14 \times 10^{-13}(T_n/300)^{2.7}\exp(-3150/T_n)$ *$_4$	2, 3

Table 5.1: The enhanced chemical network. The column titled "Num." lists the reaction number, that labelled "Reaction" details the reaction partners and products for each, "Rate coefficient" lists the adopted coefficients. In the grain surface reactions (4, 9, 11, 14 and 17) Γ_{ig} and Γ_{is} represent the current of ions (subscript i) onto large and small grains (subscripts g and s) respectively. "Ref." gives the source of each coefficient: Those denoted 1 are taken from Pilipp et al. (1990), 2 are from the UDFA database, 3 signifies Guillet et al. (2009) as the source and 4 that the value is output from another routine in the code. Rate coefficients with numbered asterisks are discussed below:

*$_1$: Reaction 1 is an amalgamation of two reactions; $H_2 + CR \rightarrow H_2^+ + e + CR$ and $H_2^+ + H_2 \rightarrow H_3^+ + H$. CR denotes a cosmic ray particle as the reaction partner. The adopted coefficient is that of the first reaction since the rate coefficient of the second reaction is so much higher that the transfer of H_2^+ to H_3^+ can be considered to occur instantaneously.

*$_2$: T_{eff} in the rate coefficient of reaction 12 defines a weighted kinetic temperature at the ion-neutral

drift speed and is given by Flower et al. (1985) as:

$$T_{eff} = (\frac{m_i T_n + m_n T_i}{m_i + m_n}) + \frac{2}{6k_b}(\frac{m_i m_n}{m_i + m_n})(u_i - u_n)^2, \quad (5.1)$$

where m_i, u_i and T_i are ion mass, x-velocity and temperature, m_n, u_n and T_n are neutral mass, x-velocity and temperature and k_b is Boltzmann's constant.

$*_3$: Reaction 15 is an amalgamation of:

$H_3O^+ + e \rightarrow OH + H_2$ ($k = 6.02 \times 10^{-8}(T_e/300)^{-0.5}$),

$H_3O^+ + e \rightarrow OH + H + H$ ($k = 2.58 \times 10^{-7}(T_e/300)^{-0.5}$) and

$H_3O^+ + e \rightarrow H_2O + H$ ($k = 1.08 \times 10^{-8}(T_e/300)^{-0.5}$).

The effective rate coefficient employed is the average of those for the three reactions above. This means that OH is not required as a separate species. This is justified since the OH produced in the first two reactions will quickly react with H_2 to yield H_2O (see $*_4$).

$*_4$: Reaction 18 is also an amalgamation of two reactions; $O + H_2 \rightarrow OH + H$ and $OH + H_2 \rightarrow H_2O + H$. The coefficient adopted is that of the first (slower) of the two. Although this reaction is very fast in the shock front, it simply converts much of the available oxygen to water. It thus affects the cooling rate but not the fractional ionization. Consequently a limit on this reaction rate is not required (see §5.3.4) since in the regime of interest the shock structure is more strongly determined by the ionization structure and grain dynamics than the thermal structure of the neutrals (as was discussed in §4.3.1).

With the addition of silicon oxide, which is produced in grain core sputtering and assumed to be inert, but considered as a potential projectile when in the gas phase (see §5.4), chemistry and sputtering can be modeled.

5.3.2 Shock chemistry predicted by the model

The outflows associated with low mass YSOs modeled in this project occur when the protostar is present but still embedded within its nascent cloud core (a class 0 object). The star formation process and the resultant outflows were discussed in §1.2.2 and §1.2.3.

As noted in chapters 3 and 4, for simulations at a shock speed of 25 km s^{-1}, the electrons attain a maximum temperature of a few thousand degrees Kelvin whereas the neutrals reach a few hundred degrees Kelvin. These temperatures are insufficient to dissociate molecular hydrogen (e.g. Roberge & Dalgarno 1982). When molecular dissociation is suppressed, most of the shock energy is dissipated as rotovibrational transitions of H_2, neutral oxygen [OI] 63 μm fine structure and molecular (CO, and H_2O) rotational and vibrational lines (e.g. Hartquist et al. 1980;

Hollenbach & McKee 1979; Neufeld & Melnick 1987). Molecules possess energy levels which are more closely spaced and at lower energies than atoms. This allows molecular rotational and vibrational transitions to provide a more effective cooling mechanism than atomic transitions over a wide range of physical conditions (see §1.1.3.2 and §1.3.4). In addition to facilitating efficient cooling in the shock region, many molecules become involved in further chemical reactions during their passage through a C-type shock and these may yield more complex species.

Previous simulations have demonstrated that the grains become highly negatively charged whilst the temperature remains low enough to preclude heavy collisional ionization. In such circumstances dust can become an important carrier of negative charge and even provide the main source of drag on the neutrals (see §1.3.2 and §2.2). Any ions colliding with negative grains will recombine with electrons on their surfaces. Such events must be accurately modeled for the chemical network to be complete (reactions 4, 9, 11, 14 and 17), since the currents of ions onto negative grains become high in many C-type shocks of interest (see below) and without such grain surface recombinations the calculation of the gas phase fractional ionization is dubious.

The reactions included in table 5.1 are those between the species which are favoured by the conditions in C-type shocks. Reactions which form efficient neutral coolants (H_2O) are important. Likewise, those reactions which affect the factional ionization by either re-combining ions and electrons or forming the more stable metallic atomic ion species Mg^+ are especially important. As noted above, the moderately higher temperatures obtained in C-type shock fronts inhibit molecular dissociation whilst permitting endothermic reactions to proceed. This combination ensures that efficient post-shock cooling is maintained and chemical diversity is enriched.

The evolution of the initial abundances occurs through both gas phase reactions and grain surface recombinations. Which reactions are viable is determined by the density and temperature conditions inside the shock. Shocks always increase the gas temperature and density so all reactions except gas phase electron recombinations will occur more frequently. Even before any simulations are undertaken, some broad predictions about the expected chemistry can be made.

Both dissociative and radiative electron recombinations in the gas phase have rate coefficients which are inversely proportional to the electron temperature in this chemical model, so these reactions are supressed at high temperatures and are unimportant inside shocks. However they remain very important in the cold pre- and post-shock regions.

As noted above, ions and electrons may also recombine on grain surfaces. Whilst gas phase radiative and dissociative recombinations are suppressed at high temperatures, those on grain surfaces become more prevalent because the currents of ions and electrons onto grains grow with temperature and relative speed. These both increase in C-type shocks. Although the grains become highly negatively charged due to the higher kinetic speeds of electrons (see §1.1.2 and chapter 3), the high ion temperatures, significant ion-neutral drift speeds and Coulomb attraction resulting from grains negative charges ensure large ion-grain currents. Since all ions incident on negative grains are assumed to stick to them and immediately recombine with electrons, high ion-grain currents reduce the fractional ionization and grain charges as well as altering the gas phase chemical abundances.

The moderately higher temperatures in C-type shocks permit endothermic reactions to proceed. The most notable endothermic reaction in the model is that which converts atomic oxygen into water. This is the only neutral-neutral reaction included in the new chemical network (see note *[4] below table 5.1). Inspection of the rate coefficient for reaction 18 and the discussion in §4.3.1 show that it will become significant as the neutral temperature passes ~ 300 K. When the temperature remains low enough to supress reaction 18, the oxygen abundance should remain almost constant through the shock. However, when reaction 18 proceeds, the abundance of O will drop sharply as water is formed in copious quantities (see §5.7.1).

The only other process which substantially augments the gas phase H_2O abundance is the sputtering of the grain mantles. In this model, water can only be destroyed in reactions with H_3^+ and HCO^+. Because the conversion of atomic oxygen and grain mantle sputtering are both expected to produce gas phase H_2O in amounts orders of magnitude larger than the H_3^+ or HCO^+ abundances, reactions 3 and 8 ought not to cause the water abundance to appreciably fall in the post-shock region. The abundances of H_3^+ and HCO^+ on the other hand will be strongly affected and so acutely depend on the presence of water.

As soon as water is formed, either in the gas phase or sputtered from grains, the H_3O^+ abundance will grow since the rate coefficient for its formation from H_3^+ and water (reaction 3) is seven times larger than that for the equivalent reaction with atomic oxygen (reaction 5). H_3O^+ can also be formed in reactions between HCO^+ and water. At all shock speeds, the H_3O^+ abundance should peak at a value determined by the availability of water and subsequently fall due to ion-neutral and grain surface recombinations (reactions 16 and 17 respectively).

Since Mg^+ is representative of metallic ions, a simple magnesium chemistry must be included to properly calculate gas phase and grain surface recombinations and hence the fractional ionization. When the ion temperature passes a few thousand degrees Kelvin, Mg^+ is very efficiently converted to MgH^+ through endothermic reactions with molecular hydrogen (reaction 12). The MgH^+ will be quickly destroyed in dissociative and grain surface recombinations (reactions 13 and 14 respectively) as soon as the temperature begins to drop, forming Mg. The only process which should contribute enough to the post-shock neutral magnesium abundance to noticeably change its profile is the sputtering of the grain cores, because one atom in every olivine molecule is magnesium (see §5.4).

5.3.3 Rate equations

The evolution of each chemical species is modeled by setting its number density (cm^{-3}) as the scalar (S). The conservation equation for a scalar in each cell takes the form:

$$\frac{\partial Q}{\partial t} + \frac{\partial F}{\partial x} = \alpha_s, \tag{5.2}$$

$$\frac{\partial S}{\partial t} + \frac{\partial S u_s}{\partial x} = \frac{dn(X)}{dt}. \tag{5.3}$$

Q is the vector of the conserved variable ($Q = S$), F is the vector of the flux (the net rate of change of the scalar in a given cell due to advection; $F = Su_s$), u_s is the speed at which the species moves (either the ion or the neural velocity) and $\alpha_s = dn(X)/dt$ is the source term; the net rate of formation or destruction of a species per unit volume due to the gas phase reactions and grain surface recombinations in table 5.1.

Equation (5.3) states that, in each cell, the time rate of change of a scalar is obtained by summing its rate of change due to all the relevant chemical reactions with its net change due to advection across the cells boundaries. The α_s term is obtained for each species by constructing a rate equation from table 5.1 to balance its formation and destruction. If R_1 is a gas phase reaction between species A and B which forms species C and proceeds with a rate coefficient $k1$, then the production rate of species C with time due to reaction R_1 is:

$$\left.\frac{dn(C)}{dt}\right|_{R_1} = +k1n(A)n(B), \tag{5.4}$$

i.e. the product of $k1$ and the number densities of both reactants ($n(A)$ and $n(B)$) must be added to the total rate equation. Similarly, if R_1 removes species C, the right hand side of equation (5.4) includes C as one of the reactants and must be subtracted from the rate equation.

If R_2 is a grain surface recombination which neutralises an ion species (D) then the current of those ions onto each grain fluid (subscripts g and s) multiplied by the number density of that grain species must be subtracted from the rate equation. The rate of destruction of species D with time due to reaction R_2 is:

$$\left.\frac{dn(D)}{dt}\right|_{R_2} = -(\Gamma_{Dg} n_g + \Gamma_{Ds} n_s). \tag{5.5}$$

$\Gamma_{Dg,s}$ is the current of ions species D onto either large (g) or small (s) grains. The current is only multiplied by the number density of the grain fluid, since the abundance of the impacting ion species is taken into account when calculating the current itself (see §2.5.4). Since reaction R_2 must produce a neutral species, exactly the same term must be added to the rate equation of those neutrals.

Application of this method to the reactions in table 5.1, considering two grain fluids, yields the following rate equations for five ion and three neutral species:

- Formation and destruction of H_3^+; this involves reactions 1, 2, 3, 4 and 5:

$$\begin{aligned}\frac{dn(H_3^+)}{dt} &= k_1 n(H_2) \\ -n(H_3^+)[k_2 n(CO) + k_3 n(H_2O) + k_5 n(O) + \Gamma_{H_3^+ g} n_g + \Gamma_{H_3^+ s} n_s].\end{aligned} \tag{5.6}$$

- Formation and destruction of HCO^+; this involves reactions 2, 6, 7, 8 and 9:

$$\begin{aligned}\frac{dn(HCO^+)}{dt} &= k_2 n(H_3^+) n(CO) \\ -n(HCO^+)[k_6 n_e + k_7 n(Mg) + k_8 n(H_2O) + \Gamma_{HCO^+ g} n_g + \Gamma_{HCO^+ s} n_s].\end{aligned} \tag{5.7}$$

- Formation and destruction of Mg^+; this involves reactions 7, 10, 11, 12 and 16:

$$\frac{dn(Mg^+)}{dt} = k_7 n(HCO^+)n(Mg) + k_{16} n(H_3O^+)n(Mg) \tag{5.8}$$
$$-n(Mg^+)[k_{10} n_e + k_{12} n(H_2) + \Gamma_{Mg^+ g} n_g + \Gamma_{Mg^+ s} n_s].$$

- Formation and destruction of H_3O^+; this involves reactions 3, 5, 8, 15, 16 and 17:

$$\frac{dn(H_3O^+)}{dt} = k_8 n(HCO^+)n(H_2O) + k_3 n(H_3^+)n(H_2O) + k_5 n(H_3^+)n(O) \tag{5.9}$$
$$-n(H_3O^+)[k_{15} n_e + k_{16} n(Mg) + \Gamma_{H_3O^+ g} n_g + \Gamma_{H_3O^+ s} n_s].$$

- Formation and destruction of MgH^+; this involves reactions 12, 13 and 14:

$$\frac{dn(MgH^+)}{dt} = k_{12} n(Mg^+)n(H_2) \tag{5.10}$$
$$-n(MgH^+)[k_{13} n_e + \Gamma_{MgH^+ g} n_g + \Gamma_{MgH^+ s} n_s].$$

- Formation and destruction of Mg; this involves reactions 7, 10, 11, 13, 15 and 16:

$$\frac{dn(Mg)}{dt} = k_{10} n(Mg^+) n_e + k_{13} n(MgH^+) n_e + n_g(\Gamma_{Mg^+ g} + \Gamma_{MgH^+ g}) \tag{5.11}$$
$$+n_s(\Gamma_{Mg^+ s} + \Gamma_{MgH^+ s}) - n(Mg)[k_7 n(HCO^+) + k_{16} n(H_3O^+)].$$

- Destruction of O; this involves reactions 5 and 18:

$$\frac{dn(O)}{dt} = \quad -n(O)[k_5 n(H_3^+) + k_{18} n(H_2)]. \tag{5.12}$$

- Formation and destruction of H_2O; this involves reactions 3, 8, 15, 16, 17 and 18:

$$\frac{dn(H_2O)}{dt} = k_{15} n(H_3O^+) n_e + k_{16} n(H_3O^+) n(Mg) + k_{18} n(O) n(H_2) \tag{5.13}$$
$$+\Gamma_{H_3O^+ g} n_g + \Gamma_{H_3O^+ s} n_s - n(H_2O)[k_3 n(H_3^+) + k_8 n(HCO^+)].$$

Considering H_3^+ as the scalar, the formation or destruction rate attained from equation (5.6) is set as dn(X)/dt, allowing equation (5.3) to be written as:

$$\frac{\partial[n(H_3^+)]}{\partial t} = (k_1 n(H_2) - n(H_3^+)[k_2 n(CO) + k_3 n(H_2O) + k_5 n(O) + \Gamma_{H_3^+ g} n_g + \Gamma_{H_3^+ s} n_s]) - \frac{\partial[n(H_3^+)u_i]}{\partial x}, \tag{5.14}$$

with similar expressions for each of the other species.

At each time-step, the rate equations (5.6) - (5.13) are solved in every cell. The solution for each becomes the source array for that species ($so[i] = \alpha_s$ = dn(X)/dt, see §5.3.4). To progress the solution over the time-step (dt), the new value of the scalar (S_{new}) is defined as the sum of its value after the previous time-step (S), its flux ($\partial \mathrm{Su}_s/\partial \mathrm{x}$) and the source term accounting for chemistry within the cell over the time-step ($so[i]dt$):

$$S_{new} = S + \left(\frac{\partial S u_s}{\partial x} + so[i]\right)dt. \tag{5.15}$$

S_{new} is calculated and set as the value for the scalar array (S) after a time dt, before moving onto the next species.

5.3.4 Implementation

To monitor the abundance of each chemical species separately, eight scalar arrays are created for the chemistry. The calculation of the net formation or destruction rate for a species within a cell due to chemical reactions ($dn(X)/dt$) is undertaken as follows: The ion-neutral relative speed is calculated from:

$$u_{in} = [(u_{ix} - u_{nx})^2 + (u_{iy} - u_{ny})^2 + (u_{iz} - u_{nz})^2]^{\frac{1}{2}}, \tag{5.16}$$

where subscripts i and n specify ions or neutrals and x, y and z specify Cartesian coordinates. This drift speed is used to calculate the effective temperature, required for the rate coefficient of reaction 12. With T_{eff}, the electron temperature and the chemical abundances from the previous time-step, all of the gas phase rate coefficients can be calculated.

The grain surface recombination rate coefficients are obtained by calculating the currents of each ion species onto each grain fluid. First, the ion-grain relative speed is calculated from:

$$u_{gi} = [(u_{gx} - u_{ix})^2 + (u_{gy} - u_{iy})^2 + (u_{gz} - u_{iz})^2]^{\frac{1}{2}}. \quad (5.17)$$

For a given grain fluid, the ion-grain relative speed is the same for all ion species since they are all assumed to move with the same velocity. Next, the current of each ion species onto each grain type is ascertained using the grain-neutral relative speed, the ion temperature, the mass of the ion species and its mass density. This is done by calling the grain current routine detailed in §2.5.4. The routine employs an equation for the current which depends on whether the product of the grain charge and impacting particle charge is positive or negative. The equation employed also varies when the ion-grain drift speed is sufficient to velocity-shift the charged particle distribution when viewed from the frame of the grains (as per Havnes et al. 1987). The current obtained from the routine is then multiplied by the number density of the relevant grain fluid to give the recombination rate per unit volume, which is included in the rate equation for the relevant ion as in equation (5.5). In the new model there are therefore two terms (one for each grain fluid) for every grain surface recombination. The method assumes that every ion colliding with a grain sticks to it and immediately undergoes a recombination with an electron already present on the surface. It is also assumed that the products are promptly released back into the gas phase. The current of each ion species onto grains in each fluid is calculated separately. These terms are used individually in the rate equations for each species (Γ terms in equations 5.6 - 5.13). They are also summed over each grain fluid because the total ion current is needed to calculate the rate of change of the grain charge (see below).

Having solved equations (5.6) - (5.13) using the relevant abundances, gas phase rate coefficients and grain terms described above, the time rate of change of each species abundance due to the chemistry in the cell (dn(X)/dt) has been obtained. This solution is the source array ($so[i]$) in equation (5.15). To have each chemical species properly advected across the grid with the flow, the scalar fluxes at the cell boundaries are required. These give the number of the species crossing a unit area of the cell boundary area per unit time ($\partial F/\partial x = \partial Su_s/\partial x$ from equations (5.2) and (5.3) with $s = i$ or n). The ion fluxes are given by:

$$f(X) = u_i S, \tag{5.18}$$

and the neutral fluxes by:

$$f(X) = u_n S, \tag{5.19}$$

where S is the number density of species X and $u_{i,n}$ is the speed of the fluid. With the fluxes, equation (5.15) can be used to progress the scalar over the time-step.

The source ($so[i]$) terms are also used to calculate the mass transfer term for the ion fluid as a whole. The ion fluid mass transfer term is the sum of the transfer terms for each ion species multiplied by the unit mass of the ion fluid (assumed to be $30\mathrm{m}_H$, see §2.5.1). This is then used to advance the total ion solution. The same process is not required for the electrons since there is only one type of them and their gas phase mass density in each cell is obtained from charge neutrality considerations.

During exploratory calculations it was noted that drastic changes in parameters like density and temperature across a single cell allowed the value calculated for $so[i]$ to change the scalar by a very large amount in a single time-step. This did not occur for every scalar but those ion species that did resulted in numerical artifacts such as positive grain charges and oscillations in the scalar downstream of the questionable cell. Spuriously high formation of an ion species can affect the grain charge if it occurs in a cell which possesses a large grain current for that species. To avoid this, the time-step is limited to restrict the maximum net change that a large value of $so[i]$ can make on the scalar, i.e. a higher value for $so[i]$, results in a smaller time-step so that n(X) can only change by 10 % per time-step. This is achieved by defining $irate$:

$$irate = \frac{(dn(X)/dt)}{n(X)}, \tag{5.20}$$

$$dt \propto \frac{1}{irate}. \tag{5.21}$$

$irate$ is calculated for every ion species individually in each cell. The value used to limit the time-step is then the maximum over the whole grid. Similar terms are not required for the neutrals since their relative abundances only affect the cooling rates and not the fractional ionization or grain charge. Therefore numerical artefacts do not occur.

5.4 Sputtering

The refractory nature of silicon means that the enhancements observed near some YSOs are most likely to come about via the processing of dust grains in shocks (e.g. Martin-Pintado et al. 1992; Bachiller 1996; Jørgensen et al. 2004). The favoured explanation is that grains are partially or totally destroyed in collisions with other grains: grain-grain collisions, e.g. Tielens et al. (1994), or abundant gas phase atoms and molecules: sputtering, e.g. Draine & Salpeter (1979). These mechanisms can only operate when neutral particles and different types of dust grain move relative to each other. Sputtering refers to the process whereby projectile particles impact dust grains with sufficient energy to dislodge bonded material, returning it to the gas phase. It is efficient in faster C-type shocks because they induce a systematic grain-neutral streaming velocity over a wide region (e.g. Draine 1980).

The previous observational and theoretical studies into sputtering were discussed in §1.3.5. It was noted there that Caselli et al. (1997) perform steady calculations for oblique multifluid shocks. Their work is the steady state analogue to the time dependent models presented here. They report that grain-grain collisions are only likely to dominate the return of grain material in the shocks associated with high mass SFRs. The current work does not consider grain-grain collisions and its conclusions therefore pertain to regions of low mass star formation.

The dust grains are assumed to comprise of a refractory core made of olivine ($MgFeSiO_4$). The core is coated in a layer of water ice known as the mantle (see §1.1.2). Because the mantle ice only weakly bonded, it is sputtered one water molecule at a time. On the other hand, the strong bonds between the molecules of core material means that olivine is sputtered one atom at a time (Draine 1995). The sputtering yield is defined as the average number of target particles which are liberated per projectile collision. The yield is initially calculated for projectiles at normal incidence and is then averaged over collision angle (from normal to tangential impact) via an integral. In order to ascertain the sputtering rate per grain, the angle-averaged yield is again integrated with respect to the impact energy. The range of impact energies for this integral is determined by the neutral velocity distribution function viewed from a frame co-moving with the grains, (see §5.4.2).

All neutral atoms and molecules in the gas phase are considered to be potential projectiles. These are H_2, CO, O, Mg (originally present in the gas phase plus any previously sputtered

from the grain cores), H_2O (formed in the gas phase plus any previously sputtered from the grain mantles) and SiO (any atomic silicon sputtered from the grain cores is assumed to be quickly transformed into SiO as shown by Schilke et al. 1997). The choice of projectiles has been motivated by previous work (e.g. Field et al. 1997; May et al. 2000; Jiménez-Serra et al. 2008), where it was noted that even with small abundances molecules can play a major role in sputtering. This is because a heavy molecule possesses more momentum than a light atom at a given streaming velocity and so becomes capable of sputtering at a lower shock speed. The particles which are sputtered are H_2O from the mantles and Mg, Si, and O from the cores. Iron is not considered.

5.4.1 Yields and sputtering rates

The yield for each projectile sputtering water from grain mantles is calculated as in Draine & Salpeter (1979), using equation (5.22). That expression is based on a quantified fit to experimental sputtering yields at low impact energies ($\leq$ 1 keV) for 202 projectile/target combinations. Equation (5.22) models the low impact energy regime which is to the left of the break in the curves of figure 5.1. The semi-empirical yield for projectiles at normal incidence and with low energy, obtained by Draine & Salpeter (1979) is given by:

$$Y(E, \theta = 0) = A\frac{(\epsilon - \epsilon_0)^2}{1 + (\frac{\epsilon}{30})^{\frac{4}{3}}}; \epsilon > \epsilon_0, \tag{5.22}$$

$$\epsilon = \frac{\eta E}{U_0}, \tag{5.23}$$

$$\eta = \frac{4\zeta M_p M_T}{(M_p + M_T)^2}, \tag{5.24}$$

$$\epsilon_0 = max[1, 4\eta]. \tag{5.25}$$

U_0 is the binding energy of a target atom, E is the impact energy (the projectile kinetic energy at the grain-neutral drift speed), M_T is the mass of the target atom and M_p is the mass of the projectile atom or molecule. ζ is an adjustable "efficiency factor" which accounts for the fact that the binding energy between molecules is less than an atomic valence bond. It is taken to be 0.8 for ice and 1 for core material. "A" is a constant which was found to be relatively

independant of the projectile and target combination. It is assumed to have a value of 8.3×10^{-4} as per Draine & Salpeter (1979). ϵ_0 is the threshold impact energy for sputtering. Other ice mantle parameters such as binding energy are preferentially taken from the more recent work of Tielens et al. (1994).

Following Draine & Salpeter (1979) (who reference table 7 from Draine 1978), it is assumed that the angle averaged yield is twice that for collisions at normal incidence, i.e.:

$$< Y(E) >_\theta \approx 2Y(E, \theta = 0) \tag{5.26}$$

This relationship is taken from experimental data on oblique incidence sputtering well above the threshold. It allows for the fact that sputtering due to near tangential impacts is up to ten times more efficient than sputtering due to near normal impacts, but tangential impacts occur less frequently.

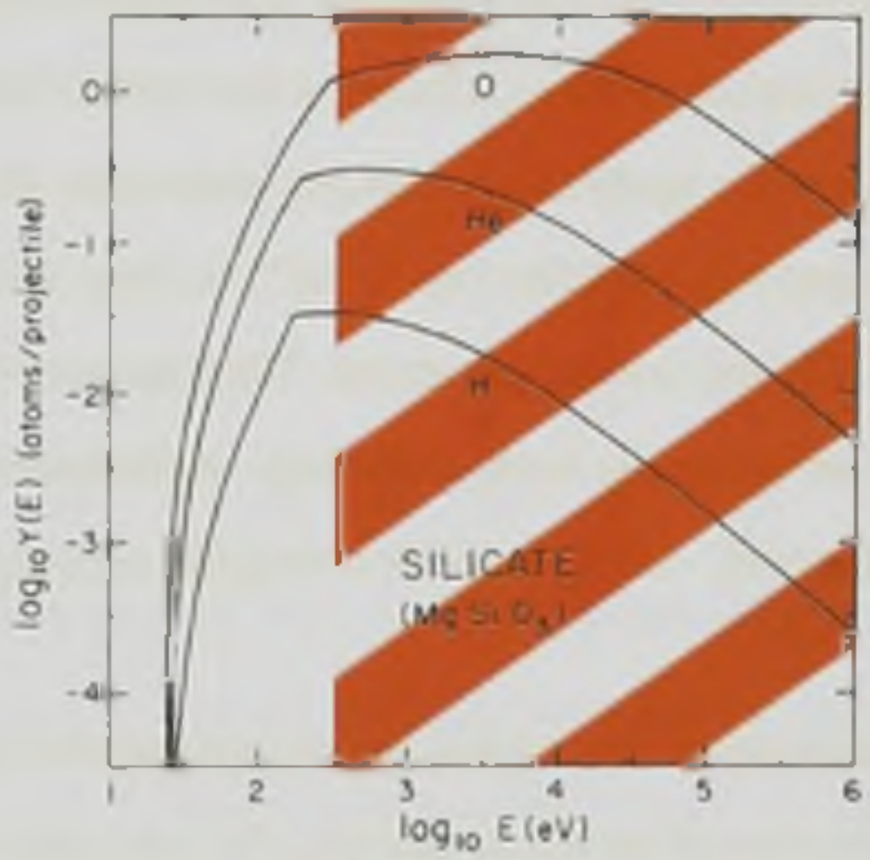

Figure 5.1: Angle averaged sputtering yields for H, He and O projectiles striking silicates as a function of the impact energy (E). Up to the breaks in the curves between 300 and 500 eV, each curve plots the angle-averaged yield (twice the value of the function 5.22 as per equation 5.26). The region marked with red bands is safely in the high energy regime but the breaks in the curves occur at impact energies which are already well above the maximum generated in any of the following models (see text below). Adapted from Draine & Salpeter (1979).

Figure 5.1 clearly shows that there is a threshold impact energy for sputtering, where $\epsilon = \epsilon_0$. That this threshold is different for each projectile species can be seen by close inspection.

The yields for heavier projectiles become non-zero at smaller impact energies than lighter ones and are also larger at any impact energy above threshold. Each yield reaches a maximum at some impact energy between a few hundred and 10^4 eV, all of which correspond to drift speeds above 100 km s^{-1}. The curves in figure 5.1 abruptly change shape at the impact energy where Draine & Salpeter (1979) switch to their high energy sputtering regime. Since the maximum shock velocity considered in this chapter is 50 km s^{-1} and the inferred grain-neutral drift speed is somewhat lower than this, the entire collision energy region is well below the break in the curves of figure 5.1. This justifies the use of the low energy yield terms (equations 5.22 - 5.25) when employing the Draine & Salpeter (1979) procedure.

The core yields for all projectiles except H_2 (see below) are taken from the more recent work of May et al. (2000). Their results comprise the best fit to a sputtering model which includes the various energies of interest for lattice bound atoms (surface binding energy, displacement energy, lattice binding energy and cut-off energy). The authors employ a code (TRIM) which was developed to simulate the transport of ions in matter. The original application of this scheme was to model the ion bombardment of surfaces relevant to the semi-conductor industry, but Field et al. (1997) modified it to calculate sputtering yields for interstellar dust grains. It follows the trajectories of very many impacting particles (up to 10^7) as they enter the surface and lose energy in a series of binary collisions with target atoms. The trajectories of any displaced atoms are also followed, allowing for projectile back scattering, implantation into the target as well as sputtering of the target material. Using suitable averaging techniques, the yields are then calculated.

The projectile angle of incidence is again taken into account since the yield strongly depends on this parameter: Like in the case of mantle sputtering, the core yield can be enhanced by up to an order of magnitude when the collision angle is close to tangential as opposed to close to normal. Collisions are assumed to be isotropic as is the case, for example, when the dust grains rotate. In such circumstances, even though the projectiles stream in one direction relative to the grains, any part of a grain surface is equally likely to be struck. The yields are found through an integration of the angular yield function; $Y(E,\theta)$, from $\theta = 0$ to $\theta = \pi/2$. May et al. (2000) calculated yields for several projectile and target combinations over a range of impact energies and angles. They discovered that a three parameter fit could be used to model the impact energy to yield relationship (see figure 5.2a). This fit takes the form:

$$Y(E) = ke^{-\beta/(E-E_{th})}, \tag{5.27}$$

where E_{th} is the sputtering threshold impact energy (eV), β is the impact energy (eV) and k is a constant which represents the maximum yield for that projectile and target combination. Values for E_{th}, β and k are given in table 4 of May et al. (2000) for various projectiles impacting on olivine to liberate Mg, Si and O and those values are adopted for the simulations in this chapter. Equation (5.27) ensures that the yield is zero for impact energies at or below E_{th}. Above threshold, the yield follows an exponential form which asymptotes towards k, (the horizontal red line in figure 5.2a). The red dash on the x-axis of figure 5.2b represents the full extent of the x-axis in figure 5.2a and the maximum extent of the x-axis in figure 5.2b is around the same impact energy as the break in the atomic hydrogen curve in figure 5.1.

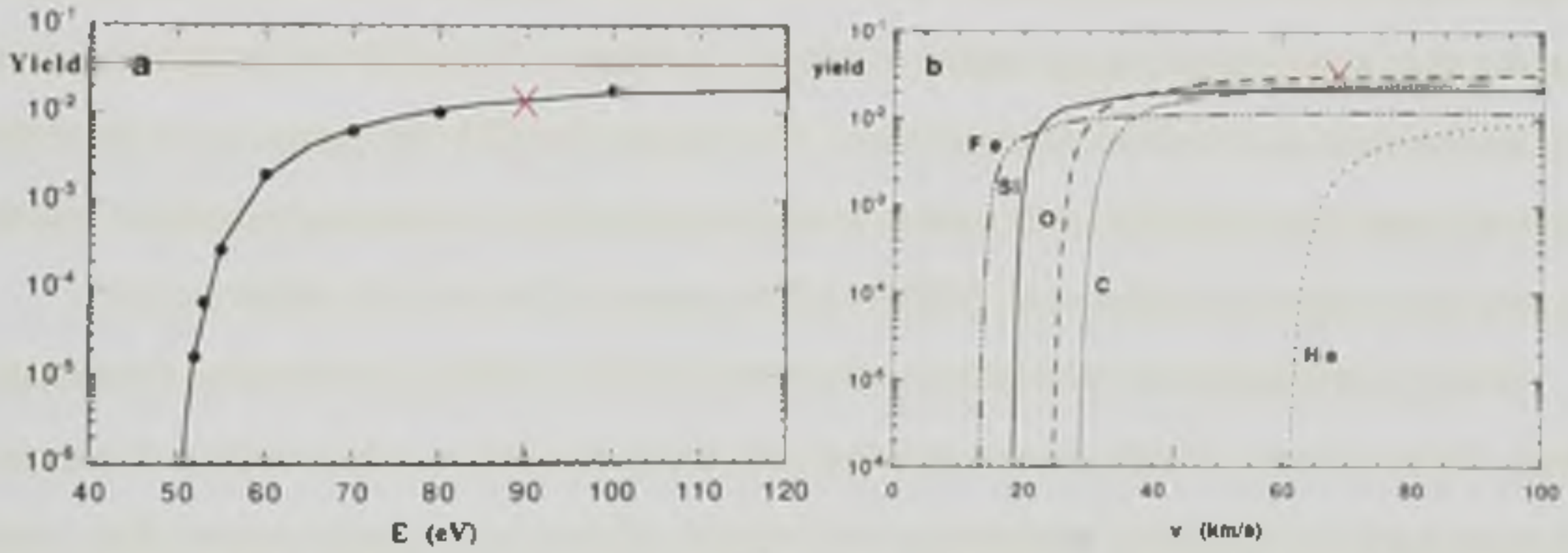

Figure 5.2: (a) The angle averaged yield of silicon sputtered from olivine by atomic oxygen as a function of impact energy. The points are data obtained from the TRIM code and the curve is the fit as per equation (5.27). The red cross and mark on the x-axis indicate the impact energy required for 50% of the maximum yield. (b) Angle averaged sputtering yields of silicon for various projectiles striking olivine as a function of the impact velocity (directly related to the grain-neutral drift speed). The red cross indicates the impact velocity required for 90% of the maximum yield for O as the projectile. Both plots have been taken from May et al. (2000).

The mantles contain a finite number of ice molecules which are relatively easily sputtered using the Draine & Salpeter (1979) procedure due to their low binding energies. It is assumed that the cores remain pristine until all of the ice has first been sputtered from the mantles. Once this has happened, so long as the impact energies are sufficient, the cores are sputtered using the

May et al. (2000) yields for all projectiles (except H_2) impacting olivine.

As mentioned in §5.4, it is assumed that atomic oxygen and silicon are sputtered from the cores but every Si atom immediately reacts with O in the gas phase to produce SiO (Pineau des Forets et al. 1997). This is in harmony with the finding of Schilke et al. (1997) who report that unless silicon is sputtered atomically or as SiO, the observed abundances of SiO cannot be reproduced. It also fits with the models of Herbst et al. (1989) who report that in dark molecular clouds SiO is likely to be the dominant form of silicon, accounting for over half of the total silicon abundance and being more common than atomic silicon by over an order of magnitude.

The Draine & Salpeter (1979) prescription is employed to obtain the core yield when considering H_2 as a projectile. This is because May et al. (2000) do not perform calculations for molecular projectiles and the lightest projectile which they consider is twice as massive as H_2. To date, Yao et al. (1998) are the only authors to have reported sputtering yields for molecules impacting grains with energies below 1 keV. This chapter therefore follows their work by assuming that in the impact energy regime of interest, the effect of projectile molecules larger than H_2 are the same as for atoms of equal mass. This means that CO will sputter as Si since they have the same mass and H_2O will sputter as oxygen since this is the atomic projectile with the nearest mass reported in May et al. (2000) and the masses of the two only differ by 10 %.

Since the projectiles are all neutral species, they have the velocity distribution of the neutral fluid. From a frame of reference co-moving with the grains this is a Maxwellian distribution characterised by the neutral temperature and velocity shifted by the grain-neutral drift speed. The angle-averaged sputtering yield must be integrated over the impact energies associated with the neutral velocity distribution function to give the sputtering rate per grain. For target species "X" . Draine & Salpeter (1979) derive:

$$\left|\frac{dn(X)}{dt}\right|_{grain} = \pi r_g^2 n_p \left(\frac{8k_bT_n}{\pi M_p}\right)^{\frac{1}{2}} \frac{1}{s} \int_{x_{th}}^{\infty} dx x^2 \frac{1}{2}[e^{-(x-s)^2} - e^{-(x+s)^2}] < Y(E) >_\theta, \quad (5.28)$$

$$s^2 = \frac{M_p u_{gn}^2}{2k_bT_n}, \quad (5.29)$$

where the term on the left hand side of equation (5.28) is the time rate of change of the number density of target atoms residing on or in a particular grain. T_n is the neutral temperature, n_p and M_p are the number density and mass of the projectile, s^2 is a ratio of the projectile kinetic

energy at the grain-neutral drift velocity to $k_b T_n$ (and is hence dimensionless) and u_{gn} is the grain-neutral drift velocity which is given by equation (5.30):

$$u_{gn} = [(u_{gx} - u_{nx})^2 + (u_{gy} - u_{ny})^2 + (u_{gz} - u_{nz})^2]^{\frac{1}{2}}. \tag{5.30}$$

The parameter x is a dimensionless form of the impact energy defined as $x^2 = E_p/k_b T_n$, where E_p is the projectile impact energy. x_{th} is the threshold value for x, corresponding to E_{th}. It is given by:

$$x_{th} = \left(\frac{E_{th}}{k_b T_n}\right)^{\frac{1}{2}}. \tag{5.31}$$

when calculating the yields as in May et al. (2000) and:

$$x_{th} = \left(\frac{\epsilon_0 U_0}{\eta k_b T_n}\right)^{\frac{1}{2}}, \tag{5.32}$$

when employing the Draine & Salpeter (1979) prescription.

Once the integral in equation (5.28) has been evaluated (see §5.4.2), one has obtained the sputtering rate per grain due to that projectile and target combination. This is multiplied by the number density of the relevant grain fluid to obtain the sputtering rate per unit volume. After completing these steps for every combination of projectile and target, the solution for each target species can be progressed in the same way as the chemistry already included in §5.3.4. Scalar arrays are therefore included to describe the amount of ice initially residing on and the amount of silicon initially residing in each grain species per unit volume. This is both to ensure that only physically present grain material can be sputtered and to monitor the fractions removed. These arrays are advected across the grid at the same speed as the relevant grain fluid (see §5.5). Their fluxes are therefore of the form:

$$f(X) = u_{g,s} n S. \tag{5.33}$$

In addition to calculating the yields, a numerical method is required to solve the integral. It must correctly evaluate the integral in the minimum possible number of operations since equation (5.28) must be solved several thousand times per time-step.

5.4.2 Integration Detail

To evaluate the integral in equation (5.28) for the sputtering rate of all projectiles except H_2 on silicate grain cores, the following two equations together with (5.27), (5.29) and (5.31) are required:

$$f(x) = x^2 \frac{1}{2}[e^{-(x-s)^2} - e^{-(x+s)^2}] < Y(E) >_\theta, \tag{5.34}$$

$$x = \left(\frac{E_p}{k_b T_n}\right)^{\frac{1}{2}}, \tag{5.35}$$

where E_p is the projectile kinetic energy at the grain-neutral drift speed.

The yield for the cores scales exponentially with impact energy. It has a value of zero at $x = x_{th}$ and asymptotes towards a constant value of k (see §5.4.1). Well above threshold the yield is therefore approximately independent of impact energy and the sputtering rate per unit volume can be reliably estimated without having to evaluate an integral. The range of grain-neutral relative velocities in the shocks of interest however demands that the function (5.34) be integrated. The yield itself is a function of x, which is why it remains in the integral. The analytic limits on the integral in equation (5.28) are the threshold x-value (x_{th}) and infinity. In a numerical scheme however, integration to infinity is not possible. To maximise computational efficiency, the minimum range required to accurately evaluate the integral is first deduced. Lower (denoted a) and upper (denoted b) limits are ascertained by calculating the range of x values for which the term inside square brackets in function (5.34) is non-zero and then comparing this range to x_{th} (see figure 5.3).

The threshold x-value is calculated from equation (5.31). The threshold sputtering energy (E_{th}) is a constant for each combination of projectile and target particle. Therefore x_{th} only depends on the neutral temperature, with higher temperatures inferring smaller values of x_{th}, as one would expect. Inspection of equation (5.34) reveals the function in square brackets to be the sum of two Gaussians centred on $x = \pm s$. The s term (given by equation 5.29) depends on both the neutral temperature and the grain-neutral drift speed. Figure 5.3 demonstrates that the range of x over which $f(x) > 0$ moves to higher values as the drift speed increases at a constant temperature (i.e. s increases). The numerical value of the function in square brackets is multiplied by x^2, so the value of $f(x)$ also becomes larger for every point. This increases the

area under the curve and the numerical value of the integral. When the temperature increases at a constant drift speed, s shrinks (see equation 5.29) and the non-zero region of $f(x)$ moves to lower values of x. The numerical value of the function $f(x)$ at each non-zero point and the area under the curve also decreases.

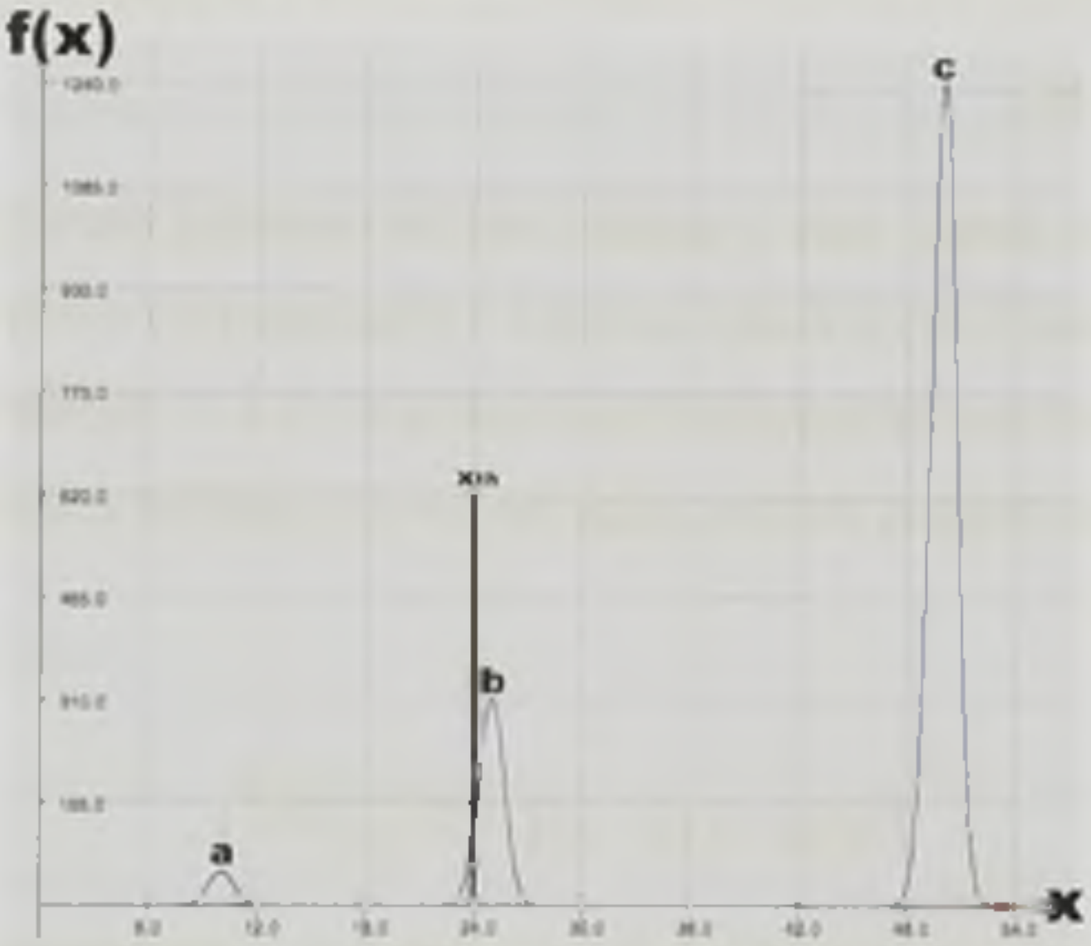

Figure 5.3: Graphical representation of $f(x) = x^2 \frac{1}{2}\left[e^{-(x-s)^2} - e^{-(x+s)^2}\right]$ as a function of x. For (a) $s = 10$, (b) $s = 25$ and (c) $s = 50$. It is clear that the term in square brackets is the sum of two Gaussians centred on $x = \pm s$. The width of either curve is independent of s, but the height of (and hence area under) the curve increases with s due to the x^2 term outside of the exponential in $f(x)$. This plot only displays the curves at positive values of x. Each curve is mirrored in the y-axis due to the $e^{-(x+s)^2}$ term. These parts of the curves are not included because they cannot contribute to the sputtering rates.

The width of the Gaussian is independent of s and calculations reveal that the exponential terms in $f(x)$ are very safely zero whenever $|x - s| \geq 30$. If the exponential is zero, then function (5.34) is also zero. At high temperatures and low drift speeds, s can be smaller than x_{th}. In cases when s is sufficiently smaller than x_{th}, the integral is zero since $<Y(E)> = 0$ for $x < x_{th}$. The curve may be entirely below, partially below or entirely above x_{th}. This results in three regimes for the limits of the integration depending on the relationship between s and x_{th}:

1. If $s \leq x_{th}$ - 30 (curve a in figure 5.3), then the integral in equation (5.28) is zero because the exponential function has a non-zero value over a range which is entirely below x_{th}. In

this region the yield is zero, so function (5.34) and the integral are also zero.

2. if x_{th} - 30 $< s <$ x_{th} + 30 (curve b in figure 5.3), then part of the curve is below x_{th} and the rest is above. Therefore $a = x_{th}$. and $b = s + 30$.

3. if $s \geq x_{th} + 30$ then the full curve is above x_{th} (curve c in figure 5.3). In this case $a = s$ - 30 and $b = s + 30$.

In the first case no further work is required and the sputtering rate is zero. For the second and third cases function (5.34) is always zero at $x = b$ because $f(x) = 0$ by definition when $x = b = s + 30$. In the third case the function is also zero at $x = a = s$ - 30, but in the second case it is not. To a first approximation, the area under the curve is modeled as a single trapezium. The trapezium rule gives:

$$\int_a^b f(x)dx \approx (b-a)\left(\frac{f(a)+f(b)}{2}\right). \tag{5.36}$$

Whatever value is obtained for the first approximation of the integral (zero or otherwise) is then set to "old integral" before refining the solution. This refinement involves splitting the region between a and b into successively more trapezia (number of trapezia = n_{trap}) and evaluating their area via the composite trapezium rule:

$$\int_a^b f(x)dx \approx \frac{b-a}{n_{trap}}\left[\left(\frac{f(a)+f(b)}{2}\right) + \sum_{j=1}^{n_{trap}-1} f\left(a + j\frac{(b-a)}{n_{trap}}\right)\right]. \tag{5.37}$$

Adding trapezia one at a time would be highly computationally expensive, so at each refinement the number of trapezia is doubled to speed up the convergence of the solution. When the number of trapezia has been doubled, one only needs to evaluate the function at values of x where it has not been previously calculated (i.e. the new trapezia edges which are half way between the old ones). The value of the "old integral" replaces $[f(a)+f(b)]/2$ and the new function values are summed as in the right hand term in the square brackets of equation (5.37). When many refinements are required for the solution to converge (see below), this method is computationally efficient.

Tests performed for all projectile and target combinations at various shock speeds (4 $< v_s <$ 35 km s^{-1}) revealed the minimum number of trapezia ever required to properly evaluate the

integral to be 32 ($n = 6$). Therefore the scheme proceeds directly from the first approximation to 32 trapezia. Each time expression (5.37) is evaluated, its new value is compared to the "old integral" to check whether the two differ by more than one percent. If they do, the new value is set to the "old integral", the number of trapezia is doubled and the integral is re-evaluated. This continues until either adding more trapezia changes the solution by less than one percent, or the number of trapezia reaches the maximum allowed (20 refinements gives 524288 trapezia). In either case the integral is then considered to be evaluated.

Whilst core sputtering was used as the example to elucidate the integration procedure, exactly the same treatment is used to evaluate the integrals required to calculate the sputtering rates of the ice mantles.

5.4.3 Numerical Tests

To confirm that the procedure to evaluate the integral is accurate, the output from the routine described in §5.4.2 can be compared to analytic results which are obtained in certain limits. Draine (1995) includes an extensive discussion of grain sputtering, complete with an analytic expression for the sputtering rate per grain in the case of low gas temperature and large streaming velocity. This is the "high s, low T" analogy to equation (5.28). The expression is:

$$\left[\frac{dn(X)}{dt}\right]_{grain} = -\pi r_g^2 u_{gn} n_p Y_{eff}. \tag{5.38}$$

The limit where this expression is valid is well above the sputtering threshold. As noted in §5.4.1, the yield is approximately independent of the impact energy in this region. It is therefore assumed to be constant with respect to x , allowing the effective yield (Y_{eff}) to be used. A routine was written where the values of T, x_{th} and u_{gn} are chosen such that T is very low and s is very high. The routine then evaluates the integral and compares the result for the sputtering rate (equation 5.28) to that obtained from equation (5.38). For a variety of input parameters (all of which satisfy the limits) the scheme detailed in §5.4.2 and the analytic expression (5.38) were found to be in exact agreement. This suggests that the integral is evaluated correctly for other values of T, x_{th} and u_{gn} even though analytic expressions for these cases are not available.

To warn the user when the integral routine has not converged by the time that $n = 20$, the code outputs the last integral value and the fractional difference between the last value and the "old

integral" to the screen. Occasions when the integral does not converge are rare. The sputtering rates in these cells are several orders of magnitude lower than the peak values across the grid. Perhaps most importantly, they only occur in cells at the upstream edge of the sputtering region. This means that any spurious effects are quickly overwhelmed as advection moves the material into cells within the shock where the sputtering process occurs most effectively. In those cells the integral always converges.

5.5 Initial Conditions

The gas phase species in the upstream region are dictated by those observed in cold, dense cloud cores in the ISM. For consistency, their initial abundances are the same as in previous chapters. It is assumed that all of the hydrogen is molecular and almost all of the carbon is in CO (see §1.1.1). Because CO is very abundant and effectively inert, a fixed CO to atomic hydrogen ratio is assumed ($\chi_{CO} = 5 \times 10^{-5}$), as in previous chapters. This abundance is high enough for formyl ions (HCO^+) to be cyclically produced from, and destroyed back to CO (see below). Whichever element is the least abundant out of carbon and oxygen in a given dense core will be almost completely incorporated into CO. Because oxygen is the third most abundant element in the Universe, in most cores, CO locks up all of the carbon. The remaining gas phase oxygen not in CO is either atomic (Millar et al. 1997 and see §1.1.1), or exists as water ice on grains (§1.1.2, §5.5 and see below). The initial gas phase atomic oxygen abundance is 4.25×10^{-4}. Metal species such as Mg are strongly refactory and are therefore largely incorporated into dust grains. Since the grain formation process is less than 100% efficient and the cloud lifetime is suitably short, it is reasonable to assume that a small fraction (~ 10 %) remains in the gas phase (see §1.1.2). Treating Mg as representative of all metals, its initial abundance is taken to be 10^{-7}. H_2O and SiO are assumed to have initial gas phase fractional abundances with respect to hydrogen of zero.

Other than CO, O and water ice, the only form which carbon and oxygen initially take in the upstream region is the formyl ion HCO^+. In addition to being initially present, HCO^+ is produced in reactions between H_3^+ and CO (reaction 2). It is destroyed in dissociative recombinations with free electrons in the gas phase (reaction 6). Because H_3^+ ions and free electrons are the two products of cosmic ray ionizations and H_3^+ is involved in HCO^+ formation whereas

electrons are involved in HCO^+ destruction, an increase in the fractional ionization increases both the formation and destruction rates of HCO^+ in this model. Coupled with the repeated observations of anomalously high HCO^+ abundances in the quiescent condensations associated with some HH objects (see Whyatt et al. 2010 and references therein), this is the reason why it is representative of molecular ions, constituting half of the initial ion abundance at the upstream boundary. Magnesium is selected to represent all metals due to its intermediate mass. In fact, with $m_{Mg} = 24$ amu, magnesium is half way between lithium and iron. Because metal ions are often atomic and atomic ions undergo radiative recombinations with electrons much more rarely than the dissociative recombination of molecular ions, any atomic ions present are more stable in the cold upstream region. Mg^+ therefore accounts for the other half of the calculated initial ion abundance.

The initial fractional ionization is calculated as in §3.3.1 and the resulting ion abundance is split equally between HCO^+ and Mg^+, both upstream and downstream. This is to remain consistent with pervious chapters, where these species were selected as they are amongst the most common metallic and molecular ion species observed in dense astrophysical plasmas (e,g, Ciolek & Roberge 2002). The ion mass is then a rounded average. The other ion species (H_3^+, H_3O^+ and MgH^+) are assumed to have initial abundances of zero.

Although there is initially no water in the gas phase, it does exist as ice mantles on the grain surfaces ($\approx 24\%$ of the total oxygen abundance; e.g. Chiar et al. 2011). The number densities of large (n_g) and small (n_s) grains are already calculated (as in §3.3.1) by demanding that the sum of the grain fluids add up to 1% of the mass density of the neutrals. This mass density is split between the grain fluids so as to maintain an MRN size distribution (Mathis et al. 1977) given by equation (1.1). It is therefore possible to calculate the amount of ice on each grain and hence the number density of ice molecules by grain species using a few additional pieces of information. The total initial fractional abundance of ice to gas phase hydrogen is taken to be $\chi_{ice} = 7.25 \times 10^{-5}$ (Whittet & Duley 1991). Large and small grains are assumed to be composed of the same materials so the surface density of bonding sites is the same for both species. It is taken to be $\rho_{sites} = 1.5 \times 10^{15}$ cm^{-2} (Tielens & Allamandola 1987). An MRN distribution demands that the population of the grain fluids be partitioned as follows:

$$n_s = 10^{2.5} n_g. \tag{5.39}$$

Because the surface density of bonding sites is a constant, it is trivial to show that the number of sites per large grain is 100 times the number of sites per small grain (the ratio of their surface areas): $N_{sites}(g) = 100 N_{sites}(s)$. The number of surface sites per unit volume is then this value multiplied by the number density of the grain species ($n_{sites}(g,s) = N_{sites}(g,s) n_{g,s}$). Using the grain size distribution and the fact that each large grain has one hundred times as many bonding sites as each small grain, it can be shown that:

$$n_{sites}(s) = N_{sites}(s) n_s = 0.01 N_{sites}(g) 10^{2.5} n_g \approx 3.16 N_{sites}(g) n_g, \tag{5.40}$$

i.e. there are 3.16 times as many bonding sites per cm^{-3} on small grains than large ones because they are much more numerous. The total fractional abundance of ice is shared between large and small grains ($\chi_{ice} = \chi_{ice}(g) + \chi_{ice}(s)$). Using the grain size distribution and the ratio of bonding sites per grain:

$$\chi_{ice} \approx \chi_{ice}(g) + 3.16 \chi_{ice}(g), \tag{5.41}$$

$$\chi_{ice}(g) \approx \frac{\chi_{ice}}{4.16}, \tag{5.42}$$

i.e. less than a quarter of the total initial ice abundance resides on large grains. The total number of ice molecules initially present on each size of grain is given by:

$$N_{ice}(g) = \frac{\chi_{ice}(g)}{\chi(g)}, \tag{5.43}$$

$$N_{ice}(s) = \frac{\chi_{ice}(s)}{\chi(s)}. \tag{5.44}$$

Here, $\chi(g)$ and $\chi(s)$ are the fractional abundances of grains of each size relative to hydrogen, (e.g. $\chi(g) = n_g/n_H$). There are 100 times more ice molecules per large grain than per small grain. Since it is assumed that dust constitutes 1% of the mass of the flow:

$$\rho_g + \rho_s = 0.01\rho_n, \tag{5.45}$$

$$\frac{4}{3}\pi r_g^3 \rho_{dust} n_g + \frac{4}{3}\pi r_s^3 \rho_{dust} n_s = 0.01 m_H n_H. \tag{5.46}$$

Here, ρ_{dust} is the mass density of the silicate grain material (3.84 g cm^{-3}; May et al. 2000) and $r_{g,s}$ are the grain radii. By substituting $n_g = \chi(g)n_H$ and $n_s = \chi(s)n_H$ into equation (5.46), noting that $\chi(s) \approx 3.16\chi(g)$, one can solve for $\chi(g)$:

$$\chi(g) \approx \frac{0.01 m_H}{\frac{4}{3}\pi\rho_{dust}(r_g^3 + 3.16 r_s^3)}. \tag{5.47}$$

This result can then be substituted into equation (5.43), using equation (5.42) to solve for the number of ice molecules per large (and hence small) grain. The number density (cm^{-3}) of ice residing on either grain species is then obtained by multiplying the number of ice molecules per grain by the number density of that grain type.

The initial gas phase abundance of SiO is zero but it is necessary to specify the abundances of silicon initially residing in each grain type. This is to ensure that only the physically present grain material can be sputtered and to monitor the fraction of the cores which have been vaporized. The individual grain mass of each dust type is already calculated and the mass of one olivine molecule is 142m$_H$. The number of olivine molecules per grain is simply the grain mass divided by the mass of an olivine molecule. This is the same as the number of silicon atoms per grain since there is one silicon atom per olivine molecule. Multiplying the number of silicon atoms per grain by the number density of grains gives the number density of silicon atoms (cm^{-3}) residing within that grain species. Using this method, the initial abundance of silicon atoms in the grain cores relative to gas phase hydrogen (χ_{Si}) is calculated to be 5.81×10^{-5}.

Therefore the amount of silicon residing in large grains per cubic centimeter is ≈ 3.16 times the amount of silicon residing in small grains whereas the amount of ice residing on large grains per cubic centimeter is ≈ 0.316 times the amount of ice residing on small grains. This means that the small grains dominate the return of water ice to the gas phase by sputtering but the return of silicon is dominated by the large grains. Since the large grains are only partially coupled to the magnetic field in the following high density (10^6 cm^{-3}) models (e.g. see chapter 3), the amount of silicon released near to threshold will differ from models where it is assumed that all

the grains are well tied to the field lines (e.g. May et al. 2000). It is assumed that the increase in grain radius due to the ice mantle is negligible.

The initial condition file is modified to calculate the chemical abundances, the number density of ice molecules residing on and the number of silicon atoms incorporated in both large and small grains. These values are ascertained up and down stream of the initial discontinuity. The un-sputtered ice and silicon arrays are associated with the grain fluids. Prior to being sputtered these arrays are advected using the grain flux expression (equation 5.33) to ensure that they move with the grains. Any particles liberated from either the mantles or cores immediately switch to being advected with the neutral flow.

5.6 Parameter space

The purpose of this work is to investigate how the return of ice and silicon oxide to the gas phase depends on the shock speed and the upstream density. To this end, two density regimes are selected to represent the denser ($n_H = 10^6$ cm^{-3}) and less dense ($n_H = 10^4$ cm^{-3}) regions of molecular cloud cores. Simulations are undertaken for shock speeds in the range $5 \leq v_s \leq 35$ km s^{-1} with $n_H = 10^6$ cm^{-3} and $10 \leq v_s \leq 50$ km s^{-1} with $n_H = 10^4$ cm^{-3}. This is sufficient to reveal the onset and saturation of mantle sputtering in both density regimes. The range also reveals the threshold for grain core sputtering at both densities although the cores are not totally destroyed in any shock.

The magnetic field scales as $B = 1\mu G\ (n_H/cm^{-3})^{-1/2}$ which is the usual relation adopted in this project (Troland & Heiles 1986). Therefore $B = 10^{-4}$ G in the low density regime and $B = 10^{-3}$ G in the high density regime. The upstream temperatures of all fluids except the grains ($T_{grain} = 0$ K) are taken to be 10 K. Most simulations are performed for oblique shocks where the magnetic field makes an angle of 45° with the shock normal. However, because of the angular dependance noted in chapter 3, additional simulations are undertaken at $\theta = 30°$ and 60° for $n_H = 10^6$ cm^{-3}, $v_s = 25$ km s^{-1} and $n_H = 10^4$ cm^{-3}, $v_s = 16$ km s^{-1}.

In previous chapters, computational efficiency was not an issue, so grids of 400 or 1200 cells were adopted with grids sized to cover ten times the estimated maximum shock widths. However with the new terms included to describe sputtering and chemistry, simulations at such high resolution proceed extremely slowly. To remedy this, exploratory (low resolution) simulations

were undertaken at each shock speed to ascertain the maximum shock width (from the ion and electron z-velocities). These were followed by high resolution (200 cells) simulations on grids two to five times the shock width. This ensures that the grid is wide enough to accommodate the full shock structure whilst retaining enough cells for the shock to be resolved without being un-necessarily wide.

Like chapter 3, all the simulations are run from an initially J-type discontinuity until a steady C-type shock is obtained.

5.7 Results

5.7.1 Chemistry

5.7.1.1 Upstream chemistry

As noted in §5.3, the chemical number densities are not fixed at the upstream boundary and their initial relative abundances are out of equilibrium. The cosmic ray ionization rate coefficient is assumed to be the same in the upstream region as everywhere else in the shock. The dissociative recombinations of molecular ions with electrons proceed most efficiently at low temperatures and ion-neutral reactions are not temperature dependent. There is therefore an evolution of the pre-shock chemical abundances to their equilibrium, during the time it takes for the initial J-type shock to become steady and C-type.

Between the high density models described in §5.6, only the flow speed varies in the upstream region. The upstream chemical abundances only vary with density, not shock speed. In dense regions the fractional ionization is at its lowest (§1.1.1 and §3.3.1). This means that only the ion-neutral reactions with the largest rate coefficients are able to alter the profiles of the neutral reaction partners. Because atomic oxygen is common in molecular clouds and H_3^+ is not, reaction 5 cannot noticeably deplete the oxygen abundance. Likewise, the $\sim 10\%$ of the neutral magnesium reservoir which is initially in the gas phase is sufficiently large compared to its reaction partners that none of the ion-neutral reactions involving magnesium are able to alter the Mg profile (7, 10, 11 and 16 in table 5.1). The abundances of neutral magnesium and oxygen consequently remain almost constant and very close to their initial boundary values of $\chi_{Mg} = (n_{Mg}/n_H) = 10^{-7}$ and $\chi_O = (n_O/n_H) = 4.25 \times 10^{-4}$ in the upstream region (see green,

dash dot and pink, long dash dot lines in the bottom left plots of figures 5.4 - 5.6).

As discussed in §5.3, ionization events in dense cores result from cosmic rays colliding with and ionising molecular hydrogen. Once formed, H_2^+ quickly reacts with another H_2 molecule to produce H_3^+ (see $*_1$ below table 5.1). The H_3^+ formation rate therefore depends on the cosmic ray ionization rate and the H_2 abundance (equation 5.6). The H_3^+ destruction rates depend on the abundances of O (reaction 5) and CO (reaction 2). These are all many (> 4) orders of magnitude less abundant than H_2 so the H_3^+ formation rate is larger than its destruction rate. Cosmic ray ionizations occuring at a rate of 3×10^{-17} s^{-1} in a medium with $n_H = 10^6$ cm^{-3} result in an upstream H_3^+ fractional abundance ($\chi_{H_3^+}$) of $\approx 10^{-11}$, independent of the shock speed (see pink, long dash dot lines in the top left plots of figures 5.4 - 5.6).

HCO^+ and Mg^+ are initially present in the upstream region, each with an abundance relative to H of 8.92×10^{-10} at $n_H = 10^6$ cm^{-3} and 8.92×10^{-9} at $n_H = 10^4$ cm^{-3} (see §5.5). The dissociative recombinations of molecular ions (reactions 6 and 15) have larger rate coefficients than the radiative recombinations of metallic ions (reaction 10) by factors of 10^4 at 10 K. Therefore, at equilibrium, there is more Mg^+ than HCO^+ in the upstream region despite them starting with the same abundances. In the high density regime, χ_{HCO^+} drops by a factor of almost 20 to $\sim 5 \times 10^{-11}$ due to electron recombinations and ion-neutral reactions with Mg (reaction 6 in table 5.1 and see the green, dash dot lines in the top left plots of figures 5.4 - 5.6). On the other hand, χ_{Mg^+} grows by a factor of ~ 5.5 to $\sim 5 \times 10^{-9}$ (see the solid blue lines in the top left plots of figures 5.4 - 5.6) because gas phase electron recombinations proceed extremely slowly whilst ion-neutral reactions removing HCO^+ augment the Mg^+ profile.

Although the other ionic and molecular species have initial abundances of zero, those values are not fixed at the upstream boundary and are out of equilibrium ahead of the shock. Therefore their abundances also evolve in this region, finding a stable equilibrium during the course of the simulations. Most notably this results in H_3O^+ being the most important molecular ion species in the upstream region. Since in this model atomic oxygen is the most common neutral species after H_2, reaction 5 dominates H_3^+ removal ahead of the shock despite having a feeble rate coefficient. This guarantees that the H_3O^+ abundance is non-zero. H_3O^+ is destroyed in gas phase reactions with Mg or free electrons. Both reactions provide a route to water which circumvents the endothermic neutral-neutral reaction with O (represented here by reaction 18). In this chemical model any H_3O^+ which forms can only be involved in reactions which convert

it to water. Similarly, water may only be converted back into H_3O^+. Because of the prevalence of oxygen, H_3O^+ becomes the most common molecular ion in the upstream region. Since the low temperature gas phase destruction reactions for H_3O^+ have rate coefficients orders of magnitude higher than its formation reaction. much of the H_3O^+ goes on to be converted into water upstream of the shock. Therefore, at equilibrium, H_3O^+ in the upstream region is typically around an order of magnitude more abundant than HCO^+, around an order of magnitude less abundant than Mg^+ and a factor of ~ 2 less abundant than water.

The equilibrium water abundances ahead of the shocks in these models are a factor of $\sim 10^3$ below those implied by standard ion-molecule chemical models ($\chi_{H_2O} \sim 10^{-6}$, e.g. Millar et al. 1997, Neufeld et al. 1995). They are however much closer to the findings of Bergin et al. (2000) who report that data from the Submillimeter Wave Astronomy Satellite (SWAS) infers water abundances of $\sim 10^{-8}$ in the quiescent molecular gas towards Orion, M17 and other sources. A more recent observation by Herschel of ortho-H_2O in a dark cloud (Caselli et al. 2010) infers $\chi_{H_2O} \sim 10^{-10}$. A possible cause of the difference is that in the current models carbon is assumed to be initially in CO rather than being atomic. This allows it to form HCO^+ which has a large rate coefficient for reactions with water. Thus the amount of water is limited and H_3O^+ becomes the most common molecular ion without recourse to postulating that oxygen freezes out onto grains as was done by Bergin & Snell (2002). Confirmation of this however will require further simulations.

The above discussion deals with the stable equilibrium found between the reactions in table 5.1 in cold, dense molecular regions devoid of any processes to deposit energy in the gas. The warmer, denser conditions found in a C-type shock facilitates further chemistry by overcoming reaction barriers and providing energy for endothermic reactions. In addition, the systematic streaming velocities induced between the charged species and grains permit efficient grain surface recombinations which have important effects on the fractional ionization. The shock conditions modify the chemical equilibrium between the species as well as producing species which are absent in unshocked regions (e.g. MgH^+).

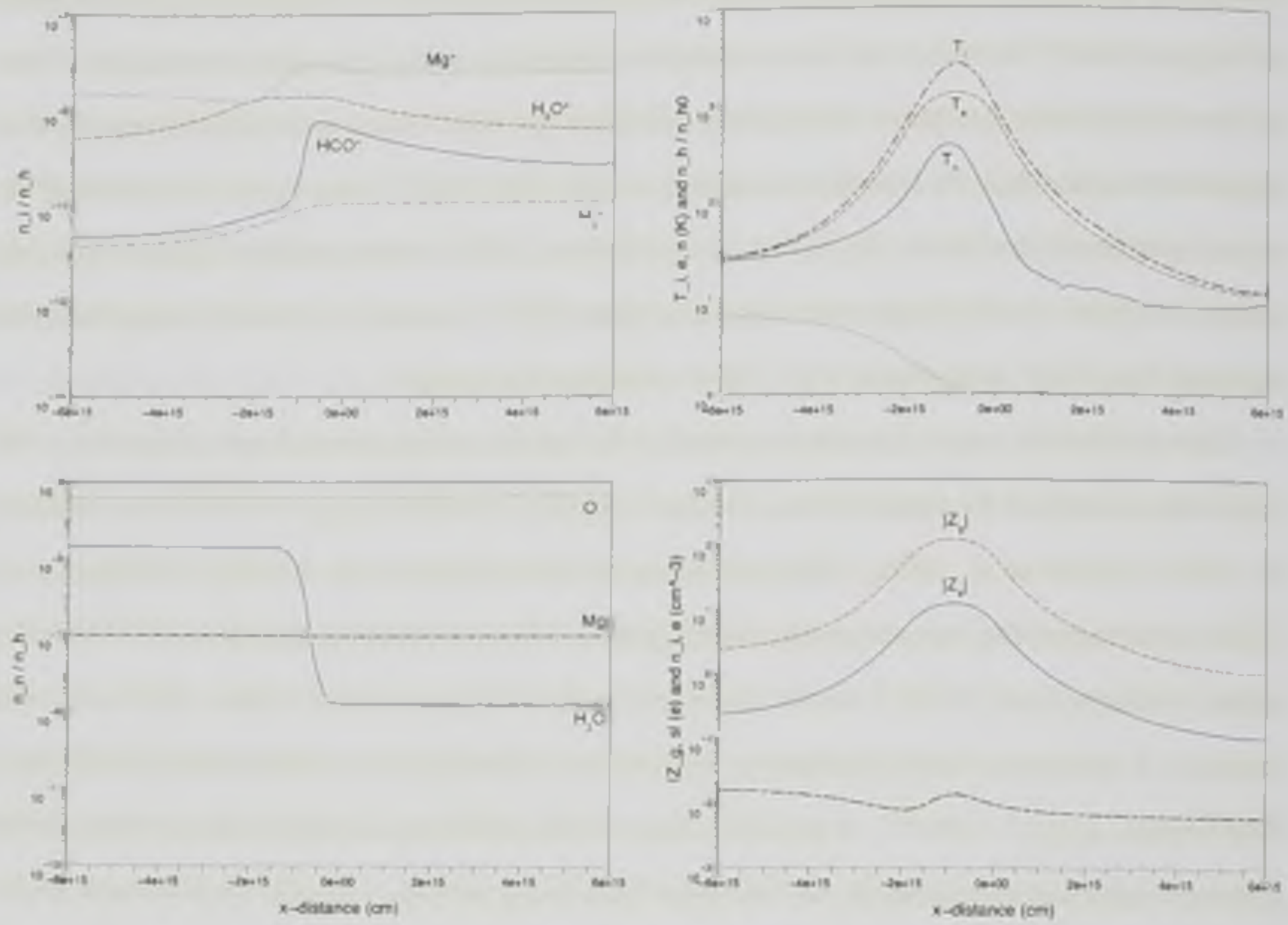

Figure 5.4: Structure of a v_s = 10 km s^{-1} shock propagating through a medium with n_H = 10^6 cm^{-3}. Top left displays the abundances relative to hydrogen of Mg^+ (green, dash dot), H_3O^+ (red, dash), HCO^+ (blue, solid) and H_3^+ (pink, long dash dot). Bottom left plots the abundances relative to hydrogen of O (green, dash dot), water (blue, solid) and Mg (pink, long dash dot). Top right are the temperatures of the ions (black, big dash dot), electrons (red, dash), and neutrals (blue, solid) as well as the fractional abundance of hydrogen normalised to its upstream boundary value (green, dash dot). Bottom right shows the absolute values of the large and (blue, solid) small (red, dash) grain charges and the gas phase number density of ions (green, big dash long dash) and electrons (black, dot dash).

5.7.1.2 Shock chemistry - high density models

The chemistry occurring in shocks is strongly dependent on the flow speed since faster shocks result in higher temperatures, larger ion-neutral streaming velocities and greater downstream densities. Higher temperatures are required for the endothermic reaction between Mg^+ and H_2 to proceed, which forms MgH^+. They also allow oxygen to be converted into water in

the gas phase. The shock conditions therefore amplify the rates of each of the reactions in table 5.1 except gas phase electron recombinations. Typically, a feature in the profile of a species can be attributed to a single reaction in table 5.1. A comparison of figures 5.4 - 5.6 therefore reveals how the relative importance of various reactions between the species change as the peak temperatures, compression ratios and drift velocities grow with shock speed. Gas phase dissociative and radiative electron recombinations favour low temperatures. Ion-neutral reactions favour high densities. Grain surface recombinations and atomic ion reactions favour high temperatures and drift speeds. Neural-neutral reactions requires high temperatures.

At the lowest shock speed (5 km s^{-1}), the chemistry is limited and is more like an extension of the upstream case. The compression is weak, only increasing the density by a factor of ~ 3. This still increases the formation rates of HCO^+ and H_3O^+ whilst a higher electron temperature suppresses their destruction in electron recombinations. Although temperatures are too low for the gas phase conversion of oxygen into water, the H_2O abundance does increase (by a factor of ~ 2) across the shock due to the presence of H_3O^+. Neutral magnesium is involved in gas phase reactions with HCO^+ and H_3O^+ but these species are typically factors of 10 - 100 less common so the profile of Mg also remains almost constant whilst the Mg^+ abundance initially rises. In the hottest part of the shock, grain surface recombinations reduce the abundances of all ionic species (as well as the fractional ionization). Grain surface recombinations stall as temperatures fall in the downstream region and are replaced by ion-neutral reactions in the denser post-shock gas. These ion-neutral reactions (2, 3, 5, 7, 8, and 16) further reduce the abundances of H_3^+, HCO^+ and H_3O^+, but since Mg^+ is not modeled to participate in such reactions, its abundance levels off earlier. By the time equilibrium is reached, the abundances of all charged species are lower than they were in the upstream region, ensuring that the fractional ionization is lower in the denser, post-shock gas, as it should be.

With a shock speed of 10 km s^{-1} (figure 5.4) temperatures remain low enough that only a very small fraction of the atomic oxygen (~ 4.6 %) is converted into water. This change is barely discernible on the oxygen profile. Therefore, the profiles of O and Mg again remain almost constant. At the upstream edge of the shock the abundances of the molecular ions rise as the electron temperature suppresses dissociative recombinations and now a small amount of water is released into the gas phase via sputtering of the small grain mantles (see §5.7.2.1).

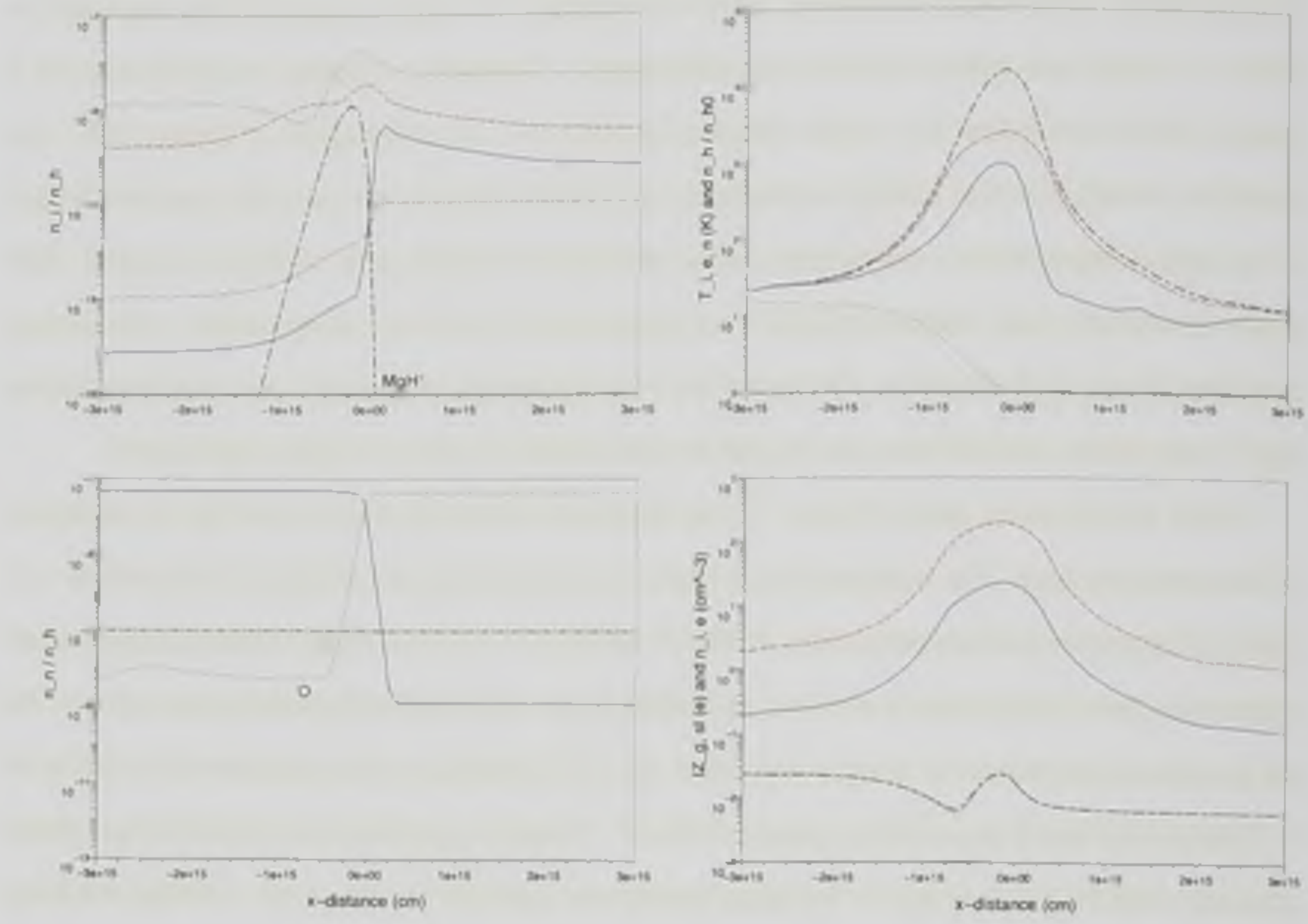

Figure 5.5: Same as figure 5.4 but for a shock speed of $v_s = 20$ km s^{-1}. The black, dash dot line on the ion abundance plot (top left) represents MgH^+.

Even though only 0.5% of the small grain mantles are eroded, the fact that almost 5 % of the atomic oxygen is converted in the gas phase causes χ_{H_2O} to grow by four orders of magnitude (from 2×10^{-9} to 2×10^{-5}). The existence of appreciable gas phase water has important consequences for the chemistry. As soon as water is present in the gas phase in larger concentrations than neutral magnesium, new reaction pathways for H_3^+ and HCO^+ become dominant. At this shock speed however it is the onset of gas phase oxygen conversion rather than mantle sputtering that provides the water to instigate these new reactions.

Once the H_2O abundance overtakes that of Mg, reactions 3 and 8 dominate the destruction of H_3^+ and HCO^+. H_3^+ reacts with water with a rate coefficient that is ~ 3.5 times larger than that for reactions with CO and ~ 7 times larger than for reactions with O. The H_3^+ abundance therefore starts to drop as soon as $\chi_{H_2O} > \chi_{Mg}$. At exactly the same point, the abundance of HCO^+ also falls. Because it is so much more abundant than H_3^+, many more reactions between HCO^+ and water occur and these are able to lower χ_{HCO^+} by a factor of ~ 60.

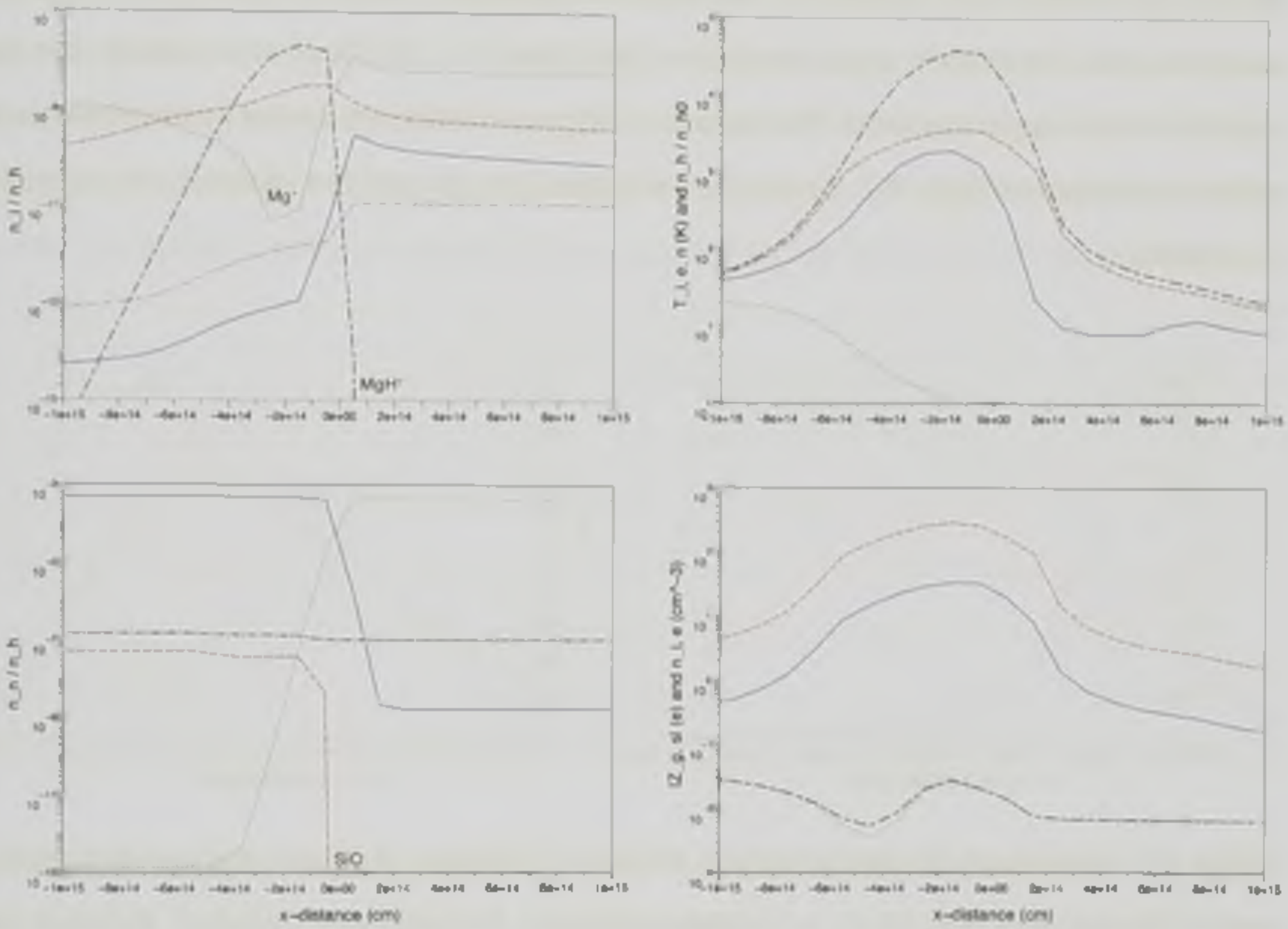

Figure 5.6: Same as figure 5.4 but for a shock speed of $V_s = 30$ km s^{-1}. The red dash line on the neutral abundance plot (bottom left) represents SiO.

When the gas phase water abundance reaches its maximum, the steep fall in the HCO^+ profile stops, by which time it has a similar abundance to H_3^+. This happens in the hottest part of the shock where (as at the lowest shock speed) grain surface recombinations again come to dominate, reducing the fractional ionization. The abundances of H_3^+, HCO^+ and Mg^+ fall whereas the rise in H_3O^+ is arrested. As the temperature falls so do the ion-grain currents, but the density is still rising so ion-neutral reactions become important. These preferentially convert H_3^+ and HCO^+ into H_3O^+ and H_3O^+ into Mg^+. The abundances of the molecular ions again fall in unison to their downstream equilibrium over this region, whereas that of Mg^+ initially increases due to the ion-neutral reactions and levels off further upstream.

With a shock speed of 20 km s^{-1} (figure 5.5), all of the small grain mantles are vaporized as are $\sim 35\%$ of the large grain mantles (see §5.7.2.1). Temperatures in the shock become sufficiently high for the gas phase conversion of oxygen to proceed in earnest lowering the downstream O abundance by almost five orders of magnitude. Because the small grain mantles

account for around three quarters of the total ice abundance and most gas phase oxygen is converted, the downstream water abundance (just below $5 \times 10^{-4} n_H$) now includes the vast majority of the oxygen reservoir. The amount of oxygen converted at several intermediate shock speeds is included as figure 5.7. Several new features have also become visible in the molecular ion profiles.

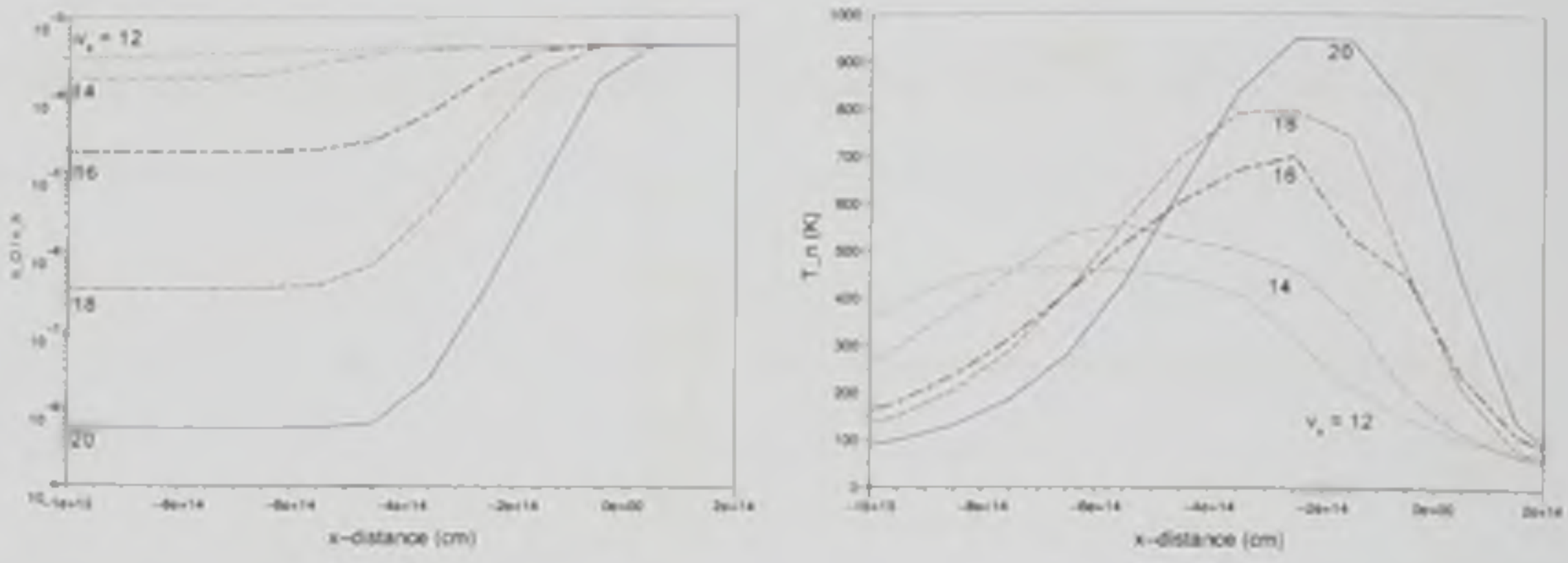

Figure 5.7: Abundances of atomic oxygen, relative to hydrogen (left plot) and neutral temperatures in Kelvin (right plot) for $v_s = 12$ (green, dash dot), 14 (pink, long dash dot), 16 (black, big dash dot) 18 (red, dash) and 20 km s^{-1} (blue, solid).

The steep fall in the HCO^+ profile is now much larger (a factor of $\sim 3 \times 10^3$ as opposed to 60 at 10 km s^{-1}), due to the copious amounts of water now present. Its downstream abundance is now more than an order of magnitude lower than H_3^+. The destruction of HCO^+ in reactions with water results in a large rise of H_3O^+, caused by reaction 8. The gentle rise noted for lower shock speeds now has an extra peak superimposed on it which coincides spatially with the steep falls in HCO^+ and H_3^+. H_3O^+ does not react with water and it is the most common molecular ion by at least a factor of 4 throughout the shock. This allows ion-neutral reactions with Mg to remain important, converting it into Mg^+. The profile of Mg^+ consequently follows that of H_3O^+ in this region.

At this shock speed, the ions achieve high enough temperatures and streaming velocities with respect to the neutrals to permit the formation of MgH^+. Already by this shock speed, sufficient MgH^+ is formed ($\sim 10^{-9}$) for it to become more common than either HCO^+ or H_3^+ in the hottest parts of the shock. Its abundance at various intermediate shock speeds is included as figure 5.8. When MgH^+ is efficiently formed, it halts the rise in the Mg^+ profile since any

Mg^+ formed from ion-neutral reactions involving H_3O^+ is quickly converted to MgH^+. Like at other shock speeds, all of the ion abundances drop in the hottest parts of the shock due to an increase in grain surface recombinations. The fractional ionization now falls more since ion-grain currents increase with temperature, drift speed and density, all of which are larger in faster shocks and the rate coefficients for MgH^+ recombinations are higher than for other species.

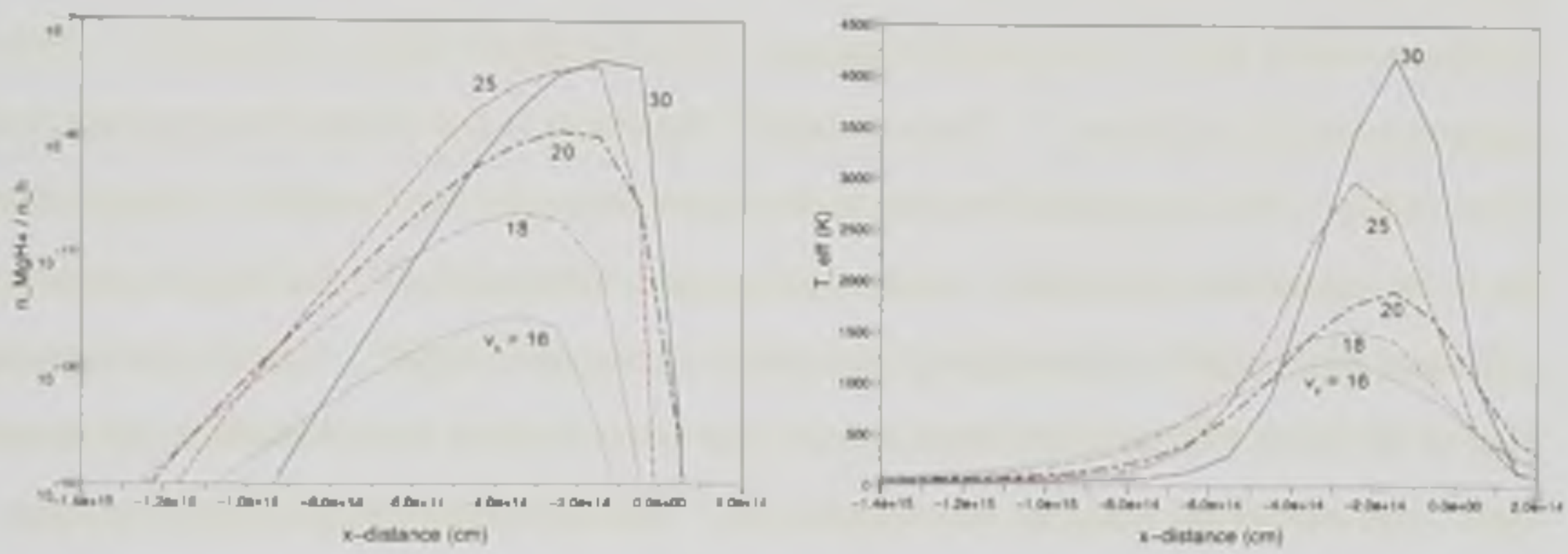

Figure 5.8: MgH^+ abundance relative to hydrogen (left plot) and effective temperature (right plot) for v_s = 16 (green, dash dot), 18 (pink, long dash dot), 20 (black, big dash dot) 25 (red, dash) and 30 km s^{-1} (blue, solid). The effective temperature is given by equation (5.1) and represents the kinetic temperature of the ions at the ion-neutral drift speed. It is measured in Kelvin.

As the temperatures and drift speeds begin to fall and the densities continue to rise towards the downstream region, like at lower shock speeds, ion-neutral reactions in the gas phase become more efficient than recombinations on grains. Although these tend to involve water and form H_3O^+, H_3O^+ is already so abundant that its fractional increase is not significant. When MgH^+ is destroyed in grain surface recombinations it forms Mg. The prevalence of ion-neutral reactions in this region then ensures that much of the new Mg quickly reacts with H_3O^+ to yield Mg^+. The profiles for MgH^+ and H_3O^+ therefore fall whilst Mg^+ rises. Near the downstream edge of the shock where temperatures are low, gas phase electron recombinations become important for MgH^+. These reactions ensure that the profile of Mg^+ levels out and the MgH^+ abundance returns to zero.

With v_s = 30 km s^{-1} (figure 5.6), all of the grain mantles are sputtered and the abundance of oxygen has dropped by almost ten orders of magnitude in the downstream region. The down-

stream water abundance now includes very nearly all of the oxygen reservoir and now reaches its maximum of 5×10^{-4}, with the downstream oxygen abundance becoming comparable to that of H_3^+. At this shock speed core sputtering of the small grains is able to proceed and the SiO abundance becomes non zero (see §5.7.2.4). Small grain core sputtering also results in a modest rise of the neutral magnesium abundance. The ion profiles are similar to the 20 km s^{-1} case, except that in the hottest part of the 30 km s^{-1} shock MgH^+ becomes the most common ion. Because so much Mg^+ is converted by reaction 12, its abundance falls by a factor of ~ 2500 as opposed to just 35 at 20 km s^{-1}. The peak MgH^+ abundance is now higher than the peak abundance of Mg^+. This is possible because in the region where the Mg^+ profile is already falling due to its conversion into MgH^+, ion-neutral reactions between H_3O^+ and Mg are producing additional Mg^+ which is immediately converted to even more MgH^+. Near the downstream edge of the shock (like at other shock speeds), gas phase electron recombinations still remove MgH^+ and ion-neutral reactions still augment Mg^+ until downstream equilibrium is reached.

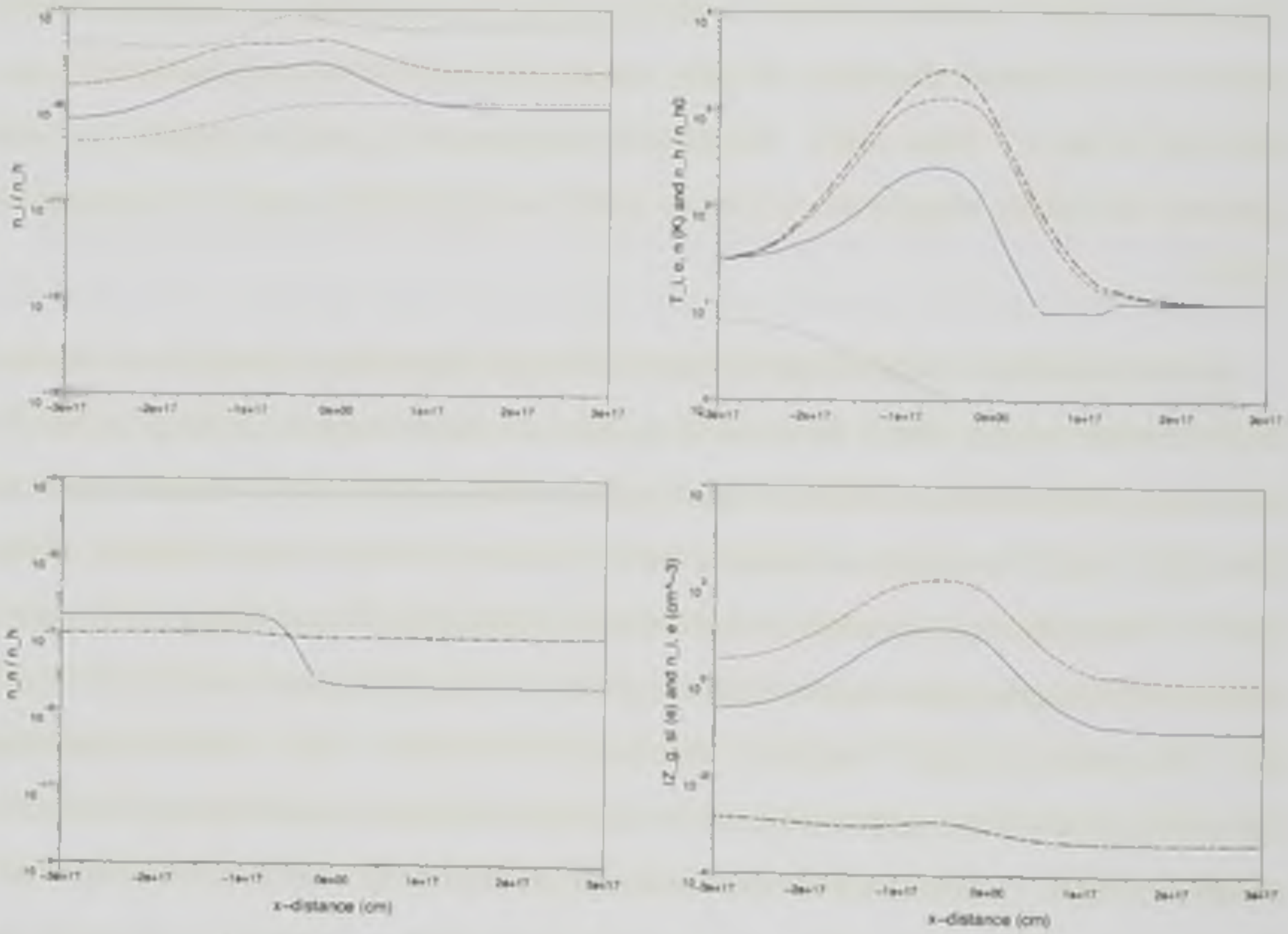

Figure 5.9: Same as figure 5.4 but for an upstream density of $n_H = 10^4$ cm^{-3}. Shock speed is 10 km s^{-1}.

5.7.1.3 Low density models

When the upstream density is reduced by a factor of 100 to $n_H = 10^4$ cm^{-3}, the upstream fractional abundances of all neutral species initially present remain constant because of the limited chemical network considered. Since the fractional ionization is higher at low densities, the ion and electron number densities only fall by a factor of 10 so the fractional abundances of the initial charged species grow by a factor of 10. Oxygen is still many orders of magnitude more common than every charged species. Therefore, similarly to the high density cases, its upstream profile is unaffected by upstream chemistry and remains very near to its initial abundance of 4.25×10^{-4}.

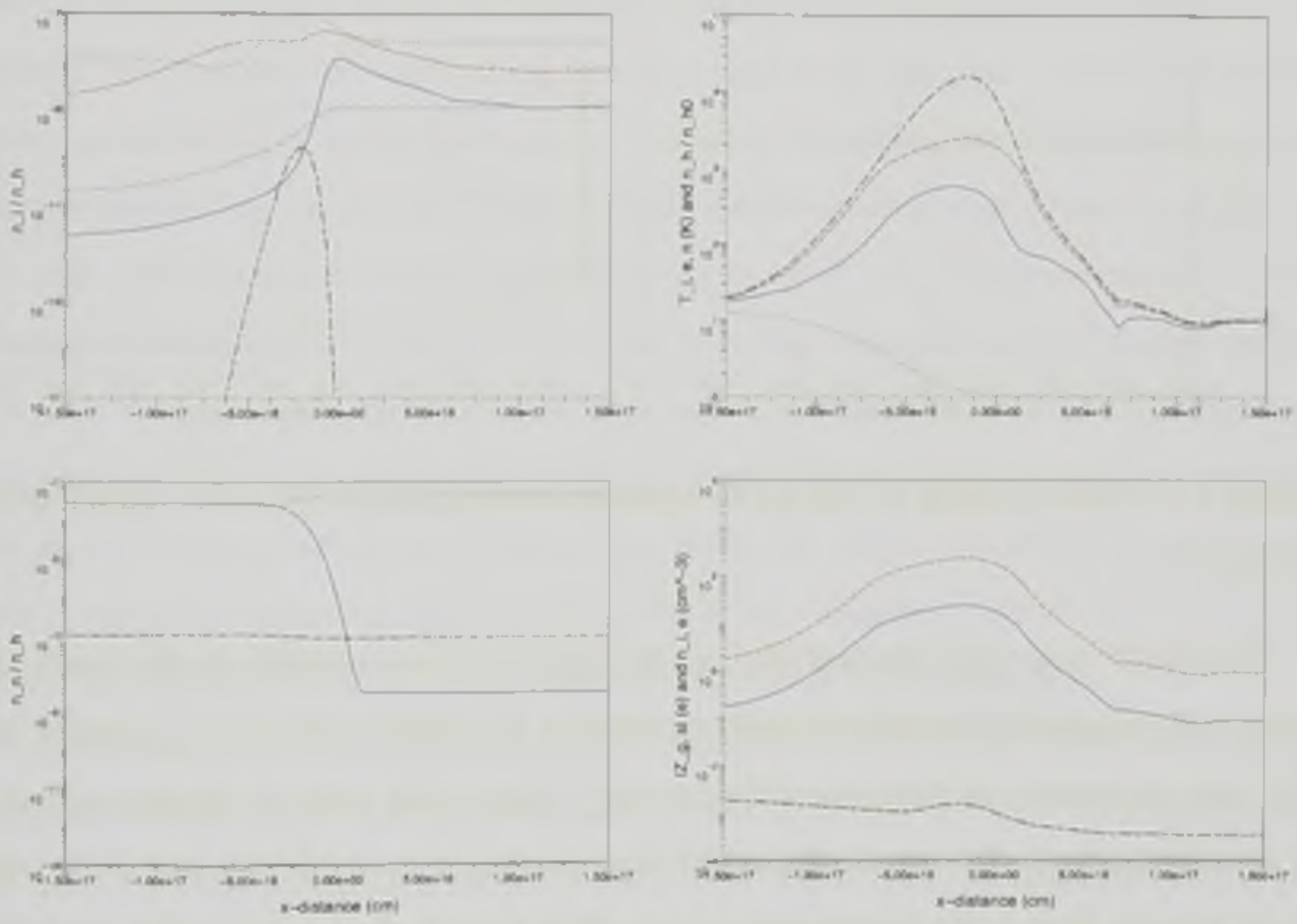

Figure 5.10: Same as figure 5.6 but for an upstream density of $n_H = 10^4$ cm^{-3}. Shock speed is 20 km s^{-1}.

HCO^+ and Mg^+ are now initially ten times more abundant (8.95×10^{-9}) in the upstream region. Again similarly to the high density models, H_3O^+ becomes the most common molecular ion ahead of the shock, despite having an initial abundance of zero. The equilibrium between the reactions which occur in the upstream region results in a HCO+ abundance which is enhanced

by a factor of 14 to $\sim 10^{-9}$ and a H_3O^+ abundance which is enhanced by a factor of 12.5 to $\sim 6 \times 10^{-9}$ over the high density cases (see figures 5.9 - 5.11).

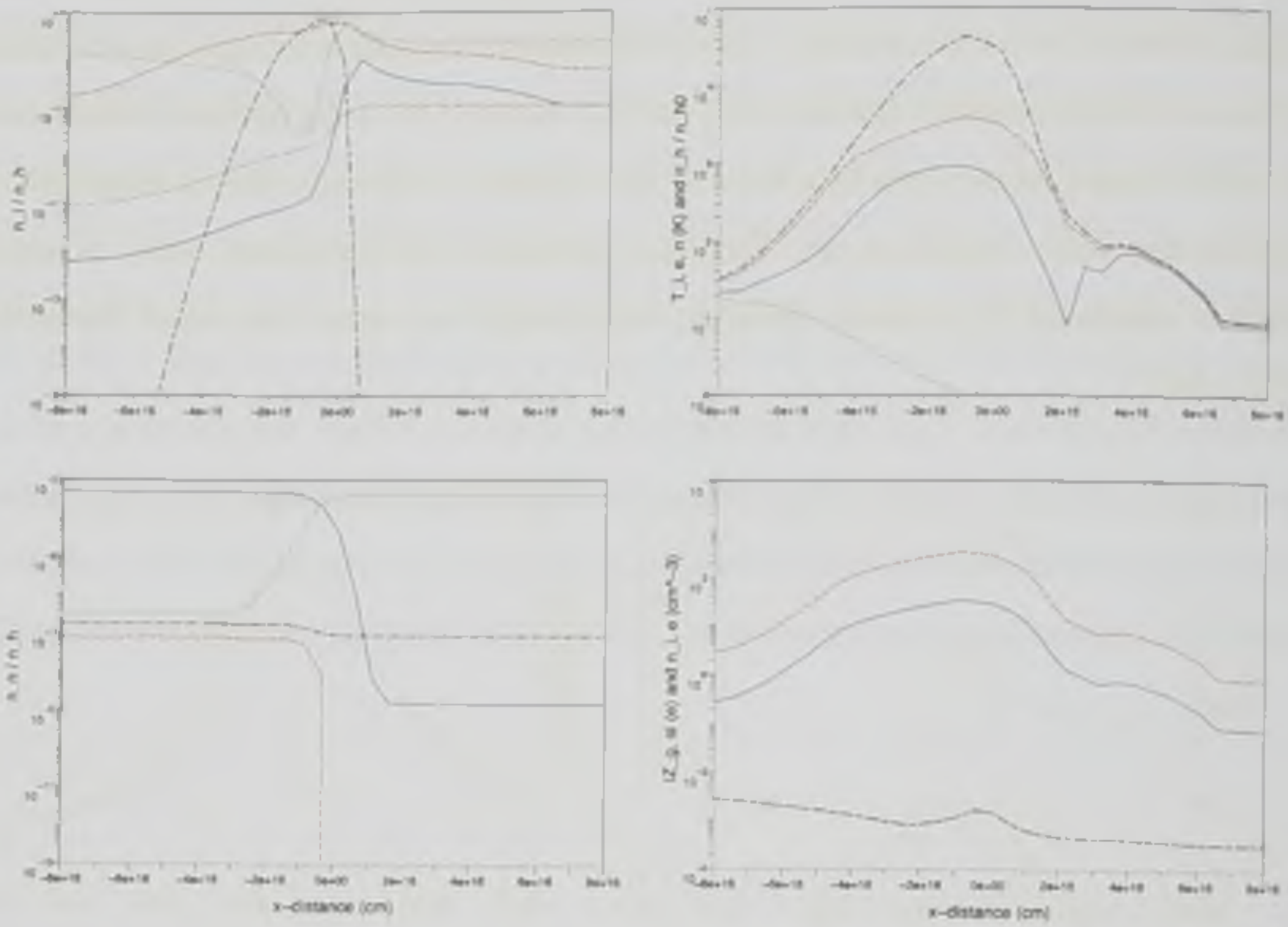

Figure 5.11: Same as figure 5.4 but for an upstream density of $n_H = 10^4$ cm^{-3}. Shock speed is 30 km s^{-1}.

Like H_3O^+ and water, Mg and Mg^+ are the only two forms available (in the upstream region) to the magnesium initially included on the grid. The initial value for χ_{Mg} remains 10^{-7}. The only destruction mechanism available to Mg^+ ahead of the shock is radiative recombinations with electrons. The rate coefficient for such reactions is a couple of orders of magnitude lower than for either of the ion-neutral reaction which form Mg^+ (7 and 16). Consequently the upstream Mg^+ abundance at equilibrium is $\sim 2.5 \times 10^{-8}$ (a factor of ~ 4 higher than the high density models) but the abundance of neutral magnesium drops slightly to $\sim 8.25 \times 10^{-8}$ due to an increase in the abundances of the partners for reactions 7 and 16.

Upon entry to the shocks, many of the same reactions occur in the low density regime so the profiles of H_3^+, Mg^+ and H_3O^+ are qualitatively similar across the two density cases when the shock speed is the same. The profiles of H_3O^+ are especially similar. The compression ratios

remain the same as they were in the high density models. Because the ions are assumed not to cool radiatively and the model includes only a single cooling mechanism for electrons (see §2.5.3 and chapter 3), the peak temperatures of both fluids are largely independent of the upstream density. The neutrals however reach only around half the temperatures in the low density models compared to the high density cases due to less collisional heating. The fractional ionization falls less in the hottest parts of low density shocks because grain surface recombinations are less prevalent when there are fewer collisions (ion-grain currents and grain charge are both lower).

At $v_s = 10$ km s^{-1} (figure 5.9), the HCO^+ profile looks very different from the high density case since it lacks the steep fall due to reactions with water (see figure 5.4). Most of the water in the $n_H = 10^6$ cm^{-3} model had become available because the peak neutral temperature of 380K permitted the conversion of $\sim 6\%$ of the atomic oxygen in the gas phase. In the low density regime, the neutrals only reach 250 K and no oxygen is converted. The water abundance still rises by a factor of 7 across the shock because there is still a small amount of mantle sputtering, but it only surpasses that of atomic magnesium by a factor of ~ 3. This stops reaction 8 from removing anywhere near as much HCO^+ as it did at the equivalent shock speed at high density. At 20 km s^{-1} (figure 5.10), the water abundance rises almost as much as in the equivalent high density case so H_3^+ and HCO^+ again fall steeply (see figure 5.10). The lower concentration of all species however means that reactions with water now only cause HCO^+ to drop by 2.5 orders of magnitude instead of the 3.5 orders noted at $n_H = 10^6$ cm^{-3}. By 30 km s^{-1} however (figure 5.11), the H_3^+ and HCO^+ profiles look much the same at both densities.

A lower fraction of the oxygen reservoir is converted to water in the gas phase at each shock speed in the low density regime. With an upstream density of $n_H = 10^6$ cm^{-3} and shock speed of 20 km s^{-1}, the peak neutral temperature reaches 950 K, allowing the abundance of oxygen to drop by a factor of $\sim 10^5$. With $n_H = 10^4$ cm^{-3}, the neutrals only achieve 600 K and the oxygen abundance consequently only falls by a factor of ~ 2. Because initially most of the oxygen is in atomic form, the downstream water abundance remains lower by a factor of 2.5 in the low density regime even though the mantle sputtering of both grain fluids is total (see §5.7.2.1). Even at 30 km s^{-1} the oxygen abundance falls by ~ 6 orders of magnitude less in the low density regime than it did in the equivalent high density simulation. It is not until $v_s = 50$ km s^{-1} that the downstream oxygen abundance drops by more than five orders of magnitude

from its upstream value.

The formation of MgH^+ is also inhibited at low densities due to the dependence of T_{eff} on T_n in its formation rate coefficient (see §5.3.3). At v_s = 20 km s^{-1} ten times less MgH^+ is formed. Well above the threshold for MgH^+ formation, the availability of more Mg^+ at low densities due to the higher fractional ionization allows more MgH^+ to be created. At 30 km s^{-1}, the peak abundance of MgH^+ is four times higher than in the equivalent 10^6 cm^{-3} simulation because Mg^+ is more common by the same factor (see figure 5.11).

5.7.2 Sputtering

5.7.2.1 Mantle sputtering - high density models

A number of high density ($n_H = 10^6$ cm^{-3}) simulations were completed over the range $5 \leq v_s \leq 25$ km s^{-1}. This range was sufficient to reveal the sputtering thresholds and the shock speeds required for complete erosion of the mantles of both grain species (see table 5.2). The small grains have had their mantles removed when v_s = 18 km s^{-1}, but the large grain mantles are not totally sputtered until v_s = 25 km s^{-1}. The threshold shock speeds vary by grain fluid at high densities because the large grains are only weakly coupled to the magnetic field due to frequent collisions with neutrals: Even though each large grains carries a factor of ~ 10 as many electrons as each small grain, each weighs 1000 times more and presents a larger collision cross section with the neutrals by a factor of 100. The large grains therefore move with velocities in between the neutrals and the other charged fluids, meaning that their peak drift speeds relative to the neutrals are lower than those of the small grains and higher shock velocities are required for them to pass the sputtering threshold.

Sputtering by any projectile is absent when v_s = 5 km s^{-1}. At 6 km s^{-1} only the heaviest projectiles (CO and Mg) successfully sputter the small grain mantles, but the ice is ejected in miniscule amounts so the fraction of ice sputtered and gas phase water enhancements may safely be rounded to zero.

At v_s = 8 km s^{-1}, all projectiles except H_2 sputter the mantles of both grains species, but at rates which remain too low to result in appreciable erosion of the ice ($>> 0.01$ %, see table 5.2). The downstream gas phase fractional abundance of water reaches only 3×10^{-8}, a concentration which can easily be ascribed to H_3O^+ chemistry and shock compression.

		Large grains		Small grains	
Shock Speed (km s^{-1})	n_{H0} (cm^{-3})	Fraction of ice removed	Contribution to downstream H_2O	Fraction of ice removed	Contribution to downstream H_2O
10	1.00(4)	1.20(-3)	3.09(-8)	3.80(-3)	2.09(-7)
12	1.00(4)	4.00(-2)	1.04(-6)	5.50(-2)	3.03(-6)
14	1.00(4)	1.75(-1)	3.05(-6)	2.00(-1)	1.10(-5)
16	1.00(4)	4.50(-1)	7.83(-6)	4.80(-1)	2.64(-5)
20	1.00(4)	1.00	1.74(-5)	1.00	5.51(-5)
8	1.00(6)	0.00	-	0.00	-
9	1.00(6)	0.00	-	$<<$1.00(-4)	$\approx$ 0.00
10	1.00(6)	0.00	-	5.00(-3)	2.75(-7)
12	1.00(6)	2.50(-3)	4.36(-8)	6.95(-2)	3.83(-6)
14	1.00(6)	2.50(-2)	4.36(-7)	2.63(-1)	1.45(-5)
15	1.00(6)	5.00(-2)	8.71(-7)	4.25(-1)	2.34(-5)
16	1.00(6)	7.78(-2)	1.36(-6)	6.07(-1)	3.34(-5)
18	1.00(6)	1.8(-1)	3.14(-6)	1.00	5.51(-5)
20	1.00(6)	3.4(-1)	5.93(-6)	1.00	5.51(-5)
25	1.00(6)	1.00	1.74(-5)	1.00	5.51(-5)

Table 5.2: Fractions of ice removed from large and small grains at various shock speeds and upstream densities. The large and small grain fraction columns refer to the fraction of the ice residing on a grain species at the upstream boundary which is in the gas phase by the downstream boundary. The contribution columns give the gas phase water enhancement (relative to hydrogen) due to the mantle sputtering of the grain fluid. Although some small grain sputtering did occur in the 9 km s^{-1}, $n_H = 10^6$ cm^{-3} case, the fraction of ice removed is < 0.01 %.

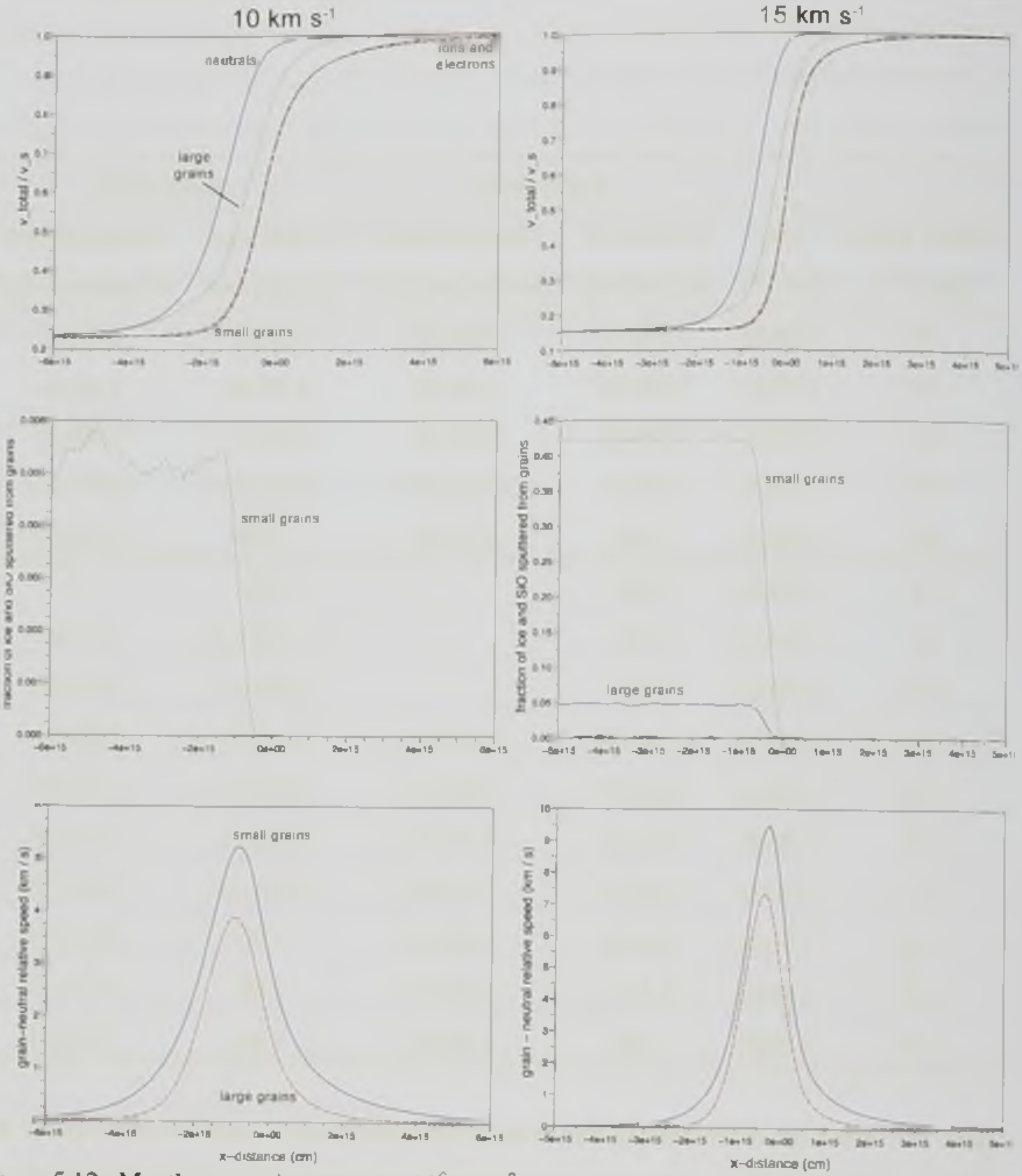

Figure 5.12: Mantle sputtering at $n_H = 10^6$ cm^{-3}, with v_s = 10 km s^{-1} (left column) and 15 km s^{-1} (right column) shocks. Top row shows the total velocities of the neutrals (blue, solid), ions and electrons (red, dash), large grains (green, dotted) and small grains (black, dash dotted) normalised to the shock velocity. Middle row displays the fraction of ice removed from the grain fluids, i.e. the fraction of ice which was on the grains at the upstream boundary but which is in the gas phase as water at the downstream boundary. The ice initially associated with the small grains is given by the green, dotted lines and that associated with the large grains by the blue, solid lines. The bottom row gives the grain-neutral relative speeds (km s^{-1}) for large grains (red, dash) and small grains (blue, solid).

Sputtering is therefore still assumed to be absent.

At 9 km s^{-1} the post-shock water abundance (4.5×10^{-7}) rises above the threshold defined by Caselli et al. (1997) (see §5.7.2.3), but this is caused by a tiny fraction of the atomic oxygen being converted to water in the gas phase, confirmed by the fact that the sputtering rates remain low (see table 5.3). It is not until v_s = 10 km s^{-1} that a significant fraction of the small grain mantles are eroded, implying that sputtering has become an effective process (see left column of figure 5.12).

The absolute threshold drift speed for even the most energetic collisions involving the heaviest projectiles to be capable of mantle sputtering is between 1.3 and 2.4 km s^{-1}, which are the peak drift speeds in the 5 and 6 km s^{-1} shocks respectively. However drift speeds of 5 - 6 km s^{-1} (which occur in the 9 and 10 km s^{-1} shocks respectively) are required for erosion to be systematic and appreciable. This speed is independent of the grain species, as one would expect because the mantle molecules are bonded with the same energy.

With v_s = 10 km s^{-1}, 0.5% of the small grain mantles are vaporized, raising the gas phase water abundance by 2.75×10^{-7}. Just this percentage of the small grain mantles plus the conversion of 6% of the atomic oxygen is sufficient to increase the gas phase water abundance past that of magnesium, instigating the chemical reactions involving water which were noted in §5.7.1.2 (see figure 5.4). By increasing the shock velocity to 12 km s^{-1}, the fraction of the small grain mantles which are sputtered grows by a factor of $\sim$ 14 to 7 %. The large grains have also passed the sputtering threshold by this speed, with 0.25% of their mantles being vaporized.

At 14 km s^{-1}, the sputtered fraction of the large grain mantles increases by a factor of 10 and that of the small grain mantles by a factor of 3.8 (see right column of figure 5.12). Further increases in the shock velocity raise the sputtered mantle fraction by progressively smaller amounts until all the ice is vaporized. The fraction of ice released from each grain species at each shock speed is included as figure 5.14.

At shock speeds too low to completely erode the mantles, the width of the sputtering region is determined by the distance for which the grain-neutral drift speed is above the sputtering threshold. This can be seen from the middle and bottom rows of plots in figure 5.12. Once the mantles are completely vaporized, further increases in the shock speed simply narrow the sputtering region because the grain-neutral velocity profiles pass the threshold speed with ever larger gradients. This is obvious from a comparison of figures 5.12 and 5.13.

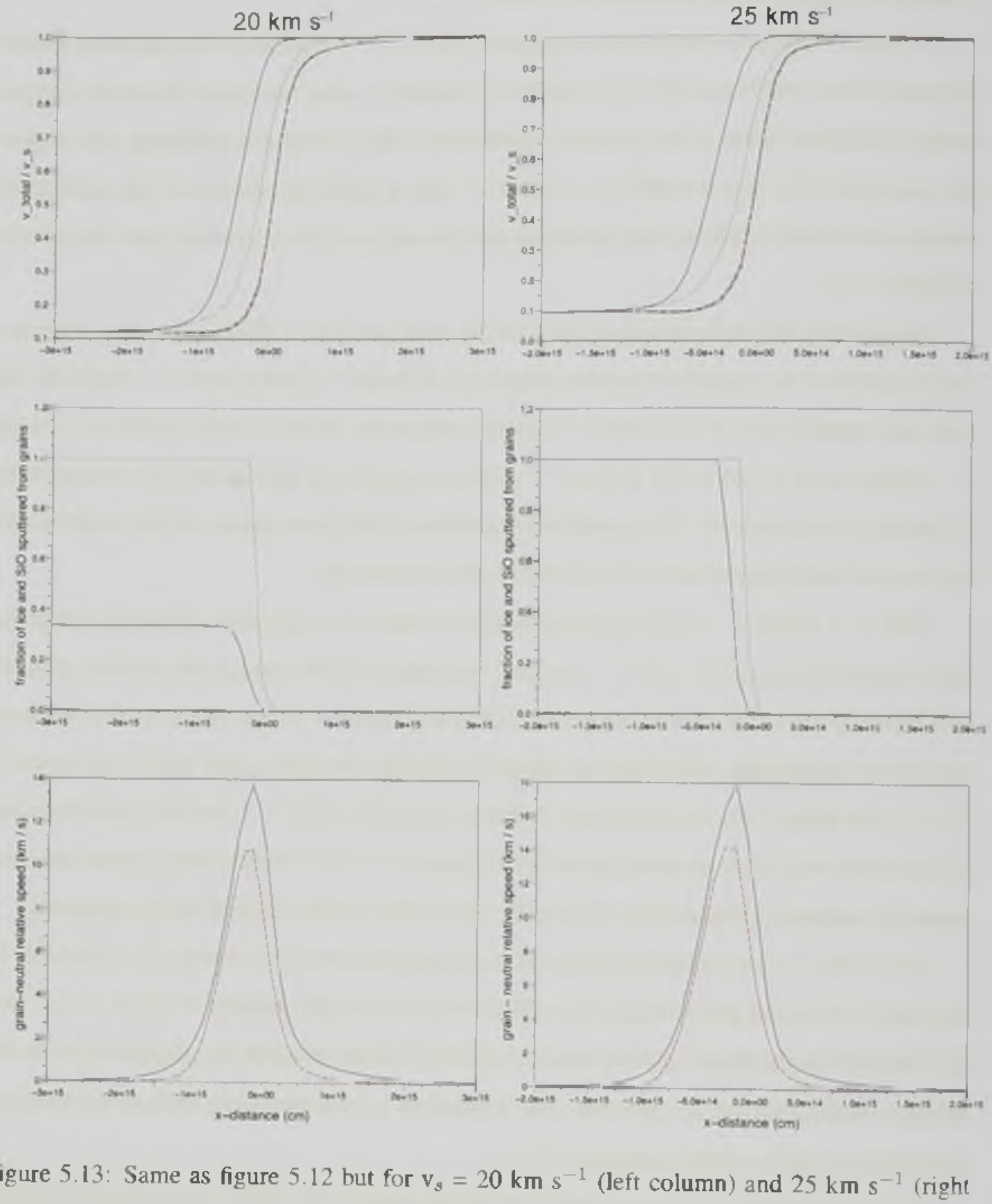

Figure 5.13: Same as figure 5.12 but for $v_s = 20$ km s^{-1} (left column) and 25 km s^{-1} (right column) shocks.

Between 25 and 30 km s^{-1} the sputtering region narrows by ~ 40 %. As well as reducing the time taken to vapourise the mantles, increasing the shock speed also affects the relative contributions of the various projectiles. Steeper gradients in the grain-neutral velocity profiles

result in the threshold drift speeds for the various projectiles becoming closer to each other in space, eventually becoming almost coincident. When all projectiles commence sputtering at almost the same point and the drift speed is high enough that all are well above threshold, the sputtering rates due to lighter but more common molecules (H_2) become more significant (see below). The peak sputtering rates ($cm^{-3}s^{-1}$) over the grid, for each projectile sputtering ice in shocks of various speeds which propagate through media with $n_H = 10^6$ cm^{-3} are included as table 5.3.

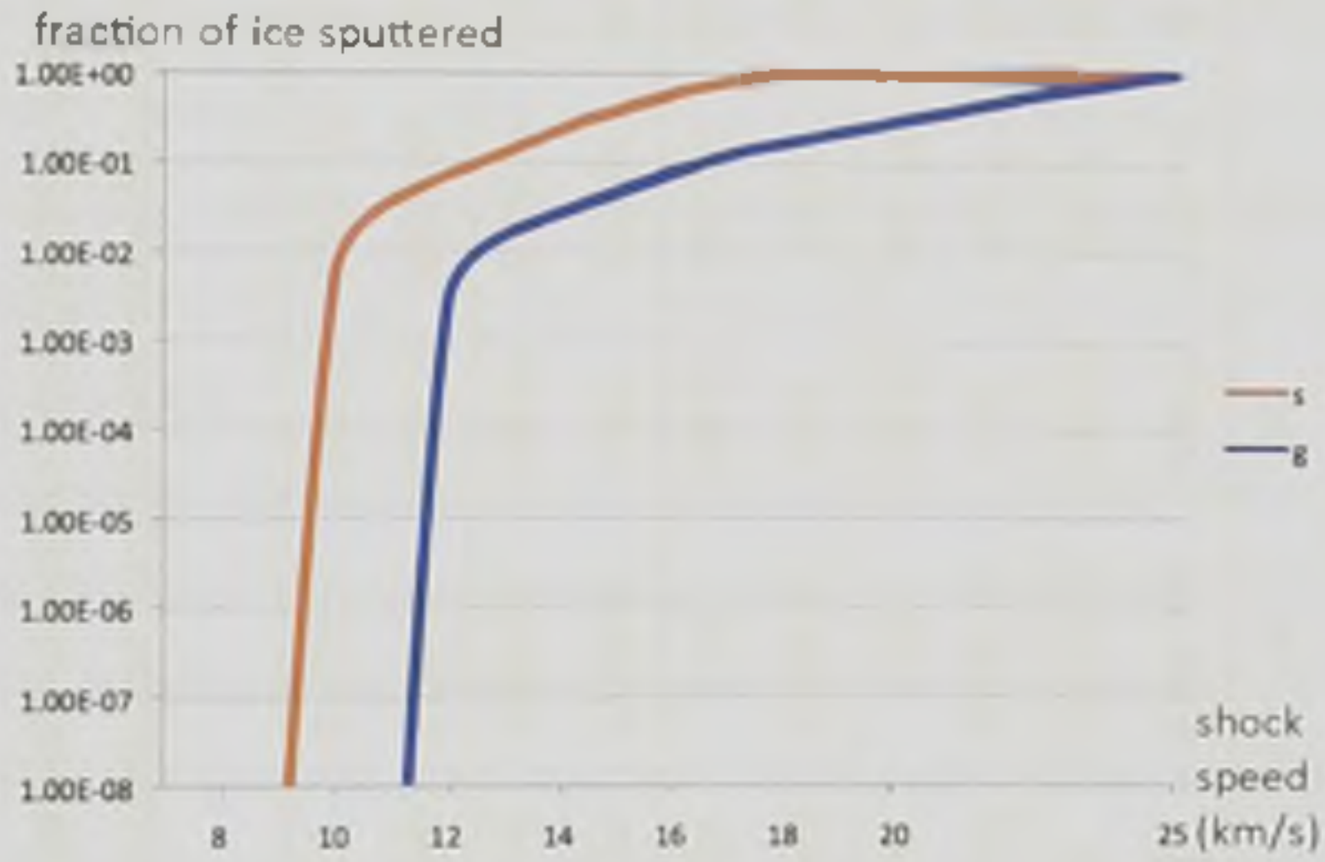

Figure 5.14: Fraction of ice sputtered from large (blue) and small (red) grains at various shock speeds.

The small grain mantles are totally sputtered at $v_s = 18$ km s^{-1}. At shock speeds above this the effectiveness of some projectiles falls due to their lower abundances. These are highlighted in red in table 5.3. The yield of each projectile follows the shape of the curves shown in figure 5.1. This means that at impact energies above the threshold for the lightest projectiles, the yields of all the species converge. Because molecular hydrogen is at least a factor of 10^3 more common than any other species, it is involved in many more collisions with grains. When its yield is within a couple of orders of magnitude of the heavier species, the H_2 sputtering rate is able to overtake those species. There are only a finite number of ice molecules in the grain mantles so as the lighter but more abundant projectiles become more effective, they do so at the expense of the less abundant heavier species which dominated at lower shock speeds. This is why the sputtering rates of CO, water and Mg fall at the highest shock speed.

Projectile Species and	Grain	Shock speed (km s^{-1})						
Adopted Mass (AMU)	Type	5	8	10	14	18	20	25
H_2	large	0.00	0.00	3.80(-16)	2.62(-7)	3.85(-1)	5.76	725.25
(2)	small	0.00	0.00	7.62(-12)	9.70(-3)	93.15	980.74	1.32(3)
CO	large	0.00	2.73(-11)	2.04(-2)	5.32	42.79	81.56	299.44
(28)	small	0.00	7.01(-3)	3.51	114.06	651.75	1.15(3)	727.73
O	large	0.00	6.35(-19)	3.49(-4)	6.52	15.25	18.71	29.93
(16)	small	0.00	8.74(-8)	1.74	250.24	545.62	672.49	1.24(3)
H_2O	large	0.00	1.47(-22)	2.04(-5)	4.05	119.21	265.63	1.24(3)
(16)	small	0.00	9.17(-12)	4.46(-2)	116.39	2.13(3)	4.27(3)	1.79(3)
Mg	large	0.00	2.04(-16)	7.28(-6)	5.23(-3)	5.01(-2)	1.00(-1)	9.83(-1)
(24)	small	0.00	5.99(-7)	2.75(-3)	1.25(-1)	8.17(-1)	1.50	4.11(-1)

Table 5.3: Peak sputtering rates (cm^{-3} s^{-1}) for the projectiles listed removing ice from each grain species in simulations where $n_H = 10^6$ cm^{-3} in the upstream region. The figures included in the table represent the peak cell values across the grid. These do not occur in the same cells for each species. Numbers in parentheses denote powers of ten and those in red are discussed in the text.

In summary, in simulations of shock speeds well above the threshold of for total mantle erosion, the yields of the various projectile species converge. H_2 comes to dominate the sputtering of both grain types for $v_s > 30\,\mathrm{km\ s^{-1}}$ due to its high abundance.

5.7.2.2 Mantle sputtering - low density models

In the $n_H = 10^4\ \mathrm{cm^{-3}}$ models, the large grains have higher drift speeds with respect to the neutrals (by almost 25% at 20 km $\mathrm{s^{-1}}$) because they are now better coupled to the field and move with the other charged species. The small grains however also have a higher drift speed in the low density models (by $\sim 0.5\%$ at 20 km $\mathrm{s^{-1}}$), due to lower collision rates in more rarefied media. Lower collision rates also result in lower neutral temperatures since there is less collisional heating. In a 20 km $\mathrm{s^{-1}}$ shock, T_n reaches only 560 K at $n_H = 10^4\ \mathrm{cm^{-3}}$ as opposed to 950 K at $n_H = 10^6\ \mathrm{cm^{-3}}$.

Lower temperatures directly decrease the sputtering rates of all projectiles since expression (5.28) includes a factor of $T_n^{1/2}$. Low temperatures also increase the values of x_{th} and s used in the evaluation of the integral since both are proportional to $T_n^{-1/2}$. x_{th} and s are altered by exactly the same amount by changes in temperature so the portion of the curve above x_{th} remains constant, but its height and hence the solution to the integral become larger (see discussion of the limits to the integral in §5.4.2). Higher drift speeds increase the sputtering rates both by directly increasing the yield (see equation 5.22 in §5.4.1) and also by increasing the value of s used in the integral (see §5.4.2). If u_{gn} grows whilst T_n shrinks, then x_{th} and s grow by different amounts since $x_{th} \propto T_n^{-1/2}$ and $s \propto u_{gn} T_n^{-1/2}$.

Because the variation in the small grain-neutral drift speeds between the density regimes at these shock speeds ($\sim 10^2\ \mathrm{cm\ s^{-1}}$) is of the same order as the difference in neutral temperature ($\sim 10^2$ K) and the sputtering rate per grain is directly multiplied by a factor of $T_n^{1/2} s^{-1}$ (where $s \propto u_{gn} T_n^{-1/2}$), the temperature difference dominates the variation in the small grain sputtering rates. Because the small grains are equally well coupled to the magnetic field at both densities, the lower temperatures ensure that small grain sputtering is slightly less effective in the low density regime. Inspection of table 5.2 reveals that this is indeed the case, with only around three quarters as much ice being eroded from the small grains in low density models with the same shock speeds. On the other hand, the variation in u_{gn} between the density regimes is of the order $10^5\ \mathrm{cm\ s^{-1}}$ due to the better coupling of the large grains to the field. This allows it to

dominate the variation in the large grain sputtering rates, which consequently get larger at low densities.

Simulations were undertaken with $n_H = 10^4$ cm^{-3} for shock speeds of 10, 12, 14, 16 and 20 km s^{-1}, with the fractions of ice sputtered included in table 5.2 and figure 5.14. At 10 km s^{-1}, with $n_H = 10^6$ cm^{-3}, a fraction of 5×10^{-3} of the small grain mantles were sputtered. At $n_H = 10^4$ cm^{-3} this fraction falls, but the mantles of both grain types are now sputtered. Whilst lower temperatures reduce the fraction of ice sputtered from the small grain mantles the better coupling of the large grains to the field lines allows their sputtered fraction to increase. The effects of the lower temperatures and better coupling of the large grains to the field lines balance so the total gas phase water enhancement due to sputtering remains almost constant between the density regimes. However, the sputtered fractions of the mantles of each species do change from the equivalent high density case so that 0.38% of the small grain mantles and 0.12% of the large grain mantles are now vaporized.

Since the enhancement in gas phase H_2O is the sum of the ice sputtered from both grain types, for simulations of shock speeds between 10 and 16 km s^{-1} the enhancement is roughly the same between the density regimes. At each shock speed, the fraction of large grain ice eroded is higher in the low density model due to their better coupling to the field, but the fraction of small grain ice eroded is lower in the low density model because of the neutral temperatures are lower (see above).

By $v_s = 20$ km s^{-1}, mantle sputtering of both grain types is total in the low density regime. This is to be expected because the large grains now move with the other charged species and the sputtering of their mantles becomes complete at the same shock speed as the small grains (18 km s^{-1}). The sputtering regions for both grain fluids are now spatially coincident.

5.7.2.3 Mantle sputtering - comparison with previous studies

Following on from the discussion in in §5.7.2.1 regarding the minute but non-zero amounts of ice sputtered in the high density models at shock speeds of 6, 8 and 9 km s^{-1}: Caselli et al. (1997) define the sputtering threshold to occur when the gas phase water abundance due to sputtering exceeds $10^{-7} n_H$ (figure 5 in their paper). This is also a sensible threshold in the current work because gas phase H_3O^+ destruction in the 5 km s^{-1} simulation was sufficient to raise χ_{H_2O} to $\sim 10^{-8}$. Because the peak abundance of H_3O^+ only rises by a factor of ~ 3

between 5 and 30 km s^{-1}, a rise in χ_{H_2O} of another order of magnitude from 10^{-8} cannot be due to H_3O^+ destruction alone, regardless of the shock speed. Some care is still required however since conversion of oxygen in the gas phase in the 9 km s^{-1} shock raised the post-shock water abundance past 10^{-7} without sputtering being an important process.

Therefore, mantle sputtering commences in the range $5 \leq v_s \leq 6$ km s^{-1} using the current model, but using $\chi_{H_2O} = 10^{-7}$ as the benchmark and inspecting the sputtering rates and atomic oxygen profiles to confirm that the rise in water can be ascribed to sputtering, the onset of appreciable mantle sputtering occurs in the velocity region $9 \leq v_s \leq 10$ km s^{-1}. That this is lower than the velocity found by Caselli et al. (1997) (~ 10.875 km s^{-1} is deduced for the same Alfvén speed as adopted here) comes as no surprise since they only considered H_2 and He as projectiles and they do not become capable of sputtering until higher shock speeds.

For shock speeds in the range $11 \leq v_s < 16$ km s^{-1}, Caselli et al. (1997) report lower total abundances of water sputtered than reported here, but for $v_s > 16$ km s^{-1} they find more. Sputtering near threshold is dominated by the heavy molecules not considered by Caselli et al. (1997) so their results are expected to be lower. Between 14 and 18 km s^{-1} the lighter H_2 starts to contribute significantly to the sputtering because of the higher drift speeds (see table 5.3). The two sets of models give similar sputtered ice fractions for $v_s = 16$ km s^{-1}. At higher shock speeds, H_2 becomes ever more important as a projectile due to its high abundance and the fact that its yield converges with those of the heavier projectiles (see §5.7.2.1). When H_2 is able to contribute significantly to the sputtering of the mantles, the fact that Caselli et al. (1997) employ the yield expression from Tielens et al. (1994) rather than that from May et al. (2000) causes their sputtered fractions to be higher (see §5.7.2.6).

Jiménez-Serra et al. (2008) report lower gas phase abundances of water due to sputtering in 10 and 20 km s^{-1} shocks propagating through media with densities of $n_H = 2 \times 10^4$ cm^{-3}, even though their selection of projectiles is similar to those adopted here (and includes the dominant molecular projectile CO). For $v_s = 10$ km s^{-1} they report a gas phase water abundance relative to atomic hydrogen of 1.5×10^{-8} whereas values of 2.75×10^{-7} and 5.18×10^{-7} are found here in the high and low density regimes respectively. At $v_s = 20$ km s^{-1}, mantle sputtering is total at both densities in the current models, yielding a gas phase water enhancement of 7.25×10^{-5}, whereas Jiménez-Serra et al. (2008) report 5×10^{-6}. The cause cannot be the density adopted by Jiménez-Serra et al. (2008), since the density regimes in the current study are both higher and

lower than that value, with the sputtered mantle fraction being higher at both densities. Because both studies employ the same expressions for sputtering, the differences between the models must arise from variations in the calculated grain-neutral drift speeds. Using a perpendicular treatment (like Jiménez-Serra et al. 2008) the drift speeds are expected to be lower than in oblique shocks of the same speed (see §3.4.1). In fact, the drift speeds predicted by Jiménez-Serra et al. (2008) for a 40 km s^{-1} shock propagating through a medium with $n_H = 2 \times 10^4$ cm^{-3} are only slightly higher than those predicted for a 30 km s^{-1} shock (with $n_H = 10^4$ cm^{-3}) using the current treatment. This can easily account for the differences in water abundances between the models.

The relative effectiveness of the projectiles at each shock speed was also noted by Jiménez-Serra et al. (2008). Figures 4 and 5 of their paper can therefore be compared to table 5.3. The sputtering rate of a projectile species depends on a combination of its mass, abundance and the shock speed. For example, H_2 is so light that its sputtering rate at 10 km s^{-1} is the lowest by around ten orders of magnitude in the current models. H_2 is also absent from the 10 km s^{-1} plots in figure 5 of Jiménez-Serra et al. (2008). Because they only consider H_2 and He as projectiles, mantle sputtering is completely absent at 10 km s^{-1} in the models of Caselli et al. (1997). At higher shock speeds, Jiménez-Serra et al. (2008) report H_2 increasing in importance as a projectile, with it becoming as significant as CO at $v_s = 30$ km s^{-1}. The results in table 5.3 would concur with this, since already by $v_s = 25$ km s^{-1} the sputtering rate due H_2 is 32% of the total on large grains and 26% of the total on small grains.

In the current models, magnesium represents all metals wheres Jiménez-Serra et al. (2008) selected iron instead. Both species are massive enough to have low impact energy thresholds to sputter ice, making them important projectiles at the lowest shock speeds, but only in the initial stages of sputtering (before the drift speed passes the threshold for lighter but more common projectile species). Neutral metals are sufficiently rare in both studies to be unimportant once species such as oxygen and water become capable of sputtering. In this respect the findings agree.

Although water is assumed to have the same mass as atomic oxygen when calculating its yield (see §5.4.1), at low shock speeds not much of it is sputtered from the mantles and very little oxygen is converted in the gas phase using the current treatment. This means that O remains a much more abundant and hence effective projectile throughout the shock. At higher shock

speeds, copious ice is sputtered and much of the oxygen is converted into water. Because the gas phase conversion happens over the same regions as sputtering occurs, oxygen is able to act as an efficient projectile near the upstream edge of the sputtering region, but is replaced by water by the downstream edge. Since converted oxygen accounts for up to 7.3 times more of the gas phase water as sputtered ice, it is reasonable to sum the sputtering rates due to O and H_2O from table 5.3 and compare this to the values for O in Jimenez-Serra et al. (2008). Because atomic oxygen has only around half the mass of a CO molecule, its sputtering threshold impact energy is higher. At 10 km s^{-1}, Jiménez-Serra et al. (2008) report the gas phase water fraction sputtered by O to be around 10^{-3} that due to CO. Given the differences in the predicted drift speeds between the models these results are consistent. By 20 km s^{-1}, Jiménez-Serra et al. (2008) report that the fraction of ice sputtered by O is a factor of 5 lower than that sputtered by CO whereas the combined sputtering rates of water and atomic oxygen are a factor of 3.5 higher than CO in this study. This is a result of the different initial abundances of CO and O: Jiménez-Serra et al. (2008) assume almost equal amounts, whereas oxygen is more abundant in the current models by a factor of 8.5. Given that consideration, the results are consistent.

From the projectiles which are considered in both projects (H_2, CO and O/H_2O), Jiménez-Serra et al. (2008) report CO to be the most effective projectile at all shock speeds. Because of the abundance differences noted above, in the current models CO is only most effective for $v_s \leq 18$ km s^{-1}. It is still the most effective at low shock speeds due to its high mass, but once the shock speed is sufficiently above the threshold for O/H_2O, these species become dominant due to their higher abundance.

5.7.2.4 Core sputtering - high density models

Once all the grain mantles have been vaporized, so long as grain-neutral collisions impart sufficient energy to atoms of the grain material, atoms from the cores begin to be sputtered. Since the core material is more strongly bonded than the material of the ice mantles, higher grain-neutral drift speeds are required to sputter atoms from the cores.

Whilst some sputtering is predicted by the model at 20 km s^{-1}, it is only through CO impacting small grains and results in a gas phase SiO abundance which is orders of magnitude below current detection limits. At v_s = 25 km s^{-1}, the gas phase abundance of silicon reaches $\sim 10^{-10}$. Since only the small grains possess high enough drift speeds to be sputtered at this

density and shock velocity and the silicon abundance initially incorporated into small grains is 1.40×10^{-5}, the post-shock gas phase SiO fraction implies that 7.37×10^{-6} (0.0007 %) of the small grains cores are vaporized. With a shock speed of 30 km s^{-1}, about 0.32% of the small grain cores are vaporized. This raises χ_{SiO} to 4.5×10^{-8}. The contribution of the large grains remains negligible. At 35 km s^{-1}, 3.26% of the small grain cores are sputtered. At this speed, around 0.1% of the large grain cores are also sputtered. Since the fractional abundance of silicon initially residing in large grains is 4.42×10^{-5}, the sputtering of the large grains at this shock speed increases the gas phase SiO abundance by 4.3×10^{-8}. In total the SiO abundance now reaches 5×10^{-7} in the downstream region.

Using the current treatment, a 40 km s^{-1} shock propagating through an upstream medium with $n_H = 10^6$ cm^{-3} is J-type with a magnetic precursor. Non thermal grain sputtering is inefficient in J-type shocks, so the SiO data for 35 km s^{-1} represents the maximum for a shock in media of this density. CO is able to sputter minute amounts of the small grain cores with a drift speed of 13.55 km s^{-1} (in the 20 km s^{-1} shock). However, the threshold grain-neutral drift velocity for core sputtering which results in gas phase SiO in abundances above 10^{-15} is ~ 16.9 km s^{-1} and like mantle sputtering is the same for both grain species and is independent of density.

The adopted grain size distribution guarantees that most of the mass is in the large grains, but the small grains are more numerous. In turn, this means that most of the initial ice abundance is on the small grains due to their larger surface area per unit volume, but most of the silicon atoms initially reside in the large grains. In fact, the ratio of water ice initially on large to small grains is 0.316, whereas the ratio of silicon initially in large to small grains is 3.162. With $n_H = 10^6$ cm^{-3}, these ratios result in around two thirds of the ice becoming available to sputtering at the lowest shock velocities above threshold, whereas two thirds of the silicon remains unavailable until the large grain-neutral drift speed passes the sputtering threshold ($\sim$ 35 km s^{-1} for the large grain cores).

Using the current treatment C-type shocks only persist to speeds barely capable of sputtering the large grain cores with $n_H = 10^6$ cm^{-3}. Furthermore, the amount of gas phase SiO produced in the model with the highest speed is only around half as much as is observed near some low mass YSOs. Therefore these results suggest that the silicon observations of Martin-Pintado et al. (1992) and others must be caused by shocks propagating through regions with upstream

		Large grains		Small grains	
Shock Speed (km s^{-1})	n_{H0} (cm^{-3})	Fraction of Si removed	Contribution to downstream SiO	Fraction of Si removed	Contribution to downstream SiO
20	1.00(4)	0.00	-	<<1.00(-4)	≈0.00
30	1.00(4)	3.62(-4)	1.60(-8)	4.58(-3)	6.40(-8)
35	1.00(4)	2.83(-3)	1.25(-7)	3.40(-2)	4.75(-7)
40	1.00(4)	5.59(-3)	2.47(-7)	1.40(-1)	1.95(-6)
45	1.00(4)	1.12(-2)	4.94(-7)	2.51(-1)	3.51(-6)
50	1.00(4)	2.60(-2)	1.15(-6)	3.04(-1)	4.25(-6)
20	1.00(6	0.00	-	0.00	-
25	1.00(6)	0.00	-	7.37(-6)	1.03(-10)
30	1.00(6)	0.00	-	3.22(-3)	4.50(-8)
35	1.00(6)	9.76(-4)	4.31(-8)	3.26(-2)	4.56(-7)

Table 5.4: Fractions of silicon removed from large and small grains at various shock speeds and upstream densities. The large and small grain fraction columns refer to the fraction of the silicon residing on a grain species at the upstream boundary which is in the gas phase by the downstream boundary.

densities low enough for the large grains to be well coupled to the magnetic field (less than 10^6 cm^{-3}).

5.7.2.5 Core sputtering - low density models

Since 35 km s^{-1} is the maximum speed for which a shock propagating through a medium with $n_H = 10^6$ cm^{-3} is C-type and the maximum SiO abundance predicted by that model is only 5×10^{-7}, more simulations are required at $n_H = 10^4$ cm^{-3} to reproduce the observed SiO abundances, since C-type shocks persist to higher speeds at low densities. Because the large grains (which carry the majority of the silicon reservoir) are also better coupled to the field when $n_H = 10^4$ cm^{-3} (and so display larger drift velocities with respect to the neutrals), additional simulations were undertaken for a range of shock speeds above 35 km s^{-1}, with other parameters selected to be suitable for the low density regime (see §5.7.1.3 and §5.7.2.2).

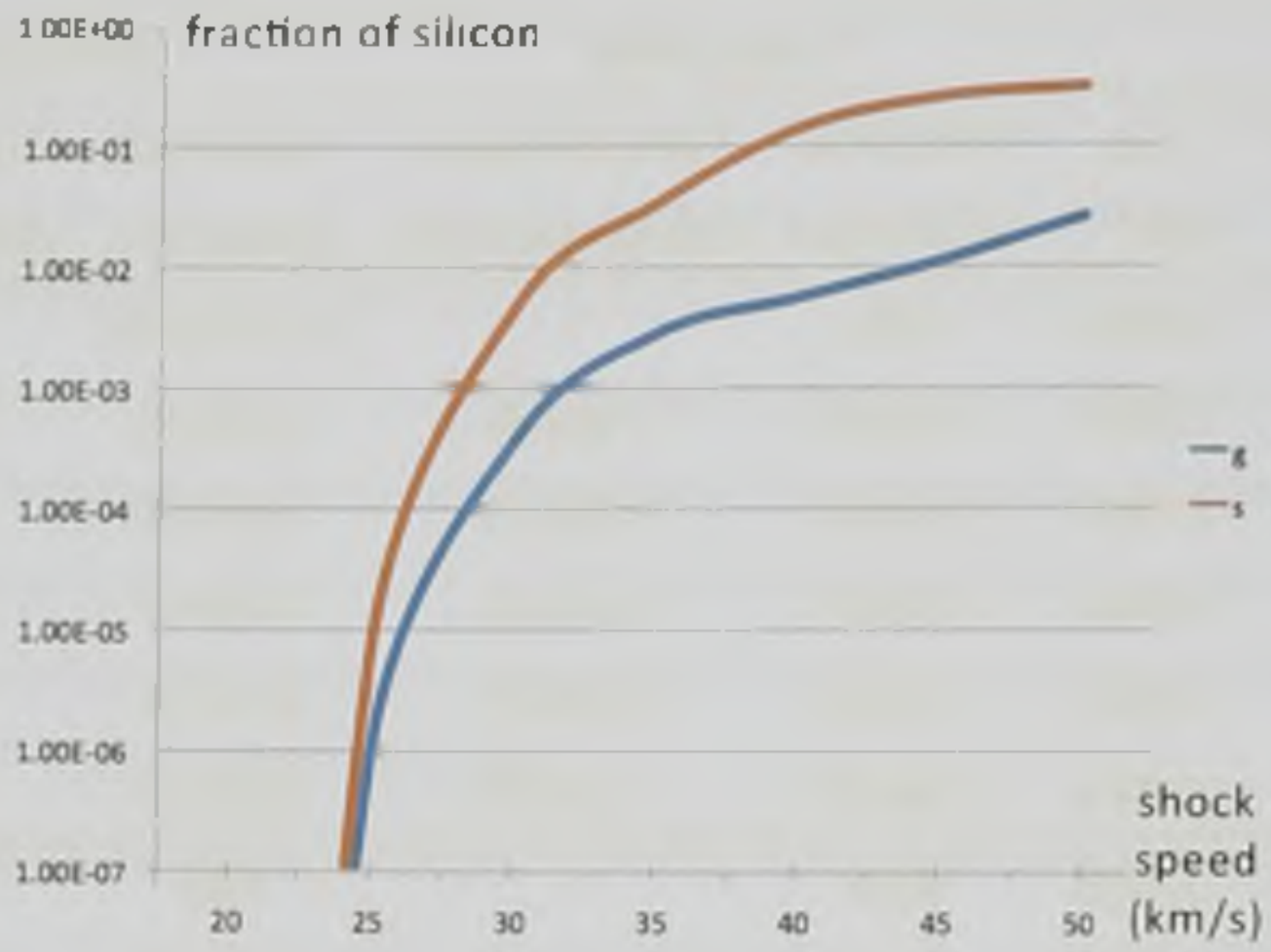

Figure 5.15: Fraction of silicon sputtered from large (blue) and small (red) grains at various shock speeds with an upstream density of $n_H = 10^4$ cm^{-3}.

Unlike the mantle sputtering regime (§5.7.2.2), at the higher shock speeds required for core sputtering, the change in T_n between the density regimes is now of the order of 10^3 K, i.e. with $n_H = 10^4$ cm^{-3} and $v_s = 30$ km s^{-1}, the peak neutral temperatures are a little under half what they were in the high density regime: 900 K, as opposed to 2000 K. The difference in the small grain-neutral drift speed is now of the order 10^5 cm s^{-1}. This means that the change in u_{sn} now dominates, so unlike mantle sputtering, small grain core sputtering is more efficient in the low density regime.

However, similarly to the mantle sputtering regime, the large grain-neutral drift speeds still differ between the density regimes by a few 10^5 cm s^{-1}, i.e. a few km s^{-1}. The collision rates and SiO abundance both differ by factors less than 10. This means that the increase in s in going from $n_H = 10^6$ to 10^4 cm^{-3} is again dominated by the change in u_{gn}. This still allows s to grow much more than x_{th}. A higher value for s guarantees a larger solution to the integral and this increases the sputtering rate of the large grains at all shock speeds with $n_H = 10^4$ cm^{-3}. Also, at shock speeds near to threshold, more of the curve is above x_{th}, so the solution to the integral grows even more.

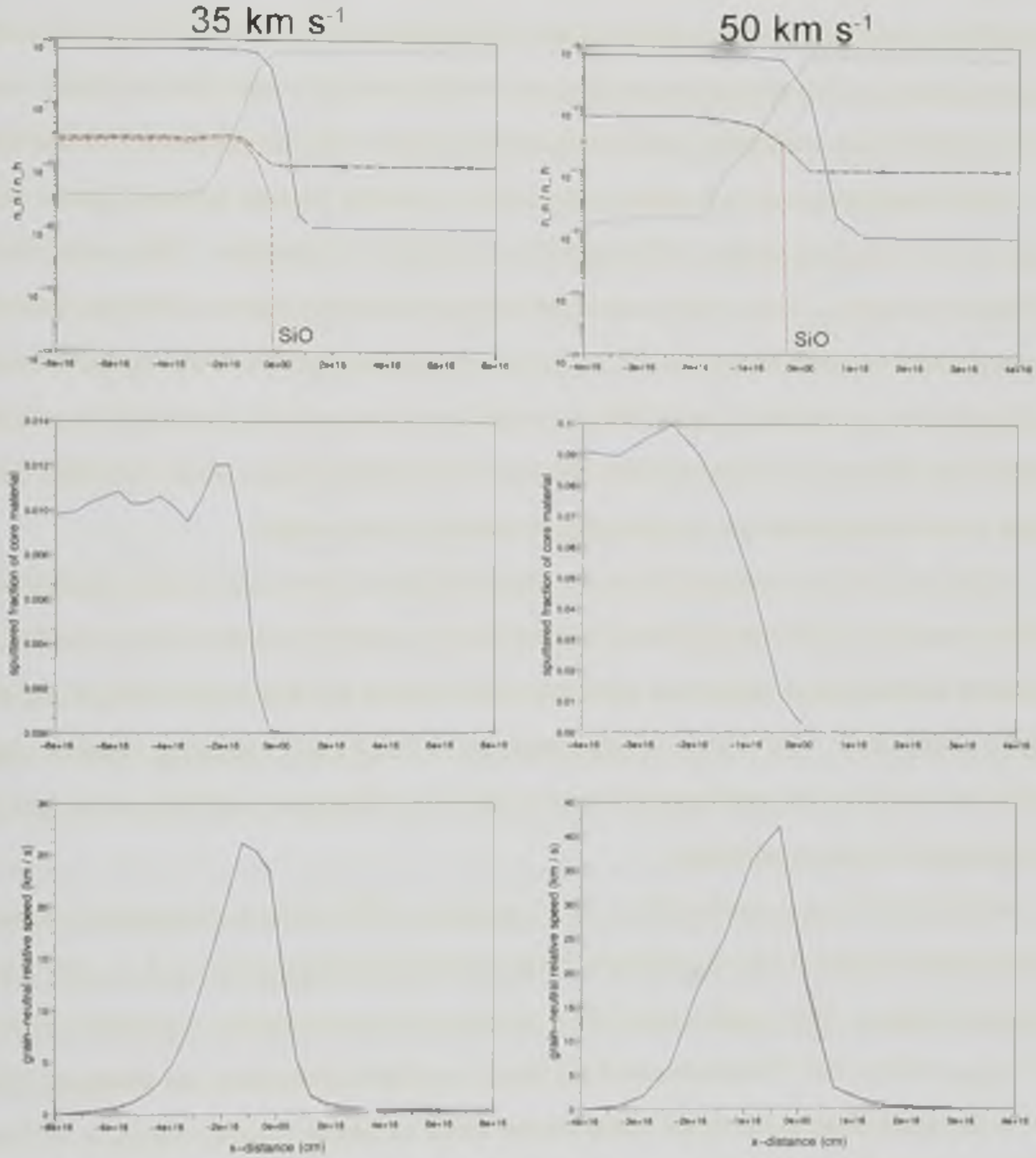

Figure 5.16: Core sputtering at $n_H = 10^4$ cm^{-3}, with $v_s = 35$ km s^{-1} (left column) and 50 km s^{-1} (right column). Top row shows the neutral chemical profiles with SiO (red, dash), O (green, dotted), water (blue, solid) and magnesium (black, dash dotted). Middle row displays the total fraction of the core material (over both grain types) which is returned to the gas phase. The bottom row gives the grain-neutral relative speeds (km s^{-1}) for large grains (red, dash) and small grains (blue, solid).

At 30 km s^{-1} with $n_H = 10^4$ cm^{-3}, the gas phase SiO abundance in the downstream region is 8×10^{-8}, almost twice that obtained from the high density case. This is due to the dynamic role of the large grains which provide a similar contribution to the gas phase SiO enhancement as the small grains at this density because they move with almost the same speed as them. Around 0.14% of the silicon available is sputtered from the grains to yield this gas phase SiO abundance.

Mantle sputtering was only weakly dependent on density because the small grains (which carry most of the ice) remain well coupled to the field at all densities. This meant that the variations in s and u_{sn} were of the same order between the density regimes, allowing the change in temperature to dominate (see §5.7.2.2). At low densities the fraction of ice sputtered from the small grains at a given shock speed fell due to the lower temperatures, but this fall was closely matched by the extra ice removed from the (now well coupled) large grains, meaning the gas phase water enhancement due to sputtering remained almost constant.

In the case of core sputtering however, the small grains carry only a small fraction of the silicon reservoir, so even though their sputtered fraction again falls slightly at low densities, that sputtered from the large grains now more than makes up for this and results in larger gas phase silicon abundances. The silicon enhancement due to large grain sputtering remains slightly lower than that from the small grains however, due to the difference in collision rates (see table 5.4 and below for an explanation).

At 35 km s^{-1}, χ_{SiO} reaches 6.0×10^{-7}, meaning 1.03% of the core material is sputtered (left column of figure 5.16). By 40 km s^{-1}, the peak SiO abundance rises to 1.1×10^{-6} in the post-shock region. This implies that 3.79% of the grain core material is vaporized. At 45 km s^{-1}, $\chi_{SiO} = 4.0 \times 10^{-6}$ downstream of the shock, so 6.88% of the cores are destroyed. 50 km s^{-1} is the upper limit to the shock speed for the shock to remain C-type with $n_H = 10^4$ cm^{-3}. With $v_s = 50$ km s^{-1}, 9.29% of the core material is sputtered, raising χ_{SiO} to 5.4×10^{-6} (right column of figure 5.16). Whilst around 30% of the small grain cores are eroded, even at this maximum shock speed only 2.5% of the large grain cores are sputtered.

Because the large grain silicon reservoir is significantly (3 times) larger than that of the small grains, it is altered less by the less sputtering which does occur. This suggests that sputtering in the the shocks associated with low mass YSOs barely affect the larger grain cores. However it is still possible to reproduce the SiO observations of Martin-Pintado et al. (1992) with shocks propagating through media with $n_H = 10^4$ cm^{-3} since most of the gas phase SiO is liberated

Projectile Species and	Grain	Shock speed (km s^{-1})				
Adopted Mass (AMU)	Type	30	35	40	45	50
H_2	large	0.00	3.62(-31)	7.57(-19)	5.61(-11)	1.14(-9)
(2)	small	0.00	1.33(-30)	2.40(-18)	2.01(-10)	3.83(-9)
CO	large	6.69(-2)	1.73(-1)	2.88(-1)	4.84(-1)	6.04(-1)
(28)	small	2.17(-1)	5.54(-1)	9.22(-1)	1.55	1.92
O	large	8.42(-7)	9.84(-3)	1.96(-1)	2.09(-1)	3.03(-1)
(16)	small	3.31(-6)	3.38(-2)	6.23(-1)	6.70(-1)	9.67(-1)
H_2O	large	1.21(-3)	4.70(-1)	1.80	3.56	6.39
(16)	small	4.44(-3)	1.53	5.76	1.13(1)	2.03(1)
Mg	large	1.12(-4)	2.09(-3)	7.84(-3)	2.96(-2)	4.51(-2)
(24)	small	3.66(-4)	6.72(-3)	2.51(-2)	9.49(-2)	1.43(-1)
SiO	large	8.26(-5)	1.56(-3)	7.02(-3)	2.07(-2)	3.86(-2)
(28)	small	2.56(-4)	5.02(-3)	2.24(-2)	6.63(-2)	1.23(-1)

Table 5.5: Peak sputtering rates (cm^{-3} s^{-1}) for the projectiles listed removing silicon from each grain species for shocks of various speeds propagating through media where $n_H = 10^4$ cm^{-3}. The figures included in the table represent the peak cell values across the grid. These do not occur in the same cells for each species. Numbers in parentheses denote powers of ten. Note that water is assumed to sputter as atomic oxygen (same adopted mass) since O is the projectile with the closest mass to water considered by May et al. (2000). Likewise, SiO is assumed to sputter as Si.

from the small grain cores.

Since more simulations were completed at 10^4 cm^{-3} than at 10^6 cm^{-3}, the rates of each projectile sputtering silicon from the cores of both grain types at various shock speeds were noted for simulations in the low density regime. These are included as table 5.5. As can be seen from inspection of that table, the sputtering rates of each projectile on the small grains remain 3.1 - 4 times higher than those for the large grains. These differences are now only 10% of those noted for the mantle sputtering rates at $n_H = 10^6$ cm^{-3} (table 5.3 in §5.7.2.1) since all the grains now have similar drift speeds with respect to the neutrals. However, these variations are

too large to be due to the slight difference between the drift speeds of the large and small grains. There are around 316 times as many small grains as large ones, but each has a collision cross section 100 times smaller. This results in 3.16 times as many small grain-neutral collisions as large grain-neutral collisions ($cm^{-3}\ s^{-1}$). It is this ratio which is reflected in the sputtering rates of the grains fluids, since the sputtering rates in table 5.5 are the actual rate per unit volume of silicon atoms being ejected rather than the fraction.

One would expect all of the large grain sputtering rates to be higher in the low density regime due to the better coupling between grains and field lines which result in more, and more energetic collisions with neutrals, even though the medium is more rarefied. Higher rates are noted for CO, O, H_2O and Mg impacting large grains using the current treatment. In contrast, one would expect the small grain sputtering rates to be lower at $n_H = 10^4\ cm^{-3}$ because their coupling remains constant, whilst the collision rates fall. Lower rates are reported for H_2, CO, H_2O and Mg impacting small grains. In order to better facilitate a comparison between the density regimes, the sputtering rates for each projectile are also noted for a 30 km s^{-1} shock propagating through a medium with $10^6\ cm^{-3}$ (table 5.6).

In the case of H_2 striking large grains, the sputtering rates are already very low despite the high frequency of collisions at $10^6\ cm^{-3}$. Their contribution to gas phase SiO enhancement is effectively negligible. By reducing the collision rates and temperature in the $10^4\ cm^{-3}$ simulation, the sputtering rate goes to zero.

As can be seen from a comparison of tables 5.5 and 5.6, the sputtering rate of SiO on large grains is higher in the low density models by a factor of 2.66. This is easily explained by SiO being almost twice as abundant in the low density model due to the sputtering of large grains being possible. The higher drift speeds obtained at low densities explain the rest of the discrepancy. The rates of SiO sputtering small grains are approximately the same at both densities rather than being lower at $n_H = 10^4\ cm^{-3}$. Again, the higher SiO abundance and drift speed explain this.

The small grain core sputtering rate due to impacts with atomic oxygen is higher in the low density regime despite the collision rates and temperatures being lower. Oxygen atoms have around half the mass of CO and SiO molecules in the evaluation of the sputtering rates (see §5.4.1). In the high density regime with $v_s = 30$ km s^{-1}, O is barely a feasible projectile, with the most feeble sputtering rate after H_2. This renders the precise variations in x_{th} and s between

Grain Type	H_2	CO	O	H_2O	Mg	SiO
Large	5.80(-30)	1.74(-5)	5.62(-27)	1.76(-16)	2.33(-11)	2.20(-4)
Small	3.54(-23)	1.26(1)	3.33(-8)	3.66(-2)	1.07(-2)	1.06(-2)

Table 5.6: Peak sputtering rates (cm^{-3} s^{-1}) for the projectiles listed ejecting silicon from the cores of each grain species in a 30 km s^{-1} shock propagating through a medium with $n_H = 10^6$ cm^{-3}. Like previously, the figures included in the table represent the peak cell values across the grid

the density regimes critical to the sputtering rate. In the low density regime T_n is lower by $\sim 10^3$ K and the small grain-neutral drift speed is higher by a $\sim 10^5$ cm s^{-1}. This results in a larger s and x_{th}, with s growing more than x_{th} which not only places more of the velocity distribution curve above x_{th} but also makes the peak of the curve higher and the area underneath it larger. Together with the direct increase that a higher drift speed produces in the yield (equation 5.27), these factors result in higher sputtering rates at low density.

The grain cores are not completely destroyed even in the shocks in which sputtering proceeds most effectively (high shock speed, low upstream density). This allows the sputtering rates for all projectiles to grow with shock speed across the full range of the simulations because the limit of silicon available to sputter never becomes an issue. The peak core sputtering rates are always at least a couple of orders of magnitudes lower than those of the mantles due to the higher binding energy of the core material.

Molecular hydrogen does not become an effective core projectile at any shock speed due to its low mass. Since core sputtering does not commence until the mantles have been vaporized by which time much of the gas phase oxygen has also been converted to water ($\sim 99\%$ at 30 km s^{-1}) the sputtering rates due to atomic oxygen are around 1% of the rates due to water. Water is the dominant projectile at all but the lowest shock speeds since it is around ten times more abundant than CO and its higher abundance is able to more than cancel its lower mass. Mg is most important at lower shock speeds where its high mass outweighs its low abundance, but it is quickly overwhelmed by the lighter but more abundant species once they pass threshold. Similarly, SiO is now itself a projectile and follows the same trend as Mg as they achieve similar gas phase abundances at high shock speeds (see figure 5.11).

5.7.2.6 Core sputtering - comparison with previous studies

Simulations of core sputtering were conducted by Caselli et al. (1997). May et al. (2000) and Jimenez-Serra et al. (2008) so their results may be compared to the current models. An arbitrary lower limit of $\chi_{SiO} \geq 10^{-15}$ is imposed on the gas phase SiO abundance to indicate that core sputtering has commenced (a little below current detection limits). Like Caselli et al. (1997) and May et al. (2000) it is found here that the SiO fraction narrowly passes this limit when $v_s = 25$ km s^{-1}.

Since Caselli et al. (1997) only consider H and He as projectiles, it comes as no surprise that their reported gas phase SiO abundances due to core sputtering are many orders of magnitude lower than the current results at $v_s = 25$ km s^{-1} for both density regimes. This is because of the close proximity of the shock speed to the sputtering threshold. The difference between the models shrinks at higher shock speeds as the light projectiles become more capable. however it is surprising how quickly this occurs. For $n_H = 10^4$ cm^{-3} and $v_s = 35$ km s^{-1} they find $\chi_{SiO} \sim 5 \times 10^{-7}$ as opposed to 6×10^{-7} found here. Since the sputtering rates due to H_2 remain feeble at all shock speeds using the Draine & Salpeter (1979) treatment. He must dominate the core sputtering in the models of Caselli et al. (1997). However, Jimenez-Serra et al. (2008) include He as a projectile and find that it does not contribute to core sputtering even at shock speeds above the maximum considered by Caselli et al. (1997). This suggests that using the May et al. (2000) treatment for core sputtering suppresses the contribution of He as a projectile since all three studies model H_2 as a projectile using the prescription of Draine & Salpeter (1979).

This can be checked using figure 2 of Caselli et al. (1997) which plots the total sputtering rates (sum of H_2 and He) for various shock speeds as a function of the upstream density. For shock propagating through an upstream density of $n_H = 10^4$ cm^{-3}, they report sputtering rates of $\sim 10^{-4}$ s^{-1} per large grain and $\sim 10^{-6}$ s^{-1} per small grain at 30 km s^{-1}. They also report $\sim 10^{-2}$ s^{-1} per large grain and $\sim 10^{-4}$ s^{-1} per small grain at 35 km s^{-1}. The current simulations find H_2 to be incapable of sputtering at 30 km s^{-1} and Jiménez-Serra et al. (2008) report no core sputtering due to either H_2 or He. At 35 km s^{-1}, the current models predict sputtering rates due to H_2 of 2.29×10^{-21} silicon atoms per large grain per second and 2.66×10^{-23} silicon atoms per small grain per second. Therefore the use of the Tielens et al. (1994) treatment for the silicon yield in the models of Caselli et al. (1997) allows He to sputter as much silicon as all

the heavy projectiles in the current project combined. In fact, figure 11 of Tielens et al. (1994) shows the threshold impact energy to be around 40 eV, with the yield reaching 5.9×10^{-2} at $\sim$ 120 eV whereas using the procedure detailed in May et al. (2000), the yield for He remains zero until the impact energy is around 85 eV and reaches only 9×10^{-3} at 120 eV.

Using the Tielens et al. (1994) procedure for the core yields due to He impact therefore results both in a lower threshold drift velocity and yields which are higher by a factor ~ 5 over the impact energy regime of interest than the May et al. (2000) treatment. Because Caselli et al. (1997) assume $\chi_{He} = 0.1$ and employ the Tielens et al. (1994) sputtering procedure, this accounts for the large difference between their and the current models. Had Caselli et al. (1997) also considered the heavier atomic and molecular projectiles included in the current model and retained the same treatment for He as a projectile, their SiO abundances would be far in excess of those observed with the grains possibly being completely destroyed.

May et al. (2000) perform calculations over the same shock speed and density range as the current work. For their $n_H = 10^4$ cm^{-3} calculations, they report silicon fractions sputtered from the cores of 6.6×10^{-2} at $v_s = 30$ km s^{-1}, 2.2×10^{-1} at $v_s = 35$ km s^{-1}, 4.5×10^{-1} at $v_s = 40$ km s^{-1} and 7×10^{-1} at $v_s = 45$ km s^{-1}. For the same shock speeds the current models predict 1.38×10^{-3}, 1.1×10^{-2}, 3.65×10^{-2} and 6.75×10^{-2} respectively. The current results are therefore lower than those found by May et al. (2000) by factors between 50 at $v_s = 30$ km s^{-1} and 10 at $v_s = 45$ km s^{-1}.

Their models (based on those of Flower & Pineau des Forets 1995) assume a single fluid of grains with radii 10^{-6} cm (one quarter the size of the small grains in the current model) which remain extremely well coupled to the field lines. This guarantees a higher collision rate per unit volume, so the sputtered fraction is expected to be larger at all speeds. The extra discrepancy at lower shock speeds can be ascribed to the fact that the large grains in the current model contribute less (around $\sim 20\%$ as much) to the SiO enhancement than the small grains but carry the majority of the silicon reservoir. Therefore having most of the silicon in large grains which have lower neutral collision rates per unit volume reduces the fraction of silicon returned to the gas phase by orders ~ 10.

In fact, May et al. (2000) note that the deduced column densities for their fastest shocks are much larger than those inferred from observations. They ascribe the difference to beam dilution effects and the assumption of a steady shock. However, the current models suggest that their

assumption of a single fluid of grains which are small enough and sufficiently charged to remain extremely well tied to the field lines may cause the difference. By including a component of large grains which carry most of the mass (and silicon) but experience a lower collision rate per unit volume, the deduced SiO column densities can be reduced to a level which agrees with observations.

Jiménez-Serra et al. (2008) perform calculations for a 40 km s^{-1} shock propagating through a medium with $n_H = 2 \times 10^4$ cm^{-3} (twice that of the current model). They report a gas phase silicon fraction due to core sputtering of $\sim 3.82 \times 10^{-6}$, whereas 5.2×10^{-6} is found in the nearest current model. At 30 km s^{-1}, with an upstream density of $n_H = 2 \times 10^5$ cm^{-3}, Jiménez-Serra et al. (2008) report gas phase silicon fractions due to core sputtering of 2×10^{-7}. Since all the grains are coupled to the field lines in their models, a comparison with the current low density model is most suitable. At $n_H = 10^4$ cm^{-3}, 8×10^{-8} is reported. These differences can be attributed to differences in temperature and drift speed between the models (see §5.7.2.3).

Jiménez-Serra et al. (2008) also evaluate the gas phase enhancements of SiO due to the sputtering by each of the species they considered. They find that well above the threshold velocity (i.e. fast enough to sputter both grains fluids at higher densities), the sputtered fractions by species are fairly insensitive to density. The current results support that assertion. They evaluate the effectiveness of each projectile in 40 km s^{-1} shocks propagating through media with $2 \times 10^4 \leq n_H \leq 2 \times 10^6$ cm^{-3}. The insensitivity to the rates on the upstream density well above threshold and the high degree of coupling between large grains and the magnetic field at 10^4 cm^{-3} allows the results of Jiménez-Serra et al. (2008) to be compared to the middle column in table 5.5 in this work, to assess the relative effectiveness of the projectiles which the treatments share.

Like the current work, Jiménez-Serra et al. (2008) find that H_2 does not contribute to core sputtering over the whole range of densities and shock speeds which they considered. They report CO and O to contribute comparable amounts of SiO at 40 km s^{-1}. This makes sense since both species are well above threshold and in their work they are assumed to have almost equal initial abundances with both being inert. In the current models, gas phase oxygen has mostly been converted into water and the combined oxygen and water sputtering rates are a factor of 6.9 higher than that due to CO. This makes sense because oxygen is initially more abundant by a factor of 8.5. At 40 km s^{-1}, Jiménez-Serra et al. (2008) report the core fraction

sputtered by Si to be a factor of $\sim 5 \times 10^4$ lower than for CO, whereas here the SiO sputtering rate is a factor of just ~ 42 lower. This is a consequence of lower gas phase SiO fractions in their case. At 40 km s^{-1}, iron is found to provide a lower contribution to gas phase SiO than Si by a factor of 10 in the models of Jiménez-Serra et al. (2008). Despite magnesium being selected to represent metals in the current work and having a lower mass than iron, because both projectiles are well above threshold at this shock speed, a similar result is found here.

5.7.2.7 Angular dependence of sputtering

Figure 5.17 presents the results of 25 km s^{-1} shocks with initial parameters suitable for the high density regime (see §5.5) which make angles of 30°, 45° and 60° with the upstream magnetic field lines.

The plots look superficially similar, with many of the same features occurring in the same positions. As the bottom row shows, the peak ion- and grain-neutral drift speeds are lowest at large angles with peak values of 18.2 km s^{-1} at 30°, 18 km s^{-1} at 45° and 17 km s^{-1} at 60°. The neutral temperatures are also lowest at large angles, peaking at 1080 K for 30°, 1050 K for 45° and 1030 K for 60°. The gas phase SiO abundance is enhanced by a factor of 50 between 60° and 45° and by a factor of 5 between 45° and 30°. The angular variation in the downstream SiO abundance must be caused by differing drift speeds rather than variations in the width of the sputtering region since the lowest SiO abundance occurs in the shock with the widest sputtering region. It is also clear that the variations in drift speed rather than temperature dominate the change in gas phase SiO since its enhancement follows the trend in drift speed, i.e. the variation in drift speed ($\sim 10^5$ cm s^{-1}) is largest between 60° and 45° whereas the change in temperature (~ 30 K) is largest between 45° and 30°.

Between 30° and 45° the downstream SiO abundance changes by 5×10^{-10} which is a factor of 5. Since only the small grains are sputtered at this shock speed in the high density regime, this difference corresponds to a difference in the evaporated small grain core fraction of 3.58×10^{-5}. Between 45° and 60° the post-shock SiO abundance falls by 9.8×10^{-11} (a factor of 5000). The difference in the fractions of small grain cores vaporized between 45° and 60° is then 7.02×10^{-6}. This means that the change in the gas phase SiO abundance is largest under variations at larger angles, but the difference in the sputtered silicon fraction is largest under variations at smaller angles.

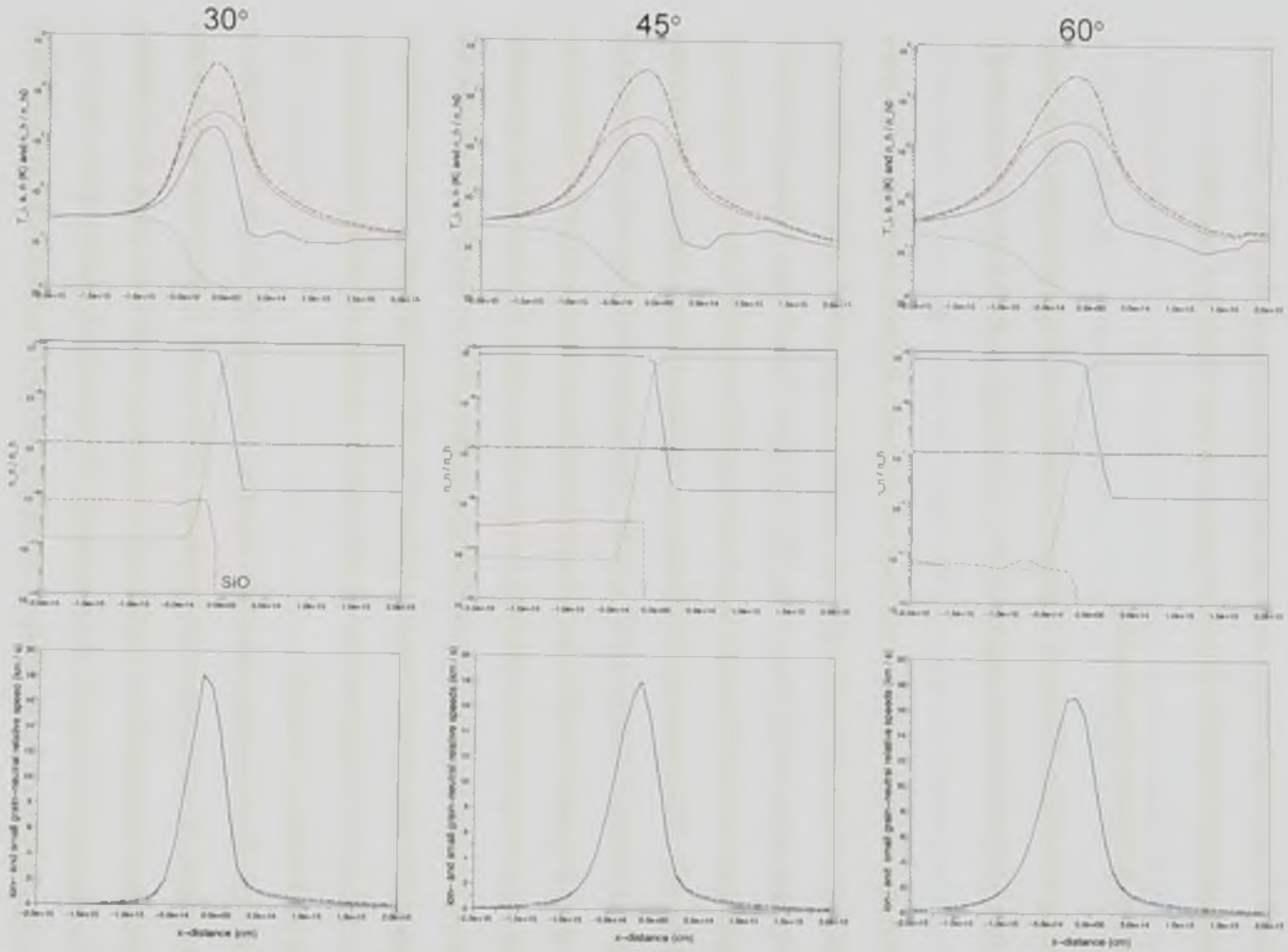

Figure 5.17: Fraction of silicon ejected from grain cores for a 25 km s^{-1} shock with $_H$ = 10^6 cm^{-3} which propagates at an angle of 30° (left column), 45° (middle column) and 60° (right column) to the upstream field. Top row is the ion (black, dash dot), electron (red, dash) and neutral (blue, solid) temperatures in Kelvin as well as the neutral density normalised to its upstream value. Middle row shows the neutral gas phase fractional abundances as per figures 5.4 - 5.11. The bottom row displays the small grain-neutral (blue, solid) and ion-neutral (black, long dash short dash) relative velocities in km s^{-1}.

Clearly, the angle between the magnetic field and the shock normal greatly alter the post-shock gas phase SiO enhancement, at least at shock speeds near to the sputtering threshold. That gas phase SiO is more abundant by a factor greater than 100 behind a 30° shock than behind a 60° shock was not expected, but it can be accounted for.

As described in §5.4.1, the yield depends on the drift speed (equation 5.27) and the sputtering rate depends on the yield, neutral temperature and drift speed. Lower neutral temperatures directly reduce the sputtering rate per grain due to the $T_n^{1/2}$ term outside the integral in equation (5.28). They also increase the values of x_{th} and s (by the same amount) which increases the value of the integral. Lower peak drift speeds infer lower impact energies and therefore reduce the yields and the value of s. In the current models, increasing the oblique angle in 15° increments reduces both the temperature (by a few tens of K) and the drift speed (by a few times 10^5 cm s^{-1}). The variation in u_{sn} therefore again dominates but unlike previously, x_{th} grows and s shrinks at larger angles. This can result in more (or potentially all) of the curve being below x_{th}. The relationship between x_{th} and s allows a small increase in θ to effectively halt the sputtering near to threshold since the yield is zero below x_{th}.

Angular variations in the velocity components of the charged fluids were noted in chapter 3 for simulations with a single fluid of large grains. Even with two grain fluids, the peak y-components of the charged fluid velocities in the current simulations still decrease by 25% (6.5 - 5 km s^{-1}) between 30° and 45° and by 35% (5 - 3.25 km s^{-1}) between 45° and 60°. The peak z-components of the charged fluid velocities decrease by 17.5% (4.25 - 3.5 km s^{-1}) between 30° and 45° and by 20% (3.5 - 2.8 km s^{-1}) between 45° and 60°. Large variations in the y-velocity components with angle are expected since those components are determined by the x-component of the magnetic field (see §3.4). The x-component of the magnetic field is largest at near parallel angles (small θ) and so are the y-velocity components of each charged fluid. The SiO variation between the angles matches the variation in the y-velocity components. The lower z-components reduce u_{sn} by the same amount in each angle interval. Therefore both the x- and y-velocity components contribute to the angular variation of the gas phase SiO fraction, but it is the y-components which cause the variation to be larger for angular variations at nearer perpendicular angles.

The effect of the lower temperatures and drift speeds (found at nearer perpendicular angles) on the sputtering rate (equation 5.28) can be summarised as follows:

- Inside the integral:
  - $Y< E >$ falls since it depends on the impact energy. This can be very important near to threshold because of the exponential shape of the yield curve (figure 5.2).
  - The exponential term in square brackets remains constant because although s falls, the range of x for the integral surrounds s and does not depend on either x or s. Therefore, the differences between x and s across the range remains constant and so does the whole term.
  - The x^2 term falls since the x-range for the integral (s-30 $\leq x \leq$ s+30 well above threshold and $x_{th} \leq x \leq$ s+30 near threshold) surrounds s, which has fallen.
  - As θ increases x_{th} grows and s falls. This increases the threshold impact energy for sputtering to occur. At shock speeds close to the sputtering threshold, an increase in θ may result in some or all of the curve being below x_{th}. As well as increasing the lower limit of the integral this can also drastically reduce the value of the solution to the integral.
- Outside the integral:
  - The sputtering rate is multiplied by $T_n^{1/2}$ so it is reduced by a factor of the square root of the temperature difference between the models. This is a small effect.
  - The sputtering rate is also multiplied by a factor of $1/s$. Since s falls, this term grows, but is overwhelmed by the decrease produced by the x^2 term once it has been integrated (see above).

The above considerations explain how very small changes in the drift speed and neutral temperature for shocks propagating at the same speed through media of the same density but at different angles to the upstream magnetic field can result in order of magnitude variations in the gas phase enhancement of silicon due to the sputtering process, especially close to threshold. In addition, those considerations makes it clear when such angular variations are to be expected. Angular variations in the sputtered fraction of silicon should occur whenever the shock speed results in partial sputtering of the cores. Because the grain cores are not completely sputtered at any shock speed in either of the density regimes considered, the angular variation should persist to the highest shock speeds for which the shock remains C-type.

If the effect noted above is indeed a result of variations in drift speed and temperature, then the same should occur in the case of mantle sputtering. To investigate this, additional simulations were completed in the shock speed region which results in partial mantle erosion. The low density regime was selected to demonstrate that the effect is not density dependent and an intermediate shock speed was selected to show that the effect is not a result of threshold effects, i.e. the SiO enhancement is dominated by the effect of the drift speed on s and not by the altered relationship between s and x_{th}. To this end, oblique simulations were carried out for 16 km s^{-1} shocks propagating through a medium with $n_H = 10^4$ cm^{-3} which make angles of 30°, 45° and 60° with the upstream magnetic field lines. All other parameters remain the same as the previous low density simulations.

The results of these simulations are included as figure 5.18. For these plots, the sputtered fractions are shown instead of the gas phase enhancements for reasons which are explained below. In the low density regime both grain fluids are involved in the sputtering process. The decrease in the downstream water abundance due to sputtering between 30° and 45° is 9.00×10^{-6}. This corresponds to around 12.5% less of the large grain mantles and 11.67% less of the small grain mantles being sputtered. Between 45° and 60°, the variation in the downstream water abundance due to sputtering is 6.9×10^{-6}. Under this variation, 10% less of the large grain mantles and 8.22% less of the small grain mantles are eroded. The variation in the total fraction of sputtered ice (the sum from both grain species) is now $\sim$ 10% between 30° and 45° and it remains $\sim$ 10% between 45° and 60°. The differences in gas phase enhancement due to sputtering are $\sim$ 20% in both cases.

Because the ice reservoir contains only 13.5% as much oxygen as is initially atomic, when temperatures are sufficient to convert most of this oxygen to water in the gas phase then the variation in the gas phase water abundance due to the angle of the field is small and difficult to detect. With $n_H = 10^4$ cm^{-3} however, mantle sputtering is total for both grain types before gas phase chemistry is able to remove more than half of the oxygen, so at 16 km s^{-1} the variation in the gas phase water is around 10% both between 30° and 45° and between 45° and 60°. Clearly other processes which are temperature and density dependent affect how observable the angular variation in mantle sputtering is (see below).

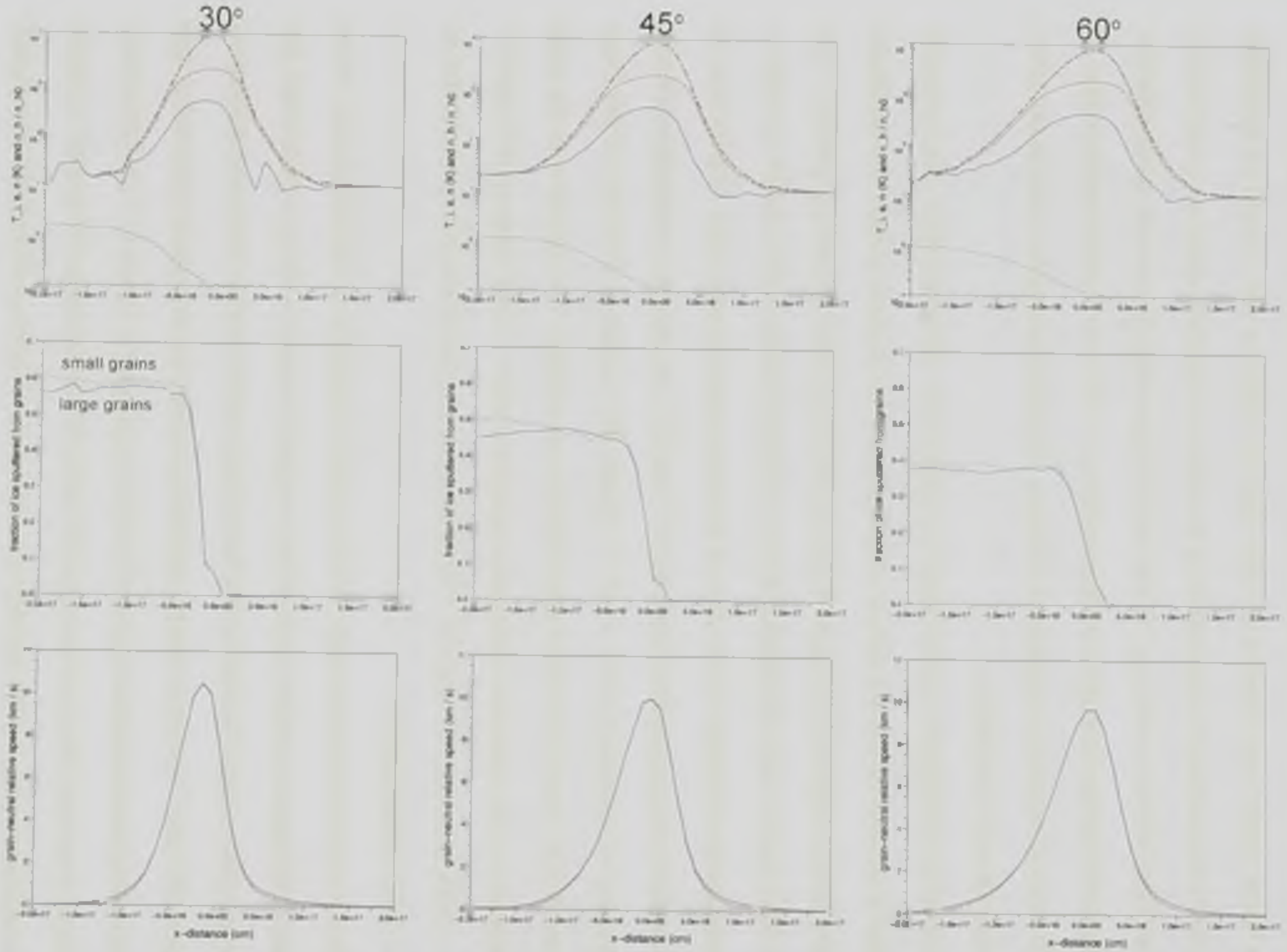

Figure 5.18: Shock structures of 16 km s^{-1} shocks propagating through upstream media with $n_H = 10^4$ cm^{-3} at angles of 30° (left column), 45° (middle column) and 60° (right column) to the upstream field. Top row is the ion (black, dash dot), electron (red, dash) and neutral (blue, solid) temperatures in Kelvin as well as the neutral density normalised to its upstream value (green, dotted). Middle row shows the fraction of ice ejected from large (blue, solid) and small (green dotted) grains as per figures 5.12 - 5.13. The bottom row displays the small grain-neutral (blue, solid) and ion-neutral (black, long dash short dash) relative velocities in km s^{-1}.

It is clear to see that largest variations in the gas phase abundance of a sputtered species due to the angle between the magnetic field lines and shock normal occur in simulations near to the sputtering threshold. It is also apparent that the large differences in gas phase enhancements between angular variations in near parallel and near perpendicular shocks largely disappear away from threshold. This suggests that such variations came about in the 25 km s^{-1} case because the lower y-velocities at large angles effectively put some of the curve below x_{th} and resulted in a total grain-neutral drift speed which produced very small yields. Well above threshold, the largest variations are still noted at small angles (because the y-velocities are still larger), but the differences are small and the change in the sputtered fractions and gas phase enhancements between angular variations are much more linear. Therefore variations in the y-velocity no longer affect the fraction of the curve below x_{th} or greatly alter the yield calculation.

Since it is the variation in the gas phase enhancement of a species which would be observed from Earth, shocks close to threshold will produce variations which are easier to observe. That said, variations of $\sim$ 10% ought to be detectable. This may not be the case at higher shock speeds for water since far more is produced from gas phase oxygen chemistry than sputtering at any angle, but any other mantle constituents (e.g. methanol) should also be enhanced by the same factors so if these species only come from the mantles, the variation in their abundances would remain much more obvious. It is also obvious (and expected) that angular variations near to the sputtering threshold will result in less variation in the sputtered fraction of the reservoir.

The two cases discussed in this section demonstrate that at shock velocities which result in partial erosion of either the grain mantles or cores, altering the angle between the upstream field lines and the shock normal changes both the fraction of the available material that is sputtered and the abundance of the sputtered species in the downstream region. Whether it is the angular variation in the sputtered fraction of the available material which is larger, or the angular variation abundance of the sputtered species in the downstream region depends on how close the shock speed is to the sputtering threshold.

5.8 Conclusions

This chapter contains multifluid MHD simulations of chemistry and grain sputtering in oblique C-type shocks propagating through dense, weakly ionized molecular media. The same source

terms as previous chapters are employed to describe the thermal and ionization structures and grain dynamics, but they are now joined by new terms to describe additional neutral and ionic species, the gas phase and grain surface recombinations which occur between those species as well as the erosion of grain mantles and cores due to sputtering. These models are the first truly time dependent simulations of gas phase chemistry and grain sputtering in oblique C-type shocks.

The chemical shock structures vary more with respect to the shock speed than with the density. Although lower neutral temperatures obtained with $n_H = 10^4$ cm^{-3} permit the onset of important reactions in the model only at higher shock speeds compared to the $n_H = 10^6$ cm^{-3} cases, away from threshold the profiles are qualitatively similar. The most notable diagnostics species for shock speed and temperature are presence and abundances of O, water, HCO^+ and MgH^+, even though the last has never been detected in such regions. The model would suggest that when metallic ions are most common and metallic molecular ions are absent, then a shock is slow. When metallic ions are most common, with molecular and metallic molecular ions having similar abundances, then the shock speed is intermediate. When metallic molecular ions dominate with metallic and molecular ions having similar and far lower abundances, then the shock speed is high.

The formation of MgH^+ also has important consequences for the fractional ionization. Although χ_e drops in all shocks as ion-grain currents become large, the formation of metallic molecular ions amplify this fall since they recombine with electrons far more willingly than the other types of ion.

Using this model, the value of water in the upstream region (a few times 10^{-9}) is close to that inferred from observations (e.g. Snell et al. 2000). Gas phase chemical models usually predict water abundances $\sim 10^3$ higher than those observed. and must invoke water freezing out onto grain surfaces to remain consistent with observations (Bergin & Snell 2002). In the models presented here, the large initial abundance of CO (as opposed to assuming that carbon is initially atomic) is able to limit the gas phase water abundance by forming HCO^+. The HCO^+ then reacts voraciously with any gas phase water available, converting it to H_3O^+. Further investigation is needed to either confirm or refute this conclusion. Whilst the current models predict a non-zero water abundance upstream of all shocks, freeze out processes are not modeled, so these are upper limits.

These models also predict the stratification of some species along the outflow direction. For example, at sufficient shock speeds to produce significant amounts of gas phase water, H_3^+ and HCO^+ are far more common in the upstream region (especially HCO^+) and MgH^+ only exists in the hottest part of the shock. Similarly, O, H_2O and SiO are also stratified along the shock propagation direction with O being more common in the upstream region and water and SiO being more common in the downstream region. Water is produced in copious quantities by grain mantle sputtering and neutral-neutral oxygen chemistry in any shock for which $v_s \geq 10$ km s^{-1}. If silicon bearing species are incorporated into grain mantles, then their abundances would also become non zero in this regime. HCO^+ on the other hand is most prevalent in the upstream region and the shock precursor, being destroyed in reactions with water upon entry to the shock.

Bachiller et al. (2001) present millimeter wavelength maps of the L 1157 bipolar outflow in several molecules. These include HCO^+ and SiO. They attribute emission features along the outflow to the shocks associated with periodic ejection episodes, because of the symmetry of such features in both the red and blue shifted lobes. They report chemical stratification along the outflow, which they demonstrate is not a result of excitation effects. This stratification includes HCO^+, which is only seen between the protostar and B0 (the most recent ejection episode) and SiO, which is only seen in association with the shocks themselves (especially its higher excitation transitions). The lack of HCO^+ can be explained in terms of this model because any shocks strong enough to result in SiO in the gas phase will also sputter the grain mantles, releasing water in copious quantities. This water will then react voraciously with any HCO^+ in the gas phase, converting it into H_3O^+. The current models therefore suggest that emission from SiO and HCO^+ will not be spatially coincident.

The mantle sputtering results from the current models at least qualitatively agree with previous work. It is noted here that fraction of ice sputtered from grains at a given shock speed is only weakly dependent on density even near threshold. This is because the small grains carry most of the ice and remain well coupled to the magnetic field lines even at the highest densities. The large grain mantles are better sputtered at low densities and the small grain mantles are better sputtered at high densities but these contributions cancel so that the gas phase enhancement due to sputtering remains constant even though the fraction of ice evaporated varies. The models require a drift speed between the grains and neutrals to produce measurable enhancements in

the water profile of 5 - 6 km s^{-1}, corresponding to a shock speed of $9 \leq v_s \leq 10$ km s^{-1}. The shock speeds for total erosion of the mantles are 18 km s^{-1} for grains which are well coupled to the field lines. Allowing for differences between the models, these results are consistent with those reported previously.

As expected, it is found that heavier projectiles dominate sputtering near to threshold where their larger masses ensure lower threshold streaming velocities, allowing them to commence sputtering at lower shock speeds. Once all the ice has been removed from a grain species, further increases in the shock speed narrows the sputtering region and increases the importance of the lighter and more abundant projectiles. This is at the expense of the sputtering rates of the heavier projectiles. The current models agree with previous work in predicting that H_2 will become the dominant projectile for mantle sputtering when $v_s > 30$ km s^{-1}.

As opposed to the mantles, where the gas phase enhancement of water due to sputtering is only weakly dependent on density even near threshold, the gas phase enhancement of SiO does depend on the density, especially near threshold. This is because the large grains contain most of the silicon reservoir and the degree of coupling between the large grains and magnetic field is strongly dependent on density.

In the case of core sputtering, the current results again broadly agree with previous findings, especially with respect to the threshold shock speed. In the case of more recent studies which consider heavier molecular projectiles, the fraction of grain core material released into the gas phase reported there is within around an order of magnitude of the current results. Because of the weak coupling between the magnetic field and the large grains at high densities, the low speed limit for C-type shocks at high densities and the fact that the large grains contain most of the silicon reservoir, high density simulations are unable to reproduce the gas phase SiO abundances inferred near some YSOs. To obtain gas phase SiO abundances greater than 10^{-6}, $v_s \geq 40$ km s^{-1} is required and shocks at this speed are only C-type when they propagate through an upstream medium with $n_H = 10^4$ cm^{-3} using the current treatment. This is because the relevant signal speeds are lower at higher densities, meaning that the shock overtakes the ion magneto-sonic waves and a J-type shock results (see §1.3).

At $n_H = 10^4$ cm^{-3}, the grain cores are still not completely destroyed even at the highest shock speeds. With $v_s = 50$ km s^{-1}, 20% of the small grains and 2.5% of the large grains are destroyed. In fact, it seems the shock speeds required for total sputtering of even the small

grain cores using this treatment would also result in copious dissociation of molecular hydrogen. Such shocks would be unlikely to remain C-type, making the effectiveness of inertial sputtering highly questionable.

This finding renders the total destruction of all the grains in any C-type shock associated with an SFR highly unlikely. Since the large grains are more resistant to sputtering even at densities where they are well coupled to the field, it seems probable that previously noted effects on the shock dynamics due to large grains such as field rotation and spiral nodes (Pilipp et al. 1990; Pilipp & Hartquist 1994, Wardle 1998) will persist throughout all such shocks even when sputtering is included. This is especially true since these effects are largest at high densities and it is the decoupling of the large grains from all of the other components which produces these effects, whilst simultaneously suppressing their sputtering.

It should be noted that the assumption that all of the grains are silicate based is not accurate. Whilst Draine (2009) points out that the strength of the extinction requires that the bulk of the grains be based on high abundance elements such as Si and C, it is thought that only around 60% of the grains are composed of silicates (e.g. Draine 2011), with much of the rest being carbon based. If the total dust mass is $\sim 1\%$ that of the flow and a significant fraction of those grains are carbon, then the gas phase SiO abundances in this study represent upper limits. Carbon based grains are also expected to be sputtered in C-type shocks (e.g. Draine & Salpeter 1979; Tielens et al. 1994). However, the fact that there is gas phase carbon already present in molecular clouds (see §1.1.1) and FUV photolysis and warm up of the accreted grain mantles (in diffuse cloud regions) can result in organic residue mantles or even the formation of amorphous aromatic carbon structures (e.g. Tielens & Allamandola 1987) makes detection of sputtered carbon products highly challenging.

If shock processing of the grain mantles followed by freeze out has occurred, then it is reasonable to assume that the mantles themselves contain a small amount of silicon bearing species which are bound with similar energies to the water ice. This silicon would then be released during the processing of the mantles during their passage through subsequent shocks. Jiménez-Serra et al. (2004) propose that just this kind of mantle sputtering in the early stages of passage through a shock precursor in L1448-mm leads to a low velocity SiO component with an abundance enhanced by an order of magnitude (to $\sim 10^{-11}$) from the quiescent cloud value. Their observations of L1448-mm also show a high abundance ($> 10^{-6}$), high velocity

SiO component which is ascribed to the sputtering of the grain cores in a shock with $v_s > 25$ km s^{-1}. Jiménez-Serra et al. (2004) report that although previous models (e.g. Caselli et al. 1997; May et al. 2000) can account for the large velocity, high abundance component, they cannot account for the low velocity, low abundance component. That much is true since none of those models considered silicon bearing species to be present in the grain mantles.

Whilst the inclusion of an arbitrary amount of silicon in the grain mantles could reproduce a two stage enhancement of the gas phase SiO abundance, some caveats are noted. Firstly, in this work it is found that the processing of the mantle and core material are not neatly delineated. At high densities, processing of the large grain mantles and small grain cores are spatially coincident because the small grain cores pass the core sputtering threshold before the large grains have lost all of their mantles. At low densities and even near threshold, core sputtering commences immediately after the mantles have been evaporated. The only reason there is no overlap is that the cores are unable to be sputtered before all of the ice has been removed in the model. This makes the prospect of distinct observable velocity components of SiO emission from the shock itself and magnetic precursor seem unlikely, even when using a one dimensional, steady treatment.

The current models do not rule out the proposal of Jiménez-Serra et al. (2008), that small amounts of silicon bearing species are ejected from grain mantles due to sputtering in shock precursors, the basis of which seems likely to occur. Rather, these findings suggest caution in the interpretation of such observations since there appear to be alternative mechanisms by which such slight SiO enhancements with different velocities can be produced. Most notably, the angle between the upstream magnetic field and the shock normal as well as the flow speed can both produce enough variation in the sputtered core fraction near threshold to result in order of magnitude differences in the gas phase SiO abundance. There is also the possibility of a bow shock geometry where the shocks in the flanks of the bow have lower speeds and make different angles with the magnetic field together with the existence of a small amount of silicon in the mantles.

Chapter 6

Conclusions

This chapter briefly summarises the main results of the thesis. The work in chapters 4 and 5 is not fully concluded and potential tasks for future research projects are mentioned.

Over the course of the research presented in chapters 3 - 5, the multifluid MHD scheme described in Falle (2003) was progressively extended to model additional physics and environments.

The basis of the research in this thesis was the proper time dependent modeling of C-type shocks. Chapter 3 presented models of steady C-type shocks in which a simplified chemical model is adopted. The simplified model still correctly determined the abundances of those species which affect the fractional ionization and contribute to cooling. The simulations in that chapter began with J-type shocks, which evolved in time to become steady C-type shocks. The results of the perpendicular simulations agreed with previous work, demonstrating that the scheme was accurate and efficient. The oblique models were the first time dependent simulations of such shocks in dense, weakly ionized molecular media. They were in harmony with the main qualitative conclusions of previous studies and because of the rigorous treatment of grain dynamics and thermal and ionization balances the results were reliable enough to compare with observations for the first time.

In oblique simulations with a single fluid of large grains, as the electrons became heated in the magnetic precursor, frequent electron-grain collisions resulted in highly charged grains which became important charge carriers and hence mediators of current. The grains switched to moving with the other charged fluids, but because of their large cross sections, frequent grain-neutral collisions in the dense gas caused them to become the dominant source of drag on the neutrals. This constrained them to move at velocities in between those of the other charged fluids and the neutrals. Because they were important negative charge carriers and moved differ-

ently to the ions and electrons, a charge separation was produced which resulted in a large Hall conductivity and Hall current along the shock propagation direction. Because the total current in that direction must remain zero in a steady shock and in oblique shocks the magnetic field component along the shock normal is non-zero, the Pedersen current along the shock propagation direction mobilised enough charges to counteract the Hall current and resulted in a rotation of the magnetic field about the shock normal. It was noted that the field rotation was most pronounced in shocks whose normals made small angles with the upstream magnetic field lines.

In addition to the field rotation, the upstream stationary point of the magnetic field switched to being a spiral node in the high density simulations. This resulted in the strong oscillations in the charged fluid velocities at the upstream edge of the precursor. This supported previous findings for steady shocks. The inclusion of a second, smaller grain fluid which possesses a high enough Hall parameter to remain well coupled to the field lines largely suppresses the field rotation and formation of the spiral node. This is due to the fact that the more numerous small grains dominate the friction with the neutrals but move with the other charged species, thus minimising the charge separation.

Since the timescales for C-type shocks to become steady inferred in previous studies ($\sim 10^5$ years) were similar to the timescale for which the accretion driven outflow from a low mass YSO persists for ($\sim 10^6$ years), it seemed unlikely that any shocks in those outflows would be steady. When coupled with the ubiquitous inhomogeneity of molecular clouds, steady shocks in molecular outflows appear even more unlikely. To this end, terms were included in the code to simulate a density inhomogeneity in the upstream medium. These inhomogeneities then interacted with the steady C-type shocks obtained as the final conditions in chapter 3. Three types of density perturbation were considered. Two were semi-finite inhomogeneities, of increasing or decreasing density and the third was chosen to accurately represent a clump as observed in molecular clouds.

Whenever a shock interacted with a semi-finite density perturbation it reacted by breaking up into transmitted and reflected waves. The reflected component travelled in the opposite direction to the original C-type shock and was either a shock or a rarefaction wave, depending on the nature of the perturbation. Shocks were reflected when the perturbation was of increasing density and rarefaction waves were reflected when the perturbation was of decreasing density. This was because the reflected wave connected the downstream region of the newly transmit-

ted shock with the downstream region of the original C-type shock. The relative strength of the transmitted and reflected components was found to be dependent on the initial shock speed and the density contrast across the perturbation, since they control the post-shock flow of the transmitted shock. The evolution of the reflected component was not followed and it was removed from the grid once a contact discontinuity had formed between it and the transmitted component.

It may be of interest to follow the reflected component instead, especially in cases where it is of comparable strength to the transmitted component and then interacts with a shock traveling in the same direction as the original C-type shock (for example due to episodic ejection events from the parent YSO).

The transmitted shock in the models of chapter 4 always contained a neutral J-type sub-shock and a precursor. The J-type sub-shock subsequently evolved back to being a C-type shock with a different width and velocity. This occurred on a timescale comparable to the ion flow time through the final shock structure and was the same as the evolution of the initial conditions in chapter 3. The ion flow time was found to be relevant for perturbations both of increasing and decreasing density. It was therefore concluded that any shock which encounters density inhomogeneities more frequently than the ion crossing time cannot be steady. Sufficiently upstream parts of the transmitted shock precursor in all semi-finite cases were found to be quasi-steady and the quasi-steady region expanded to form the new stable C-type shock. This validated the prior quasi-steady models of C-type shocks in dusty media since such approaches had only been previously justified for dustless shocks. However, it was noted that such quasi-steady models were only valid after an initial adaption phase, as the flow adjusted to the changing upstream conditions and were only applicable in cases when the driving force of the flow would remain steady until steady state was obtained.

The case of a C-type shock interacting with a clump was less straightforward and could not be described by combining the results for monotonically increasing and decreasing densities. The initial behaviour of the shock as it moved up the density gradient was similar to the early evolution of a shock interacting with a semi-finite perturbation of increasing density. However, the transmitted shock had insufficient time to become C-type before it met the backside of the clump where the density decreased. This meant that a J-type shock with precursor travelled down the density gradient. The precursor developed a second neutral sub-shock and a rarefac-

tion wave was reflected. The velocities of the neutral and charged components did not converge between the secondary and primary sub-shocks, which resulted in an extended region with non-zero charged fluid-neutral drift speeds. It was noted that such cases are likely to be common in molecular clouds and cannot be modeled using quasi-steady approximations. They may result in wide sputtering regions for some shock parameters. Indeed, the observed clumpiness in molecular clouds makes even one dimensional simulations of such interactions including sputtering terms highly desirable.

Near the outflows associated with some low mass YSOs, silicon bearing species have been observed with abundances enhanced by factors of up to 10^6 from those consistently inferred in quiescent clouds. The refractory nature of silicon meant that these enhancements were likely to have come about due to the processing of dust grains in shocks. The extended region for which the charged fluids stream through the neutrals in C-type shocks provides a mechanism for this processing by facilitating collisions between the charged dust grains and neutral species. Sufficiently energetic grain-neutral collisions may eject atoms or molecules from the grain cores or mantles in a process known as sputtering. In addition to terms to describe the sputtering, a more comprehensive chemical model was required since near the sputtering threshold impact energy, heavier molecules make much more efficient projectiles, necessitating an accurate determination of their abundances.

The equilibrium upstream water abundances were found to be within order of magnitude agreement ($10^{-9} \leq \chi_{H_2O} \leq 10^{-8}$) with observations of dense molecular cloud regions. Other, more complex gas phase chemical models have predicted abundances $\sim 10^3$ times higher than this. One explanation could be that those models typically use atomic species as their initial conditions whereas in the current work, all of the carbon is already in CO. The CO limits the upstream gas phase water abundance by forming HCO^+. HCO^+ reacts with and removes much of the water. Confirmation or refutation of this conclusion will require further investigation.

The chemical model includes a treatment of the gas phase conversion of atomic oxygen into water in the shock through neutral-neutral reactions. Since atomic oxygen and water are assumed to have the same mass in the sputtering calculation, this was only important for the neutral cooling calculation. More than 90% of the atomic oxygen is converted to water in shocks with velocities in excess of 16 km s^{-1} at $n_H = 10^6$ cm^{-3}, but lower collision rates and neutral temperatures push this up to $v_s \sim 25$ km s^{-1} for $n_H = 10^4$ cm^{-3}. Chemical reactions

in the hottest part of the shock front resulted in the formation of metallic molecular ions. Their subsequent recombinations (gas phase and grain surface) occurred as soon as the temperatures began to fall and proceeded more efficiently than any other ion type (metallic or molecular). This had important consequences for the gas phase fractional ionization. Whenever conditions permitted MgH^+ to become the most common ion in a shock, highly efficient recombinations caused the fractional ionization to strongly fall in the region where it was destroyed.

The new chemical model resulted in the segregation of some chemical species along the flow. Most notably, HCO^+ is common in the upstream region, but almost absent downstream, whilst the opposite is true for water and SiO. These findings are in harmony with recent (millimeter) observations of L1557, which suggests that the abundances of HCO^+ and water are linked.

Due to the differences in bonds between ice molecules of the mantle and atoms of the core, the mantle particles are more weakly bound. Drift speeds of 5 - 6 km s^{-1} were needed to result in systematic mantle sputtering and were obtained in shocks with velocities in the range $9 \leq v_s \leq 10$ km s^{-1}. The cores however remained impervious to neutral bombardment until the drift speeds reaches ~ 17 km s^{-1}, which occurred in 25 km s^{-1} shocks at both densities.

Above threshold, the fraction of the silicon and ice sputtered follow exponential relationships with the drift speed, determined by their yield expressions. At shock speeds which result in grain-neutral drift speeds well above the sputtering threshold, even the lightest projectiles are capable of sputtering. Despite its low mass, molecular hydrogen is able to dominate mantle sputtering due to its high abundance. Its growth to dominance occurs at the expense of heavier but less common projectiles that dominate near to threshold. The shock speed required for the complete mantle erosion of grains which are well coupled to the magnetic field was found to be 18 km s^{-1}. When the density is high enough to decouple the large grains from the field, their mantles persist until higher shock speeds ($20 \leq v_s \leq 25$ km s^{-1}). The shock speed at which all the ice mantle are removed is therefore determined by the degree of coupling between the large grains and the field and varies with the upstream density.

With higher upstream densities, the maximum shock speed of a C-type shock falls. At the same time, the large grains become less well coupled to the field lines resulting in lower large grain-neutral drift speeds. This meant that the simulations in the high density regime were unable to reproduce the high abundances of silicon bearing species observed near some low mass

YSOs. An upstream density of $n_H = 10^4$ cm^{-3} and shock speed of 40 km s^{-1} was required to produce a gas phase SiO abundance above 10^{-6}. Even when the large grains were coupled to the field lines, most of this silicon (> 90 %) still came from the small grains because they are more numerous, so even with smaller cross sections, they are still involved in more collisions. Due to the high bonding energies of the core material, even the fastest shocks possible at $n_H = 10^4$ cm^{-3} destroy less than one third of the small grain cores and less than 5% of the large grain cores. However this was sufficient to reproduce the gas phase SiO abundances observed.

Given the differences between models, the models in chapter 5 largely confirm the findings of previous studies with regards to threshold shock speed for sputtering and the fraction of the core and mantle material eroded at each shock speed above threshold. Whenever sputtering of the cores or mantles occurred, but did not result in complete erosion, then the angle between the shock normal and the upstream magnetic field strongly affected the sputtering rates. This was because the magnitude of the upstream field component parallel to the shock normal (x-direction) strongly affected the charged particle dynamics in the other direction containing a non-zero upstream field component (y-direction). Large x-components of the upstream field produced y-velocity components of up to $\sim 25\%$ of the shock speed.

The additional drift speeds of the grains with respect to the neutrals increased the energies of the impacts and resulted in larger gas phase enhancements of the sputtered species. Near to threshold, the differences in enhancement were orders of magnitude for a change in the field configuration of just 45°. Well above threshold the variation in the fraction of material eroded was the same between large angles as it was between small angles. In the case of the mantles, $\sim 10\%$ drops in the ice sputtered were noted both between 30° and 45° and 45° and 60°. These resulted in smaller variations in the gas phase enhancement and therefore minimised the observable differences.

Recent observations of some outflows had resulted in some researchers assigning slightly enhanced SiO abundances moving at low speeds to the early stage interaction between neutrals and dust grains in shock precursors. Whilst the new models do not discount this possibility, they do suggest caution in the interpretation of such results. This is because of the angular dependence noted above. When the findings from chapter 4 are also considered, it becomes clear that two dimensional simulations including sputtering and the interaction of the shock with density perturbations are desirable, since it is quite likely that these would result in complex SiO

abundance and velocity profiles.

It is hoped that by running two dimensional sputtering simulations, including terms to calculate expected intensities and ratios of emission lines and adding perturbations in the upstream medium which are selected to match those of observed clumps, detailed simulations of specific outflows may be undertaken. The results may then be compared to observations. In this case, the neglect of the grain inertia should be rectified even despite the ability of the scheme of Falle (2003) to model neutral sub-shocks. This is because the drag length of the grains are not negligibly small in J-type shocks.

It would also be interesting to model different sizes and compositions of grains. Draine & Li (2007) speculate that the extinction bump near 2175 Å is produced by a large population of polycyclic aromatic hydrocarbons since these are required to explain a number of IR emission features. Very small grains can equally be considered as large molecules. These include perhaps ~ 50 carbon atoms (e.g. Tielens 2011). When they are charged they will remain exceptionally well coupled to the magnetic field, making them candidates for sputtering at the lowest shock speeds. However being large molecules as opposed to crystalline or amorphous solids makes it likely that new terms would be required for their yields and sputtering rates. These terms may render polycyclic aromatic hydrocarbons more resistant to shock processing (see Micelotta et al. 2011).

In addition, a recent revision of the fraction of carbon which is incorporated into grains (from 0.33 to 0.67) was suggested by Sofia & Parvathi (2009). The life cycle of interstellar grains involves them repeatedly cycling between dense regions where gas phase accretion occurs and diffuse regions where exposure to the FUV flux results in photolysis. This can ultimately produce organic residue mantles (e.g. Tielens & Allamandola 1987). Such mantles can equally form on silicate or carbonaceous grains and recent observations of L1157 (Arce et al. 2008) have indicated not only that complex organic molecules form on grain surfaces, but also that outflow processing (sputtering and evaporation) of the grain mantles releases them back into the gas phase.

The inclusion of carbon based grains that are sputtered in the outflow shock could raise the gas phase abundances of carbon, water and other organic species in warm, dense regions ready for further gas phase processing to take place. By modeling the constituents of such mantles, perhaps using a grid of models employing a variety of parameters, it would be possible

to estimate the return of organic and other carbon based material to the gas phase. This is of considerable interest to research into the origins of organic material in the solar system since it would provide a first estimate of the composition and abundance of such material which becomes initially available in proto-planetary disks. It is certainly interesting to note the close association of water and organic molecules, even at these earliest stages.

This research project has marked a large step forward in our ability to model the return of refractory core as well as complex mantle material to the gas phase in non-steady shocks. While the above discussion recommends a couple of specific future research directions, the applications of such a code are wide and varied. It is now relatively simple for new chemical species and reactions to be modeled. both in the gas phase and on grain surfaces. Additional grain species of varying sizes and compositions may also be added at will. With the inclusion of a second dimension in the models and sufficient computer power to run the simulations, it is now possible to model almost any astrophysical flow, and produce results which are reliable enough to compare with observations. Given the prevalence of such flows on all scales, from the accretion flows associated with single YSOs, through supernovae, the outflows associated with the central black holes in spiral galaxies right up to flows on cosmological scales, many interesting and relevant applications can be envisaged.

Bibliography

Acord, J. M., Walmsley, C. M., & Churchwell, E. 1997, ApJ, 475, 693

Ahrens, T. J., & O'Keefe, J. D. 1972, Moon, 4, 214

Andre, P., & Montmerle, T. 1994, ApJ, 420, 837

Andre, P., Ward-Thompson, D., & Barsony, M. 1993, ApJ, 406, 122

Arce, H. G., Shepherd, D., Gueth, F., Lee, C.-F., Bachiller, R., Rosen, A., & Beuther, H. 2007, Protostars and Planets V, 245

Arce, H. G., Santiago-García, J., Jørgensen, J. K., Tafalla, M., & Bachiller, R. 2008, ApJL, 681, L21

Ashmore, I., van Loo, S., Caselli, P., Falle, S. A. E. G., & Hartquist, T. W. 2010, A&A, 511, A41

Bachiller, R., Martin-Pintado, J., Tafalla, M., Cernicharo, J., & Lazareff, B. 1990, A&A, 231, 174

Bachiller, R. 1996, ARA&A, 34, 111

Bachiller, R., Pérez Gutiérrez, M., Kumar, M. S. N., & Tafalla, M. 2001, A&A, 372, 899

Bally, J., & Lada, C. J. 1983, ApJ, 265, 824

Barlow, M. J. 1978, MNRAS, 183, 367

Barnard, E. E. 1927, Chicago: University of Chicago Press, 1927,

Bergin, E. A., et al. 2000, ApJL, 539, L129

Bergin, E. A., & Snell, R. L. 2002, ApJL, 581, L105

Beuther, H., Schilke, P., & Gueth, F. 2004, ApJ, 608, 330

Bok, B. J., & Reilly, E. F. 1947, ApJ, 105, 255

Bontemps, S., Andre, P., Terebey, S., & Cabrit, S. 1996, A&A, 311, 858

Caselli, P., Hartquist, T. W., & Havnes, O. 1997, A&A, 322, 296

Caselli, P., Walmsley, C. M., Terzieva, R., & Herbst, E. 1998, ApJ, 499, 234

Caselli, P., Keto, E., Pagani, L., et al. 2010, A&A, 521, L29

Cazaux, S., & Tielens, A. G. G. M. 2004, ApJ, 604, 222

Chapman, J. F., & Wardle, M. 2006, MNRAS, 371, 513

Chieze, J.-P., Pineau des Forets, G., & Flower, D. R. 1998, MNRAS, 295, 672

Chemin, L. M., Masson, C. R., & Fuller, G. A. 1994, ApJ, 436, 741

Cherchneff, I. 1998, The Molecular Astrophysics of Stars and Galaxies, edited by Thomas W. Hartquist and David A. Williams. Clarendon Press, Oxford, 1998., p.265, 4, 265

Chiar, J. E., Pendleton, Y. J., Allamandola, L. J., et al. 2011, ApJ, 731, 9

Ciolek, G. E., & Roberge, W. G. 2002, ApJ, 567, 947

Codella, C., Bachiller, R., & Reipurth, B. 1999, A&A, 343, 585

Combes, F., & Wiklind, T. 1995, A&A, 303, L61

Crutcher, R., Heiles, C., & Troland, T. 2003, Turbulence and Magnetic Fields in Astrophysics, 614, 155

Crutcher, R. M., Wandelt, B., Heiles, C., Falgarone, E., & Troland, T. H. 2010, ApJ, 725, 466

Dartois, E. 2006, A&A, 445, 959

Downes, D., Genzel, R., Hjalmarson, A., Nyman, L. A., & Ronnang, B. 1982, ApJL, 252, L29

Draine, B. T. 1978, Ph.D. Thesis,

Draine, B. T. 1980, ApJ, 241, 1021

Draine, B. T. 1986, MNRAS, 220, 133

Draine, B. T. 1995, Ap&SS, 233, 111

Draine, B. T. 2009, Cosmic Dust - Near and Far , 414, 453

Draine, B. T. 2011, Physics of the Interstellar and Intergalactic Medium by Bruce T. Draine. Princeton University Press, 2011. ISBN: 978-0-691-12214-4,

Draine, B. T., & Salpeter, E. E. 1979, ApJ, 231, 77

Draine, B. T., Roberge, W. G., & Dalgarno, A. 1983, ApJ, 264, 485

Draine, B. T., & Sutin, B. 1987, ApJ, 320, 803

Draine, B. T., & McKee, C. F. 1993, ARA&A, 31, 373

Draine, B. T., & Li, A. 2007, ApJ, 657, 810

Edwards, S., & Snell, R. L. 1982, Bull. AAS, 14, 912

Edwards, S., & Snell, R. L. 1983, ApJ, 270, 605

Edwards, S., & Snell, R. L. 1984, ApJ, 281, 237

Falle, S. A. E. G. 1991, MNRAS, 250, 581

Falle, S. A. E. G. 2003, MNRAS, 344, 1210

Falle, S. A. E. G., & Komissarov, S. S. 2001, Journal of Plasma Physics, 65, 29

Falle, S. A. E. G., & Raga, A. C. 1993, MNRAS, 261, 573

Field, G. B., Goldsmith, D. W., & Habing, H. J. 1969, Bull. AAS, 1, 240

Field, D., May, P. W., Pineau des Forets, G., & Flower, D. R. 1997, MNRAS, 285, 839

Flower, D. R., & Pineau-Des-Forets, G. 1990, MNRAS, 247, 500

Flower, D. R., & Pineau des Forets, G. 1994, MNRAS, 268, 724

Flower, D. R., & Pineau des Forets, G. 1995, MNRAS, 275, 1049

Flower, D. R., & Pineau des Forêts, G. 1999, MNRAS, 308, 271

Flower, D. R., & Pineau des Forêts, G. 2003, MNRAS, 343, 390

Flower, D. R., Pineau des Forets, G., & Hartquist, T. W. 1985, MNRAS, 216, 775

Flower, D. R., Le Bourlot, J., Pineau des Forêts, G., & Cabrit, S. 2003, MNRAS, 341, 70

Flower, D. R., Pineau Des Forêts, G., & Walmsley, C. M. 2007, A&A, 474, 923

Frenklach, M., Carmer, C. S., & Feigelson, E. D. 1989, Nature, 339, 196

Gail, H.-P., & Sedlmayr, E. 1998, The Molecular Astrophysics of Stars and Galaxies, edited by Thomas W. Hartquist and David A. Williams. Clarendon Press, Oxford, 1998., p.285, 4, 285

Garay, G., Ramirez, S., Rodriguez, L. F., Curiel, S., & Torrelles, J. M. 1996, ApJ, 459, 193

Garrod, R. T., Williams, D. A., Hartquist, T. W., Rawlings, J. M. C., & Viti, S. 2005, MNRAS, 356, 654

Garrod, R. T., Williams, D. A., & Rawlings, J. M. C. 2006, ApJ, 638, 827

Genzel, R. 1991, NATO ASIC Proc. 342: The Physics of Star Formation and Early Stellar Evolution, 155

Gibb, A. G., Wyrowski, F., & Mundy, L. G. 2004, ApJ, 616, 301

Gibb, E. L., et al. 2000, ApJ, 536, 347

Gould, R. J., & Salpeter, E. E. 1963, ApJ, 138, 393

Gueth, F., Guilloteau, S., Dutrey, A., & Bachiller, R. 1997, A&A, 323, 943

Gueth, F., & Guilloteau, S. 1999, A&A, 343, 571

Guillet, V., Pineau Des Forêts, G., & Jones, A. P. 2007, A&A, 476, 263

Guillet, V., Jones, A. P., & Pineau Des Forêts, G. 2009, A&A, 497, 145

Gusdorf, A., Pineau Des Forêts, G., Cabrit, S., & Flower, D. R. 2008, A&A, 490, 695

Habing, H. J., & Olofsson, H. 2003, Asymptotic giant branch stars, by Harm J. Habing and Hans Olofsson. Astronomy and astrophysics library, New York, Berlin: Springer, 2003,

Haro, G. 1952, ApJ, 115, 572

Hartigan, P., Morse, J. A., Tumlinson, J., Raymond, J., & Heathcote, S. 1999, ApJ, 512, 901

Hartquist, T. W., Dalgarno, A., & Oppenheimer, M. 1980, ApJ, 236, 182

Hartquist, T. W., Caselli, P., Rawlings, J. M. C., Ruffle, D. P., & Williams, D. A. 1998, The Molecular Astrophysics of Stars and Galaxies, edited by Thomas W. Hartquist and David A. Williams. Clarendon Press, Oxford, 1998., p.

Havnes, O., Hartquist, T. W., & Pilipp, W. 1987, NATO ASIC Proc. 210: Physical Processes in Interstellar Clouds, 389

Hedstrom, G. W. 1979, Journal of Computational Physics, 30, 222

Heiles, C. 1976, ARA&A, 14, 1

Herbig, G. H. 1951, ApJ, 113, 697

Herbst, E., Millar, T. J., Wlodek, S., & Bohme, D. K. 1989, A&A, 222, 205

Hildebrand, R. H. 1988, Astrophysical Letters Communications, 26, 263

Hollenbach, D., & McKee, C. F. 1979, ApJS, 41, 555

Hollenbach, D., & McKee, C. F. 1989, ApJ, 342, 306

Hollenbach, D., & Salpeter, E. E. 1971, ApJ, 163, 155

Hollenbach, D., Kaufman, M. J., Bergin, E. A., & Melnick, G. J. 2009, ApJ, 690, 1497

Hueckstaedt, R. M., Hunter, J. H., & Lovelace, R. V. E. 2006, MNRAS, 369, 1143

Ioppolo, S., Palumbo, M. E., Baratta, G. A., & Mennella, V. 2009, A&A, 493, 1017

Jiménez-Serra, I., Martín-Pintado, J., Rodríguez-Franco, A., & Marcelino, N. 2004, ApJL, 603, L49

Jiménez-Serra, I., Caselli, P., Martín-Pintado, J., & Hartquist, T. W. 2008, A&A, 482, 549

Jiménez-Serra, I., Caselli, P., Tan, J. C., Hernandez, A. K., Fontani, F., Butler, M. J., & van Loo, S. 2010, MNRAS, 406, 187

Johnstone, D., et al. 2010, A&A, 521, L41

Jones, A., & Tielens, A. 1994, The Cold Universe, 35

Jones, A. P., Tielens, A. G. G. M., Hollenbach, D. J., & McKee, C. F. 1994b, Bulletin of the American Astronomical Society, 26, 1355

Jørgensen, J. K., Hogerheijde, M. R., Blake, G. A., van Dishoeck, E. F., Mundy, L. G., & Schoier, F. L. 2004, A&A, 415, 1021

Kaufman, M. J., & Neufeld, D. A. 1996, ApJ, 456, 611

Kimura, H., Mann, I., Jessberger, E. K., & Weber, I. 2003, Meteoritics and Planetary Science Supplement, 38, 5211

Kivelson, M. G., & Russell, C. T. 1995, Introduction to Space Physics, Edited by Margaret G. Kivelson and Christopher T. Russell, pp. 586. ISBN 0521451043. Cambridge, UK: Cambridge University Press, April 1995.,

Krumholz, M. R., & McKee, C. F. 2008, Nature, 451, 1082

Kwan, J., & Scoville, N. 1975, ApJL, 195, L85

Lada, C. J. 1985, ARA&A, 23, 267

Laney, C. B, Computational Gas Dynamics. Cambridge University Press. Cambridge, 1998., p.

Larson, R. B. 1981, MNRAS, 194, 809

Ledrew, G. 2001, Journal of the Royal Astronomical Society of Canada, 95, 32

Lee, C. W., & Myers, P. C. 1999, ApJS, 123, 233

Lee, C.-F., Ho, P. T. P., Palau, A., Hirano, N., Bourke, T. L., Shang, H., & Zhang, Q. 2007, ApJ, 670, 1188

Lefloch, B., Cernicharo, J., Pacheco, S., & Ceccarelli, C. 2011, A&A, 527, L3

Lefloch, B., Castets, A., Cernicharo, J., & Loinard, L. 1998, ApJL, 504, L109

Lesaffre, P., Chièze, J.-P., Cabrit, S., & Pineau des Forêts, G. 2004, A&A, 427, 147

Lesaffre, P., Chièze, J.-P., Cabrit, S., & Pineau des Forêts, G. 2004, A&A, 427, 157

Mac Low, M.-M., Norman, M. L., Konigl, A., & Wardle, M. 1995, ApJ, 442, 726

Lipshtat, A., & Biham, O. 2005, MNRAS, 362, 666

Lizano, S. 1989, Revista Mexicana de Astronomia y Astrofisica, 18, 11

Martin-Pintado, J., Bachiller, R., & Fuente, A. 1992, A&A, 254, 315

Masson, C. R., & Chernin, L. M. 1993, ApJ, 414, 230

Mathis, J. S., Rumpl, W., & Nordsieck, K. H. 1977, ApJ, 217, 425

May, P. W., Pineau des Forêts, G., Flower, D. R., Field, D., Allan, N. L., & Purton, J. A. 2000, MNRAS, 318, 809

McKee, C. F., & Ostriker, J. P. 1977, ApJ, 218, 148

Mestel, L., & Spitzer, L., Jr. 1956, MNRAS, 116, 503

Meyers-Rice, B. A., & Lada, C. J. 1991, ApJ, 368, 445

Micelotta, E., Jones, A., & Tielens, A. 2011, IAU Symposium, 280, 257P

Mikami, H., Umemoto, T., Yamamoto, S., & Saito, S. 1992, ApJL, 392, L87

Millar, T. J., Farquhar, P. R. A., & Willacy, K. 1997, A&AS, 121, 139

Mullan, D. J. 1971, MNRAS, 153, 145

Myers, P. C. 1991, Molecular Clouds, 133

Myers, P. C., & Goodman, A. A. 1988, ApJ, 329, 392

Myers, P. C., Heyer, M., Snell, R. L., & Goldsmith, P. F. 1988, ApJ, 324, 907

Neufeld, D. A., & Melnick, G. J. 1987, ApJ, 322, 266

Neufeld, D. A., Lepp, S., & Melnick, G. J. 1995, ApJS, 100, 132

Oppenheimer, M., & Dalgarno, A. 1974, ApJ, 192, 29

Ouyed, R., & Pudritz, R. E. 1997, ApJ, 482, 712

Pelletier, G., & Pudritz, R. E. 1992, ApJ, 394, 117

Pilipp, W., Hartquist, T. W., & Havnes, O. 1990, MNRAS, 243, 685

Pilipp, W., & Hartquist, T. W. 1994, MNRAS, 267, 801

Pineau des Forets, G., Flower, D. R., & Chieze, J.-P. 1997, Herbig-Haro Flows and the Birth of Stars, 182, 199

Poglitsch, A., Herrmann, F., Genzel, R., Madden, S. C., Nikola, T., Timmermann, R., Geis, N., & Stacey, G. J. 1996, ApJL, 462, L43

Pudritz, R. E. 1985, ApJ, 293, 216

Raga, A., & Cabrit, S. 1993, A&A, 278, 267

Rawlings, J. M. C. 1998, The Molecular Astrophysics of Stars and Galaxies, edited by Thomas W. Hartquist and David A. Williams. Clarendon Press, Oxford, 1998., p.393, 4, 393

Reynolds, S. P. 1986, ApJ, 304, 713

Roberge, W., & Dalgarno, A. 1982, ApJ, 255, 176

Roberge, W. G., & Ciolek, G. E. 2007, MNRAS, 382, 717

Rodriguez, L. F., Moran, J. M., Ho, P. T. P., & Gottlieb, E. W. 1980, ApJ, 235, 845

Salpeter, E. E. 1977, ARA&A, 15, 267

Sandford, S. A., & Allamandola, L. J. 1988, Icarus, 76, 201

Santiago-García, J., Tafalla, M., Johnstone, D., & Bachiller, R. 2009, A&A, 495, 169

Savage, B. D., & Mathis, J. S. 1979, ARA&A, 17, 73

Schilke, P., Walmsley, C. M., Henkel, C., & Millar, T. J. 1991, A&A, 247, 487

Schilke, P., Walmsley, C. M., Pineau des Forets, G., & Flower, D. R. 1996, VizieR Online Data Catalog, 332, 10293

Schilke, P., Walmsley, C. M., Pineau des Forets, G., & Flower, D. R. 1997, A&A, 321, 293

Schwartz, R. D. 1975, Bull. AAS, 7, 548

Seab, C. G. 1987, Interstellar Processes, 134, 491

Shang, H., Lizano, S., Glassgold, A., & Shu, F. 2004, ApJL, 612, L69

Shu, F., Najita, J., Ostriker, E., Wilkin, F., Ruden, S., & Lizano, S. 1994, ApJ, 429, 781

Shu, F. H., Najita, J., Ostriker, E. C., & Shang, H. 1995, ApJL, 455, L155

Smith, M. D., & Mac Low, M.-M. 1997, A&A, 326, 801

Snell, R. L., Loren, R. B., & Plambeck, R. L. 1980, ApJL, 239, L17

Snell, R. L., Howe, J. E., Ashby, M. L. N., et al. 2000, ApJL, 539, L101

Smith, M. D., Brand, P. W. J. L., & Moorhouse, A. 1991, MNRAS, 248, 451

Sofia, U. J., & Parvathi, V. S. 2009, Cosmic Dust - Near and Far, 414, 236

Spitzer, L., Jr. 1941, ApJ, 93, 369

Spitzer, L. 1978, New York Wiley-Interscience, 1978. 333 p.,

Stahler, S. W., & Palla, F. 2005, The Formation of Stars, by Steven W. Stahler, Francesco Palla, pp. 865. ISBN 3-527-40559-3. Wiley-VCH , January 2005.,

Sternberg, A., & Dalgarno, A. 1995, ApJS, 99, 565

Swings, P., & Rosenfeld, L. 1937, ApJ, 86, 483

Tafalla, M., & Bachiller, R. 1995, ApJL, 443, L37

Tafalla, M., Myers, P. C., Caselli, P., & Walmsley, C. M. 2004, Ap&SS, 292, 347

Tielens, A. G. G. M. 2005, The Physics and Chemistry of the Interstellar Medium, by A. G. G. M. Tielens, pp. . ISBN 0521826349. Cambridge, UK: Cambridge University Press, 2005.,

Tielens, A. G. G. M. 2011, EAS Publications Series, 46, 3

Tielens, A. G. G. M., & Allamandola, L. J. 1987, Interstellar Processes, 134, 397

Tielens, A. G. G. M., McKee, C. F., Seab, C. G., & Hollenbach, D. J. 1994, ApJ, 431, 321

Torrelles, J. M., Ho, P. T. P., Rodriguez, L. F., & Canto, J. 1985, ApJ, 288, 595

Trumpler, R. J. 1930, PASP, 42, 214

Troland, T. H., & Heiles, C. 1986, ApJ, 301, 339

van Dishoeck, E. F. 2004, ARA&A, 42, 119

van Loo, S., Ashmore, I., Caselli, P., Falle, S. A. E. G., & Hartquist, T. W. 2009, MNRAS, 395, 319

Walmsley, C. M. 1987, NATO ASIC Proc. 210: Physical Processes in Interstellar Clouds, 161

Wardle, M. 1998, MNRAS, 298, 507

Weingartner, J. C., & Draine, B. T. 2001, ApJ, 548, 296

Whittet, D. C. B. 1993, Dust and Chemistry in Astronomy, 9

Whittet, D. C. B., & Duley, W. W. 1991, A&A Rev., 2, 167

Whyatt, W., Girart, J. M., Viti, S., Estalella, R., & Williams, D. A. 2010, A&A, 510, A74

Williams, D. A. 2007, Diffuse Matter from Star Forming Regions to Active Galaxies, 19

Williams, J. P., Blitz, L., & Stark, A. A. 1995, ApJ, 451, 252

Williams, J. P., Bergin, E. A., Caselli, P., Myers, P. C., & Plume, R. 1998, ApJ, 503, 689

Wood, P., et al. 2007, Why Galaxies Care About AGB Stars: Their Importance as Actors and Probes, 378, 251

Wright, M. C. H., Plambeck, R. L., Vogel, S. N., Ho, P. T. P., & Welch, W. J. 1983, ApJL, 267, L41

Yao, Y., Hargitai, Z., Albert. M., Albridge, R. G., Barnes, A. V., Gilligan, J. M., Pratt, Ferguson, B., Lupke, G., Gordon, V. D., Tolk, N. H., Tully, J. C., Betz, G., & Husinsky, W. 1998, Phys. Rev. Lett., 81. 550

Ziurys, L. M., Friberg, P., & Irvine, W. M. 1989, ApJ, 343, 201

Zuckerman, B., Kuiper, T. B. H., & Rodriguez Kuiper, E. N. 1976, ApJL, 209, L137